Fermilab

FERMILAB-THESIS-2001-02

Inner Structure and Outer Limits: Precision QCD and Electroweak Tests from Neutrino Experiments

Bonnie Tamminga Fleming

Submitted in partial fulfillment of the

requirements for the degree

of Doctor of Philosophy

in the Graduate School of Arts and Sciences

COLUMBIA UNIVERSITY

2002

ABSTRACT

Inner Structure and Outer Limits: Precision QCD and Electroweak Tests from Neutrino Experiments

BONNIE TAMMINGA FLEMING

Neutrinos are both excellent probes for discovering the secrets of QCD and elusive particles continually surprising us. This thesis reports first on a proton structure measurement, specifically the extraction of the proton structure function F_2 from CCFR neutrino-nucleon differential cross sections. The F_2 results are in good agreement with the F_2 measured in muon scattering above $Q^2 = 1$ GeV^2. Comparison of the two sets of data below $Q^2 = 1$ GeV^2, which provides information on the axial vector contribution, is discussed. The thesis also addresses the nature of neutrinos. Do neutrinos have mass? Do they have other Beyond-the-Standard-Model properties that can give us clues to their nature? Recent evidence from neutrino oscillation experiments from around the world indicate that neutrinos may oscillate between their different flavors and therefore may have mass. The MiniBooNE experiment discussed here will be able to address this oscillation phenomenon as well as other possible beyond Standard Model neutrino properties.

Contents

List of Tables

List of Figures

Acknowledgments

There are too many neutrinos to thank in the space I have allotted here. I am grateful to have the opportunity to acknowledge the many people who have encouraged, supported, and guided me over the course of my graduate career.

First and foremost, I am deeply grateful to my advisor, Janet Conrad, who has taught me how to be a scientist, encouraged and guided me, has set a high bar and been a wonderful example for me. She invested a lot of time in me right from the start in graduate school for which I owe her tremendous thanks. She is a great scientist and educator and I feel lucky to have been her student.

I would also like to thank Mike Shaevitz whose patience and wisdom have guided me though many a tough problem over the years. I hope to continue working with him for many years to come. I owe a great deal to Bill Seligman (and SAKAW) for all his help over the course of my thesis analysis, patiently answering my many questions even when I asked them more than once, providing advice even when I thought I had not asked and always making me smile.

I am also grateful to my fellow graduate students at Columbia, Joe Formaggio, Leven Wadley, Hayn Park, Michael Larkin, Michel Sorel and Jocelyn Monroe who have helped me get through the long haul of graduate school. Joe, Leven, and Hayn made studying for the quals a game of sorts. Michael's work in outreach and teaching taught me a great deal and set a great example for me. Michel, the PAW god, helped me make many a thesis plot look better. Jocelyn, as an undergraduate, Fermilab

employee and graduate student has made my life much more fun and has challenged me in many a road trip physics conversation. Although I have not seen him in over two years and I will be leaving just as he is returning, I am particularly grateful for Hayn's friendship and support during my first few years at Columbia.

The last few years of my graduate work at Fermilab have been a very exciting time for me. There are many people there I owe thanks to for their support and guidance. Un-Ki Yang's advice on many aspects of my structure function analysis was very helpful as was the guidance of Randy Johnson, Tim Bolton, Arie Bodek, and Lucyna de Barbaro. Paul Nienaber continues to provide endless help on absolutely everything I put in print. In particular, I would like to acknowledge Sam Zeller, my fellow NuTeV grad student, who has always had time to help me with a problem, scientific or otherwise and has been a great friend.

It has been a wonderful opportunity to work on two seperate experiments during graduate school because, among other things, I have been able to work with a number of different people. There are many people on MiniBooNE I would like to thank for the impact they made on my gradaute career. Jen Raaf, my office mate for the last year we were out at Lab E at Fermilab, worked with me on PMT testing, aided me greatly with her pest control abilities, and weathered many a strange haiku in the height of my thesis writing frenzy. Morgan Wascko helped keep me writing during trying computer times at Lab E and, along with Jen, made trailer life downright fun. Starting from the summer I spent at Los Alamos in my first year, Rex Tayloe has continued to be a great teacher and friend. Many thanks to Darrel Smith, Vern Sandberg, Randy Johnson, and Len Bugel who all spent lots of time working with me and all those PMTs. I have had the pleasure of collaborating with John Beacom within the last year and owe him many thanks for all his help with this thesis, for his guidance and humor. I would also like to thank Bill Louis for his attention, advice, and style. His attitude toward science and life make him a pleasure to work for and with.

I would like to thank Ann Therrien and Elaine Schmidt from Nevis Labs whose help made graduate student life run much more smoothly. Lalla Grimes has gone out of her way time and time again to not only make my life easier at Columbia but also make me happier about it in the process. Thank you Lalla.

The faculty at Columbia has been very encouraging and helpful over the course of my graduate career. In addition to whom I have already mentioned, I am particularly grateful for the help and support of Tim Halpin-Healy, Richard Friedberg, Yang Pang, Al Mueller, Steve Kahn, and Allan Blaer. The reason I pursued physics as an undergraduate is largely due to my undergraduate advisor, Tim Halpin-Healy. From the start he encouraged and helped me and made time for me whenever I had a problem. I am very grateful for his guidance both during my undergraduate studies, graduate school, and afterwards.

My family has been a great source of support throughout my graduate career. In particular, my sister, Cristan, has always been willing to listen to me complain and provide important scientific proofs when necessary. My mother, Carol, has set a great example for me as a scientist. Her guidance as such and as a mom has been invaluable.

Finally, I would like to thank my husband, George, for his endless well of patience, his support, and most of all, his friendship. His many readings of my thesis and interest in the content has helped to shape and strengthen my work.

Chapter 1

Introduction

The universe is one big puzzle, just when you think you know something, you take one more step forward and realize how little you really understand. I have had the privilege of seeing this first hand in the neutrino sector during the last five years....What fun! What an adventure. Neutrinos are ghostly little particles that can help us probe matter but still leave us guessing.

1.1 Neutrinos and the Standard Model

The neutrino or "little neutral one" was introduced in 1930 by Wolfgang Pauli as a means for explaining the missing energy carried away in beta decay [1]. Since then, scientists have studied these elusive particles in order to fit them into our picture of the universe. Figure 1.1 shows the building blocks of matter in our universe organized into a periodic table. These particles comprise the Standard Model of particle physics.

The twelve particles on the left of figure 1.1, and listed in table 1.1, are fermions, meaning they carry spin $\frac{1}{2}$. Each fermion has an anti-particle partner. As shown in table 1.2, the quarks form the building blocks of the proton, neutron and other composite particles. Neutrinos, on the other hand, are members of the lepton family

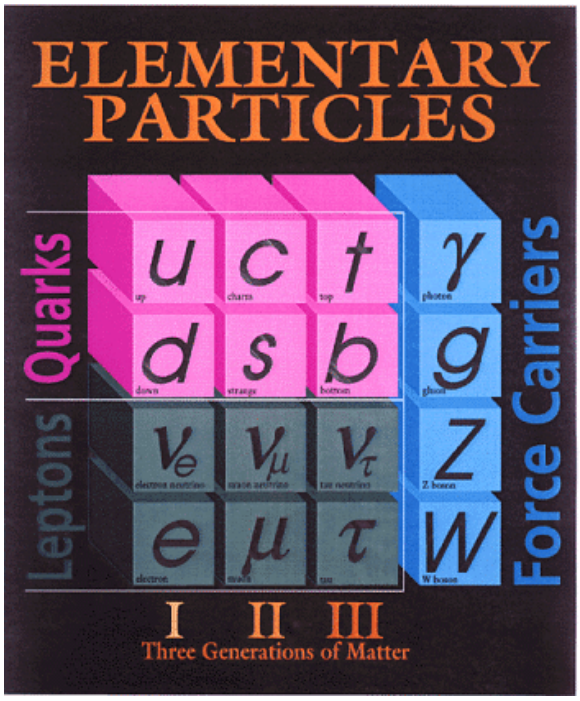

Figure 1.1: The Standard Model building blocks, the quarks and leptons, and force carriers for the strong, weak, and electromagnetic forces.

(from the Greek word "leptos," or thin), a group of particles which are independent in nature and do not form bound states. Neutrinos come in three flavors forming a partnership with each of the three different more well known charged leptons: the electron, the heavier muon and the still heavier tau. These tiny particles are electrically neutral and very shy, hardly interacting at all. A 100 GeV neutrino has a mean free path of 3×10^9 meters in steel, and so we say the interaction involving neutrinos is "weak."

The Standard Model describes the interactions of the leptons and quarks via three of the fundamental forces of nature: weak, strong and electromagnetic. The interactions are described in terms of particle exchange where particle mediators listed in table 1.3 are the force carriers in the interactions. Neutrinos are unique in the theory in that they only interact via one of these three fundamental forces, the weak force. Because the theory describes the expectation for the weak interaction very well,

Name	Symbol	Charge	Mass, Mass Range or Mass Limit
up	u	$+\frac{2}{3}$	1.5 to 5.0 MeV
charm	c	$+\frac{2}{3}$	1.1 to 1.4 GeV
top	t	$+\frac{2}{3}$	173.8 ± 5.2 GeV
down	d	$-\frac{1}{3}$	3 to 9 MeV
strange	s	$-\frac{1}{3}$	60 to 170 MeV
bottom	b	$-\frac{1}{3}$	4.1 to 4.4 GeV.
electron	e	-1	$0.51099907 \pm 0.00000015$ MeV
muon	μ	-1	105.658389 ± 0.000034 MeV
tau	τ	-1	$1777.05^{+0.29}_{-0.26}$ MeV
electron neutrino	ν_e	0	$< 3\ eV$
muon neutrino	ν_μ	0	< 0.17 MeV
tau neutrino	ν_τ	0	< 18.2 MeV

Table 1.1: Masses of the fermions in the Standard Model [2].

Quarks	Fundamental particles which interact via the strong, weak and electromagnetic forces. They carry fractional electric charge.
Leptons	Fundamental particles that do not interact via the strong force. They may have integral electric charge or be neutral.
Hadrons	Any particle made up of quarks
Mesons	Hadrons made of quark-anti-quark pairs (*e.g.* the pion)
Baryons	Hadrons made of three quarks (*e.g.* the proton)

Table 1.2: Definitions of particles used in this text.

Interaction	Relative strength [a]	Mediator	Charge	Mass	Participating fermions
strong	1	gluons (g)	0	0	quarks
electro-magnetic	10^{-2}	photon (γ)	0	$< 2 \times 10^{16}\ eV$	quarks and charged leptons
weak	10^{-5}	$W^{\pm}$, Z^0	± 1, 0	80.41 $\pm$ 0.10 GeV, 91.187 $\pm$ 0.007 GeV	all

Table 1.3: Interactions in the Standard Model. The relative strengths of the forces are roughly indicated, for short distance scales of a few GeV^{-1}.

[a] for 100 GeV particle interaction

neutrinos are excellent probes for new physics as well as for understanding the constituents of the matter with which they interact. Figure 1.2 shows the different types of physics that can be learned by studying different aspects of neutrino interactions with matter.

To begin with, there are still many unanswered questions concerning the properties of the incoming neutrino at the top left corner of figure 1.2. For example, all of the charged fermions that make up matter in our universe have a measurable mass except, so far, the neutrino... Do neutrinos have mass? The answer to this question could alter our understanding of the cosmos as well as how these ghostly particles fit in the Standard Model of particle physics. With approximately 10^9 remnant neutrinos from the Big Bang in every cubic meter of space, even a tiny mass will affect the large scale galactic structure and the expansion of the universe. Neutrino masses may give us clues to the lepton mass hierarchy as well as require introduction of new particles and interactions to the theory.

Neutrinos are so light that we have not been able to measure their mass by conventional methods. Instead, clues to their mass, like neutrino oscillations, have been used to indirectly measure neutrino mass. If neutrinos oscillate between their different flavors, for instance, a ν_μ turns into a ν_e, then quantum mechanics tells us

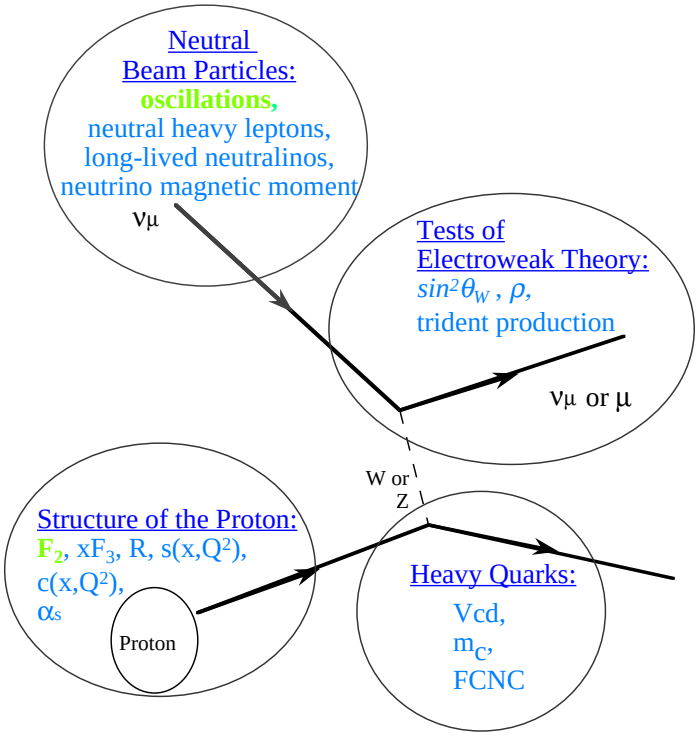

Figure 1.2: Neutrinos help us study a gamut of interesting physics.

neutrinos have mass. This flavor mixing phenomena has been observed in the hadron family where quark flavors can mix.

Do neutrinos have other "Beyond the Standard Model" interactions we have not yet observed? A variety of extensions to the Standard Model such as those that incorporate neutrino mass, Supersummetry(SUSY), or Large Extra Dimensions, predict non-zero neutrino magnetic moments. A non-zero neutrino magnetic moment would indicate that neutrinos are not so exclusive as they would have us think. It would indicate that neutrinos interact electromagnetically as well as weakly.

Continuing clockwise on figure 1.2, one can see that the outgoing particle can either be a charged lepton or a neutrino. If a charged lepton comes out, then we call this a charged current (CC) interaction. If a neutrino comes out, we call this a neutral current (NC) scatter. The CC interaction results in a charged lepton because a $W^{\pm}$ is emitted and charge must be conserved at the interaction vertex. This is

quite different from your typical elastic interaction, where what comes in is always what comes out.

In the CC interaction, the type of charged lepton which results from the interaction "tags" the type of neutrino which was involved. An electron neutrino will always produce an electron in the final state of the CC interaction. Similarly, muon neutrinos always produce muons and tau neutrinos always produce taus. Without the CC interaction, we would not be able to tell the three types of neutrinos apart.

The ratio of the NC to CC interactions is a fundamental parameter of the Standard Model, typically parameterized as $\sin^2\theta_W$. This parameter can be constrained from other types of experiments, such as e^+e^- scattering and hadron collisions, and these results can be compared to measurements from neutrino experiments. Deviations between the measurements would indicate physics beyond the Standard Model. Measurement of this parameter has been an important goal of recent neutrino experiments [3, 4], however we will not explore this in further detail in this thesis.

This brings us to the bottom of figure 1.2. We can use the W's emitted by neutrinos as probes of nucleon structure. We can then compare our studies with data from charged lepton scattering, where the photon is used as the probe, in order to understand the quarks which reside in the nucleon.

In the early twentieth century, scientists thought that protons, the positively-charged inhabitants of atomic nuclei, were fundamental and could not be divided into smaller sub-particles. In the years that followed, as experiments probed more deeply into the nature of nuclear matter, this theory had to be modified. In 1964, Murray Gell-Mann proposed that protons were built from more elementary constituents that he called "quarks." [5, 6] The quark model was confirmed by experiments in the 1970's.

The big improvement in these later experiments had to do with their resolving power, the minimum size or distance scale to which the experiment could determine

intra-particle detail. Figure 1.3 depicts the proton viewed at increasingly finer levels of resolution. Protons are probed by bombarding them with other particles and inspecting the particle debris leftover after the collision. In the early experiments, the proton appeared as an undifferentiated whole, a point-like object. But, with increasing energy in later investigations, researchers could resolve features at finer and finer levels of detail. They discerned distinct component objects, consistent with three "valence quarks," within the nucleon. The quantum numbers of the valence quarks define the type of nucleon, much like its DNA. For example a proton has two up valence quarks and one down valence quark. A neutron has two down and one up quark. However, the nucleon cannot consist of only the three quarks, because the electromagnetic interactions between these particles and the other particles in the universe would make the system unstable. Quarks adhere to each other by means of the give and take of gluons. As the proton is probed at still higher resolution, indications of these gluons can be seen. Inside the proton, these gluons can transmute themselves into quark-anti-quark pair, and then back again. These particle-anti-particle pairs live for brief periods under one of the rules of quantum physics, the Heisenberg Uncertainty Principle. Since the characteristic properties of each produced particle, its quantum numbers, are counterbalanced by the opposite numbers of the anti-particle, no laws of nature are violated in this production. These short-lived pairs, revealed at high levels of resolution, form a background "sea" of quarks and gluons surrounding the three valence quarks. Thus, as we increase resolution we reveal the ebb and flow of quarks and gluons into and out of existence as described by the theory of strong interactions, Quantum Chromodynamics (QCD). As a family, the quarks and gluons are called partons.

Neutrinos are particularly good at probing nucleon structure. Because they interact via the weak force, they can pick out individual contributions to the nucleon from its constituents, or partons. This is because the W is charged. A W^+ can interact with a d ($-\frac{1}{3}$ charge) quark to produce a u ($+\frac{2}{3}$ charge), but not a $\bar{d}$ ($+\frac{1}{3}$

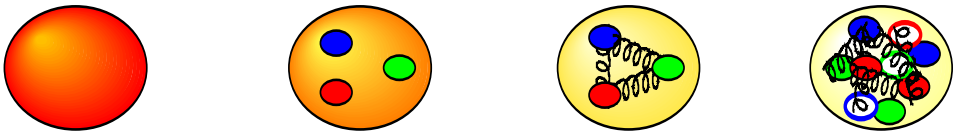

Figure 1.3: A nucleon viewed with increasing resolution, or Q^2, from left to right.

charge) since there is no corresponding $+\frac{4}{3}$ charged quark to be produced. Therefore neutrinos have the unique advantage of looking inside nucleons and picking out the different quark species inside. We describe combinations of parton distributions in terms of structure functions (F_2, xF_3, R, etc). We can also identify the flavor of the quark which was hit by looking for the characteristic signature of production of a heavy quark, like charm.

Coming full circle in figure 1.2, it is clear that the neutrino is an excellent tool for understanding and going beyond the Standard Model. Just during my tenure as a graduate student, there have been many new surprises from this tiny particle. The future of neutrino physics will certainly be an adventure.

1.2 Synopsis of this Thesis

This thesis addresses two experiments. The first, on which I present an analysis of data, is CCFR, a high energy neutrino experiment which took data in the late 1980's. The second, MiniBooNE, is a moderate energy neutrino experiment presently under construction. I have been a member of MiniBooNE since its proposal stage. I have participated in its construction, and considered its capability in the near and far future.

In topics, this thesis will cover the gamut of neutrino physics. The organization will follow the chronological order of the neutrino experiments, and reverse order of

the discussion of figure 1.2 above. The first part of this thesis describes a measurement of the F_2^ν structure function in high energy neutrino scattering using data from the CCFR experiment. The second part describes the search for nonstandard neutrino interactions such as neutrino oscillations and neutrino magnetic moment searches using the ongoing MiniBooNE experiment. I then extend these ideas to a possible future experiment using a conventional neutrino superbeam. Taking these two parts as a whole, this thesis can be said to probe both inner structure and outer limits of high energy physics through neutrinos.

Part I

Proton Structure Measurements from Neutrino Scattering

Chapter 2

Neutrino Deep Inelastic Scattering and Precision QCD

2.1 The Formalism of Neutrino Deep Inelastic Scattering

You can never be too light, too neutral, or too exclusive. Neutrinos are excellent nucleonic probes because they are effectively massless, neutral, and interact only via the weak force. A typical neutrino-nucleon interaction is shown in figure 2.1. The variables used to describe the interaction are the parameter Q^2, the momentum transferred to the proton as it is probed, and "Bjorken x," the fraction of the proton's total momentum carried by the quark struck by the incoming probe. Q^2 characterizes the resolution of the probe. As Q^2 increases, the resolving power increases and the interior of the proton can be seen in finer and finer detail as shown in figure 1.3 in the previous chapter.

The evolution of the proton from the left side of figure 1.3 to the right is not as simple as it may appear. In order to describe this, the interaction cross section is written not as single particle exchange, but rather it is parameterized in terms of

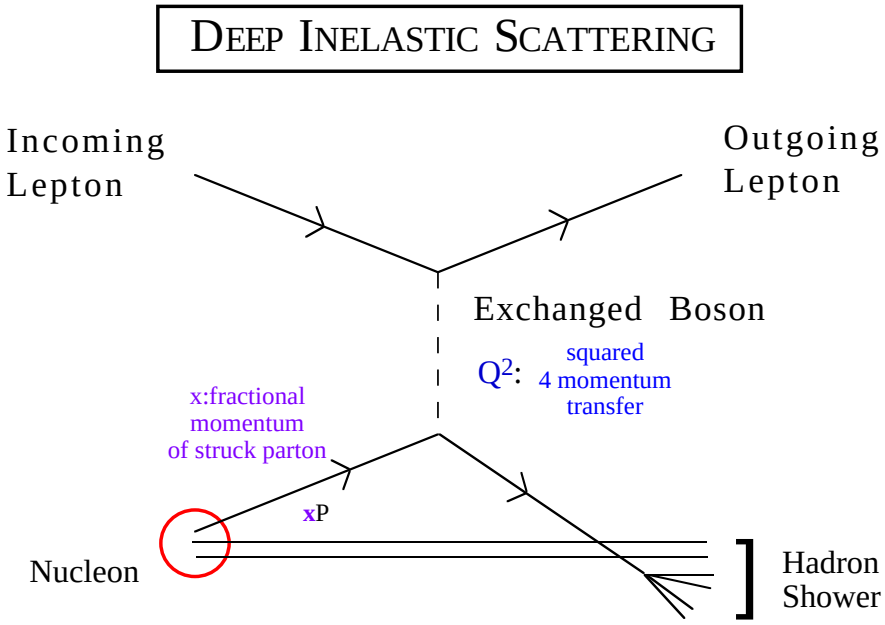

Kinematic Quantities

Energy Transfer	$\nu = E_{had}$
Fractional Energy Transfer	$y = \nu/(E'+E_{had})$
Negative squared 4-momentum Transfer	$Q^2 = 4(E'+E_{had})E'sin^2(\theta/2)$
Fractional momentum of struck quark	$x = Q^2/2M\nu$

Figure 2.1: Neutrino-nucleon interaction.

quantities called "structure functions." This is underlined by the Feynman diagram of this process commonly drawn as in figure 2.2. The W boson-proton vertex drawn as a black circle, is still not well understood.

The differential cross-sections for the neutrino-nucleon charged-current process $\nu_\mu\,(\overline{\nu}_\mu) + N \rightarrow \mu^-\,(\mu^+) + X$ in the limit of negligible quark masses and neglecting lepton masses, in terms of the Lorentz-invariant structure functions F_2, $2xF_1$, and xF_3 is:

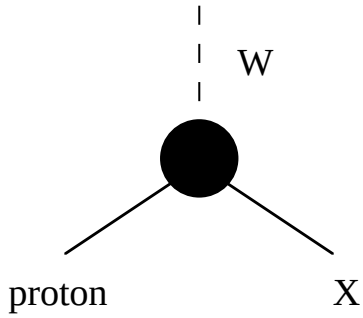

Figure 2.2: Feynman diagram of W boson-proton interaction. X may be a nucleon or hadronic debris.

$$\frac{d\sigma^{\nu,\overline{\nu}}}{dx\,dy} = \frac{G_F^2 M E_\nu}{\pi}\left[\left(1-y-\frac{Mxy}{2E_\nu}\right)F_2\left(x,Q^2\right) + \frac{y^2}{2}2xF_1\left(x,Q^2\right) \pm y\left(1-\frac{y}{2}\right)xF_3^{\nu,\overline{\nu}}\left(x,Q^2\right)\right] \tag{2.1}$$

where G_F is the weak Fermi coupling constant, M is the nucleon mass, E_ν is the incident ν energy, Q^2 is the square of the four-momentum transfer to the nucleon, the scaling variable $y = E_{\mathrm{HAD}}/E_\nu$ is the fractional energy transferred to the hadronic vertex with E_{HAD} equal to the measured hadronic energy, and $x = Q^2/2ME_\nu y$, the Bjorken scaling variable, is the fractional momentum carried by the struck quark. See [7] for a complete derivation of this formula. The structure function $2xF_1$ is expressed in terms of F_2 by $2xF_1(x,Q^2) = F_2(x,Q^2) \times \frac{1+4M^2x^2/Q^2}{1+R(x,Q^2)}$, where $R = \frac{\sigma_L}{\sigma_T}$ is the ratio of the cross-sections of longitudinally- to transversely-polarized W bosons.

F_2 can be thought of as the probability of finding a quark with momentum fraction x. If there were only three valence quarks in the nucleon, each one would carry a third of the proton's momentum. In this case, F_2 as a function of x is sharply peaked at x = 1/3 (see figure 2.3; the diagram at the far left). If these quarks were exchanging gluons, their momentum would be smeared out as shown in the middle diagram. The presence of sea quarks leads to a pile up of low momentum (lox x) quarks as shown at the far right. F_2 also changes as a function of Q^2. Q^2 can be thought of as probe

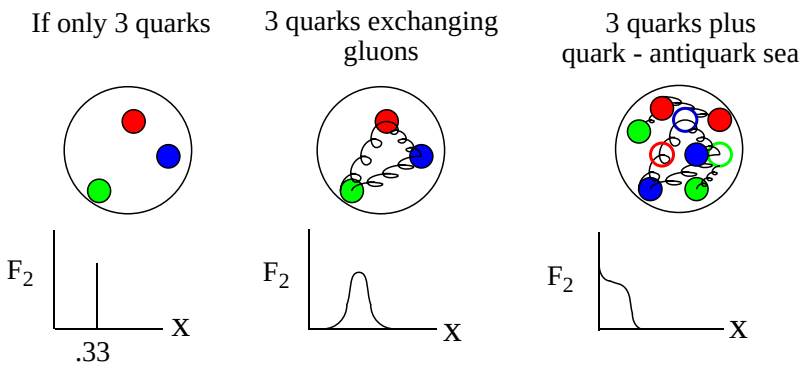

Figure 2.3: F_2 as a function of x for a proton that has only three quarks (left), three quarks sharing gluons(middle), or three quarks, many sea quarks and many gluons (right).

whose wavelength corrresponds to it's strength. As shown in figure 2.4, at low Q^2, the wavelength of the probe is large and the proton is resolved as a structureless object. As Q^2 increases and the wavelength of the probe increases, the quarks and gluons can be resolved. At high Q^2, the structure funciton F_2 becomes independent of Q^2 indicating that the quarks themselves appear structureless on this scale. That F_2 is dependent only on x and high Q^2 is known as Bjorken scaling.

In the leading order (LO) quark-parton model, F_2 is the sum of the momentum densities of all interacting quark constituents while xF_3 is the difference of these, written as:

$$F_2^{(\nu,\overline{\nu})}\left(x,Q^2\right) = q\left(x,Q^2\right) + \overline{q}\left(x,Q^2\right) \approx q_{\text{valence}} + q_{\text{sea}} \tag{2.2}$$

$$xF_3^{(\nu,\overline{\nu})}\left(x,Q^2\right) = q\left(x,Q^2\right) - \overline{q}\left(x,Q^2\right) \approx q_{\text{valence}}. \tag{2.3}$$

F_2 describes the behavior of all the quarks in the nucleon, the valence and the sea, while xF_3 describes only the valence quarks. Figure 2.5 shows that as x decreases and more of the quark sea is resolved, the momentum carried by the valence plus the sea quarks, F_2, increases relative to that carried by the valence quarks only, xF_3.

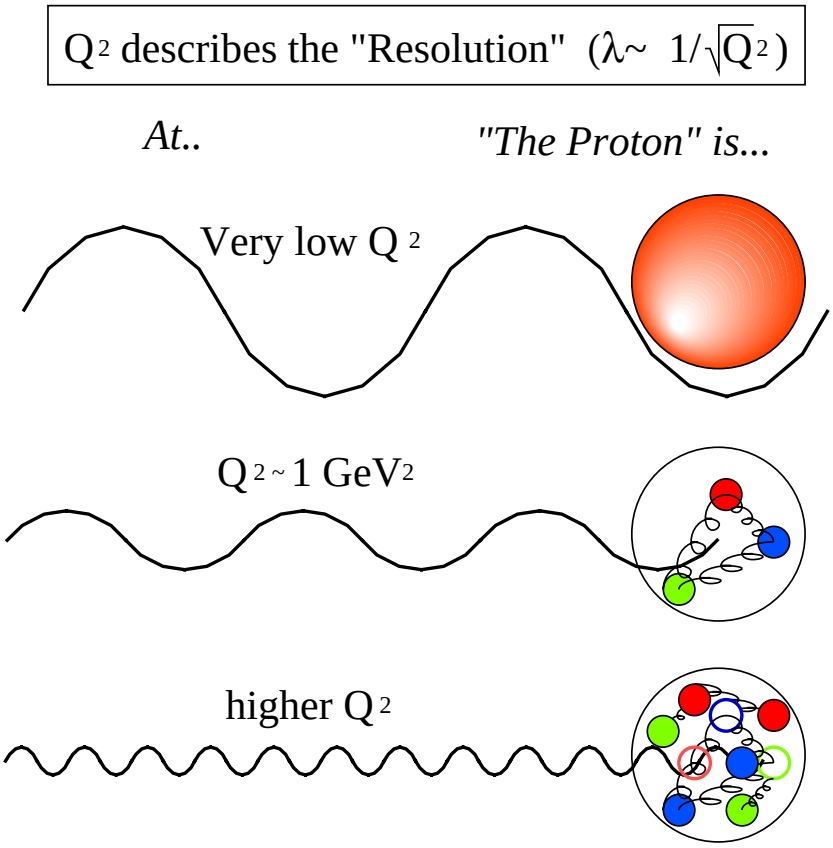

Figure 2.4: The proton probed at different values of Q^2. At low Q^2, the proton appears to be a structureless object. As Q^2 increases, quarks and gluons can be resolved.

Quark and gluon distributions, known as parton distribution functions (PDFs) can be determined from these structure functions.

For a given neutrino energy, two variables, for example x and Q^2, are necessary to define the interaction of the probe with the proton and hence, both are necessary to quantitatively describe proton structure. While we understand the general dependence of F_2 and xF_3 over a broad range of x and Q^2, the behavior of the quarks and gluons inside the proton in some regions of the space mapped out by x and Q^2 is not well understood – in particular, the region of low x and low Q^2. In this region, several questions persist: How do these momentum densities, or structure functions, vary as the probe is changed? Does the momentum density of the struck quark tend

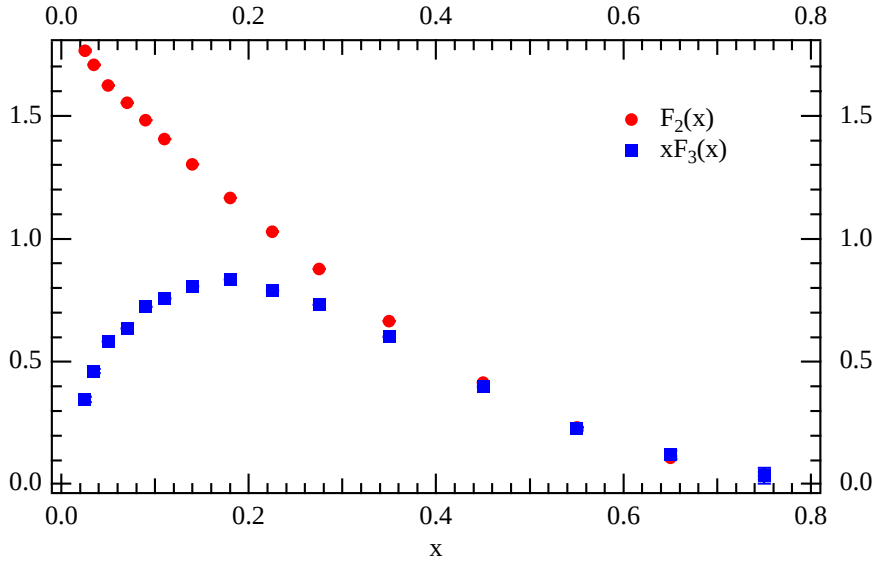

Figure 2.5: F_2 and xF_3 as a function of x [7].

to zero as $Q^2 \to 0$ GeV^2?

Several experiments from accelerator laboratories around the world have made measurements of the proton structure function, F_2 [8, 9, 10]. It is particularly interesting to compare results from experiments that use fundamentally different probes to measure proton structure, for example, using neutrinos versus charged leptons. One would expect the structure to be essentially the same, and the results to agree independent of the probe employed, unless there is some fundamental difference in the way in which the probes and the proton interact. Figure 2.6 shows the kinematic coverage of most of the deep inelastic scattering experiments conducted. The charged lepton experiments may use electrons or muons as probes. Comparisons between structure function measurements from these experiments and from neutrino scattering experiments can teach us about proton structure particularly in the low x, low Q^2 region.

2.2 Cross Sections at Low x and Low Q^2 and Adler's Relation

At low x and low Q^2, the structure function F_2 from neutrino scattering experiments should not necessarily agree with results from charged lepton scattering experiments. Theoretical predictions indicate [11] that in this limit, as $Q^2 \to 0$ GeV^2, F_2 for muon scattering should go to zero, but F_2 for neutrino scattering should go to some positive constant. The reason for this difference lies in the ways neutrinos and muons interact with protons. For leptons with electric charge, the primary interaction with protons is electromagnetic by exchange of a photon, or γ. As $Q^2 \to 0$, the photon becomes real and the structure function $F_2^{e,\mu}$ is constrained to vanish linearly with Q^2 because the photon is massless due to gauge invariance. It is theorized that because of the Partially Conserved Axial Current (PCAC) of the weak interaction, the proton structure function, F_2, from neutrino scattering experiments will not go to zero at $Q^2 = 0$, but will have some residual, non-zero value. How does this value arise?

At small Q^2, the exchange W boson becomes real and can fluctuate to another particle, for example, a pion. The interaction can then be drawn as in figure 2.7 where the pion, instead of the W boson, interacts with the nucleon. Adler [11] used this interaction picture to rewrite the cross section for neutrino-nucleon scattering in terms of the pion-nucleon cross section. A consequence of this theory is the prediction that F_2^ν approaches a non-zero constant as $Q^2 \to 0$, confirmation of the PCAC nature of the weak interaction.

This analysis measures the structure function, F_2^ν in a previously unexplored kinematic region at low x and low Q^2. The results are compared to $F_2^{\mu,e}$. Using this data, tests of Adler's predictions for neutrino scattering are made. In the following three chapters, the experiment used to obtain this measurement is described, the analysis method is discussed and the conclusions are presented.

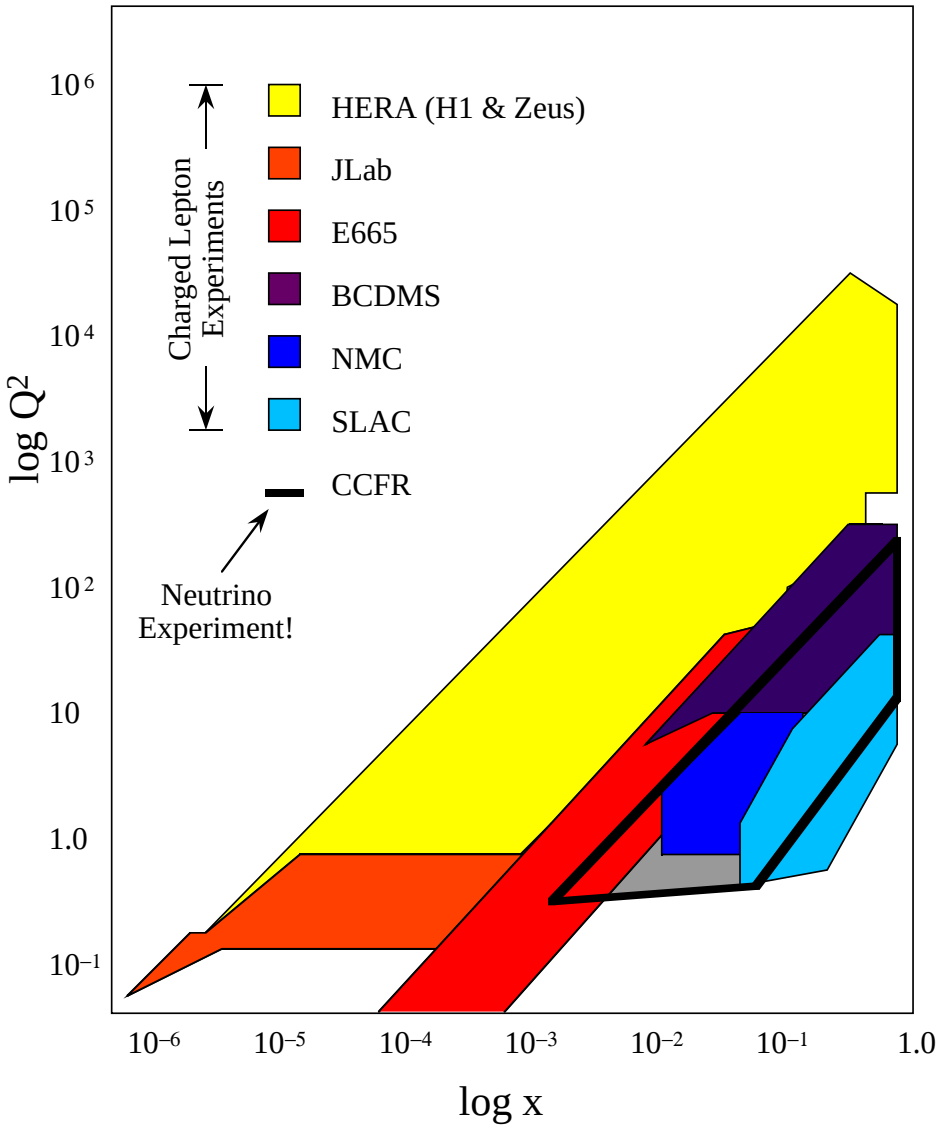

Figure 2.6: Kinematic coverage of neutrino and charged lepton deep inelastic scattering experiments as a function of log x shown across the bottom axis and log Q^2 (GeV^2) down the side axis.

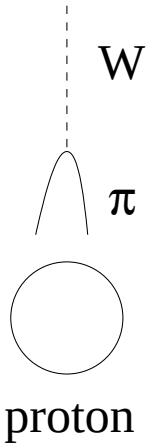

Figure 2.7: W boson fluctuates to a π which then interacts with the proton.

Chapter 3

CCFR Neutrino Beam and Detector

The weak force isn't called weak for nothing. Neutrinos interact only via the weak force and even then, very infrequently. Therefore, neutrino detectors must be massive – hundreds of tons – and neutrino beams must be intense, in order to raise the probability of a neutrino interaction to something sizable enough for significant measurements.

The CCFR neutrino experiment was performed at the Fermi National Accelerator Laboratory. Fermilab's 800 GeV proton beam was used to produce a wide-band, intense beam of neutrinos and anti-neutrinos incident on the CCFR detector in Lab E. The detector consisted of a 690 ton iron sampling calorimeter followed by a muon spectrometer. It was both the target in which the neutrinos scattered and the instrument that measured the properties of the neutrino events. The data were gathered in two runs:

- E744: February-August, 1985
- E770: June-February, 1987

This chapter describes the experimental apparatus: the accelerator facilities at Fermilab, the neutrino beam, and the CCFR detector.

3.1 The Fermilab TeVatron

The CCFR experiment took place at the Fermilab TeVatron, the highest energy accelerator in the world at the time of this writing. A schematic diagram of the neutrino beamline in the Fermilab accelerator complex is shown in figure 3.1. A brief description of the accelerating process follows. A more complete description can be found in reference [21].

In "fixed-target mode" the TeVatron operates on a 60 s cycle during which 10^{13} protons are accelerated and delivered to the neutrino beamline. The protons' trip through the machines begins in the Cockroft-Walton where they are accelerated to 750 keV and injected into the 200 MeV LINAC. From here, they travel to the 140 m diameter Booster synchrotron. The Booster brings the proton energy up to 8 GeV and sends them into the Main Ring and then the TeVatron ring. The Main Ring, a 2 km in diameter synchrotron with conventional, copper-coiled magnets, accelerates the particles up to 150 GeV. They are then injected into the TeVatron, a superconducting proton synchrotron that sits directly below the main ring. The TeVatron accelerates the protons to 800 GeV and holds them at their maximum energy for about one third of the cycle before extraction to the switchyard and neutrino beamline.

The neutrino beam is created from TeVatron fast extracted proton spills called pings which are of millisecond duration. This fast spill structure is used to minimize the number of cosmic rays which might enter the detector during the beam-on period.

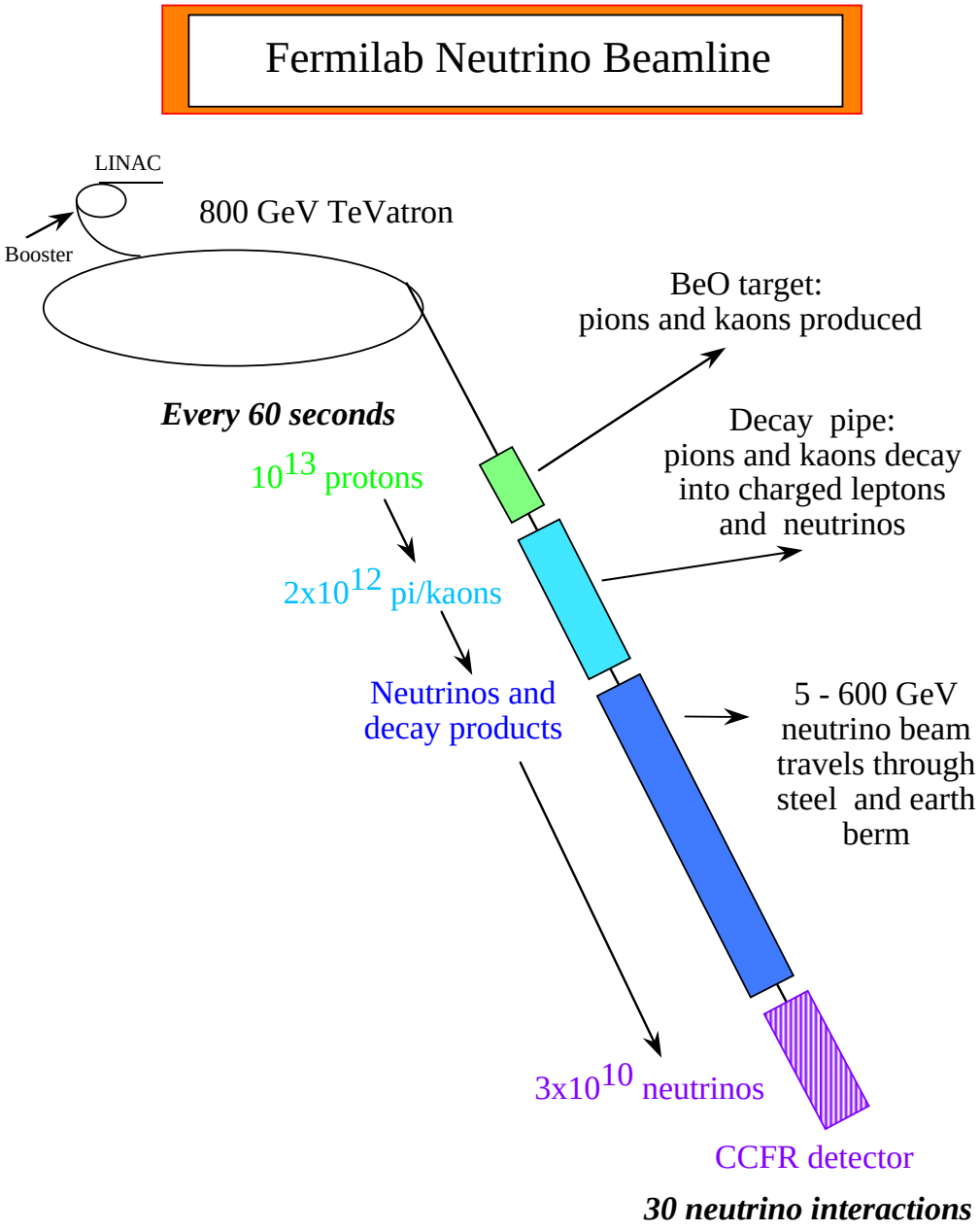

Figure 3.1: Fermilab neutrino beamline layout.

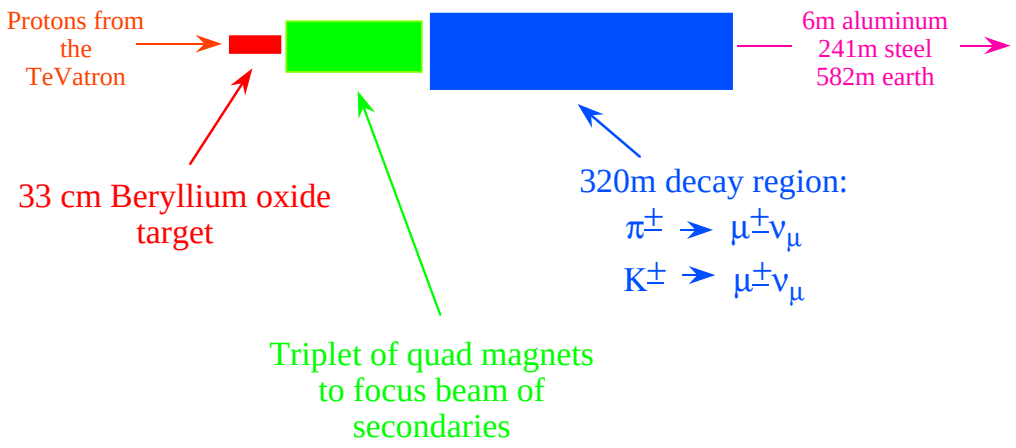

Figure 3.2: CCFR target area and decay region

3.2 Neutrino Beam

For neutrino production, the proton beam was steered onto a beryllium-oxide target 33 cm long. This produced a secondary beam of mesons focused by a triplet of quadrupole magnets toward a 320 m decay region 221 m beyond the target. Figure 3.2 shows the target and decay region. The highest possible neutrino flux downstream can be achieved only if no sign or momentum selection is done. The result is a "wide-band" beam, that is, one with large momentum acceptance. The mesons produced at the target, primarily pions and kaons, decay in flight, with dominant decay modes:

$$\pi^+ \to \mu^+\nu_\mu,\ \pi^- \to \mu^-\overline{\nu}_\mu \quad BR = 99.99\% \tag{3.1}$$

$$K^+ \to \mu^+\nu_\mu,\ K^- \to \mu^-\overline{\nu}_\mu \quad BR = 63.5\% \tag{3.2}$$

The maximum neutrino energy in the beam is determined by the mass ratio of the muon and the decaying particle:

$$E_\nu^{max} = E_{\pi,K}\left[1 - \left(\frac{m_\mu}{M_{\pi,K}}\right)^2\right] \tag{3.3}$$

This produces a neutrino beam with a dichromatic spectrum, with the more energetic neutrinos coming from the kaon decays:

$$\left(E_\nu^{max}\right)_K = 0.95E_K \tag{3.4}$$

$$\left(E_\nu^{max}\right)_\pi = 0.43E_\pi \tag{3.5}$$

The neutrinos and anti-neutrinos produced had an average neutrino energy of about 140 GeV with maximum neutrino energies as high as 600 GeV. Figure 3.3 shows the double peaked neutrino energy spectrum for E770 and E744.

About 6-7% of the mesons decay in the decay region. The undecayed mesons are dumped into a 6 m block of aluminum followed by steel shielding downstream of the decay channel. 241 m of steel shielding and 582 m of earth berm follow the decay region. Muons or mesons that penetrate the steel shielding downstream of the decay channel range out in the steel and earth berm.

Almost all of the neutrinos pass through the berm to the detector. However those that do interact in the berm can produce muons which can penetrate to the detector. These muons are identified by interaction in a veto wall just upstream of the detector, and are used for calibration purposes. The neutrinos strike the target calorimeter at near normal incidence, having an incident angle no larger than $\sim$ 1 mrad.

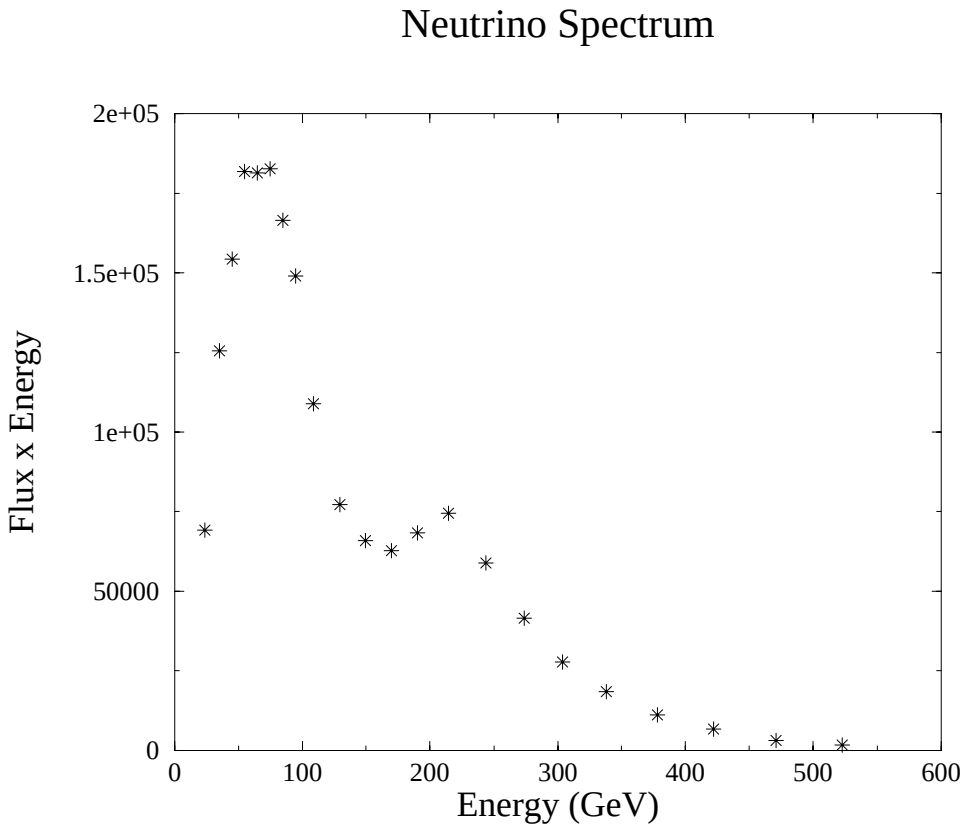

Figure 3.3: Neutrino spectrum from E770. Spectrum is double-peaked corresponding to neutrinos from pion decay at lower energies and kaon decays at higher energies.

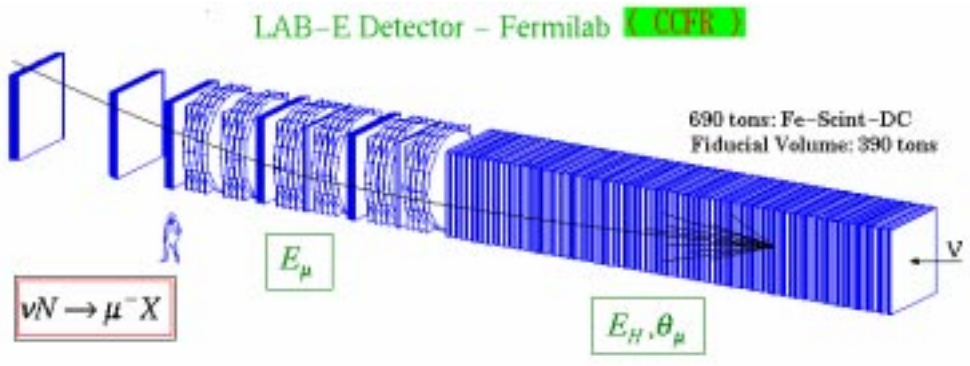

Figure 3.4: Schematic representation of the CCFR detector. The neutrino beam enters from the right into the target calorimeter. The muon spectrometer follows.

3.3 CCFR Detector and Trigger

The following sections briefly describe the elements of the CCFR detector and trigger system. Please see [12, 13] for a more complete description. Figure 3.4 shows a schematic of the entire CCFR neutrino detector with a person shown to indicate the scale. In this schematic, the beam enters from the right. The detector is a target calorimeter consisting of steel, scintillator and drift chambers shown at the right of figure 3.4 followed by a muon spectrometer. Neutrinos interact via charged or neutral current interactions in the detector as shown in figures 3.5 and 3.6. In these event displays, the drift chamber hits are indicated with crosses. Energy deposited in the scintillator planes of the calorimeter is shown by the histogram at the top of each figure. The hallmarks of an event are: no upstream hits, a shower at the interaction vertex, and for charged current events, an outgoing muon. The detector measures three kinematic quantities for each event: the energy of the outgoing hadron shower, E_{HAD}, and the angle and momentum of the outgoing muon in charged current events, θ_μ and p_μ respectively. The curvature of the outgoing muon in the muon spectrometer tags the charge of the muon and therefore the species of the neutrino, ν or $\overline{\nu}$.

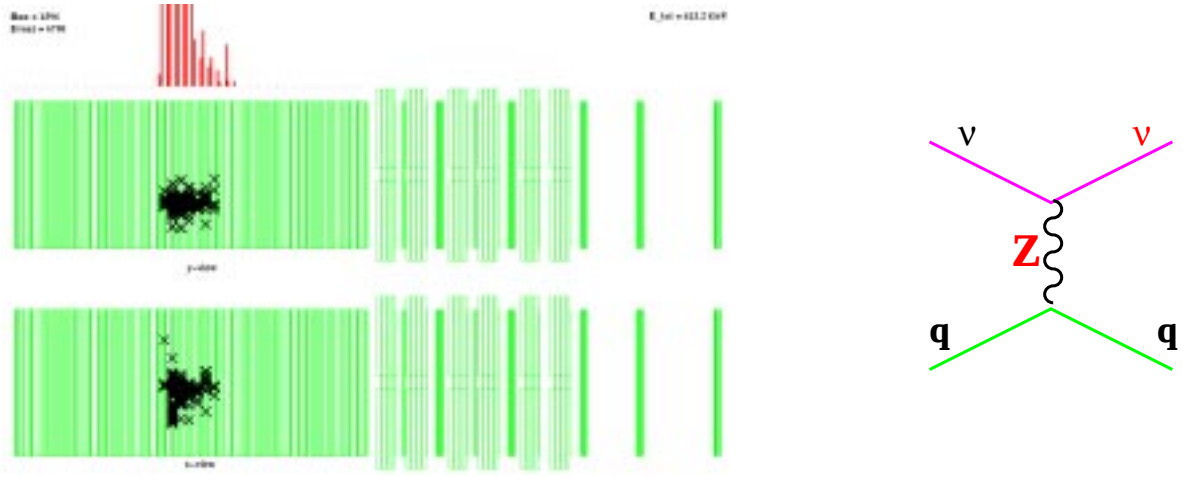

Figure 3.5: A typical neutral current event in the detector. In this picture, the beam comes from the left incident on the target calorimeter which is followed by the toroid spectrometer.

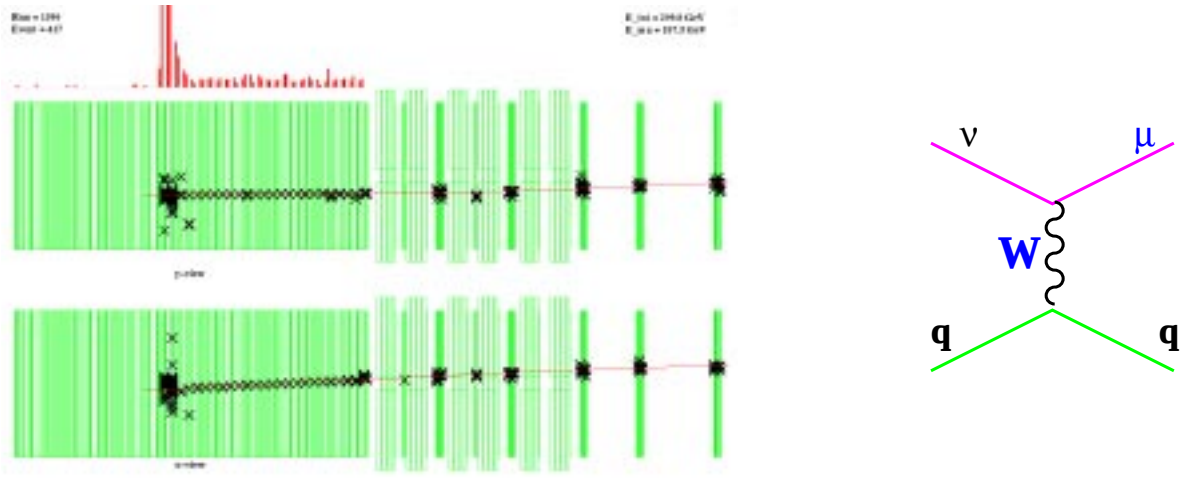

Figure 3.6: A typical charged current event in the detector. In this picture, the beam comes from the left incident on the target calorimeter which is followed by the toroid spectrometer.

3.3.1 Target Calorimeter

The Target Calorimeter was a 690 ton stack of steel plates and instrumented planes that served as both the target for the neutrinos and the instrument to measure properties of the interaction. The steel plates were the neutrino target while scintillator planes and drift chambers interspersed allowed for energy deposition measurements and particle tracking. The entire stack was 3×3 m transversely and 17.7 m long. It was comprised of 6 modules called carts. Each cart contained 28 steel plates, 14 scintillator planes, and 7 drift chambers. These components are described in detail in table 3.1.

3.3.2 Muon Spectrometer

A muon spectrometer following the target calorimeter was used to track muons emerging from charged current neutrino interactions. The spectrometer was comprised of three large toroidal iron magnets separated into three instrumented carts. There were five sets of five drift chambers immediately downstream of each cart and at 3 m and 7 m after the last cart. Plastic scintillator for fast detection of muons were located after the first two toroid carts. The toroid provided a magnetic field to deflect the muon, while the drift chambers provided tracking to record the particle deflection, allowing for measurement of the muon's momentum. The toroid could be run in either polarity to focus positively- or negatively-charged muons. The components comprising the spectrometer are described in table 3.2.

Table 3.1: **Target Calorimeter Components**

Target Calorimeter Component	Purpose	Size	Makeup	Resolution	Readout
Veto Wall	To veto beam related backgrounds	17.5 × 4.5 m	Scintillation counters downstream of a 1 m thick concrete shielding wall located just upstream of target Calorimeter		
Steel Plates	Target for neutrino interactions	5.15 cm thick, 3 × 3 m transversely	Steel		
Drift Chambers	Record path of charged particles by detecting the liberation of ionizing electrons	8.87 cm thick, 3 × 3 m transversely	24 horizontal and 24 vertical cells. Each cell is 1.27 cm across and 1.9 cm thick with three wires in each	Position resolution: 225 μm	Signal sent to two coupled TDC digitizers with 4 ns resolution and total live time of 2 μs
Scintillation Counters	Measures energy deposition of passing charged particles when particles excite fluors. Excited light travels to counter edges and piped to PMTs.	6.84 cm thick, 3 × 3 m transversely	Plastic boxes filled with mineral oil doped with scintillating fluors coated with light tight material. PMTs at each corner (RCA 6342A) run at 1400 V	Sensitivity to a muon traveling through the center of the counter is 2.5 PE's per PMT.	PMT readout: digitized by LeCroy 4300 FERA. Counter readout: ADC channels with gate width: 244 ns starting 30 ns before PMT leading edge. Resolution leads to 11.7 μs of dead time. Overall event time resolution: 2.4 ns from TDCs on each PMT.

Table 3.2: **Muon Spectrometer Components**

Muon Spectrometer Component	Purpose	Size	Makeup	Resolution
Toroid	Provides magnetic field to bend charged particles	Toroid is separated into three instrumented carts with 8" thick cylinders called washers. Washers have an outer radius of 70" and an inner radius of 5". Eight washers make up one cart.	Four copper coils of 12 turns each encircle the magnet at 90 degree intervals. 1200 A produce a $1.55-1.9$ T magnetic field.	A muon traveling the length of the spectrometer receives a 2.4 GeV transverse momentum component from the magnetic field.
Drift Chambers	Tracks muons to make muon momentum measurement	3×3 m transversely	Comprised of one wire cells staggered by $\frac{1}{4}$ cell width to resolve left-right ambiguity	Aligned to within 380 μm. Position resolution$= 0.5$ mm
Plastic Scintillator :T2 after the first cart and T3 after the second.	ast detection of muons for triggering	3×3 m transversely	Counters equipped with 56AVP phototubes, referred to as hodoscope, meaning a counter capable of making a good measurement of particle position	No position measurement made since counters are to fire triggers
Acrylic Counters: between washers	Define trigger conditions	3×3 m transversely	Acrylic counter plane positioned after every washer. Each plane divided into four separate counters to determine through which quadrant muon passed.	

3.4 Data Acquisition and Event Triggers

Readout from the CCFR detector was recorded for calibration and data analysis. To reduce the amount of data recorded, events of interest were selected according to the event triggers defined in table 3.3. This table also shows the number of events passing each trigger which were written to tape. Two triggers of particular importance to this analysis are Trigger 1 and Trigger 3, which recorded CC events.

3.5 Detector Calibration

In order to absolutely determine the three quantities CCFR measures, the energy of the hadron shower($E_{\rm HAD}$), and the angle and momentum of the outgoing muon (θ_μ and p_μ), the detector response as a function of particle interaction, time and detector position must be well understood. Calibration of detector components using neutrino data, test beam data, and field measurements helped to determine conversion between readout quantities and absolute measurements. Table 3.4 lists results of calibration of the CCFR detector components.

Energy deposited in any material by a high energy particle is referred to as the minimum-ionizing energy. It is mostly independent of particle type and particle energy. The total amount of energy measured in one scintillator divided by the amount of minimum ionizing energy for particles in the detector is a measure of the number of "minimum-ionizing particles," or MIPs, that passed through that detector component. Units of MIPs are used throughout the following sections.

3.5.1 Hadron and Muon Energy Calibration

Hadron shower energy, $E_{\rm HAD}$, is defined as the energy deposited in the scintillation counters over which the shower spans minus the energy due to the exiting muon in

Table 3.3: **Event Triggers written to tape.**

Trigger	Purpose	Requirements to pass trigger	Events passing Trigger	
			E744	E770
1	Selects CC events with muon originating in the target and penetrating into the toroid for momentum analysis	Presence of charged particle in last target cart and first toroid cart with no veto fire. Either two out of last four scintillation counters, (SCs), (1-4) fire along with a MIP signal in toroid gaps 1 & 2, or two out of four SCs (1-4) and (9-12) fire with a MIP signal in gap 1.	1740427	1981136
2	Selects NC events with hadron shower but no muon track	At least 8 GeV of energy deposited in 8 adjacent SCs coincident with two MIPs deposited in two of four consecutive SCs with no veto fire.	2267724	2915707
3	Selects CC muon events in calorimeter	16 counters in target fire with 4 GeV of energy deposited in 8 consecutive counters with no veto fire.	1611230	2001988
4	Used to measure Trigger 1 inefficiency found to be $< 10^{-4}$.	Uses counters (5-8) and (13-16) instead of (1-4) and (9-12) as required for Trigger 1. Toroid requirement is: PTOR (2 out of 4 ACs in same quadrant in each of the half carts fire) must be satisfied instead of a signal in toroid gaps 1 and 2.	696664	806985
5	Select test beam events	Test beam incident on target	16447	64627
6	Selects straight through muons produced upstream of detector hall passing through entire detector	One out of four counters in each target cart fire along with a veto fire. Muon must penetrate the spectrometer and satisfy PTOR requirement (see above).	166682	1406410
Total			3235717	5095487

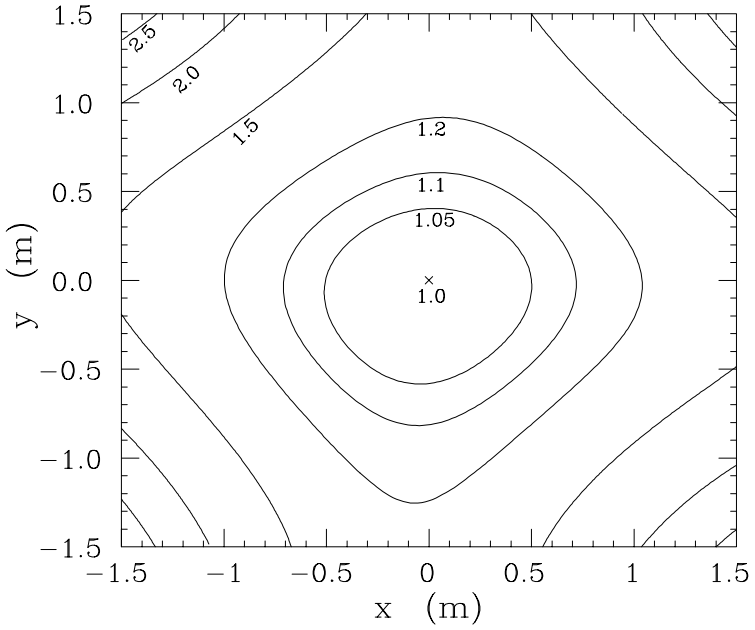

Figure 3.7: Contours indicating relative muon response for one of the CCFR counters. (counter 37, from reference [21])

a charged current event. The beginning of the shower is defined as the first counter in the most upstream pair to receive more than 4 MIPs of deposited energy. Shower end is defined as the first downstream counter to be followed by three consecutive counters with less than 4 MIPS of energy deposited. Total shower length in number of counters is then the distance between the shower beginning to shower end plus the next 5 downstream counters. The energy deposited in the shower from an outgoing muon in a charged current event is defined as 1 MIP per counter for each muon that passes through. The calibration process for detector components to accurately determine absolute hadron and muon energy is described in table 3.4.

3.5.2 Muon Tracking

Most muons from neutrino interactions in CCFR penetrate the calorimeter and toroid leaving long particle tracks indicated by hits in the drift chambers. In principle,

Table 3.4: **Hadron and Muon Energy Calibration**

Instruments Calibrated	Purpose of Calibration	Procedure	Results
Scintillation Counters: Energy Response	Determine total hadron shower energy from fraction of hadron shower energy deposited in the scintillation counters in the target calorimeter	Triggers 1 & 6 data used to calibrate counter response to muon energy deposits using toroid momentum measurement.	Energy in MIPS for each counter is: $\Delta E_i = \beta_i \sum_{j=1}^{4} a_{ij} A_{ij}^{LO}$ where A_i refers to response of counter i, B_i is each counters calibration coefficient, and a_{ij} are calibration coefficients for each PMT.
Scintillation Counters: Position Response	Counter response changes as a function of position due to att. of light in oil and wave shifters, and changes in PMT gains.	Position dependence determined by mapping counter response to muons traveling through at different sections of the counter divided into 9×9 in. square bins.	Example map corrections thus determined shown in figure 3.7
Scintillation Counters: Time Response	Counter response changes as a function of time due to degradation of scintillator oil and changes in PMT response	Time variations determined by measuring counter response at the center of a counter as a function of time. Relative measurement of the PMT gains were made frequently.	Energy loss in MIPS due to combined effects of time and position variation given by: $\Delta E_i = \frac{\eta_i(t) \sum_{j=1}^{4} A_{ij}^{LO}(t) G_j(0)/G_j(t)}{\Delta E_i(0,0,t) R_i(V_x,V_y,0)}$ where G refers to PMT gain, and R is the map correction.
Calorimeter Hadron and Muon Energy Calibration	Hadron test beams from test beam line used to absolutely calibrate calorimeter twice during the course of both runs.	Charge and momentum selected particles (πs, some ps and es, a few ks and μs) from test beam allowed to pass through detector.	Calorimeter calibration constants shown in table 3.6

Table 3.5: **Calorimeter Calibration Constants**

Particle Type	Calibration Constant	$\frac{\sigma}{E}$
hadrons	$4.73 \pm 0.02 \ \frac{MIPs}{\text{GeV}}$	$\frac{0.847}{\sqrt{E}} + \frac{0.30}{E}$
e	$5.25 \pm 0.10 \ \frac{MIPs}{\text{GeV}}$	$\frac{0.60}{\sqrt{E}}$
μ range outs	$6.33 \pm 0.17 \ \frac{MIPs}{\text{GeV}}$	0.17

Table 3.6: The calibration constants give the relation between the observed MIPs and the real energy loss for various particles.

tracks in the target calorimeter are straight while those in the spectrometer are curved as the muons are bent by the magnetic field. Measurements of θ_μ and p_μ using these tracks are complicated by the effects of multiple scattering of the muons as they travel through the detector, and by the fact that the measured θ_μ and p_μ are correlated and therefore must be determined simultaneously.

The iterative process to determine θ_μ begins with a crude estimate of p_μ using the track deflection in the first toroid in the spectrometer. This momentum measurement is used to estimate the effects of multiple scattering along the track the muon makes in the target calorimeter. The RMS deflection due to multiple scattering along each segment of track the muon traverses is used as an error to form a χ^2 function which is minimized to fit the track. θ_μ is then determined by fitting for a track in the six chambers closest to the vertex, including the tracking vertex offset described in table 3.7. This process is repeated using the more precise measurement of the muon momentum, p_μ, described below.

The momentum measurement is determined using the same iterative procedure as the track fitting in the calorimeter. An initial crude estimate of the muon angle and momentum are used to predict the muon track through the toroid. A χ^2 is formed comparing drift chamber hits and predicted track hits and minimized by varying the momentum. This procedure is repeated until the momentum differs by less than

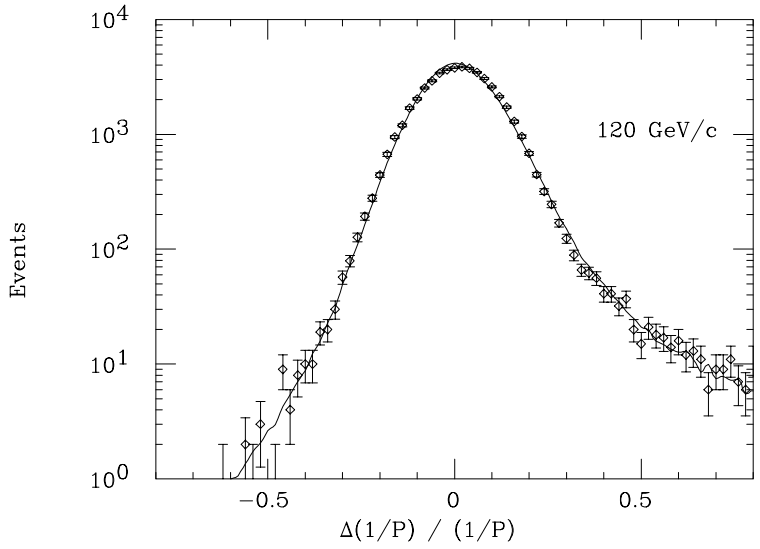

Figure 3.8: Muon momentum resolution function for 120 GeV muons from reference [21]. Measurements of test beam muon momentum resolution indicated by diamonds. Solid line indicates an independent Monte Carlo prediction. The tail due to overestimate of the muon momentum is caused by catastrophic energy loss while the tail due to underestimate is caused by hard single scatters.

0.5% from the previous iteration. Table 3.7 describes the calibration procedure for calorimeter and spectrometer elements used to determine muon angle and momentum.

Table 3.7: **Muon Angle and Momentum Calibration**

Instruments Calibrated	Purpose of Calibration	Procedure	Results
Drift Chambers: Track fitting near the vertex	Vertex angle determined by fitting track near vertex. Hadron shower near vertex complicates tracking ability so track length used to determine θ_μ was varied as a function of shower energy.	Trigger 1 data used. To include a chamber in the vertex fit, probability for choosing a good hit had to be twice that of choosing a bad hit.	Chambers nearest vertex position omitted comprise the tracking vertex offset. Showers with $E_{\rm HAD} < 25$ GeV: no offset. Showers with 25 GeV $< E_{\rm HAD} <$ 50 GeV: offset by one chamber. Showers with $E_{\rm HAD} > 50$ GeV: offset by 2 chambers. See [7] for a more detailed description of this study.
Drift Chambers: Resolution of θ_μ	Determine the resolution of θ_μ	Trigger 6 sample of stiff muon tracks with $75 < p_\mu < 200$ GeV. Upstream and downstream track segments compared with θ_μ determined at simulated vertex at track center.	Angular resolution: $\sigma_\theta = a + \frac{b}{p_\mu}$ (mrad) with a and b given in table 3.8
Muon Spectrometer: Muon Momentum Measurement	B field in toroid must be well understood in order to properly determine p_μ. Multiple scattering effects in the spectrometer limit the resolution of the muon momentum.	Hall probe measurements were used in order to prepare a detailed B field map up to an overall normalization. The normalization was determined using 120 GeV momentum analyzed test beam muons. Effect of multiple scattering estimated by considering a track that passed through the entire spectrometer.	Multiple scattering effects: for a muon receiving 2.4 GeV p_T kick traveling length of the spectrometer, $\theta_{\rm BEND} = \frac{p_T}{p_\mu} = \frac{2.4}{p_\mu}$. Error due to multiple scattering: $\sigma_{\theta_{\rm MCS}} = \frac{0.015}{p_\mu}\sqrt{\frac{500}{1.76}} = \frac{0.25}{p_\mu}$. This gives an estimate of spectral resolution: $\frac{\sigma}{\phi} = \frac{\sigma_{\theta_{MS}}}{\theta_{bend}} \approx 10\%$. Results, (figure 3.8) show that the central region follows a Gaussian with an RMS width of 10.1% as estimated.

Table 3.8: **Muon Angular Resolution as a Function of Energy**: Parameters to describe angular resolution at different energies as a function of track length. See table 3.7 for resolution function.

Track Length	$E_{\mathrm{HAD}} < 25$ GeV		25 GeV $< E_{\mathrm{HAD}} <$ 50 GeV		$E_{\mathrm{HAD}} < 50$ GeV	
	a	b	a	b	a	b
4	0.535	35.4	0.547	46.0	0.407	75.0
5	0.366	49.5	0.393	57.3	0.343	77.8
6	0.294	56.6	0.361	59.4	0.260	84.9
7	0.235	61.5	0.337	62.2	0.235	87.0
8	0.235	61.5	0.337	65.8	0.235	87.7

3.6 Analysis Cuts

A series of analysis cuts on the data reduce it from triggers recorded online to events used in the analysis. To be used in the analysis, events must take place in the active part of the detector and in enough of the detector to make a good measurement. Events must also be in an energy range that can be reconstructed by the detector and that can be modeled by the Monte Carlo. These analysis cuts are described below. The number of events that passed each cut are shown in table 3.9.

- RUN/GATE/NSTIME: removes runs when beam was of poor quality or detector was malfunctioning, when data was taken between neutrino pings, or when multiple neutrino interactions occurred in the same detector event.
- NO DIMUONS: eliminates events with a second track entering the spectrometer or traversing more than 19 counters. These dimuon events cannot be included in the structure function analysis because it is unclear which muon was created by the incoming particle and therefore unclear whether the incoming particle was a neutrino or an anti-neutrino.
- 20 <PLACE< 80: keeps only those events whose hadron shower is contained longitudinally in the detector.
- -50 in. $< V_x <$ 50 in., -50 in. $< V_y <$ 50 in.: keeps only those events whose hadron shower is contained transversely in the detector.
- Trigger 1: ensures muon entered the spectrometer.
- Target Track: ensures enough hits are detected in target drift chambers in order to identify a muon track in the calorimeter.
- Toroid Containment: ensures muon track, extrapolated from the calorimeter with multiple scattering effects included, has a radius $<$ 64 in. at the front face of the toroid and has a radius $<$ 55 in. at T2.

- Toroid Track: ensures enough hits are detected in the toroid drift chambers in order to identify a muon track in the toroid.
- Good Fit: ensures that the muon track is fit in the toroid.
- Fit Quality: ensures a good fit of the muon track in the toroid, specifically that the χ^2 per degree of freedom of the fit is less than 10 with the muon passing through at least 10 chambers.
- Two Gaps: ensures the muon passes through the first two gaps in the toroid in order to have good reconstruction efficiency of muons.
- $\theta_\mu < 150$ mr and R_{eff} (R at the front face of the toroid) > 8 in: ensures good acceptance of muon track in muon spectrometer and that the muon does not pass through the hole in the center of the spectrometer.
- $E_\mu > 15$ GeV: 15 GeV is the lower limit of spectrometer acceptance.
- $E_{\text{HAD}} > 10$ GeV: minimizes correlations between the flux and structure function data sample.
- $Q^2 > 0.3$ GeV^2: Lower limit is set by model used in this analysis.
- 30 GeV $< E <$ 360 GeV: Lower limit is set by energy acceptance and uncertainty in the neutrino flux, upper limit is chosen due to large smearing effects.

Table 3.9: **Triggers and events that passed each trigger:** F=Toroid polarity set to focus μ^-, D=Toroid polarity set to focus μ^+.

	E744				E770			
Cut	ν(F)	ν(D)	$\overline{\nu}$(F)	$\overline{\nu}$(D)	ν(F)	ν(D)	$\overline{\nu}$(F)	$\overline{\nu}$(D)
RUN/GATE/NSTIME	596544	682503	79777	101451	798375	845578	116641	133156
NO DIMUONS	589538	674839	78550	99668	789394	836435	115021	131044
20 <PLACE< 80	516764	591114	67949	86483	691305	731882	99961	113813
Vertex	442935	508164	59459	73880	592262	625308	88812	99822
Trigger 1	326395	369124	59344	73099	434570	447520	88706	98800
Target Track	326152	368988	59331	73077	434348	447269	88691	98767
Toroid Containment	290201	335404	54938	65612	387875	407750	82158	88894
Toroid Track	289195	330076	54938	65612	386275	401164	82158	88894
Good Fit	289127	329945	54900	65519	386145	401008	82103	88771
Fit Quality	288752	329428	54784	65364	385648	400200	81938	88512
Two Gaps	282796	284111	48150	64182	377324	345357	71984	86960
$\theta_\mu < 150\ mr$	280262	283833	48134	64018	373959	345068	71958	86738
$E_\mu > 15$ GeV	276420	283205	48002	63077	368985	344379	71805	85419
$E_{\rm HAD} < 10$ GeV	227607	230696	32766	43444	305783	282170	48438	58326
$Q^2 > 0.3\text{GeV}^2$	226256	229278	32383	42931	303988	280445	47865	57685
30 GeV $< E <$ 360 GeV	225824	229006	32356	42847	303438	280099	47834	57585

3.7 Analysis Tools

This analysis used the standard CCFR software tools. As in many HEP experiments, the CCFR data went through two basic data analysis passes. The first pass, called stripping, took raw data and resolved issues relating to timing and ADC pedestals etc., creating a first pass of calibrated raw data. The second pass, called crunching, used the stripped data to calculate the physics quantities used in the CCFR analyses. These physics quantities were gathered onto data summary tapes (DSTs) where they could be accessed for further analysis using the standard CCFR analysis tools called the CCFR Analysis Package [14].

In addition to the data manipulation analysis code, there were three CCFR Monte Carlos written during the course of the CCFR/NuTeV experiments. This analysis used a Fast Monte Carlo designed to described the CCFR detector and run, as its name implies, quickly. This Monte Carlo relied upon parameterizations of hadron shower development and muon track evolution in the toroid. This Monte Carlo was checked against a hit level GEANT3[15] Monte Carlo [16] which simulated the detector in great detail. The Full Monte Carlo simulated tracking of the muons in the toroid in detail. An overview of the code is described in reference [17].

The CCFR Fast Monte Carlo took the neutrino flux as an input. Monte Carlo *Generated Events* were weighted according to the normalized cross section. Parton distributions from PDFLIB[18] or individualized distributions could be used in the cross section. The order of the cross section calculation, as well as other effects such as application of radiative corrections and inclusion of higher twist effects, could be selected. Generated events were then modified to simulate muon energy and angle smearing, and hadron energy smearing, resulting in *Smeared Events*. Muons were tracked through the steel, and ionization energy loss as well as catastrophic loss was simulated. Multiple Coulomb scattering in the steel was included. The functions which described the detector smearing were determined using the test beam and

Trigger 6 events.

For this analysis, 27 million Monte Carlo events (roughly ten times the number of data events) were produced to estimate the effects of resolution and smearing in the detector. Before any Monte Carlo correction was applied, the data events were divided up into eight categories according to their experiment (E744 or E770), their neutrino species (ν or $\overline{\nu}$) and whether or not the muon spectrometer was set to focus positively or negatively charged muons.

Other data analysis programs used to read and re-weight events, extract structure functions and fit the data were Fortran-based programs written by the CCFR collaboration.

3.8 Parton Distribution Functions

Parton distribution functions (PDFs) along with a parametrization of the cross section define the cross section used in analyses. The cross section model used in the CCFR Fast Monte Carlo takes a leading order (LO) model of the cross section and a PDF set as input. At $Q^2 > 1.35$ GeV^2 this model is determined from a set of parton distribution functions fit from the results of the previous iteration along with a Buras-Gaemers type Leading Order parameterization [19] of the neutrino-nucleon cross section. Note that this analysis does not use the Buras-Gaemers PDFs. It uses the *form* of the PDFs first described by Buras and Gaemers. The Buras-Gaemers LO model uses parton densities representing the momentum densities of the valence and the sea quarks inside the nucleon, the PDFs, to construct differential cross sections. Specifically, the valence quark momentum densities inside the proton are parametrized as:

$$xu_V + xd_V = A_V(s)\, x^{\eta_2(s)} (1-x)^{\eta_2(s)} \left[1 + \frac{1}{2}\frac{\eta_1(s) + \eta_2(s) + 1}{\eta_2(s) + 1}(1-x)\right] \tag{3.6}$$

with $\eta_1(s) = \eta_{10} + \eta_{11} \times s$, $\eta_2(s) = \eta_{20} + \eta_{21} \times s$ and $s = log\left(\frac{log\left(\frac{Q^2}{\Lambda^2}\right)}{log\left(\frac{Q_0^2}{\Lambda^2}\right)}\right)$. The value of $Q_0^2 = 12.6$ GeV^2, picked for historical reasons, has no effect on the final results. In this calculation, it is assumed, according to the proton quark counting rule, that there are two valence u quarks and one valence d quark inside the proton. The normalization, A_V, of the valence quark distribution is allowed to vary while retaining Q^2 dependence as predicted by NLO QCD given by:

$$\int_0^1 \frac{dx}{x}\left[xu_V\left(x, Q^2\right) + xd_V\left(x, A^2\right)\right] = A_1\left(1 - \frac{4}{\left(11 - \frac{2}{3}n_f\right) log\left(\frac{Q^2}{\Lambda^2}\right)}\right) \tag{3.7}$$

where $n_f = 4$ is the number of flavors contributing to the cross sections.

Buras-Gaemers sea densities contain a light quark piece and a charmed piece. The charmed component is assumed to be zero. The strange component has a different shape than the non-strange component, which is accounted for as described below. The sea density is paramterized as:

$$xS\left(x, Q^2\right) = A_S(s)(1-x)^{\eta_S(s)} \tag{3.8}$$

.

The strange sea is given by:

$$xS_S\left(x, Q^2\right) = xS\left(x, Q^2\right)\frac{\left(\beta_S(s) + 1\right)}{\eta_S(s) + 1}(1-x)^{\alpha} \tag{3.9}$$

where $\beta(s) = \eta_S(s) + \alpha$ gives the shape difference between the strange and the non-strange sea.

Typically, any cross section models used in an analysis must be of the same order as any others used. However, this does not apply to the cross section models used here

to construct correction factors since although the differences in leading order versus next-to-leading (NLO) order models may be large, the differences in the correction factors due to the models are small. In other words:

$$\frac{\sigma_{LO}\,(bare\ proton\ target)}{\sigma_{LO}\,(physical\ Fe\ target)} \approx \frac{\sigma_{NLO}\,(bare\ proton\ target)}{\sigma_{\mathrm{NLO}}\,(physical\ Fe\ target)}. \tag{3.10}$$

The Buras-Gaemers model fits the structure function data poorly at lower x and Q^2. Previous CCFR structure function analyses [7] did not extract the data below $Q^2 = 1.0$ GeV^2 because of the lower limit on the viability of this model and thus allowed the model to be flat below $Q^2 = 1.0$ GeV^2. This analysis extends the reach in x and Q^2 below which the Buras-Gaemers model is expected to be valid by using an appropriate model for low x and low Q^2, normalized to the Buras-Gaemers model at $Q^2 = 1.35$ GeV^2. We use the GRV model of the parton distributions [20]. The inclusion of this model at low x and low Q^2 caused a shift in the radiative corrections calculation as well as an overall normalization shift from the previous structure function analysis [7] as described in subsection 4.8.2.

Chapter 4

Structure Function F_2

This analysis extends the previous CCFR Structure Function analyses [8, 22] to low x and low Q^2. The previous analyses did not measure below $x = .0075$ and $Q^2 = 1.0$ GeV^2 [8]. This analysis extends the reach to $x = .0045$ and $Q^2 = 0.3$ GeV^2. Thus, the x range presented here in which there is new data at low Q^2 is $.0045 < x < 0.035$. Data at higher x are again measured to indicate differences from the previous extraction due to improvements made in this analysis.

4.1 Method of Structure Function Extraction

The structure function, F_2 can be calculated from the observed number of neutrino and anti-neutrino events combined with the neutrino and anti-neutrino fluxes. We start by writing the cross section for neutrino-nucleon scattering in terms of the structure functions as in chapter 2, equation 2.1.

The number of neutrino and anti-neutrino events in bins of x and Q^2 is given by:

$$N^{\nu,\overline{\nu}}\left(x,Q^2\right) = \rho L N_A \int_{x-bin} dx \int_{Q^2-bin} dQ^2 \int_{all\ energies} dE \frac{d\sigma^{\nu,\overline{\nu}}}{dxdQ^2} \Phi^{\nu,\overline{\nu}}(E) \qquad (4.1)$$

where $\rho L N_A$ is the number of scattering centers in the target. Combining equations 2.1 and 4.1, the number of events in each x and Q^2 bin can be written in terms

of the structure functions as:

$$N^{\nu,\overline{\nu}}\left(x,Q^2\right) = \frac{G^2 M}{\pi}\int dx \int \frac{dQ^2}{2MEx}\int dE E\Phi^{\nu,\overline{\nu}}\left(E\right) \tag{4.2}$$
$$\times\left[\left(1-y-\frac{Mxy}{2E}+\frac{y^2}{2}\frac{1+\frac{4M^2x^2}{Q^2}}{1+R\left(x,Q^2\right)}\right)F_2\left(x,Q^2\right)\pm y\left(1-\frac{y}{2}\right)xF_3^{\nu,\overline{\nu}}\left(x,Q^2\right)\right]$$

in a simpler form:

$$N^{\nu}\left(x,Q^2\right) = A^{\nu}F_2\left(x,Q^2\right)+B^{\nu}xF_3^{\nu}\left(x,Q^2\right) \tag{4.3}$$

$$N^{\overline{\nu}}\left(x,Q^2\right) = A^{\overline{\nu}}F_2\left(x,Q^2\right)-B^{\overline{\nu}}xF_3^{\overline{\nu}}\left(x,Q^2\right) \tag{4.4}$$

Inputing the number of events measured and the coefficients A and B, comprised of the flux and known constants, it is simple to solve the two equations for the unknowns, F_2 and xF_3 assuming that $xF_3^{\nu} = xF_3^{\overline{\nu}}$ and that $R\left(x,Q^2\right)$ is known.

Now that I have made this look really easy, let me discuss the elements of this that make it tricky. The number of events must be corrected for acceptance, resolution smearing, physics model effects, and bin center corrections. The flux must be calculated. In constructing the corrections and determining the flux, a model of the parton distribution functions must be used. Models for R and ΔxF_3 must be input. The structure function extraction yields F_2 and xF_3, which gives us a new set of PDFs. In order to make sure that the structure functions are independent of the input PDF set, the process is iterated with the extracted PDF set from the previous iteration used as input for the next. When the PDF set does not change from iteration to iteration, we say the process has converged. Figure 4.1 shows this iteration process.

The following sections describe each element that goes into this process finishing with the extracted structure function, F_2, and its associated error.

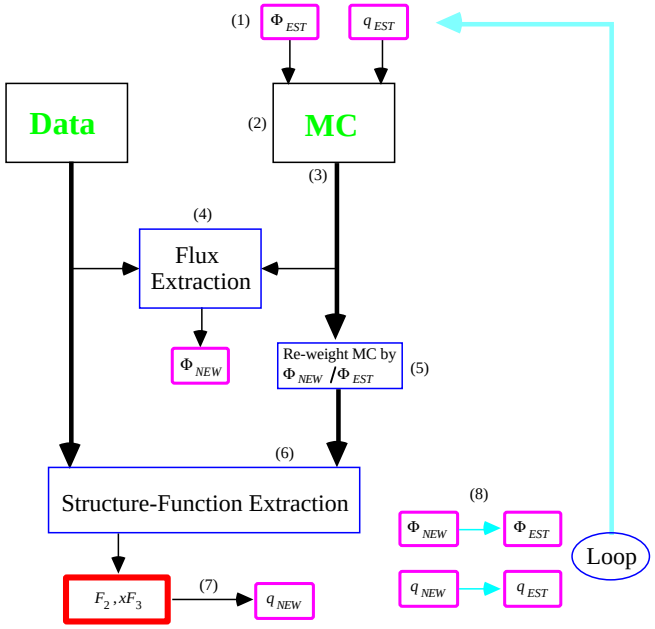

Figure 4.1: Iterative extraction process for structure functions.

4.2 Binning the Data

The neutrino deep inelastic scattering data were collected in two high energy, high statistics runs, FNAL E744 and E770. There are 1,030,000 ν_μ events and 179,000 $\overline{\nu_\mu}$ events in the data sample after fiducial volume, geometric, and kinematic cuts described in section 3.6. Events are binned in x and Q^2 bins based on Monte Carlo studies. Bin widths are chosen to be as small as possible while large enough so that at least 30% of the events generated in that bin remain in the bin after detector effects are simulated (a.k.a. after "being smeared"). Figures 4.2 along with table 4.1 show the effects of the smearing between x bins for the low x region newly accessed by this analysis. These Monte Carlo distributions show the generated value of x for each bin which will be measured ($x_{smeared}$). We can then define the x resolution as $x_{generated} - x_{smeared}$ as shown in figure 4.3.

Table 4.1: Results of smearing between x bins for the lowest bins.

x min	x max	% events generated within the bin
0.003	0.006	45%
0.006	0.010	41%
0.010	0.015	40%
0.015	0.020	34%
0.020	0.030	47%
0.030	0.040	40%

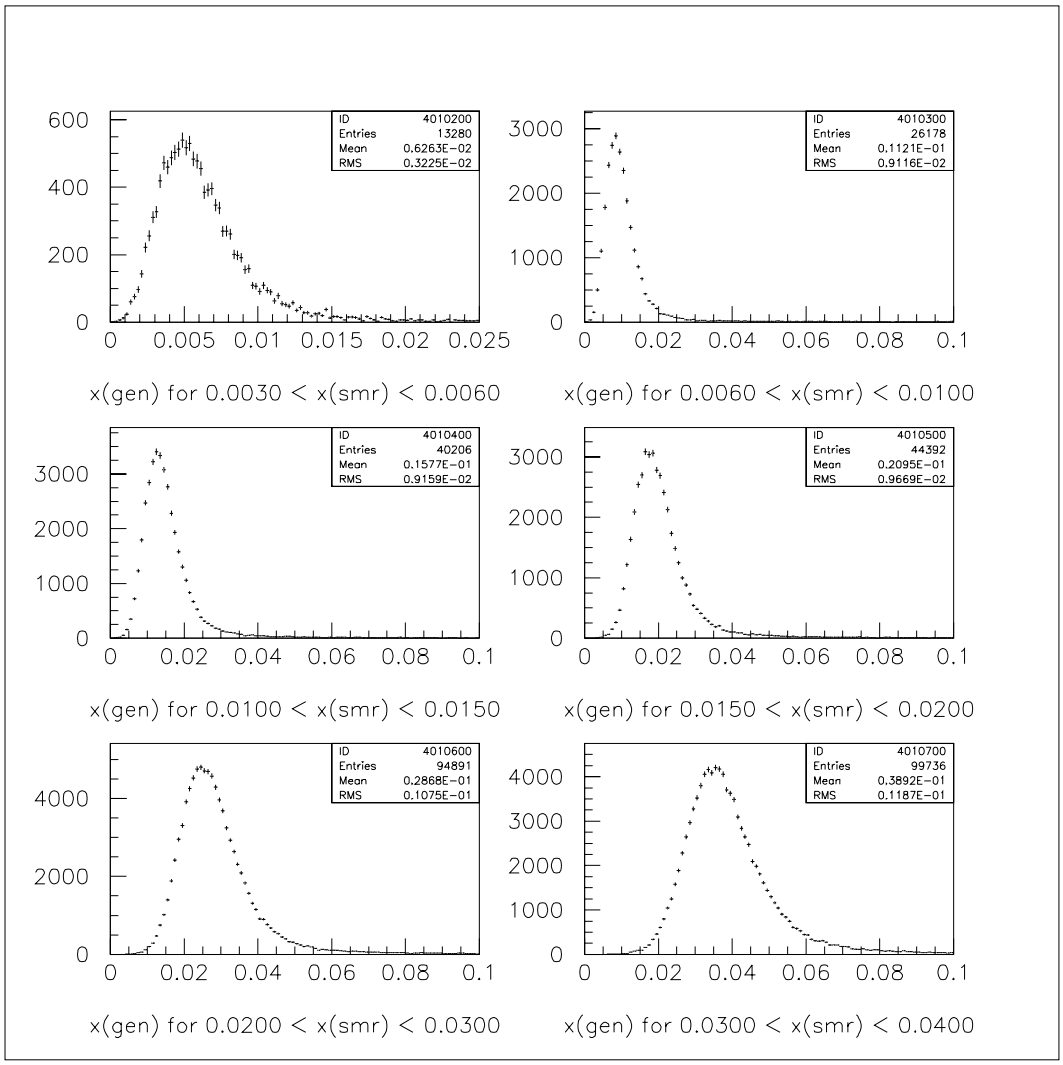

Figure 4.2: x_{GEN} for $0.00 < x_{SMR} < 0.04$.

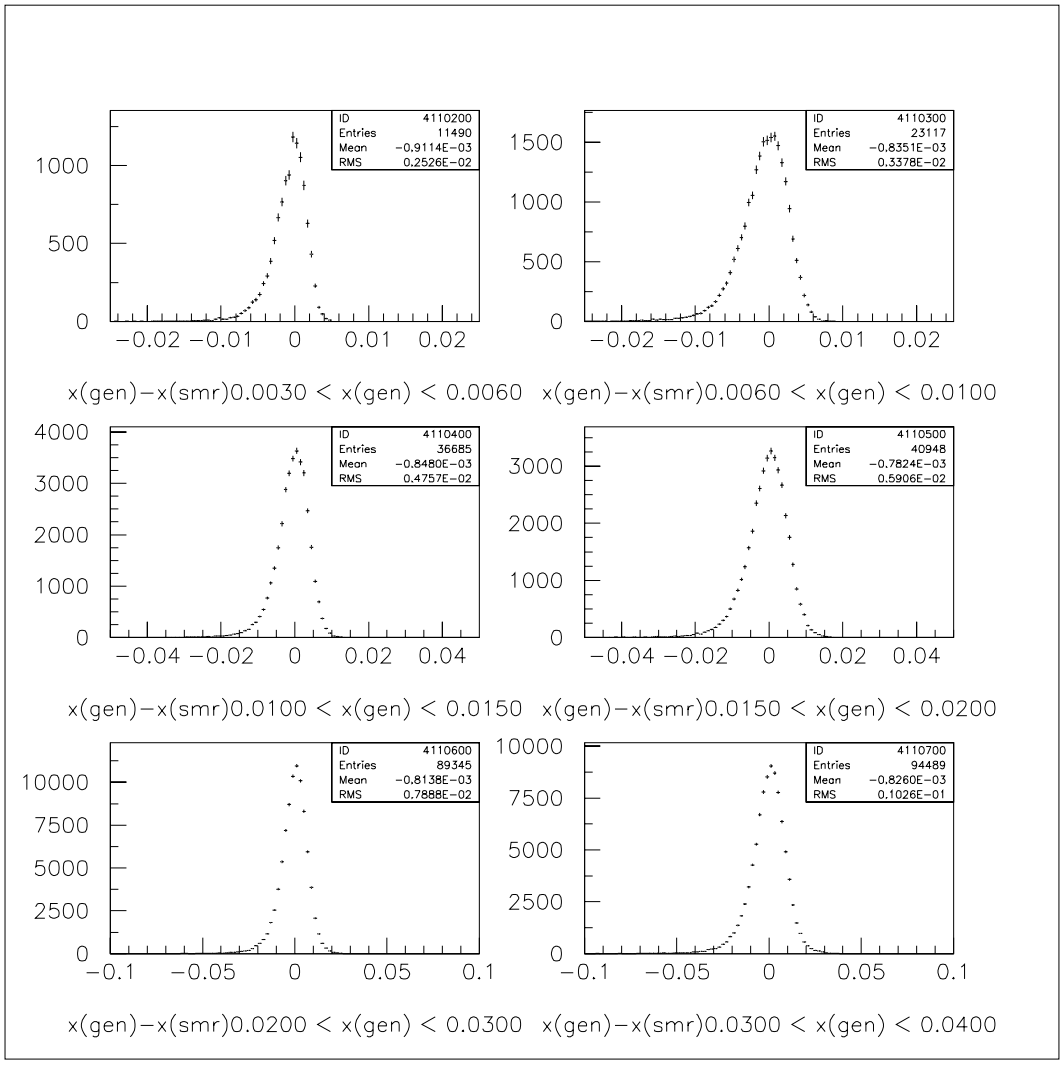

Figure 4.3: Resolution in x, lowest bins. x_{GEN} - x_{SMR} Width of the bins are on the order of the widths of the distributions, respectively.

4.3 Correcting the Data

4.3.1 Data/Monte Carlo Comparisons

The Monte Carlo is used to correct the data as described in section 4.3.2. In order to ensure the corrections are calculated properly, the agreement between the data and the Monte Carlo description must be verified. In particular, does the Monte Carlo accurately reproduce quantities that CCFR measures, such as $E_{\rm HAD}, \theta_\mu$, p_μ, and E_ν? Data/Monte Carlo comparisons of these quantities are shown in figures 4.4 and 4.5. The Monte Carlo predictions indicated by the solid line, accurately describe the data.

4.3.2 Data Correction Method

Before extraction, the data must be corrected for the effects of detector geometry, detector resolution, kinematic cuts, and various physics effects. All but the physics effects are accounted for in the Monte-Carlo corrections. The physics model corrections depend upon a model of the physical cross-section in terms of parton distributions. The corrections applied to the data are:

- *Monte Carlo Corrections:*
  - Monte Carlo correction, $C^{\rm MC}$, accounts for effects of acceptance, resolution smearing and removal of the dimuon events.
- *Flux Correction:* $C^{\rm flux}$, accounts for effects of flux re-weighting in the analysis.
- *Physics Model Corrections:*
  - Isoscalar target correction, $C^{\rm iso}$, accounts for the difference in the number of protons and neutrons in the iron target calorimeter.
  - Radiative effects correction, $C^{\rm rad}$, accounts for photon radiation off the quark or charged lepton legs in a neutrino-nucleon interaction.

  - Propagator correction, C^{W}, accounts for the finite mass of the W boson.

- *Bin-Center-Correction:* C^{bc}, accounts for differences in the value of a quantity at the center of a bin versus the average value in the bin.

Corrections to account for these effects in the data are calculated separately for each of the eight separate categories of neutrinos as described in section 3.7: for each neutrino species each focussed positively or negatively in the spectrometer and for each data set E744 or E770. Eq 4.6 shows all these corrections as they are applied to the data.

$$\begin{aligned} & DATA^{\mathrm{corrected}} \\ & = DATA^{\mathrm{recon.}} \times C^{\mathrm{MC}} \times C^{\mathrm{flux}} \times C^{\mathrm{iso}} \times C^{\mathrm{rad}} \times C^{\mathrm{W}} \times C^{\mathrm{bc}} \end{aligned} \tag{4.5}$$

Except for the flux re-weighting and the dimuon correction, calculated on an event by event basis, an average correction is determined within each kinematic bin and the correction applied to the sum of the reconstructed data events in that bin.

A correction for the mass of the charm quark applied in previous analyses accounts for the large mass of this quark. This correction, now known to be too simplistic, is not applied here. The reasons for this are described in detail in section 4.3.2 and the effect of the removal of the correction shown in chapter 5.

Monte Carlo Corrections

In modeling the detector, the Monte Carlo can account for how acceptance and resolution smearing affect the number of data events. Detector resolution in the Monte Carlo, determined by detector calibration, results in the smearing for the Monte Carlo variables

- E_ν

- E_{HAD}
- E_{μ}
- E_{μ} at the front face of the toroid
- muon angle parameters
- energy loss in the detector
- event vertex location

Acceptance corrections are accounted for by the number of events left after the same analysis cuts applied to the data are applied to the Monte Carlo. The ratio of the number of generated Monte Carlo events without cuts to the smeared Monte Carlo events with cuts is the correction factor which accounts for acceptance and resolution smearing effects. Figures 4.6 and 4.7 show the acceptance and resolution smearing corrections as a function of Q^2 in x-bins. Note that the corrections are not steeply changing as a function of both x and Q^2.

Dimuon events are removed from the data sample due to the ambiguity of the sign of the leading muon in these events. Dimuons must also be removed from the reconstructed Monte Carlo sample to correspond to the data. The cross section for production of dimuon events is removed from the Monte Carlo event sample by re-weighting the number of reconstructed events accordingly. The Monte Carlo correction factor incoporating acceptance, resolution smearing and the dimuon correction is given by:

$$C^{\mathrm{MC}} = \frac{MC^{\mathrm{generated}}_{\mathrm{No\ cuts}}\,(\text{with dimuon cross section})}{\mathrm{MC}^{\mathrm{smeared}}_{\mathrm{cuts\ applied}}\,(\text{without dimuon cross section})} \tag{4.6}$$

Flux Correction

As described in the beginning of this chapter, the structure function extraction process is an iterative procedure requiring a new set of PDFs and a new flux at each

iteration based on the previous iteration. The flux correction re-weights individual events in the Monte Carlo to account for the new flux. The flux correction factor is given by:

$$C^{\text{flux}} = \frac{\Phi^{\text{NEW}}}{\Phi^{\text{estimated}}} \tag{4.7}$$

Physics Model Corrections

The physics model corrections, itemized below, take into account the non-isoscalarity of the target, radiative effects, propagator mass effects, and the charm mass. Each depends on the input PDF set and therefore can vary until the iteration process has converged.

- Isoscalar Correction: The CCFR calorimeter does not, in reality, consist of isoscalar nuclei. The parameter $v_f = \frac{\text{number of neutrons}-\text{number of protons}}{\text{number of nucleons}} = 0.0567$ describes the asymmetry between the number of protons and the number of neutrons. The effective quark and anti-quark momentum densities seen by the neutrinos are scaled according to v_f. The isospin correction factor is given by:

$$C^{\text{iso}} = \frac{\sigma\left(\text{isoscalar target} : v_f = 0\right)}{\sigma\left(\text{iron target} : v_f = 5.67\%\right)} \tag{4.8}$$

- Radiative Correction: The outgoing charged particles in a charged current neutrino DIS interaction can radiate photons as shown in figures 4.8 and 4.9. These QED effects must be included when calculating the cross sections. The radiative corrections which account for these effects are calculated using a standard algorithm, the Bardin radiative corrections [23]. The Bardin calculations used here with m_c=0, and the model described above in section 3.8 are plotted in figure 4.10. These corrections differ greatly from those used in the previous analysis due to the inclusion of the GRV model of the PDFs at low x. Shown

for comparison in figure 4.10 are the radiative corrections without inclusion of the GRV model at low Q^2. The large difference in the correction below $Q^2 = 1.0$ GeV^2 arises from the change in the cross section in this region. The cross section in the previous analysis was flat below $Q^2 = 1.0$ GeV^2 while in this analysis, it follows the GRV model in this region, decreasing with decreasing Q^2. The new radiative corrections have a significant effect on F_2 in the lowest x bins, decreasing them by as much as 5% in the lowest x bin and by 2-3% up to $x = .0175$. The radiative effects correction factor is given by:

$$C^{\text{rad}} = \frac{\sigma\,(\text{no Radiative Cor.})}{\sigma\,(\text{Radiative Cor.})} \tag{4.9}$$

- Propagator Correction: The neutrino cross section is reduced slightly at high Q^2 due to the W propagator mass. This effect is accounted for by redefining the Fermi coupling constant as:

$$G_F^2 = \frac{G_F^2}{\left(1 + \left(\frac{Q^2}{(m_W = 80\ \text{GeV}/c)^2}\right)^2\right)} \tag{4.10}$$

The propagator correction factor is give by:

$$C^W = \frac{\sigma\,(m_W = 0)}{\sigma\,(m_W = 80\ \text{GeV})} \tag{4.11}$$

The convolution of all the physics model corrections in x and Q^2 bins are shown in Figure 4.11.

Finally, the bin-center correction accounts for the number of events at the average value of the kinematic in each bin versus the value at the center of the bin. The value of the bin-center correction in x and Q^2 bins is shown in Figure 4.12. The total value of the Monte Carlo corrections, the physics model corrections and the bin-center corrections is shown in figure 4.13. Note that the overall corrections are not steeply changing as a function of x and Q^2.

Charm mass correction: In order to directly compare neutrino DIS with charged lepton DIS, the neutrino structure functions must be corrected to a world where the charm mass is zero. Making the charm mass zero in the neutrino scattering events allows the neutrino and muon interactions to look the same with respect to quark mass and therefore allows for a direct comparison. In previous analyses, a slow-rescaling scheme was used to account for these effects of charm production with a massive charm quark. This scheme rescaled Bjorken x to ξ given by:

$$\xi = x\left(1 - \frac{m_c^2}{Q^2}\right) \tag{4.12}$$

Recent next-to-leading order calculations including massive charm production are very different from the LO calculations, the slow rescaling correction used in the previous analysis. Figure 4.14 shows the differences in the NLO and LO calculations both as a function of x and Q^2 [24]. These differences most likely indicate that the LO calculation is too simplistic and at least indicate there is a large uncertainty in the slow rescaling correction. In order to evade this problem, the slow rescaling charm correction is removed and the ratio of data/theory for neutrino and charged lepton structure functions are compared. See chapter 5 for details.

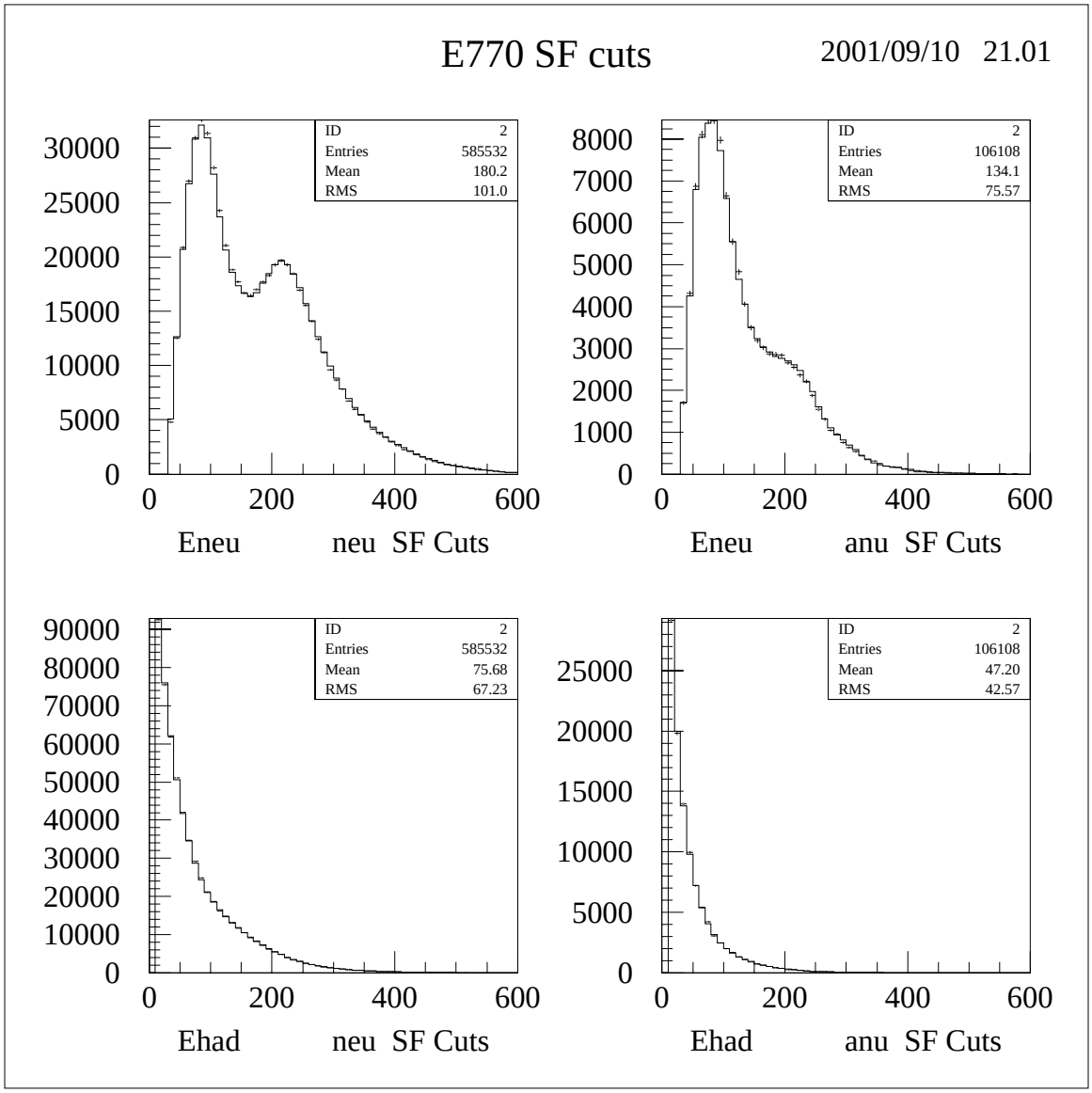

Figure 4.4: E_ν and $E_{\rm HAD}$ distributions comparing data indicated by the points, and Monte Carlo indicated by the histogram, for E770. "neu" corresponds to neutrino distributions. "anu" corresponds to antineutrino distributions. Agreement is similar for E744.

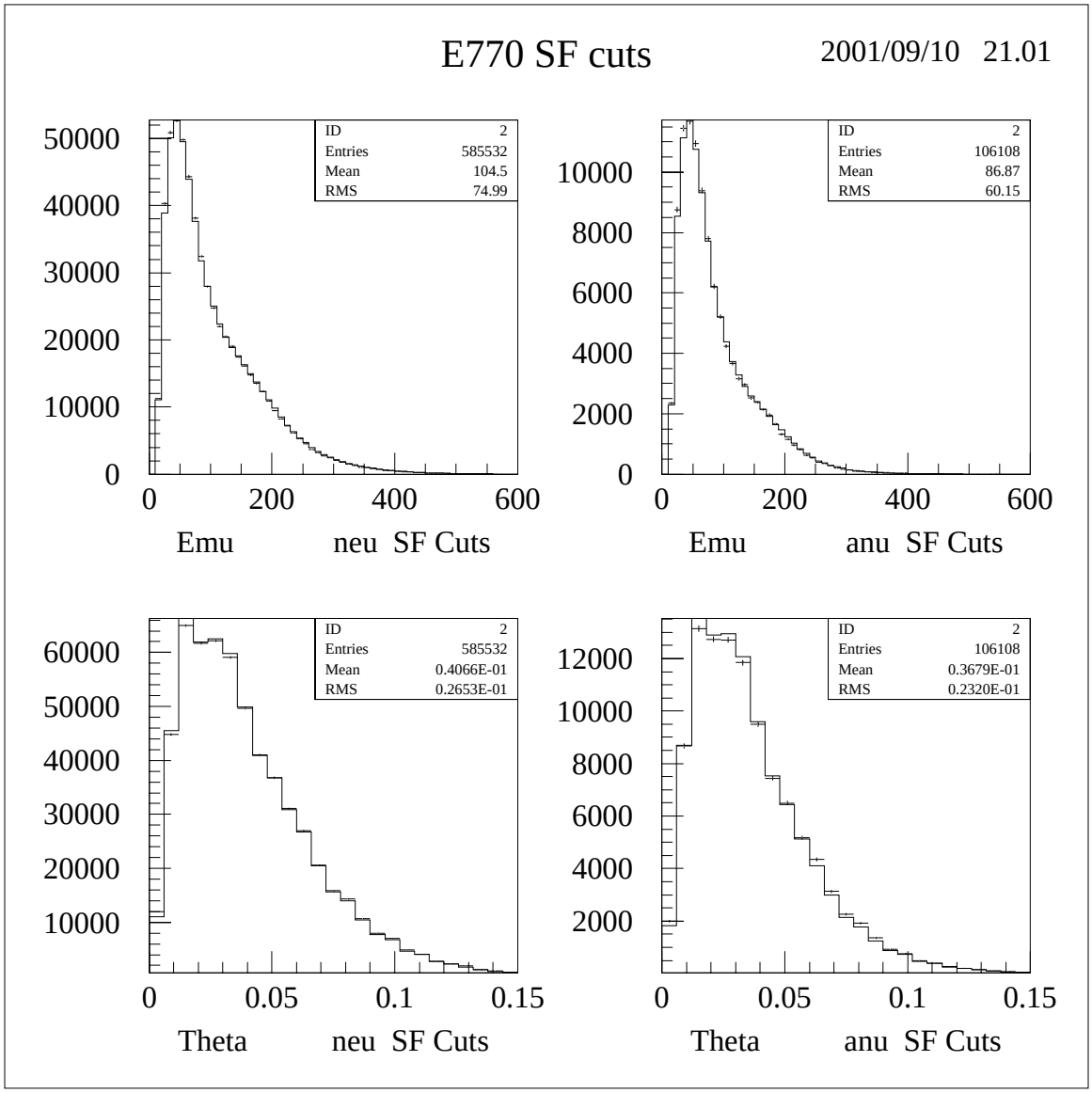

Figure 4.5: E_μ and θ_μ distributions comparing data, indicated by the points, and Monte Carlo, indicated by the histogram, for E770. "neu" corresponds to neutrino distributions. "anu" corresponds to antineutrino distributions. Agreement is similar for E744.

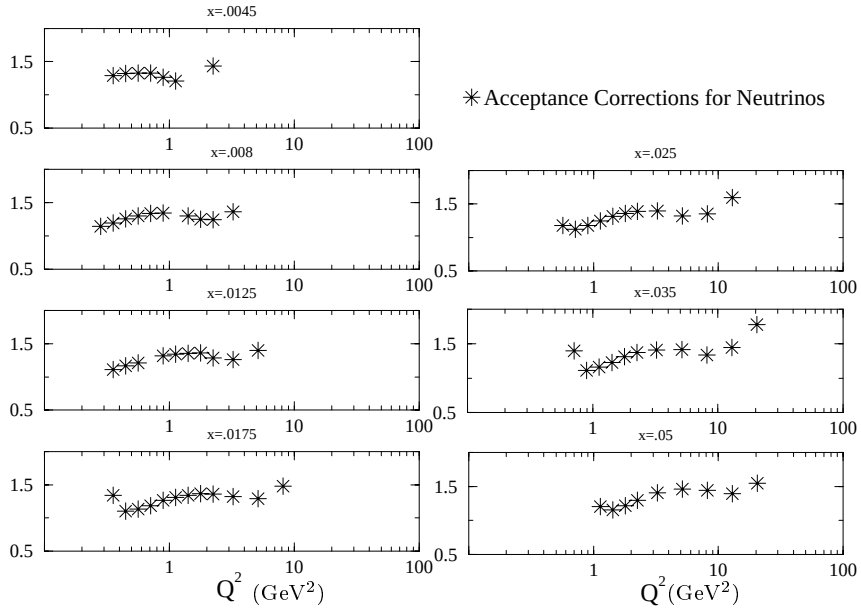

Figure 4.6: The acceptance corrections, the ratio of Monte Carlo events without cuts applied to Monte Carlo events with cuts applied, for neutrinos are shown. Corrections for anti-neutrinos are similar.

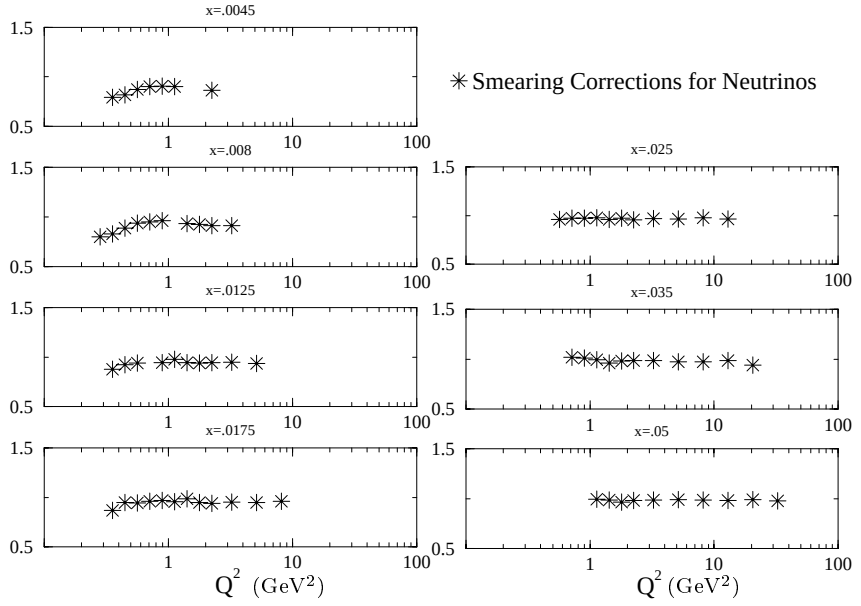

Figure 4.7: The smearing corrections, the ratio of the number of generated Monte Carlo events to the number of smeared Monte Carlo events, applied to neutrino events in the structure-function analysis. Corrections for anti-neutrinos are similar.

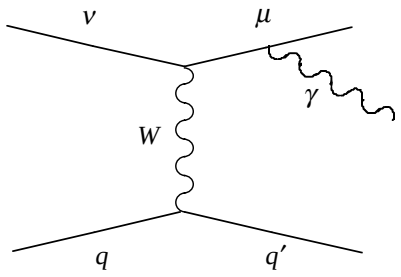

Figure 4.8: Photon radiating off muon leg [7].

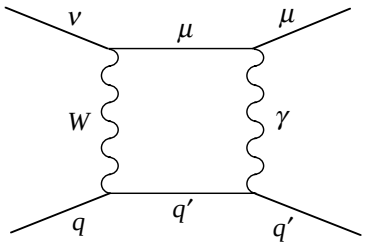

Figure 4.9: Photon radiating off quark and muon leg [7].

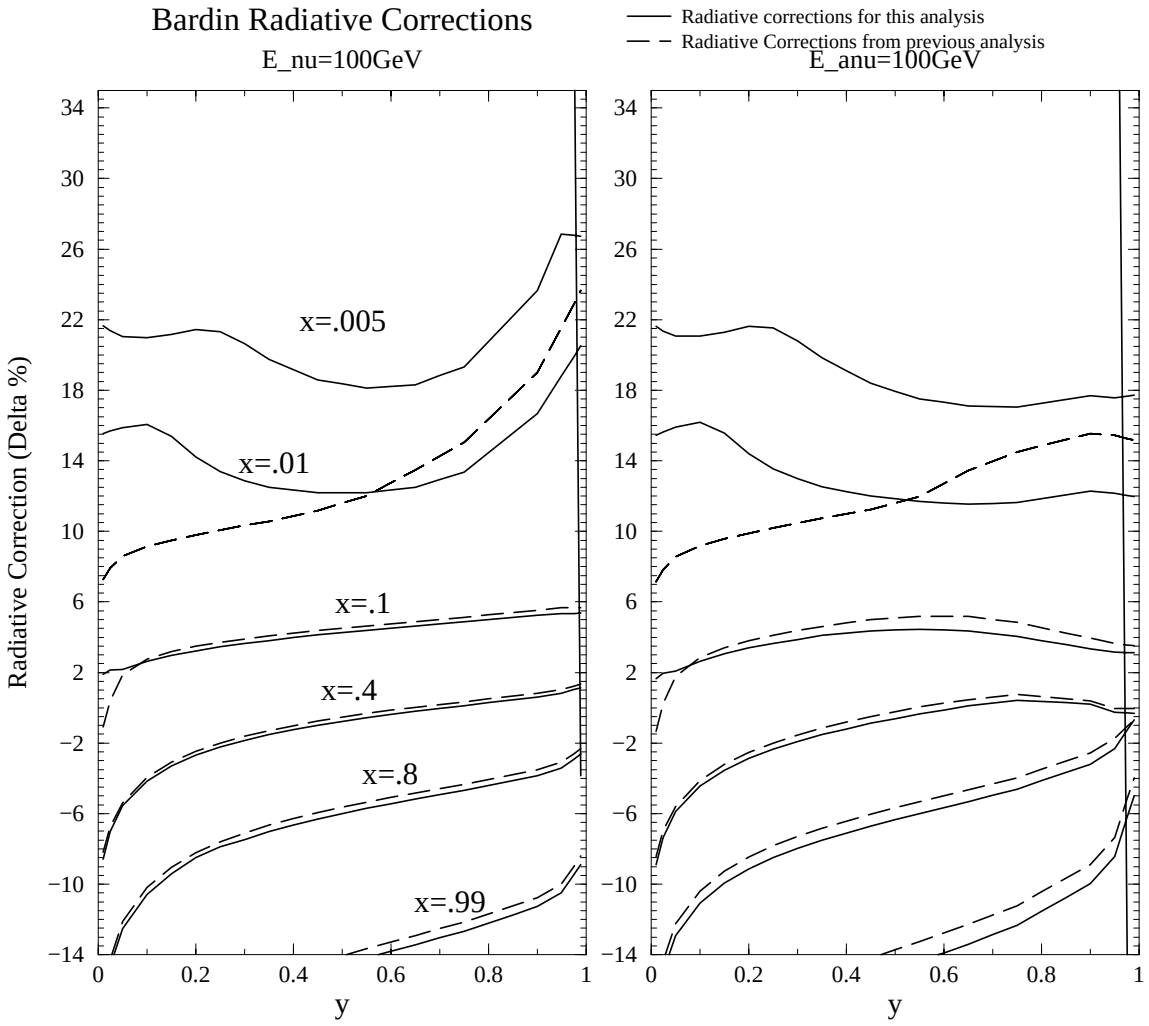

Figure 4.10: Radiative corrections from this analysis with the GRV model at low Q^2 versus from the previous analysis without the GRV model at low Q^2. Correction for neutrinos (anti-neutrinos) shown on the left (right).The rise in the correction at very low y occurs because this is a region where the cross section calculation is not valid. This region is not included in the structure function extraction.

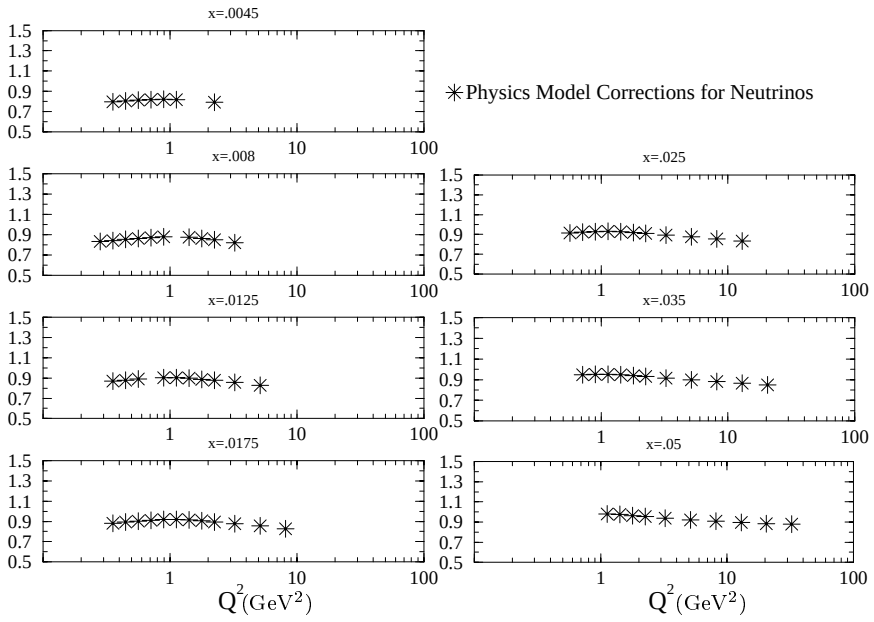

Figure 4.11: The physics model corrections applied to neutrino events in the structure function analysis. Corrections for anti-neutrinos are similar.

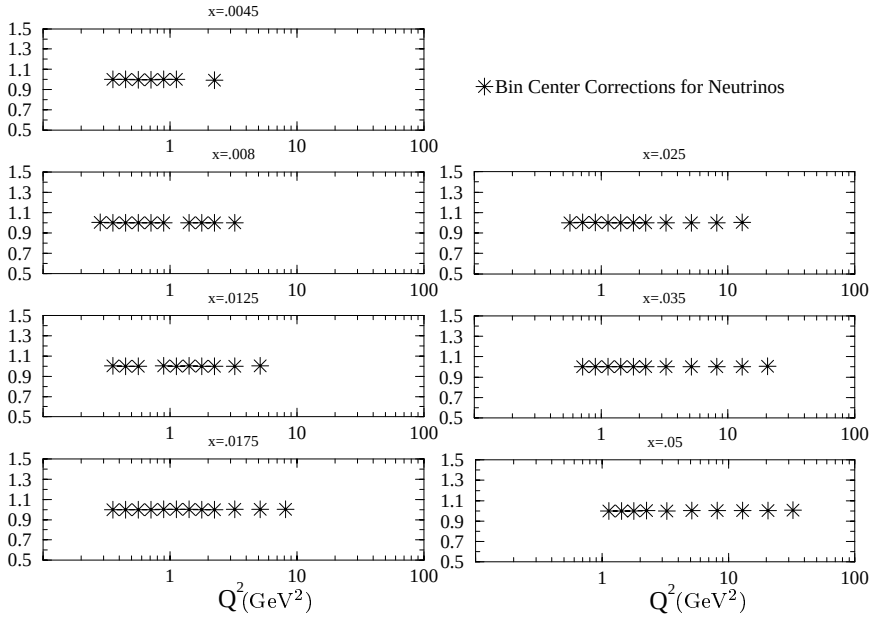

Figure 4.12: The bin-center corrections applied to neutrino events in the structure-function analysis. Size of these corrections are all less than 1%. Corrections for anti-neutrinos are similar.

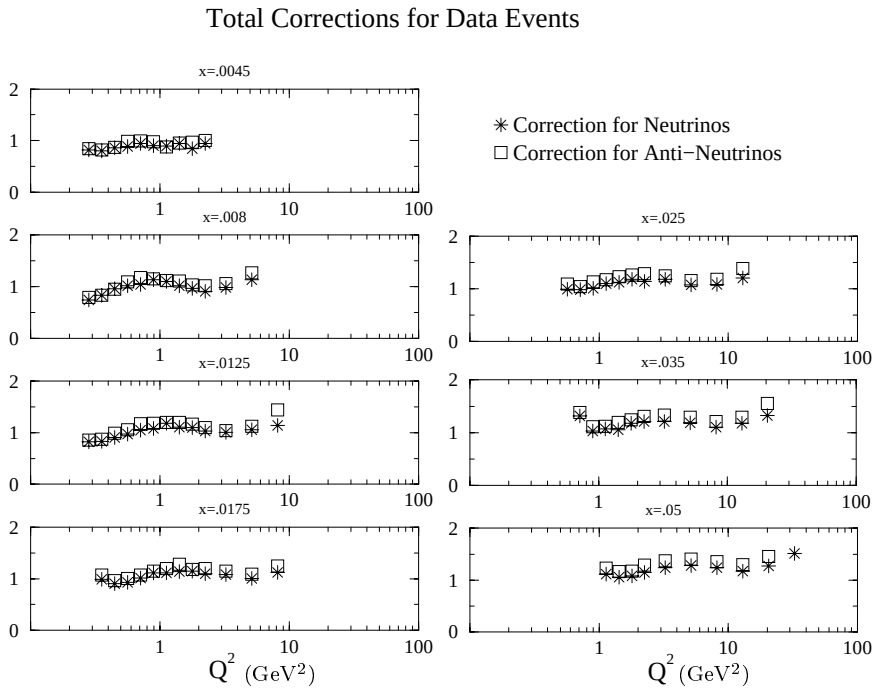

Figure 4.13: The total corrections applied in the structure-function analysis: $*$'s indicate corrections for neutrinos while the squares indicate correction for antineutrinos.

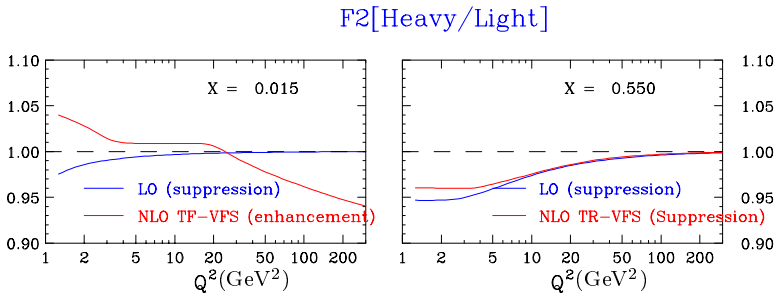

Figure 4.14: The ratio of F_2 with massive charm versus with massless charm using LO and NLO calculations [24].

4.4 Flux and Cross Sections

In order to solve equation 4.3 for the structure functions, the flux, $\Phi(x, Q^2)$, must be determined. Deducing the absolute flux from the secondary particle spectrum is made difficult by the wide energy spectrum and intensity of the beam. Instead, the relative flux is determined using a subset of the charged current events and is normalized to the world cross section to determine an absolute flux.

The relative flux, specifically, the relative flux between two energy bins and the relative flux between neutrinos and anti-neutrinos, is determined using low y events via the "fixed-ν" method. This flux extraction method is described by its author in reference [7]. Low y events provide a representative sample of the charged current events but, since these events have predominantly low E_{HAD} and the structure function events have relatively high E_{HAD}, are not correlated to the data sample used for the structure function analysis. The "fixed-ν" method rewrites the neutrino-nucleon cross section, binned in E_{HAD}, in factors of $\frac{\nu}{E}$ where $\nu = E_{\mathrm{HAD}}$. The number of events in E_{HAD} bins is then given by:

$$\frac{dN}{d\nu} = \Phi(E)\left(A + \frac{\nu}{E}B - \frac{\nu^2}{2E^2}C\right) \tag{4.13}$$

where A, B, and C are given by:

$$A = \frac{G^2 M}{\pi}\int_{\mathrm{energy}} F_2 \tag{4.14}$$

$$B = -\frac{G^2 M}{\pi}\int_{\mathrm{energy}} (F_2 \mp xF_3) \tag{4.15}$$

$$C = B - \frac{G^2 M}{\pi}\int_{\mathrm{energy}} F_2 R \tag{4.16}$$

Integrating equation 4.13 up to a small value of $\nu = \nu_0$ so that the energy dependence of the term in parentheses will be small, and regrouping according to $\frac{B}{A} = -\left(1 \mp \frac{\int xF_3}{\int F_2}\right)$ gives:

$$N(\nu < \nu_0) = \Phi(E)\int_0^{\nu_0} d\nu A\left(1 + \frac{\nu}{E}\left(\frac{B}{A}\right) - \frac{\nu^2}{2E^2}\left(\frac{B}{A} - \frac{\int F_2 R}{\int F_2}\right)\right) \tag{4.17}$$

Using the above formula and the number of events in E_{HAD} bins, we can obtain the flux.

4.4.1 Flux Sample

The low-ν, charged current event sample used for the flux analysis must pass the fiducial volume and geometric cuts listed in section 3.6 as well as the following kinematic cuts:

- $\theta_\mu < 150$ mr to ensure good acceptance of the muon track in the spectrometer.
- $E_\mu > 15$ GeV where 15 GeV is the lower limit of acceptance in the muon spectrometer.
- 30 GeV $< E_\nu <$ 360 GeV where 30 GeV is high enough to avoid a large acceptance correction and 360 GeV is low enough to avoid a large smearing correction.
- $E_{\mathrm{HAD}} < \nu_0$ to allow for high statistics in the flux data sample while avoiding significant overlap with the structure function data sample.

Events passing these cuts are subdivided into 17 E_ν bins and within these into E_{HAD} bins. The E_{HAD} bins are limited by smearing and statistics to be 2 GeV wide. The events, corrected for detector acceptance, resolution smearing and physics model effects are binned in E_ν and E_{HAD}. We form a $\frac{dN}{d\nu}$ distribution and, applying equation 4.17, extract the flux. Events near zero hadron energy due to quasi-elastic scattering and resonance production, are removed from the fit by requiring $E_{\mathrm{HAD}} > 4$ GeV. They are included in the flux after the number events at higher E_{HAD} are determined according to equation 4.17. The fitting procedure begins by determining $\left\langle \frac{B}{A} \right\rangle$ for all E_ν bins by fitting in each individual energy bin and taking an average over the different bins. The $\Phi(E)$ term is treated as a normalization and allowed to float in

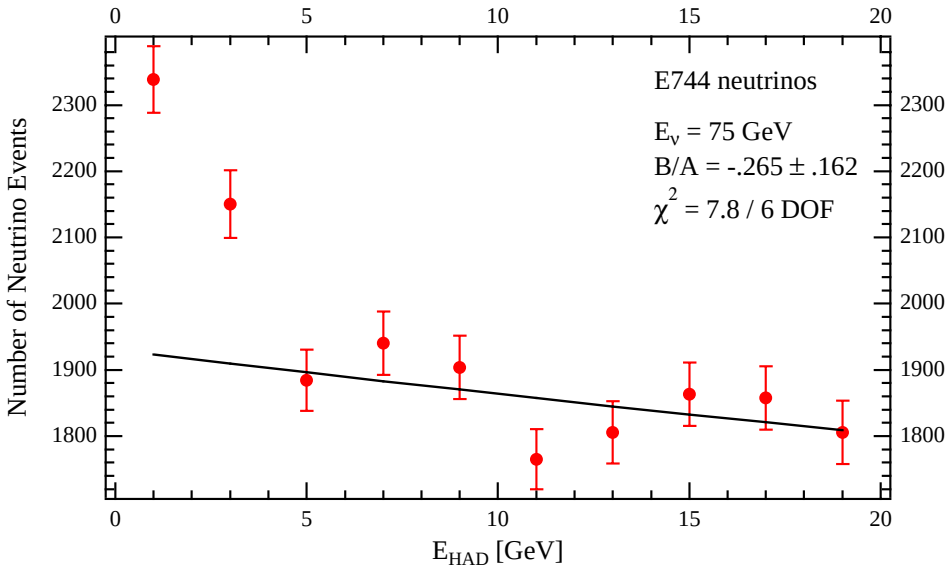

Figure 4.15: A typical fit for $\frac{B}{A}$ to the $\frac{dN}{d\nu}$ distribution. The peak in events at low $E_{\rm HAD}$ is due to resonance production and is removed from the data sample [7].

the fit. Figure 4.15 shows an example of the fit to $\left\langle \frac{B}{A} \right\rangle$ for one E_ν bin and figure 4.16 shows the results of a fit to all the energy bins. The fully corrected flux multiplied by the energy spectrum for E744 and E770 is shown in figure 4.17

The most important systematic errors to consider for the flux extraction are the uncertainties in the $E_{\rm HAD}$ calibration, the E_μ calibration and the values of $\left\langle \frac{B}{A} \right\rangle^{\nu,\overline{\nu}}$. Error due to muon and hadron energy calibration uncertainty is determined by re-extracting the flux with muon and hadron energy scales shifted separately by the amount listed in table 4.7. The error in the flux due to $\left\langle \frac{B}{A} \right\rangle^{\nu \text{ and } \overline{\nu}}$ is determined by considering the difference in $\left\langle \frac{B}{A} \right\rangle$ as calculated in E770 versus E744. This difference is attributed to an unaccounted for systematic error and the difference is incorporated in the error quoted for the measurement. Other systematic errors considered in the flux extraction are the model systematic error, the slow-rescaling correction error and the sensitivity to the assumption in the flux analysis that F_2 is constant for $\nu < \nu_0$.

The absolute flux is determined by constraining the overall normalization of the flux such that the measured total neutrino-nucleon cross section for neutrinos equals

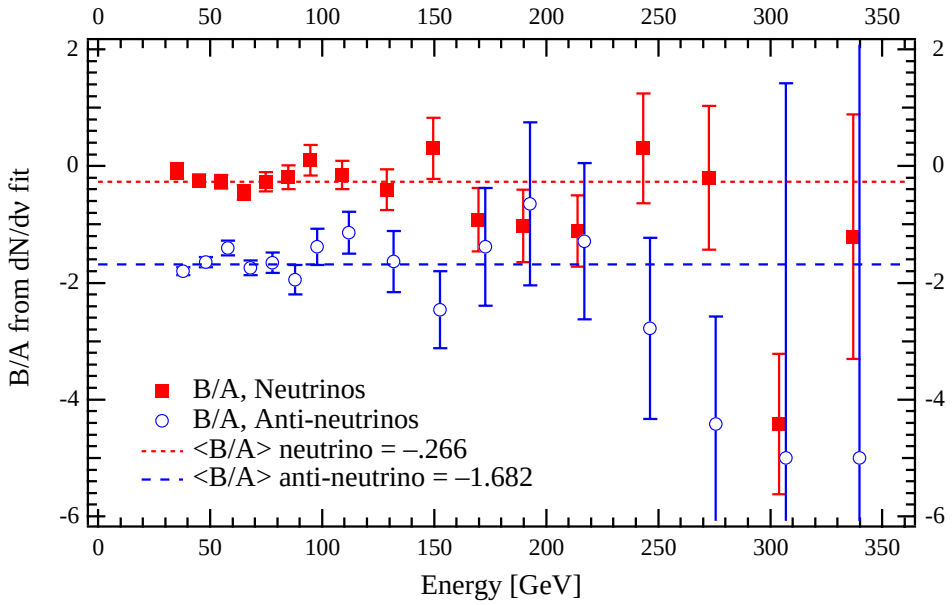

Figure 4.16: Typical fits for $\frac{B}{A}$ in all energy bins [7].

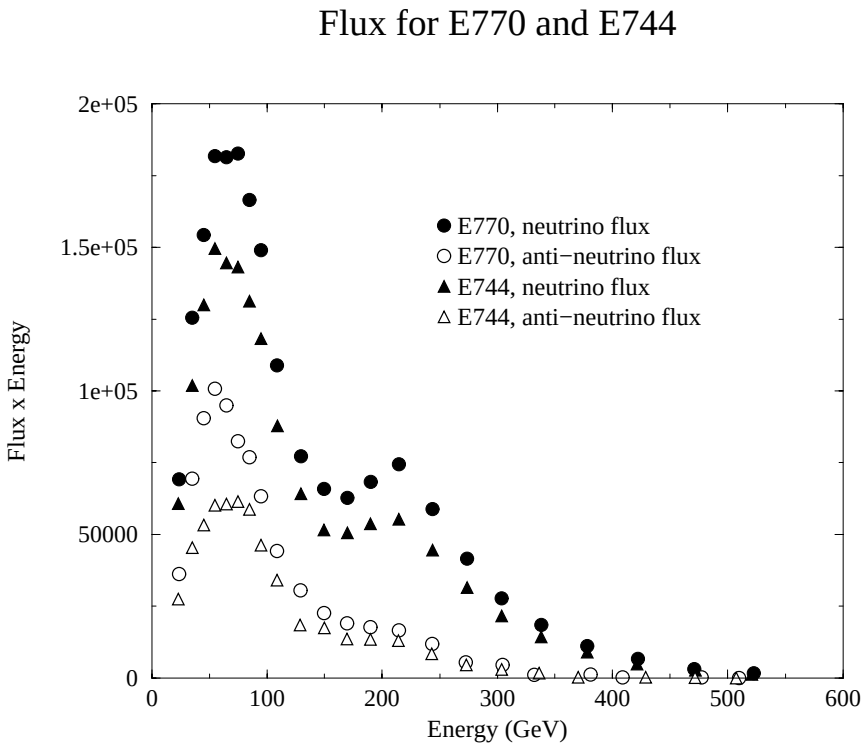

Figure 4.17: Neutrino flux separated according to neutrino type (ν or $\overline{\nu}$), and experiment (E744 or E770).

the world average cross section for isoscalar corrected iron target experiments, $\frac{\sigma^{\nu Fe}}{E} = (0.677 \pm 0.014) \times 10^{-38}\text{cm}^2/\text{GeV}$ [25, 27, 26, 28]. For anti-neutrinos, the measured total cross section equals the world average cross section including this experiment for isoscalar corrected iron target experiments, $\frac{\sigma^{\overline{\nu}Fe}}{E} = (0.340 \pm 0.007) \times 10^{-38}\text{cm}^2/\text{GeV}$

4.5 The Longitudinal to Transverse Absorption Cross Section, $R = \frac{\sigma_L}{\sigma_R}$

The neutrino-nucleon cross section is described by three structure functions. This analysis method can extract two of the three of these by measuring two quantities, N^{ν} and $N^{\overline{\nu}}$. The third, $R_{\text{Longitudinal}} = \frac{\sigma_L}{\sigma_T}$, the longitudinal to transverse absorption cross section, must be determined using other measurements. The value of $R_{\text{Longitidinal}}$ used in this analysis comes from an empirical parameterization to world data on R [29]. Recent experimental data [30] indicate that R may be smaller than expected at low x; however these data are in disagreement with a previous measurement made in this kinematic region. Figure 4.18 shows the world's available data on R at the lowest possible x bins where data are available. Also indicated on the plots are the world average fits to R and R_{eff}, modified to account for heavy quark production in the final state for neutrino scattering, and recent NNLO calculations for R. The NNLO calculation [31] becomes negative, and therefore unphysical, at lower Q^2 in the lowest x bin indicating the unreliability of this fit. Other theoretical calculations [32] may solve the problems with this fit and also indicate a lower R than previously measured or calculated in this region. The experimental and theoretical data in this region may point to an R as low as $R = 0.25$, lower than the value of R_{world}. A precise determination of R in this region is difficult at this time based on the experimental and theoretical evidence. Therefore, R is chosen to be the existing best fit to the world's data, R_{world}. Systematic errors are applied to account for the experimental

and theoretical predictions indicating a lower R. The systematic error is chosen to be $\pm 15\%$ of R_{world}. In the regions where this lower limit is larger than $R = 0.25$, the systematic error is chosen to be $R = 0.25$. Figure 4.20 shows solid error bars including error estimated for R_{world} $\pm 15\%$ as has been published [33], along with dashed error bars which include the more conservative estimate for the error on R_{world} as described here.

4.6 The Strange Sea Correction

In the leading order parton model, $F_2^{\nu} = F_2^{\overline{\nu}}$ but $xF_3^{\nu} \neq xF_3^{\overline{\nu}}$. Using equation 2.3 and:

$$q^{\nu N} = \frac{1}{2}\left[u(x) + d(x) + 2s(x)\right] \tag{4.18}$$

$$q^{\overline{\nu} N} = \frac{1}{2}\left[u(x) + d(x) + 2c(x)\right] \tag{4.19}$$

$$\overline{q}^{\nu N} = \frac{1}{2}\left[\overline{u}(x) + \overline{d}(x) + 2\overline{c}(x)\right] \tag{4.20}$$

$$\overline{q}^{\overline{\nu} N} = \frac{1}{2}\left[\overline{u}(x) + \overline{d}(x) + 2\overline{s}(x)\right] \tag{4.21}$$

it is clear that while $F_2^{\nu} = F_2^{\overline{\nu}}$, $\Delta xF_3 = xF_3^{\nu} - xF_3^{\overline{\nu}} \neq 0$ because of the difference between the strange and charm quark momentum densities in the nucleonic sea, $x\,(s - c)$. In order for the physics model corrections to apply to the extraction procedure, a correction must be applied to account for this difference. The correction is calculated using a leading order determination of ΔxF_3. The recent CCFR ΔxF_3 measurement [22] is higher than this LO model [19] and all other current LO and NLO theoretical predictions in this kinematic region. A systematic error is applied to account for the differences between theory and this measurement.

4.7 Statistical and Systematic Errors

Statistical errors on the structure function analysis are computed by considering both the statistical error on the number of events and the statistical error in the Monte Carlo correction. The error on the number of events is just:

$$\left(\Delta N^{\nu,\overline{\nu}}_{meas}\right)^2 = N^{\nu,\overline{\nu}}_{meas} \tag{4.22}$$

The error on the Monte Carlo correction is more difficult to calculate due to how the events migrate from bin to bin as events are re-weighted and smeared. The statistical error is calculated by extracting the corrections separately for ten independent sets of Monte Carlo events. The standard deviation of the resulting values of the number of events in each x and Q^2 bin is taken to be this error.

Systematic errors, itemized below, were determined by varying each quantity by its uncertainty listed in table 4.7. The Monte Carlo was re-weighted accordingly and the extraction process repeated using the same input PDFs as from the base structure functions. If it was not necessary to extract a new flux, the same one used for the base structure functions was used. Within each bin, the systematic error reported is:

$$\frac{(F_k(1\delta) - F)}{|(F_k(1\delta) - F)|} \times \frac{|(F_k(1\delta) - F)| + |(F_k(-1\delta) - F)|}{2} \tag{4.23}$$

- *Energy Calibration errors:*
  - *Hadron energy calibration:* Uncertainty in calibrating the detector with test beam measurements caused the 1% uncertainty in the hadron energy calibration.
  - *Hadron energy shift:* Disagreement between the Monte Carlo model of the low hadron energy region and the data causes a correction with some uncertaintly, conservatively estimated to be $\pm$110MeV.

SOURCE OF UNCERTAINTY		$\delta\ F_2^\nu$
Statistics:	low x	2-3%
	higher x	$\sim 1\%$
Energy Calibrations/Shifts:	Hadron energy calibration($\pm 1\%$)	1-2%
	Hadron energy shift(± 100 MeV)	2-3%
	Muon energy calibration($\pm 1\%$)	2-3%
	Muon energy shift(± 100 MeV)	2-3%
Physics Models:	Charm mass ($\pm 18\%$)	1-2 %
	Charm branching ratio ($\pm 7\%$)	$< 1\%$
	Strange sea normalization ($\pm 12\%$)	$< 1\%$
	Strange sea shape ($\pm 26\%$)	$< 1\%$
	Cross section normalization ($\pm 2.1\%$)	2-3%
	Cross section ratio ($\pm 1.4\%$)	$< 1\%$
	Physics model ($\pm 1\sigma$)	3-5%
	$\mathrm{R_{world}}\ (^{+15\%}_{min(-15\%,0.25)})$	$< 2\%$
	ΔxF_3 model,low x	5%
	ΔxF_3 model, higher x	$\sim 1\%$
	Radiative corrections model ($\pm 1\sigma$), low x	3%
	Radiative corrections model ($\pm 1\sigma$), higher x	$\sim 1\%$
	Flux determination	$< 1\%$

- *Muon energy calibration:* Uncertainty in calibrating the detector with test-beam measurements cause a muon energy calibration error of 1%.

- *Physics model errors:*

  - *Charm mass:* As reported in [34], $m_c = 1.31 \pm 0.24$. Charm mass error from this measurement assumed here.

  - *Charm branching ratio:* As reported in [34], $B_c = 0.105 \pm 0.007$. Charm branching ratio error from this measurement assumed here.

  - *Strange Sea Normalization:* As reported in [34], $\kappa = 0.373 \pm 0.046$. Strange sea normalization error from this measurement used here.

  - *Strange Sea Shape:* As reported in [34], $\alpha = 2.50 \pm 0.65$. Strange sea shape error from this measurement assumed here.

  - *Cross section normalization:* 2.1% error on world average of the neutrino-iron cross sections used as systematic shift on normalization.

  - *Cross section ratio:* 1.4% shift in cross section ratio determined from statistical, low ν-extrapolation, and acceptance correction errors in cross section analysis.

  - *Physics Model:* Systematic error due to the model used is estimated by shifting the structure functions by 2σ statistical error, fitting these shifted structure functions for a PDF set, and using this PDF set as input to a new iteration. The corresponding shift in F_2 is at most 3% in the lowest x bin.

  - R_{world}*:* Lower limit of R assumed to be 0.25 or 15% smaller than R_{world}, whichever is smaller. See section 4.5 for details. Upper limit allowed to be 15% higher than R_{world}.

  - ΔxF_3 *model:* Systematic error on the LO model used to estimate the ΔxF_3 model comes from the difference between data and theory at low x and

low Q^2. See section 4.6 for details.

- *Radiative corrections model:* error due to variations in the input PDF set estimated by using the same shifted model used in the model systematic error calculation as an input to the radiative correction calculation. Shift in the radiative corrections as a result is shown in figure 4.19. Corresponding shift in the structure functions due to shifted radiative corrections is approximately 3% in the lowest x bin and decreases to $< 1\%$ in higher bins.
- *Flux Determination:* Error due to $\left\langle \frac{B}{A} \right\rangle$ determined in flux extraction and cross section model used for flux extraction modify structure functions by $< 1\%$. Cross section model used in systematic error estimate in flux extraction is linear.

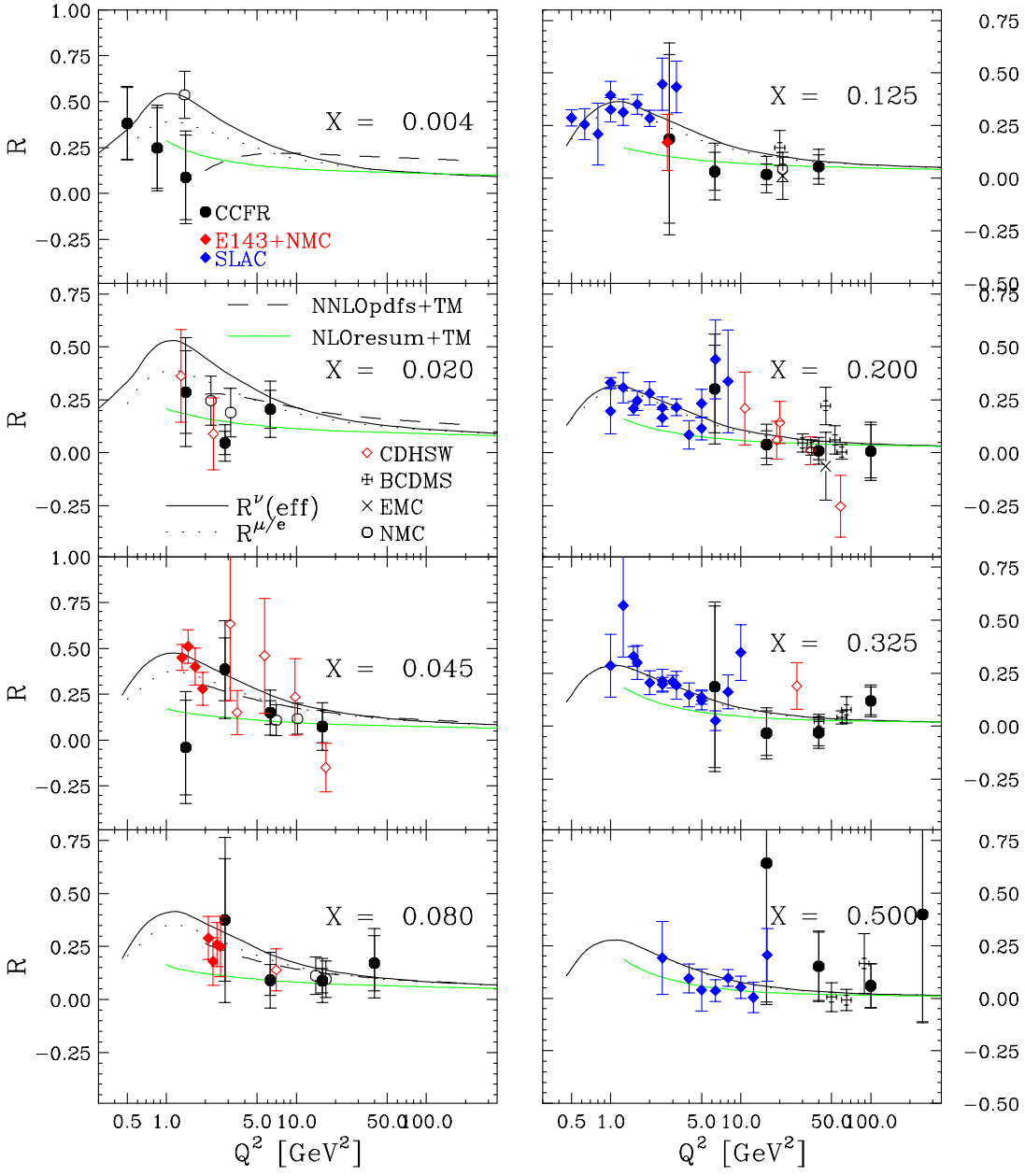

Figure 4.18: $R_{\mathrm{Longitudinal}}$: data and theoretical predictions [30].

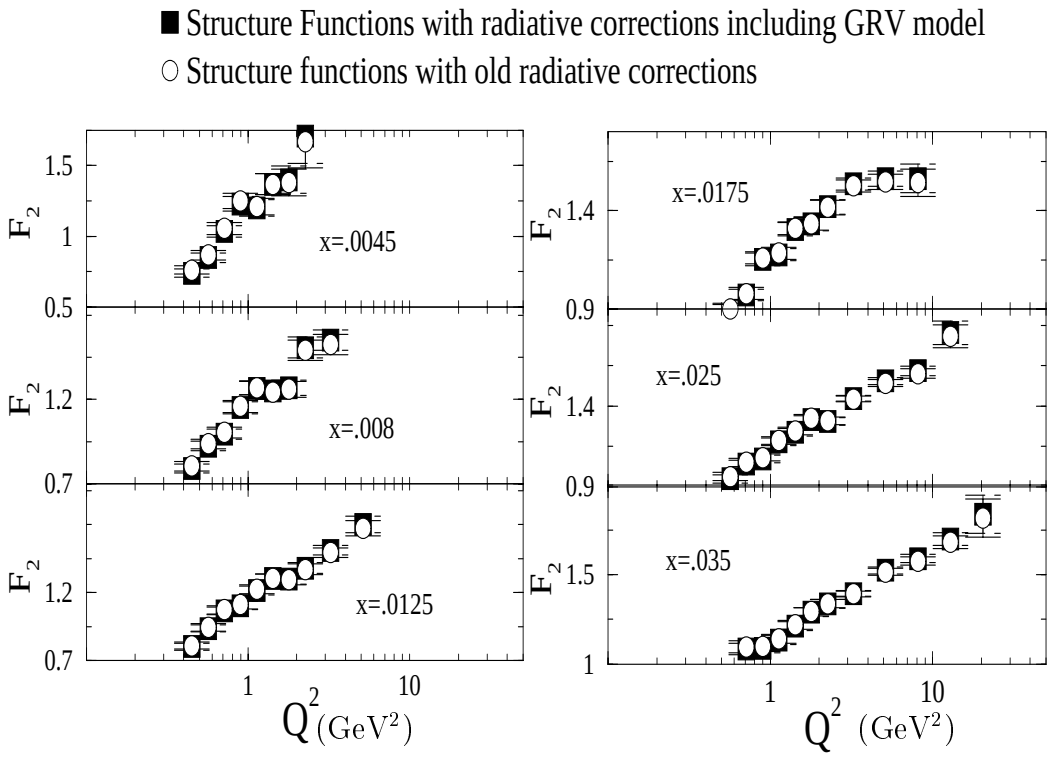

Figure 4.19: Structure functions with and without shift from radiative corrections sytematic error.

4.8 The Structure Function Measurement

4.8.1 Data at Low x and Low Q^2

The results of this analysis, the structure function F_2 at low x and low Q^2, are shown in figure 4.20 [33]. Errors are statistical and systematic added in quadrature. A line is drawn at $Q^2 = 1.0$ GeV^2 to highlight the new kinematic region accessed by this analysis.

Appendix A lists the central values and error bars shown in figure 4.20 as well as a breakdown of the error contribution from statistical and systematic errors in each x and Q^2 bin.

4.8.2 Improvements to Data at Higher x and Q^2

A number of corrections to the previous analysis modify the structure functions significantly and therefore warrant comment here. The modifications and their effects are as follows:

- *Slow rescaling correction:* The slow rescaling correction used in the previous analysis is now known to be too simplistic [35, 22]. Removal of this correction results in a decrease in F_2 for $x < 0.1$ as large as 5%. Figure 4.21 shows the ratio of F_2 with and without this slow rescaling correction applied. After this correction is removed, the structure functions can no longer be compared directly to the charged lepton results. See section 5.1 for details.

- *F_2 normalization correction:* The previous structure function analysis [7] assumed a flat cross-section below $Q^2 = 1.0$ GeV^2. This turns out to be far too crude an approximation. The modified GRV model now used at low x steadily decreases below $Q^2 = 1.0$ GeV^2 causing a decrease in the number of Monte-Carlo events that pass the cross section cuts. As a result, F_2 shifted overall by

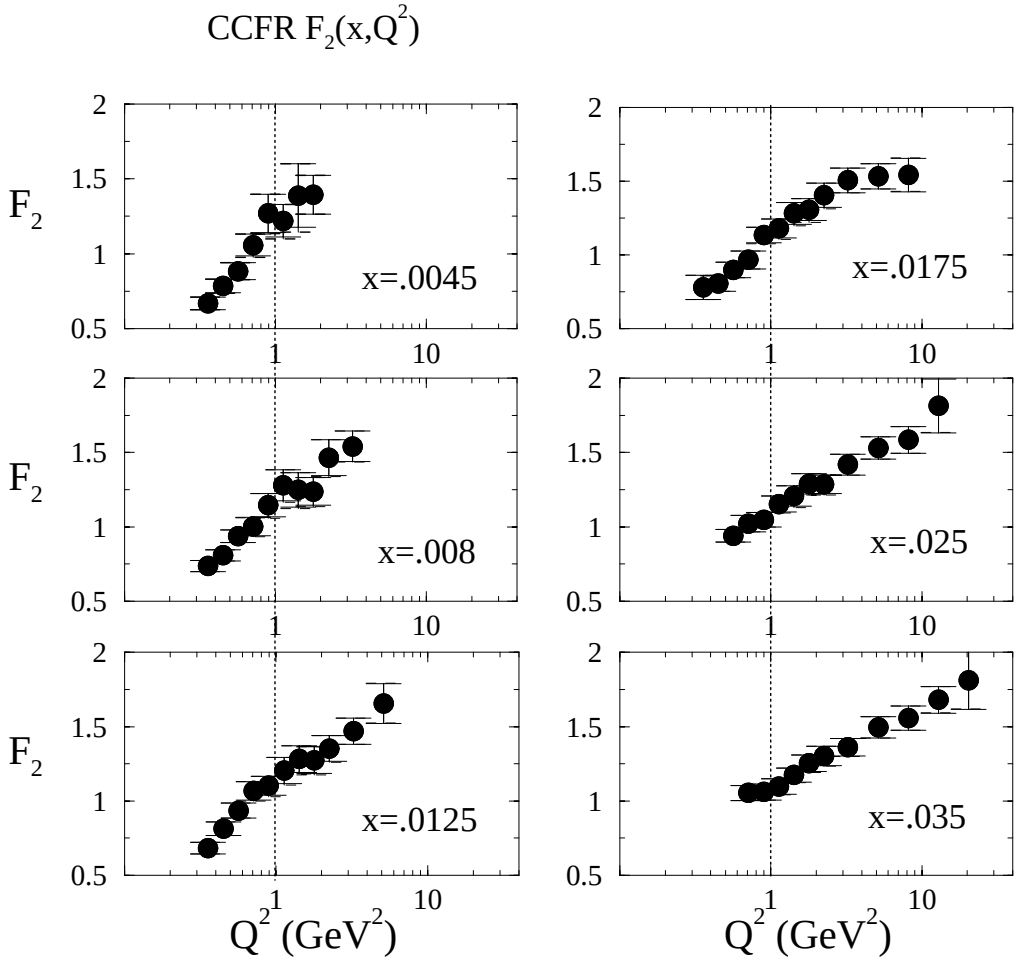

Figure 4.20: F_2 at low x and low Q^2. Line is drawn at $Q^2 = 1.0$ GeV^2 to highlight new data accessed by this analysis.

2% for neutrinos and 3-4% for anti-neutrinos. Figures 4.22 and 4.23 show F_2 from the previous analysis as compared with the results from this analysis.

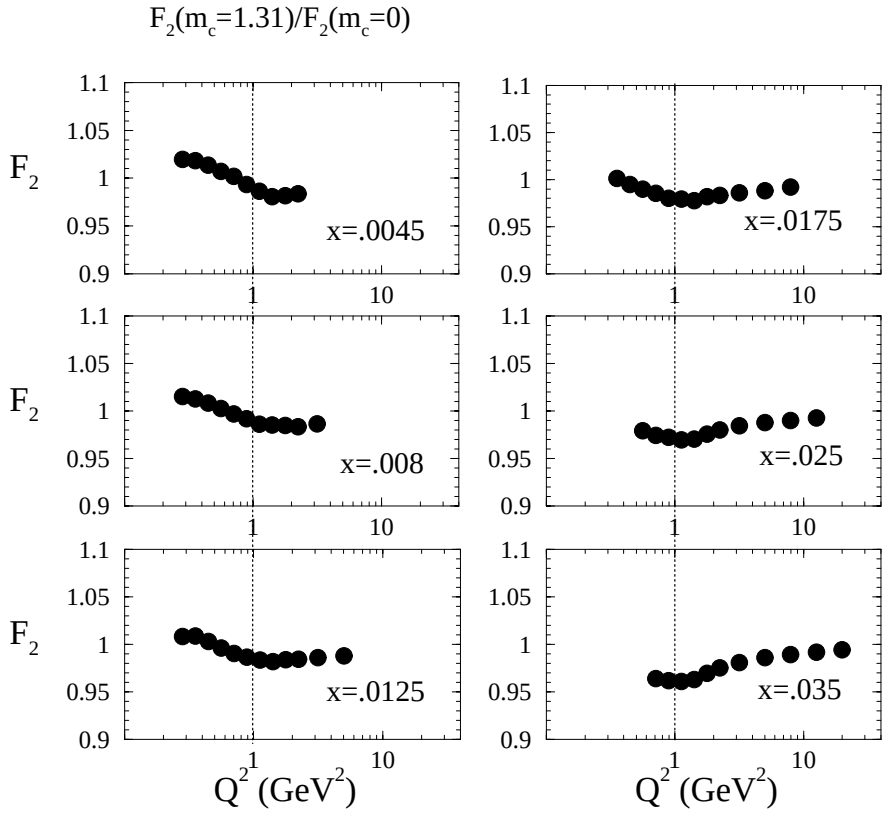

Figure 4.21: Effects of removal of the slow rescaling correction. Ratio shown is F_2 without the slow rescaling correction ($m_c = 1.31$) over F_2 with the slow rescaling correction ($m_c = 0$).

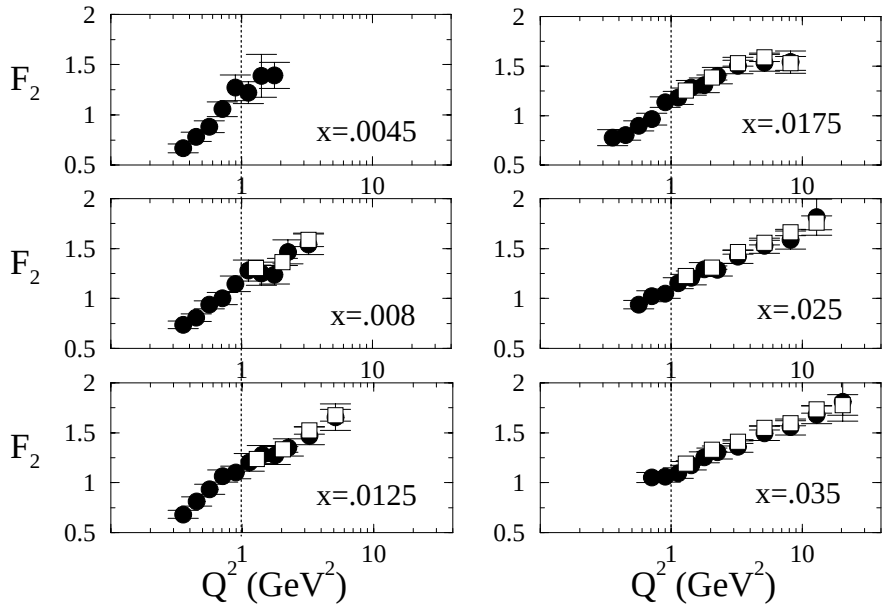

Figure 4.22: Effects of the overall normalization shift in the lowest x bins. Results from previous CCFR structure function analysis indicated by the squares [7] as compared to the results of this analysis indicated by the circles.

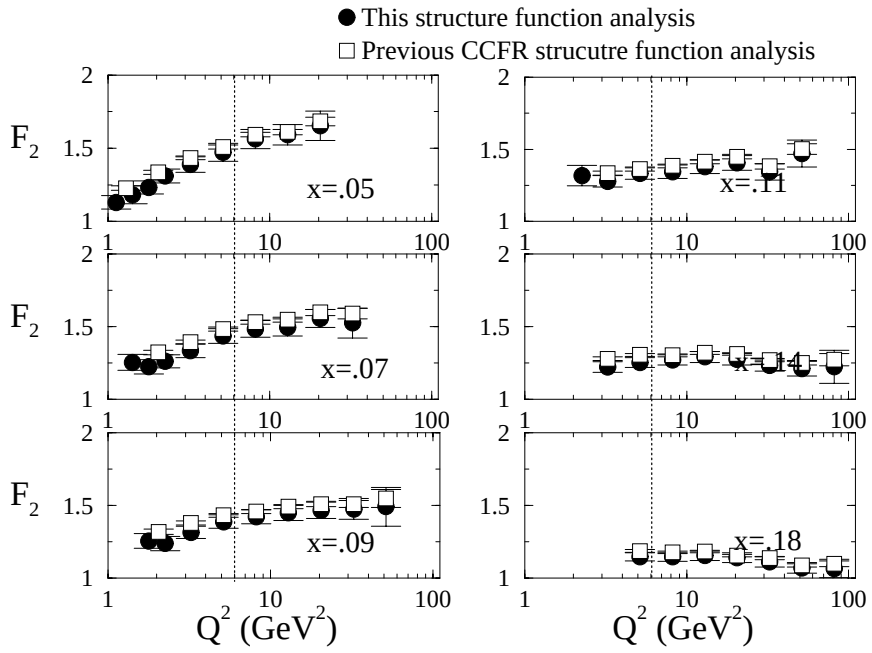

Figure 4.23: Effects of the overall normalization shift in higher x bins. Results from previous CCFR structure function analysis indicated by the squares [7] as compared to the results of this analysis indicated by the circles.

Chapter 5

Low x Low Q^2 Structure Function F_2: Comparisons and Conclusions

High energy neutrino scattering experiments such as CCFR provide a rich body of data on proton structure. Using neutrinos as probes instead of the more typical charged lepton can give us a new window to proton structure, particularly at low Bjorken x. The structure function data presented in chapter 4 can be compared to charged lepton data in the same kinematic region. Differences between the data sets may be due to theoretical predictions as described below.

5.1 Comparisons to Other Experiments

The universality of parton distributions can be tested by comparing neutrino scattering data to charged lepton scattering data. Past measurements for $.0075 < x < 0.1$ and $Q^2 < 1.0$ GeV^2 have indicated that F_2^ν differs by as much as $10 - 20\%$ as shown in figures 5.1 and 5.2. Recent reanalyses of CCFR data [35, 22] have largely resolved this long standing discrepancy. A number of possible reasons for the discrepancy have been explored and rejected. For example:

- Is the strange sea wrong at low x? The strange sea would have to be increased by a factor of two to account for the discrepancy.

- Is the strange sea different from the anti-strange sea? For this to be the reason, the anti strange sea would have to be negative, a result which is unphysical.

- Are nuclear effects different than previously calculated? This has been studied by [35] and can account for only as much as 5% of the discrepancy.

- Is the discrepancy a result of charge symmetry violation ($\delta\overline{d} = \overline{d}^p - \overline{u}^n \neq 0$, $\delta\overline{u} \neq 0$)? This possibility has been ruled out by a CDF W asymmetry measurement [36].

- Is the discrepancy due to the assumptions about how to incorporate the effects of massive charm in the extraction procedure, for example slow-rescaling effects and a ΔxF_3 correction as proposed in the recent reanalyses [35, 22]?

In fact, removing the slow-rescaling correction, now thought of as too simplistic a calculation, and using a new CCFR measurement of ΔxF_3 resolved the longstanding discrepancy between F_2 from neutrino scattering versus F_2 from muon scattering above $x = .015$ [22].

In previous analyses the slow rescaling correction had been applied to allow direct comparison between F_2^ν and $F_2^{\mu,e}$. To compare the two data sets without the slow rescaling correction, neutrino and charged lepton DIS data must be compared within the framework of charm production models, accomplished by plotting the ratio of data to theoretical model. The theoretical calculation corresponding to the CCFR data employs NLO QCD including heavy flavor effects as implemented in the TR-VFS(MRST99) scheme [37, 38]. (We have used the post DIS 2000 MRST corrected code). The theoretical calculation corresponding to NMC [9] and E665 [10] data is determined using TR-VFS(MRST99) for charged lepton scattering. Other theoretical predictions such as ACOT-VFS(CTEQ4HQ) [39, 40] and FFS(GRV94) [41] do not

Table 5.1: Kinematic range of charged lepton experiments discussed.

Experiment	Probe Used	x Range	Q^2 Range (GeV^2)	Reference
E665	μ	$0.0008 < x < .4$	$.229 < Q^2 < 64$	[10]
NMC	μ	$0.0045 < x < .5$	$.75 < Q^2 < 65$	[9]
SLAC	e	$0.2 < x < .5$	$1 < Q^2 < 10$	[42]

significantly change the comparison. As a reminder, the ratio of data to theoretical prediction will be presented as F_2 (data/theory).

The neutrino data are neutrino-iron scattering while the charged lepton data are typically charged lepton-light nucleus. The effects of using a heavy versus light target in these interactions must be taken into account before the data sets can be directly compared. The charged lepton data are corrected to an iron target prior to the comparison.

The combination of the inclusion of the GRV model at low x and low Q^2, its effect on the radiative corrections, and removal of the slow rescaling correction help to resolve the longstanding discrepancy between the neutrino and charged lepton DIS data above $x = 0.015$ as shown in the results in figure 5.3 from a recent CCFR analysis [22]. Charged lepton data shown which overlap the kinematic region accessed by this analysis (see figure 2.6) are as described in table 5.1.

While we expect, and have now observed, that parton distribution universality holds in this region, this need not be the case at lower values of x and Q^2. Figure 5.4 compares F_2 (data/theory) for CCFR, NMC, and E665. There is agreement to within 5% down to $x = 0.0125$. Below this, as x decreases, CCFR F_2^{ν} (data/theory) becomes systematically higher than NMC F_2^{μ} (data/theory). Deviations from this universality at lower Q^2 are expected due to differences in vector and axial-vector components. Vector currents are conserved (CVC) but axial-vector currents are only

partially conserved (PCAC). Adler proposed [11] a test of the PCAC hypothesis using high energy neutrino interactions, a consequence of which is the prediction that F_2 approaches a non-zero constant as $Q^2 \to 0$.

In charged lepton DIS, the structure function F_2^μ is constrained by gauge invariance to vanish linearly with Q^2 as $Q^2 \to 0$. Following the work of Donnachie and Landshoff [43], the form of F_2^μ in the low x and Q^2 region can be described as:

$$C\left(\frac{Q^2}{Q^2+A^2}\right). \tag{5.1}$$

However, in the case of neutrino DIS, the axial component of the weak interaction may contribute a nonzero component to F_2^ν as Q^2 approaches zero. Similarly, F_2^ν should follow a form with a non-zero contribution at $Q^2 = 0$:

$$\frac{C}{2}\left(\frac{Q^2}{Q^2+A^2}+\frac{Q^2+D}{Q^2+B^2}\right). \tag{5.2}$$

Using NMC and E665 data, corrected in this case to be equivalent to scattering from an iron target using a parameterization of SLAC Fe/D data [7], we do a combined fit to the form predicted for μ deep inelastic scattering and extract the parameter $A = 0.81 \pm 0.02$ GeV with $\chi^2/DOF = 27/17$. Results of fits in each x bin for each experiment are shown in Table 5.2 for comparison to parameters in the CCFR fit. The error on A is incorporated in the systematic error on the final fit.

Inserting this value for A into the form predicted for neutrino-nucleon deep inelastic scattering, we fit CCFR data to extract parameters B, C, and D, and determine the value of F_2^ν at $Q^2 = 0$. Only data below $Q^2 = 1.4$ GeV^2 are used in the fits. The CCFR x-bins that contain enough data to produce a good fit in this Q^2 region are $x = 0.0045$, $x = 0.0080$, $x = 0.0125$, and $x = 0.0175$. Figure 5.5 and table 5.3 show the results of the fits. Error bars consist of statistical and systematic terms added in quadrature but exclude an overall correlated normalization uncertainty of $1-2\%$. The values of F_2^ν at $Q^2 = 0$ GeV^2 in the three highest x-bins are statistically significant and are within 1σ of each other. The lowest x bin has large errors but is

within 1.5σ of the others. Taking a weighted average of the parameters B, C, D, and F_2^ν yields:

- $B = 1.53 \pm 0.02$ GeV
- $C = 2.31 \pm 0.03$ GeV
- $D = 0.48 \pm 0.03$ GeV
- $F_2^\nu(Q^2 = 0) = 0.21 \pm 0.02$.

Figure 5.6 shows $F_2^\nu(Q^2 = 0)$ for the different x bins. Inclusion of an x dependence of the form x^β in a combined fit to all four x bins does not significantly improve the overall fits or χ^2.

The above analysis is simplistic for the following reason. In order for the charged lepton F_2 structure function to be consitent with the photoproduction cross section as Q^2 goes to zero, the form of F_2 must go to zero linearly with Q_2. The form $f(x) \times Q^2/(Q^2 + A^2)$ used above will not go to zero linearly since $x = Q^2/2M\nu$. A suggested way to handle this [44] is to use the scaling variable $\xi = x(1 + \mu^2/Q^2)$ and the form $f(\xi) \times Q^2/(Q^2 + A^2)$. This phenomeological form will go to zero linearly with Q^2 and thus assure the relation between F_2 and the photoproduction cross sections.

The F_2 data binned in x bins, used for the previous fits, can be modified for binning in ξ. The slopes dF_2/dx for each Q^2 bin are obtained and then the value for $F_2(\xi) = F_2(x) + dF_2/dx \times (\xi - x)$ where $\xi = x(1 + \mu^2/Q^2)$ for the given bin with $\mu^2 = (0.53)^2$ GeV^2. The value for μ is chosen such that the scaling turns on as the W becomes real and can fluctuate to a π. Specifically, $\mu^2 = W_0^2 - m_p^2$ where $W_0 = m_\pi + m_p$ and W is defined as the total energy of the system, $W = 2M\nu - Q^2 + M^2$.

This procedure has been used for both the NMC and CCFR data. The results are given in tables 5.4 and 5.5 and compared to the previous values. As shown, the fit parameters only change by about one sigma since the F_2 slopes dF_2/dx are very small

Table 5.2: Results for NMC and E665 data fit to Eq. 5.1.

x	A	χ^2/N	N
$0.0045(NMC)$	0.87 ± 0.16	0.02	2
$0.0045(E665)^a$	0.90 ± 0.10	0.43	4
$0.0045(E665)^b$	0.94 ± 0.09	0.31	5
$0.0080(NMC)$	0.75 ± 0.07	0.38	3
$0.0080(E665)^c$	0.87 ± 0.10	0.24	4
$0.0080(E665)^d$	0.85 ± 0.11	1.19	4
$0.0125(NMC)$	0.81 ± 0.05	0.55	5
$0.0125(E665)$	0.97 ± 0.14	1.12	4
$0.0175(NMC)$	0.78 ± 0.06	0.38	5
$0.0175(E665)$	0.76 ± 0.13	0.88	5

[a]Bin center corrected from $x = 0.004$
[b]Bin center corrected from $x = 0.005$
[c]Bin center corrected from $x = 0.007$
[d]Bin center corrected from $x = 0.009$

at low Q_2. Thus, the result shows very little devation from the simplistic assumptions and gives some idea of the size of the systematic error from the phenomenology.

In summary, a first measurement of F_2^ν at low x and low Q^2 has been made. A comparison of F_2 from neutrino deep inelastic scattering to that from charged lepton deep inelastic scattering shows good agreement above $x = 0.0125$, but shows differences at smaller x. This low x discrepancy can be explained by the different behavior of F_2 from neutrino deep inelastic scattering to that from charged lepton deep inelastic scattering as $Q^2 \to 0$. CCFR F_2^ν data favor a non-zero value for F_2^ν as $Q^2 \to 0$ as predicted by Adler.

Table 5.3: Fit results for CCFR data. CCFR data are fit to Eq. 4 with $A = 0.81 \pm 0.02$ as determined by fits to NMC and E665 data. B, C, D, and F_2 at $Q^2 = 0$ GeV^2 results shown below. $N = 4$ for all fits.

x	B	C	D	$F_2^\nu(Q^2 = 0)$	χ^2/N
0.0045	1.49 ± 0.02	2.62 ± 0.26	0.06 ± 0.17	0.04 ± 0.10	0.5
0.0080	1.63 ± 0.05	2.32 ± 0.05	0.50 ± 0.05	0.22 ± 0.03	0.5
0.0125	1.63 ± 0.05	2.39 ± 0.05	0.40 ± 0.05	0.18 ± 0.03	1.0
0.0175	1.67 ± 0.05	2.20 ± 0.05	0.65 ± 0.07	0.26 ± 0.03	0.5

Table 5.4: NMC data binned in ξ as compared to x.

x or ξ	$x = .0045$	$x = .008$	$x = .0125$	$x = .0175$
A using x bins	0.87	0.75	0.81	0.78
A using ξ bins	0.86	0.73	0.78	0.75
Error in A	0.16	0.07	0.05	0.06

Table 5.5: CCFR data binned in ξ as compared to x.

x or ξ	$x = .0045$	$x = .008$	$x = .0125$	$x = .0175$
B using x bins	1.49	1.63	1.63	1.67
B using ξ bins	1.49	1.61	1.62	1.65
Error in B	0.02	0.05	0.05	0.05
C using x bins	2.62	2.32	2.39	2.20
C using ξ bins	2.58	2.25	2.28	2.07
Error in C	0.26	0.05	0.05	0.05
D using x bins	0.06	0.50	0.40	0.65
D using ξ bins	0.09	0.57	0.50	0.79
Error in D	0.17	0.05	0.05	0.07
$F_2(Q^2 = 0)$ using x bins	0.04	0.22	0.18	0.26
$F_2(Q^2 = 0)$ with ξ bins	0.05	0.24	0.21	0.30
Error in $F_2(Q^2 = 0)$	0.10	0.03	0.03	0.03

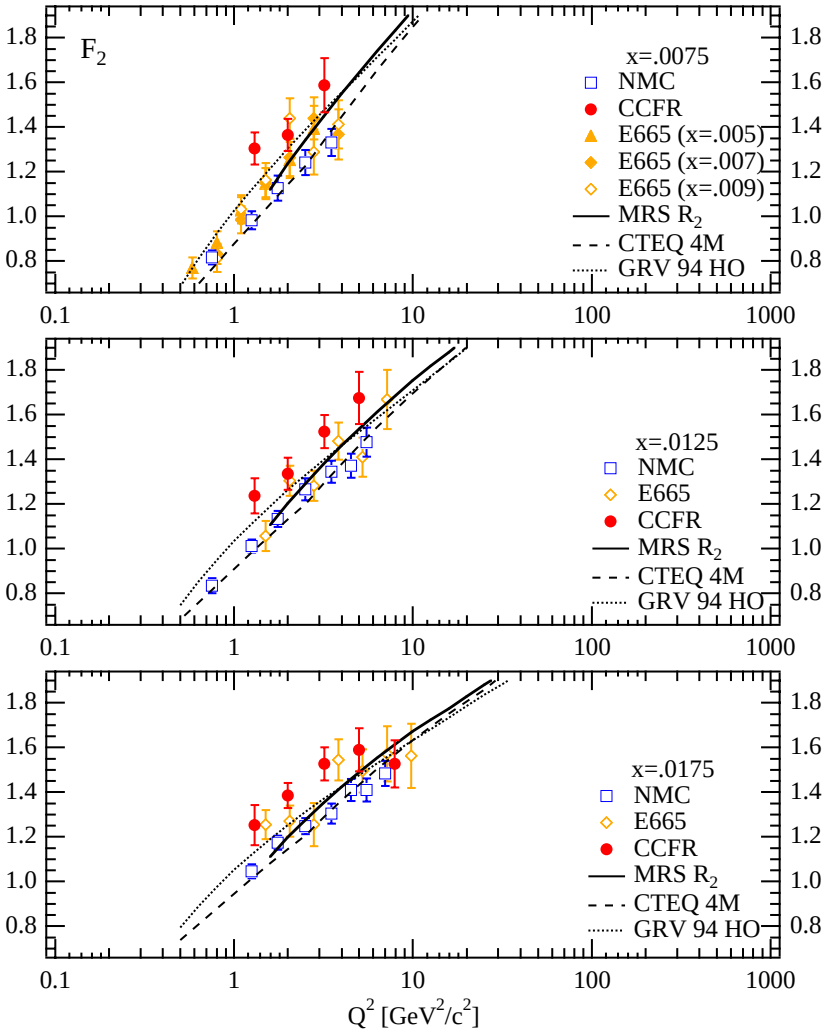

Figure 5.1: Results of previous analysis [7] compared to charged lepton data in the lowest x bins

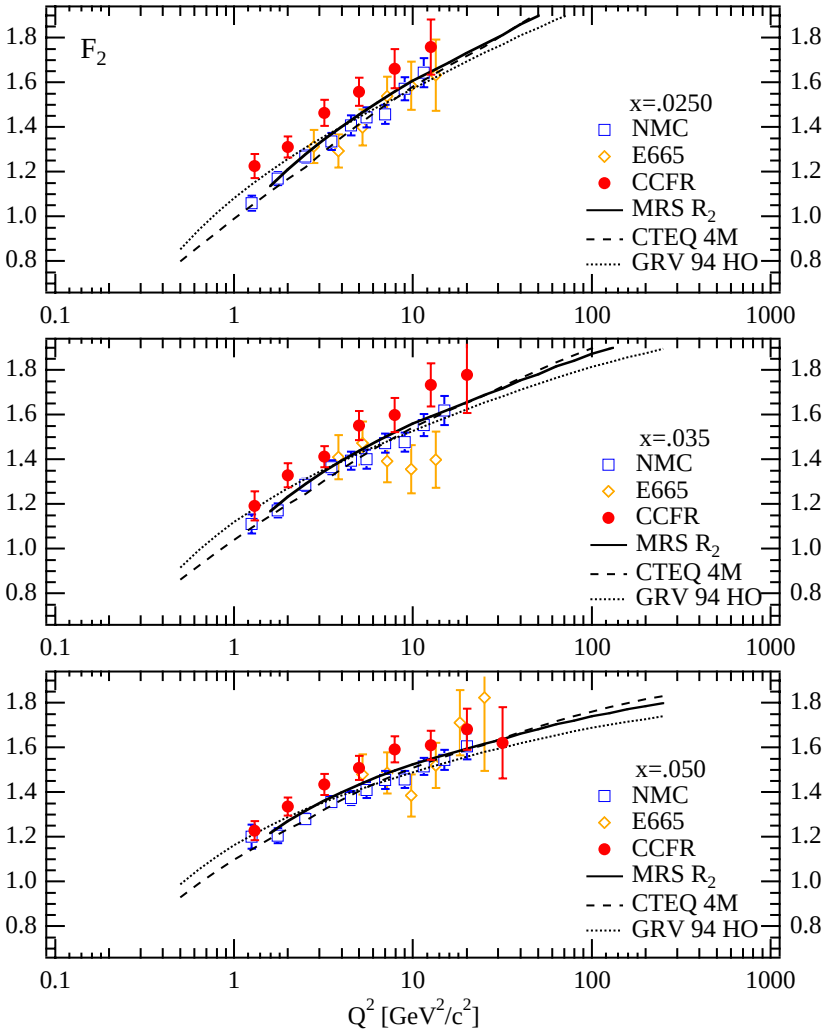

Figure 5.2: Results of previous analysis [7] compared to charged lepton data in higher x bins

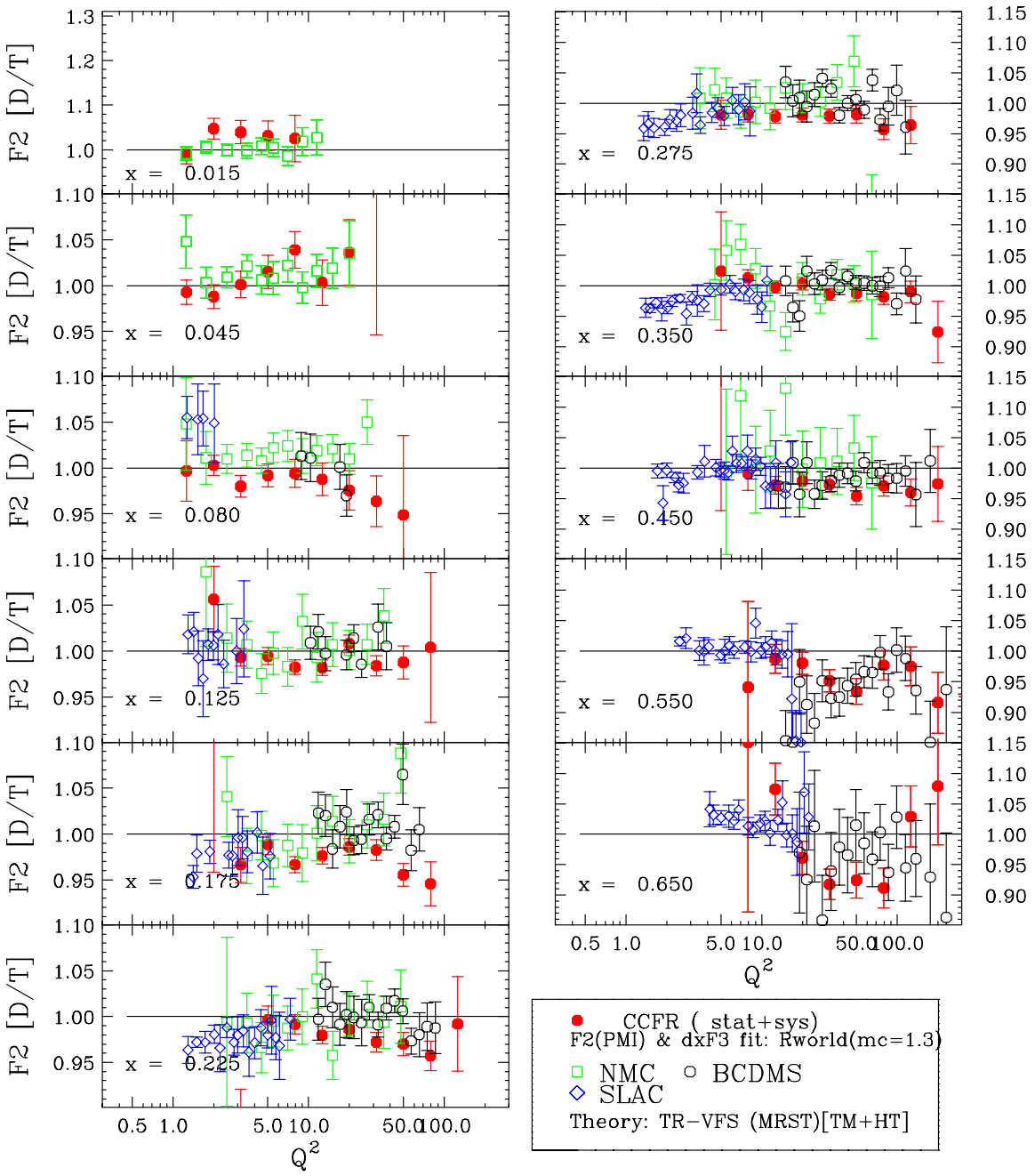

Figure 5.3: F_2(data/theory) for CCFR as compared to the charged lepton data for $x = 0.015$ and higher

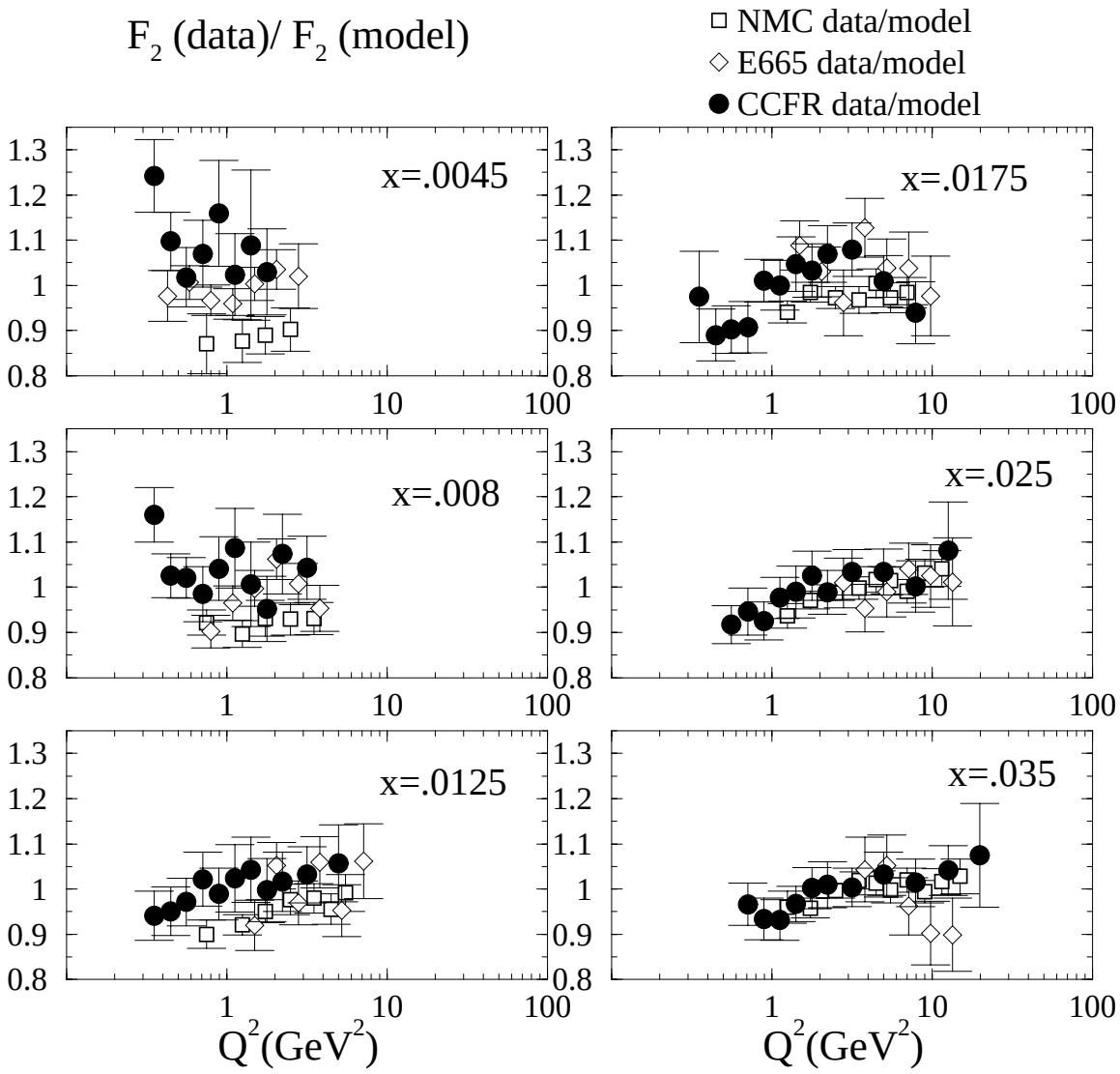

Figure 5.4: F_2(data/theory) from CCFR ν-Fe DIS compared to F_2 from NMC and E665 DIS. Errors bars are statistical and systematic added in quadrature. Theoretical predictions are those of TR-VFS(MRST99).

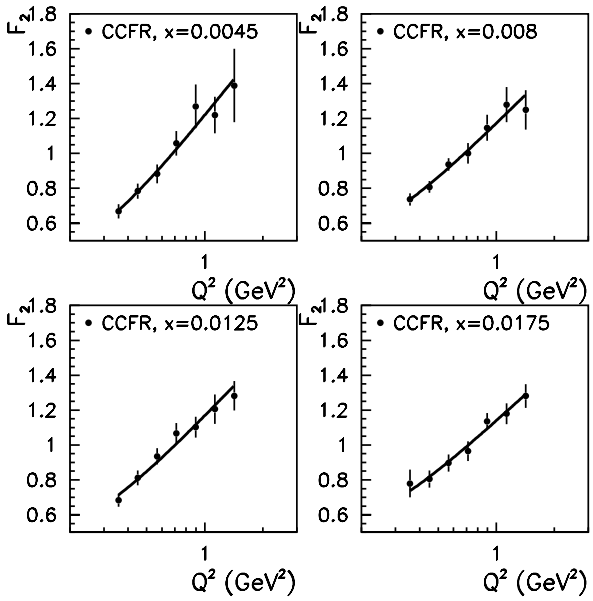

Figure 5.5: Results from fit to CCFR data to extrapolate to $F_2(Q^2 = 0\ \mathrm{GeV}^2)$.

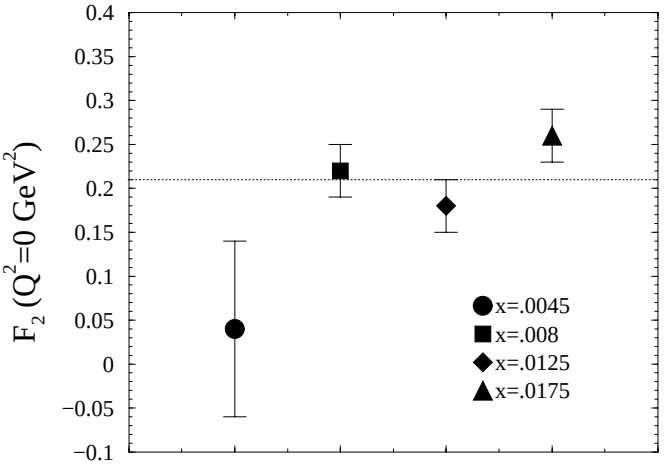

Figure 5.6: $F_2(Q^2 = 0\ \mathrm{GeV}^2)$ from different x bins. A line is drawn at the weighted average of all four measurements.

Part II

Non-Standard Neutrino Interactions

Chapter 6

Beyond Standard Model Neutrino Interactions

Have you ever just sat down with a neutrino for a chat about the finer points of lepton life? This turns out to be a really difficult prospect. Neutrinos are extremely shy and not likely to sit still for very long if at all. They seem to be particularly shy about their weight. At the heart of the debate about the nature of neutrinos is whether or not they have mass.

Neutrinos are one of the Standard Model building blocks of matter. Within the Standard Model, neutrinos are massless. Beyond the Standard Model, neutrinos may be massive....If they do have mass, we know from past experiments that it is very small [2]. Even so, a little neutrino mass will have big implications for the Standard Model.

In the Standard Model, massive, charged particles have intrinsic magnetic moments by virtue of their spin. If we introduce neutrino mass into the theory, an effective neutrino magnetic moment can arise. How neutrino mass fits into the Standard Model, be it via a standard Dirac mechanism, SUSY, or something else, affects the size and origin of this magnetic moment. Thus, we can use a neutrino magnetic

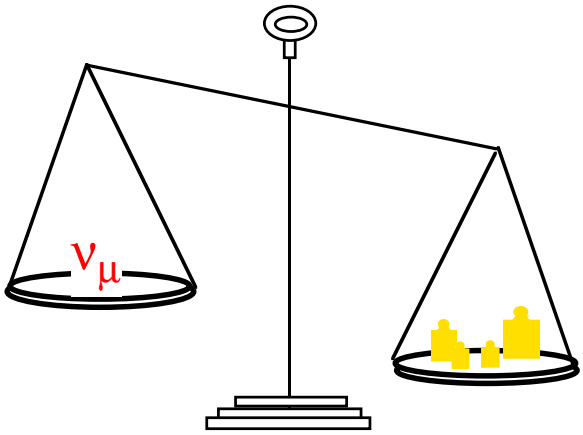

moment measurement to tell us about how neutrinos fit into the larger theory.

6.1 Neutrino Mass in the Standard Model

What implications will neutrino mass have for the Standard Model?

- Neutrino mass may lead to the introduction of new particles and interactions into the theory.
- Neutrino mass could be put into the Standard Model in a variety of ways such as the See-Saw mechanism, using Extra Dimensions, or generation by the Higgs field and more.
- The nature of neutrinos, be they Dirac or Majorana particles, explained below, will affect their place in the Standard Model.
- An understanding of neutrino masses may give us clues to the lepton mass hierarchy.

6.1.1 Handedness and the Sterile Neutrino

Neutrinos appear to be entirely left-handed unlike their charged lepton partners which can be both left-handed and right-handed. Are there right-handed neutrinos not yet observed which exist in a non-interacting state, (a.k.a. sterile neutrinos)?

In the late 1950s, it was observed that neutrinos are left-handed and anti-neutrinos are right-handed [45]. The correct handedness of the weak interaction can be forced in calculations by requiring a factor of $\frac{(1-\gamma^5)}{2}$ at every weak vertex. This picks out only left-handed spinor states where $\Psi_{\mathrm{L,R}} = \frac{1}{2}(1 \pm \gamma^5)\Psi$. Thus, right-handed neutrinos would not interact via the weak interaction. Like neutrinos, they also could not interact via the two other Standard Model forces, the electromagnetic or strong force. These "sterile" neutrinos are undetectable directly because they simply do not interact at all at present energy scales. They could have come into existence if there is a right-handed weak interaction accessible at energy scales well beyond the range of present experiments.

6.1.2 Dirac verus Majorana

In the Standard Model, neutrinos, like their charged lepton partners, are classified as Dirac particles. This means the neutrino and the anti-neutrino are distinct particles just as the electron and positron are distinct. The Dirac nature of the charged leptons can be observed in lepton number conservation where neutrinos ($L = +1$) must produce μ^- ($L = +1$) and anti-neutrinos ($L = -1$) must produce μ^+ ($L = -1$). A different interpretation of the neutrino's nature, put forth by Majorana [46], supposes that the neutrino and anti-neutrino are two helicity states of the same particle referred to as a Majorana neutrino, or ν^{Maj}. So, for example, a π^+ decay would produce the left-handed ν^{Maj} while a π^- decay would produce the right-handed ν^{Maj}. This explanation can supply a complete description of the data without invoking lepton number and it requires fewer total number of particles. Its downside, however, is that

it leaves the neutrino in a class of its own, different from the other Standard Model fermions.

6.1.3 Incorporating Neutrino Mass into the Theory

The simplest method to introduce neutrino mass into the Standard Model is to assume neutrinos are massive Dirac particles, like their charged lepton partners. This allows a small neutrino mass, but an entirely unmotivated one. Theorists have therefore looked for other more physically insightful approaches. The first of these proposed was the See-Saw mechanism, which fits in well with Grand Unified Theories (GUTs). Theories involving Extra Dimensions can account for neutrino mass by allowing neutrinos to live outside of 3 + 1-space. In another approach, the Higgs sector can be modified to accommodate neutrino mass. The more common, simplest schemes are outlined here. Most of the options introduce at least one Electroweak isosinglet, a right-handed sterile partner of the left-handed neutrino which is either light (< 1 eV) or heavy ($> 10^{16}$ eV) depending upon how the theory incorporates neutrino mass.

The general form of the mass term in the Lagrangian is of the form $m\overline{\psi}\psi$. Using $\overline{\psi} = \psi^{\dagger}\gamma^{0}$ and the projections of the left-handed and right-handed portions of the general spinor, $\psi_{L,R} = 1/2(1 \mp \gamma^{5})\psi$ or $\overline{\psi}_{L,R} = 1/2\overline{\psi}(1 \pm \gamma^{5})$, we find that:

$$\overline{\psi}\psi = \overline{\psi}\Big[\frac{1+\gamma^{5}}{2} + \frac{1-\gamma^{5}}{2}\Big]\Big[\frac{1+\gamma^{5}}{2} + \frac{1-\gamma^{5}}{2}\Big]\psi = \overline{\psi}_{L}\psi_{R} + \overline{\psi}_{R}\psi_{L}. \tag{6.1}$$

The scalar "mass" term mixes the right-handed and left-handed states of the fermion. If the fermion has only one chirality, the mass term will automatically vanish. Hence, a standard mass term for the neutrino requires both a right-handed neutrino and left-handed anti-neutrino state.

The most straightforward way to motivate this mass term is via the Higgs mechanism as is done for the electron in the Standard Model. The electron mass arises

this way by introducing a spin-0 Higgs doublet, (h^0, h^+), in the Lagrangian. This gives rise to terms like:

$$g_e\overline{\psi}_e(\psi_\nu(h^+)^\dagger + \psi_e(h^0)^\dagger) \tag{6.2}$$

where g_e is the coupling constant. The second piece in equation 6.2 is identified as the Dirac mass term, $m_e\overline{\psi}_e\psi_e$. Letting $\langle h^0\rangle = v/\sqrt{2}$ we obtain $g\langle h^0\rangle\overline{\psi}_e\psi_e$ and $m_e = g_e v/\sqrt{2}$. This converts electron mass, m_e, into a coupling to the Higgs, g_e and a vacuum expectation value (VEV) for the Higgs, v. By analogy, the neutrino would have a Dirac mass term with $m_\nu = g_\nu v/\sqrt{2}$. The VEV for neutrinos, v, has to be the same as for the electron and all other leptons. This means the neutrinos' small mass must be due to a very small coupling, g_ν, as small as $g_\nu > 2\times 10^{-5} g_e$. While this procedure does introduce neutrino mass, it has shifted the arbitrary magnitude of that mass into an arbitrary coupling without any physical insight as to why the relative couplings (or lepton masses) should be so different.

We can instead consider Majorana mass terms in addition to Dirac mass terms which arise naturally if the neutrino and anti-neutrino are different helicity states of the same particle. This is true if the neutrino is its own charge conjugate, $\psi^c = \psi$. In this case, the operators which appear in the Lagrangian for the neutrino are:

- $(\psi_L, \psi_R, \psi^c_L, \psi^c_R)$
- $(\overline{\psi}_L, \overline{\psi}_R, \overline{\psi}^c_L, \overline{\psi}^c_R)$.

Some bilinear combinations of these in the Lagrangian can be identified as Dirac masses such as $m(\overline{\psi}_L\psi_R + ...)$ while we also get a set of Majorana mass terms, $(M_L/2)(\overline{\psi}^c_L\psi_L) + (M_R/2)(\overline{\psi}^c_R\psi_R) + ...$, which mix the pair of charge-conjugate states of the fermion. If $\psi^c \neq \psi$, then these terms automatically vanish. The mass terms of the Lagrangian can be written in matrix form as:

$$(\overline{\phi}\ \ \overline{\Phi})\begin{pmatrix} M_L & m \\ m & M_R \end{pmatrix}\begin{pmatrix} \phi \\ \Phi \end{pmatrix}, \tag{6.3}$$

where $\phi = (\psi_L^c + \psi_L)/\sqrt{2}$ and $\Phi = (\psi_R^c + \psi_R)/\sqrt{2}$. Here, ϕ and Φ are not describing states with definite mass. The Dirac mass, m, is on the off-diagonal. The Majorana masses, M_L, M_R are on the diagonal. The physical masses can be obtained by diagonalizing the matrix.

Majorana neutrinos, although different in nature than their charged lepton partners, are actually a theoretical improvement over the idea of Dirac neutrinos because one can invoke See-Saw models that motivate small observable neutrino masses. Left-right symmetric GUT's motivate mass matrices that look like [47]:

$$\begin{pmatrix} 0 & m_\nu \\ m_\nu & M \end{pmatrix}. \tag{6.4}$$

Diagonalizing the above matrix to obtain the physical masses leaves two states which are measurable.

- $m_{\text{light}} \approx m_\nu^2/M$
- $m_{\text{heavy}} \approx M$

GUTs favor the existence of a heavy sterile neutrino, m_{heavy}. Experiments have so far only set limits in searches for this particle, also known as a neutral heavy lepton. In the case that the Dirac mass terms for the leptons are approximately equal ($m_\nu \approx m_e$), then $m_{\text{light}} < 1$ eV. In this theory neutrinos have only approximate handedness. The light neutrino would be mostly left-handed, as observed, and the neutral heavy lepton would be right-handed and difficult to observe because of its large mass and sterile nature.

The downside to explaining neutrino mass in the context of GUTs lies in the fact that GUTs have big experimental problems. In the simplest GUT's, protons decay at a rate which is much higher than the experimental limits. In order to stabilize the proton, very elaborate GUTs must be constructed, which makes this solution less fashionable than other extensions to the Standard Model. Another apparent downside

is that GUTs produce at least 12 extra, arbitrary parameters none of which have been observed experimentally.

Other beyond the Standard Model theories are tidier and may motivate why the neutrino mass is light, why all masses are $\ll M_{\text{Planck}}$, why protons are stable, and why gravity is weak. For example, theories involving extra dimensions can provide explanations for the above list of problems. In these theories, the universe has many dimensions, but we are "localized" to only 3+1 dimensions within the multidimensional "bulk." Only electroweak singlet states such as the graviton or the light-mass sterile neutrino [48] can propagate through the bulk. Thus, these theories are one way in which light sterile neutrinos can be motivated.

As illustrated by these examples, there are a number of different ways to introduce neutrino mass into the the theory. The usual approach is not physically motivated while other approaches require lots of beyond Standard Model physics. What we need is data. Experiments need to cover the widest possible set of models to address these possible solutions.

6.2 Phenomenology of Neutrino Oscillations

If neutrinos oscillate between their different flavors, for instance, a muon neutrino turns into an electron neutrino, then quantum mechanics tells us neutrinos have mass. An analogous flavor mixing phenomenon has been observed in the hadron family where quark flavors can mix. In the case of neutrinos, massive neutrinos will necessarily have non-zero mass eigenstates. Different components of the mass eigenstates make up the different flavor eigenstates, ν_e, ν_μ and ν_τ. As the neutrino travels a certain distance, the components of the mass eigenstates comprising a flavor state can change until one flavor state has turned into another. This is most easily illustrated considering a two-generation neutrino model. With only two generations, "neutrino space" can be completely described by two orthogonal vectors called ν_e and

$$\begin{pmatrix} \nu_e \\ \nu_\mu \end{pmatrix} = \begin{pmatrix} \cos\theta & \sin\theta \\ -\sin\theta & \cos\theta \end{pmatrix} \begin{pmatrix} \nu_1 \\ \nu_2 \end{pmatrix}$$

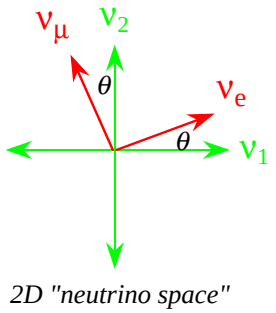

Figure 6.1: Transformation matrix between neutrino mass eigenstates and neutrino flavor eigenstates

ν_μ, the flavor eigenstates. This space can be equally as well represented by another set of orthogonal eigenvectors rotated with respect to the flavor eigenstates. We'll call these ν_1 and ν_2, the mass eigenstates. A simple rotation matrix transforms the flavor representation to the mass representation as shown in figure 6.1.

Using the transformation matrix in figure 6.1, a pure ν_μ state written in terms of its mass eigenstate components is given by:

$$|\nu_\mu(0)\rangle = -\sin\theta|\nu_1\rangle + \cos\theta|\nu_2\rangle. \tag{6.5}$$

After some time, t, the state has evolved and is given by, with $\hbar = c = 1$:

$$|\Psi(t)\rangle = -\sin\theta e^{-iE_1 t}|\nu_1\rangle + \cos\theta e^{-iE_2 t}|\nu_2\rangle \tag{6.6}$$

$$= (\cos^2\theta e^{-iE_1 t} + \sin^2\theta e^{-iE_2 t})|\nu_\mu\rangle + \tag{6.7}$$

$$\sin\theta\cos\theta(e^{-iE_2 t} - e^{-iE_1 t})|\nu_e\rangle \tag{6.8}$$

The probability that the original, pure ν_μ flavor state has oscillated to the other flavor state, ν_e, after time, t, can be determined by taking the inner product:

$$P_{osc} = |\langle\nu_e|\Psi(t)\rangle|^2 \tag{6.9}$$

$$= \frac{1}{2}\sin^2 2\theta[1-\cos(E_2-E_1)t] \tag{6.10}$$

Using $E_{1,2} = \sqrt{p^2+m_{1,2}^2} \approx p + m_{1,2}^2/2p$ and $(t/p) = (tc)/(pc) = L/E$ and converting units gives the probability that a ν_μ will oscillate to a ν_e after some time, t, given by:

$$P(\nu_\alpha \rightarrow \nu_\beta) = sin^2(2\theta)\, sin^2\left(\frac{1.27\Delta m^2 L}{E_\nu}\right) \tag{6.11}$$

where Δm^2 is the mass difference between the two neutrinos, θ is the amount of mixing between the flavor states, L is the distance the neutrino traveled before oscillating and E is the energy of the neutrino. The oscillation probability for two generation mixing given by equation 6.11 is depicted pictorally in figure 6.2.

The extention to a three generation model is messy but straightforward. For three neutrino generations, the neutrino mixing matrix is written as:

$$\begin{pmatrix} \nu_e \\ \nu_\mu \\ \nu_\tau \end{pmatrix} = \begin{pmatrix} U_{e1} & U_{e2} & U_{e3} \\ U_{\mu 1} & U_{\mu 2} & U_{\mu 3} \\ U_{\tau 1} & U_{\tau 2} & U_{\tau 3} \end{pmatrix} \begin{pmatrix} \nu_1 \\ \nu_2 \\ \nu_3 \end{pmatrix}.$$

The oscillation probability is then:

$$\begin{aligned} \text{Prob}(\nu_\alpha \rightarrow \nu_\beta) &= \delta_{\alpha\beta} - \\ &\quad 4\sum_{j>i} U_{\alpha\, i} U_{\beta\, i} U^*_{\alpha\, j} U^*_{\beta\, j} \sin^2\left(\tfrac{1.27\ \Delta m^2_{i\,j}\ L}{E}\right) \end{aligned} \tag{6.12}$$

where $\Delta m^2_{i\,j} = \left|m_i^2 - m_j^2\right|$. Note that there are three different Δm^2 (although only two are independent) and three different mixing angles.

Results from neutrino oscillation experiments are typically mapped out in "parameter space." This depicts all possible combinations of the fundamental parameters, Δm^2 and $sin^2 2\theta$, governing neutrino oscillations in a log-log plot of these parameters. An experiment that sees a signal for neutrino oscillations plots an "allowed region" shown as a blob in parameter space in figure 6.3. An experiment that observes no oscillations plots an exclusion region in this space where all combinations of the

fundamental parameters up and to the right of this exclusion line are ruled out. All blobs and lines in the plots shown in this thesis are at the 90% confidence level.

Two approaches to looking for neutrino oscillations, beginning with, say, a pure muon neutrino beam, are:

- looking for a decrease in the number of muon neutrinos after some time t. Experiments using this method are called *Disappearance Experiments*
- looking for an increase in the number of electron or tau neutrinos, or sterile neutrinos after some time, t. Experiments using this method are called *Appearance Experiments*.

By modifying the experimentally controlled parameters, L and E, experiments can look for oscillations in different regions of space defined by the fundamental parameters, Δm^2 and $\sin^2 2\theta$.

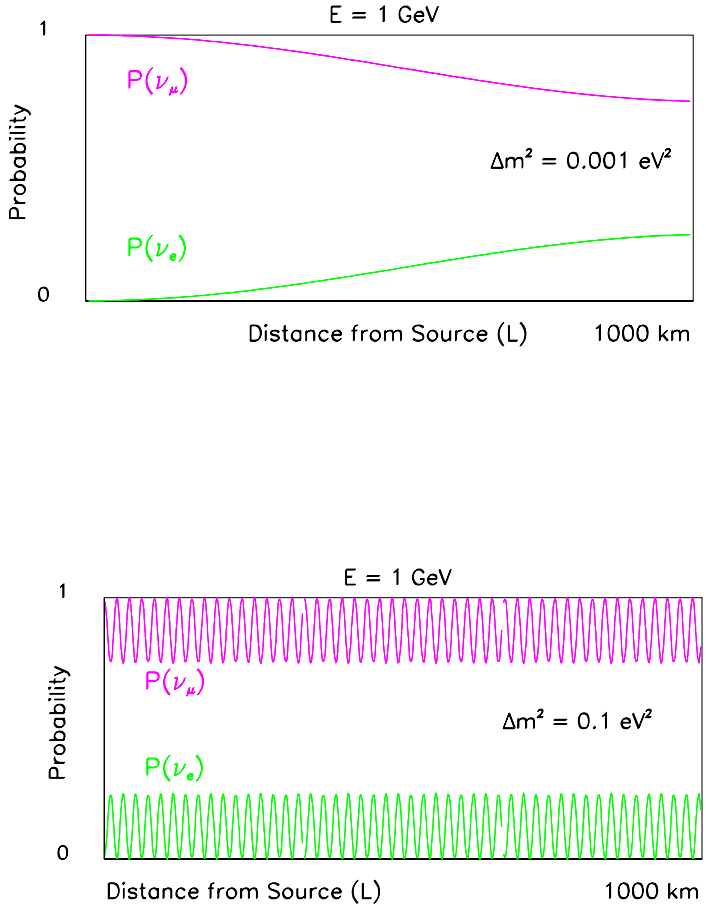

Figure 6.2: If Δm^2 is small, an experiment needs a large L/E to observe a large oscillation probability (top). If $\Delta m^2 \gg L/E$, then rapid oscillations are smeared by statistics, variations in beam energy and detector effects, causing an experiment to be unable to resolve individual wiggles in the oscillation probability. Instead, they measure the average value of the oscillation (bottom). If $\sin^2 2\theta$ is small, an experiment needs lots of statistics [49].

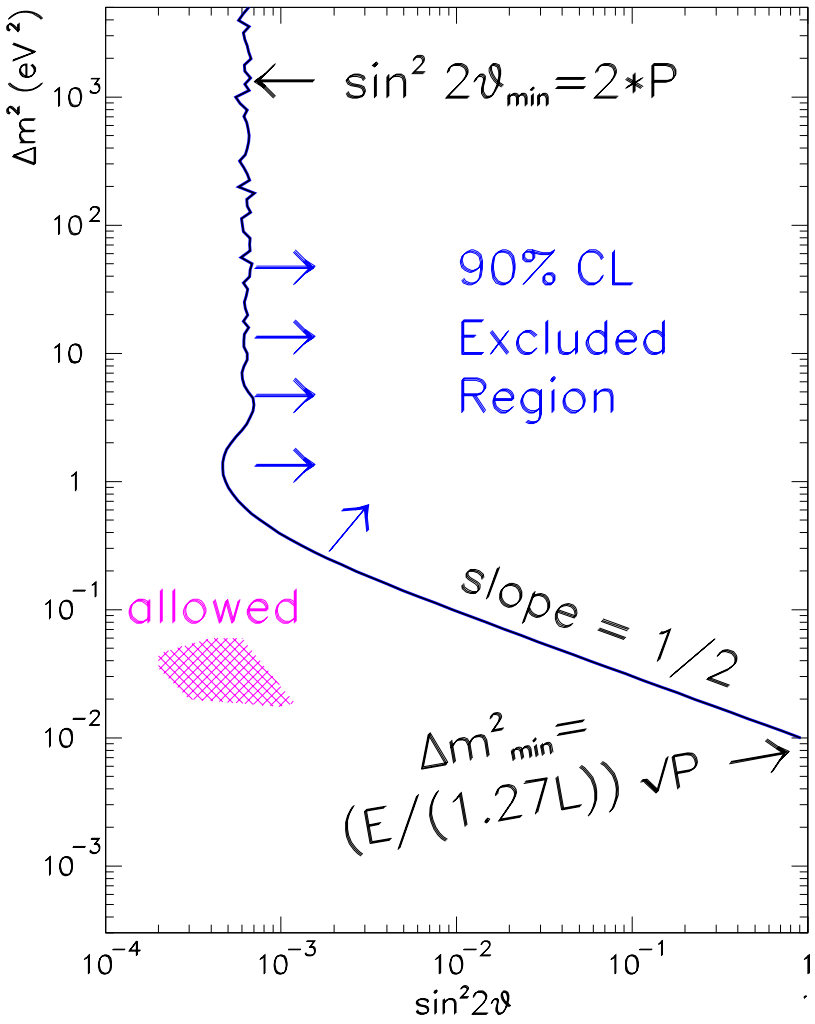

Figure 6.3: Generic example of a neutrino oscillation plot. The region to the right of the solid line is excluded at 90% CL. The shaded blob represents an "allowed" region [49].

6.3 Hints of Oscillations from Around the World

Neutrinos are so light that we have not yet been able to measure their mass by conventional direct mass searches such as studying the kinematics of particle decays. We have as yet only set limits using this method. One can access much smaller neutrino masses through oscillations. This method only measures the difference of squared masses. However, if we assume, as in the charged lepton sector (see table 1.1), that the lowest mass neutrino is much lighter than the others, then $\sqrt{\Delta m^2}$ is approximately the mass of the heavier neutrino.

The first hint for neutrino oscillations comes from experiments observing the Solar Neutrino Deficit [50, 51, 52, 53]. The Standard Solar Model [54] predicts the number of electron neutrinos produced by reactions in the Sun. Detectors on Earth look up at the Sun and count the number of Solar electron neutrinos, but come up short by a factor of two. A possible explanation is that the electron neutrinos are oscillating to another type of neutrino. There are two solutions which can explain this deficit in terms of neutrino oscillations. The "Just-So" solution [55, 56, 57, 58, 59, 60] assumes oscillations are occurring in the vacuum between the Earth and the Sun. The MSW solution [61, 62, 63] accounts for matter effects on the neutrinos that can occur in the Sun and in the Earth. Recent data favors the MSW solution [64].

The second hint comes from experiments looking for neutrinos produced in the atmosphere [65, 66]. Cosmic ray showers in the atmosphere produce muon and electron neutrinos at a rate of approximately $2:1$. Experiments observe fewer muon neutrinos per electron neutrino than they expect. Furthermore, they observe a length dependence in the probability for oscillation in agreement with the expectation for oscillations. The length dependent measurements come from comparing neutrinos produced in the atmosphere directly over the detectors which travel a distance $L = 30$ km to the detector, versus those that are produced in the atmosphere on the opposite side of the Earth and have to travel a distance $L = 6400$ km to the detector.

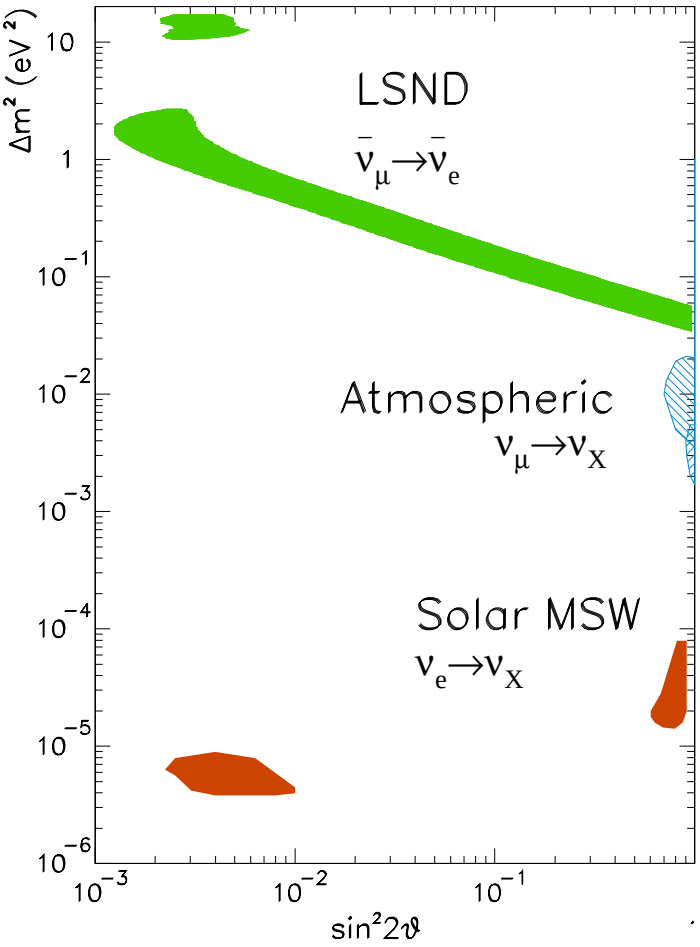

Figure 6.4: Three hints for neutrino oscillations mapped in parameter space

Finally, there is an accelerator experiment, LSND (Liquid Scintillator Neutrino Detector) [67], that sees an indication of oscillations from muon neutrinos to electron neutrinos. The LSND experiment begins with an initially pure muon neutrino beam that is allowed to travel 30 m to the detector where the appearance of electron neutrinos in the detector are observed. The LSND allowed regions along with the atmospheric and solar are shown in figure 6.4.

Taken at face value, these signals cannot all be explained with the three Standard Model neutrinos. Given only three neutrinos, there are only two independent mass differences between them. The third mass difference is just the sum of the first two. These three distinct signals indicate three mass differences which can be explained

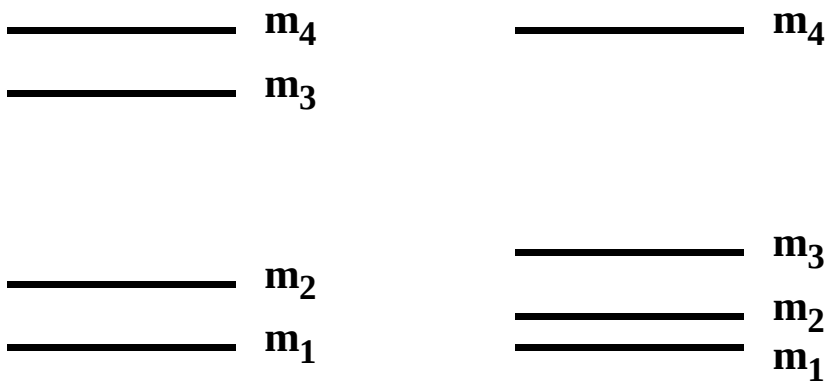

Figure 6.5: Hierarchy of neutrino mass eigenstates in the $2+2$ model(left) and the $3+1$ model(right) which may also have the smallest Δm^2 splittings as more massive than the largest.

within certain models that contain the three Standard Model neutrinos and a sterile neutrino. These models are named after the neutrino mass hierarchy they follow. The 3+1 model [68, 69, 70] has three light neutrinos and one heavy, while the 2+2 model [71, 72, 73, 74, 75] has two groupings of two neutrinos each, one lighter and one heavier (see figure 6.5).

In order to understand which mixing scenario is occurring or if any of the experiments are seeing an effect other than oscillations, other experiments must confirm or rule out these signals. Among these experiments is MiniBooNE at Fermilab.

6.4 Neutrino Magnetic Moment

Neutrino magnetic moments can arise through a variety of beyond Standard Model mechanisms. In the minimally extended Standard Model, massive Dirac neutrinos of mass m_ν can have a neutrino magnetic moment of:

$$\mu_\nu = \frac{3eG_F}{8\sqrt{2}\pi^2} m_\nu \sim 3 \times 10^{-19} \mu_B \left(\frac{m_\nu}{1\text{eV}}\right). \tag{6.13}$$

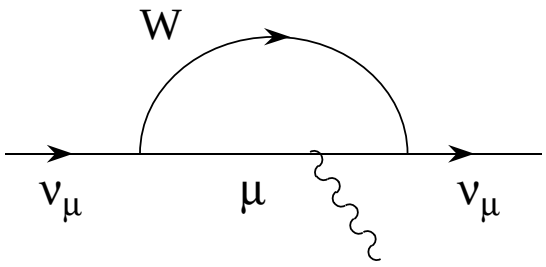

Figure 6.6: Standard Model neutrino magnetic moment Feynman diagram. Photon radiates off the lepton leg.

arising from one loop radiative corrections in diagrams with W-boson exchange as in figure 6.6. A neutrino turns into a W boson and a lepton, the lepton (or W boson) emits a photon and flips spin. The W boson and lepton then reinteract to form the neutrino which must have flipped spin in order to conserve spin at that vertex. Note that the neutrino, with a different spin, has flipped helicity which it can only do if it has mass.

We can place neutrinos with non-zero magnetic moments in the context of a larger theory such as SUSY and Extra Dimensions. These extensions to the Standard Model such as the super symmetric left-right model predict larger neutrino magnetic moments of the size [76]:

$$\mu_{\nu_e} \cong 5 \times 10^{-15} - 10^{-16}\mu_B \tag{6.14}$$

$$\mu_{\nu_\mu} \cong 1 \times 10^{-12} - 10^{-13}\mu_B \tag{6.15}$$

$$\mu_{\nu_\tau} \cong 2 \times 10^{-12}\mu_B. \tag{6.16}$$

Theories involving Extra Dimensions produce an effective neutrino magnetic moment as large as $10^{-11}\mu_B$ [77]. A non-zero neutrino magnetic moment would also have important implications in cosmology in the development of stellar models. Astrophysical limits such as plasmon, or photon wave packets, decay rates from horizontal branch stars and neutrino energy loss rate from supernovae allow a neutrino magnetic moment as large as $10^{-11}\mu_B$ [78, 79, 80].

A non-zero neutrino magnetic moment will give rise to an electromagnetic contribution to neutral current neutrino scattering. This is most easily measured using neutrino-electron elastic scattering. This electromagnetic contribution to the cross section for neutrino-electron elastic scattering is of the form:

$$\sigma_{EM} = f^2 \pi r_0^2 \left[\frac{T_e^{\min}}{E_\nu} - ln\left(\frac{T_e^{\min}}{E_\nu}\right) - 1 \right] \tag{6.17}$$

where r_0 is the classical electron radius, $T_e^{\min}$ is the minimum kinetic energy of the recoil electron, E_ν is the neutrino energy and f is the neutrino magnetic moment in units of Bohr magnetons.

At low $y = T_e/E_\nu$, the electromagnetic contribution to the neutrino-electron cross section increases rapidly while the Standard Model contribution increases only gradually. The resulting shape dependence in the differential cross section can be used to look for a signal in a high statistics experiment like MiniBooNE. The differential cross section contributions for weak and electromagnetic components of the neutrino-electron elastic scattering cross section are given by:

$$\frac{d\sigma^{weak}}{dT_e} = \frac{2m_e G_F^2}{\pi} \left[g_L^2 + g_R^2 \left(1 - \frac{T_e}{E_\nu}\right)^2 - g_R g_L \frac{m_e}{E_\nu}\frac{T_e}{E_\nu} \right] \tag{6.18}$$

$$\frac{d\sigma^{EM}}{dT_e} = \frac{\pi \alpha^2 \mu_\nu^2}{m_e^2} \left(\frac{1}{T_e} - \frac{1}{E_\nu} \right) \tag{6.19}$$

where T_e=electron recoil energy and E_ν= neutrino energy.

Present limits set on neutrino magnetic moments are many orders of magnitude away from the Standard Model prediction including massive Dirac neutrinos. They are, however, only one to two orders of magnitude away from predictions from certain beyond Standard Model theories and astrophysical limits. The most stringent limits set by experiments for neutrino magnetic moments for each neutrino flavor are listed in table 6.1. The experimental limit for the muon-neutrino magnetic moment coming

ν Flavor	Limit Set(μ_B)	Experimental Data	Process	Reference
ν_e	1.5×10^{-10}	Super Kamiokande	shape of differential cross section	[82]
$\overline{\nu_e}$	1.8×10^{-10}	combination of $\overline{\nu_e}$ reactor experiments	excess in total cross section	[83, 84]
ν_μ	6.8×10^{-10}	LSND	excess in total cross section	[81]
ν_τ	5.4×10^{-7}	DONUT	excess in total cross section	[85]

Table 6.1: Limits set on neutrino magnetic moments.

from the LSND experiment is an upper limit of $\mu_{\nu_\mu} < 6.8 \times 10^{-10}\mu_B$ [81] set by measuring the total neutrino-electron elastic scattering cross section. MiniBooNE and upgrades to MiniBooNE may be able to improve this limit significantly as discussed in section 8.2.

Chapter 7

MiniBooNE Neutrino Beam and Detector

The MiniBooNE experiment is designed to search for $\nu_\mu \rightarrow \nu_e$ oscillations with high precision in order to confirm or refute the LSND oscillation interpretation. It is an accelerator based oscillation experiment under construction at Fermi National Accelerator Laboratory in Illinois. A nearly pure muon neutrino beam is created and allowed to travel 500 m to the MiniBooNE detector where muon neutrinos and electron neutrinos are tagged to look for muon neutrino disappearance and electron neutrino appearance as in the LSND experiment. Differences in neutrino energy, E, and distance the neutrinos travel to the detector, L, make the MiniBooNE background errors significantly different than those in the LSND experiment. This allows MiniBooNE to look for the same oscillation signal that LSND reports with a very different experiment, making this a decisive test of the LSND signal.

MiniBooNE can also address a variety of other interesting physics including neutrino-nucleon cross sections, proton structure measurements, supernovae detection, and beyond Standard Model neutrino interactions. This thesis will explore the last issue in greater detail in chapter 8.

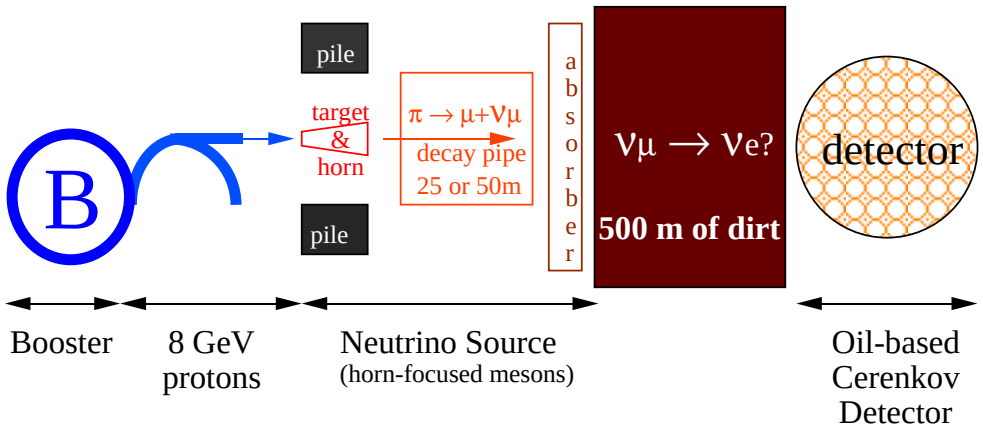

Figure 7.1: Schematic of the MiniBooNE beamline starting from the Booster.

7.1 The MiniBooNE Beamline

Neutrinos for the MiniBooNE experiment are produced from 8 GeV protons accelerated by the Booster described in chapter 3. Protons from the Booster headed for other experiments continue on to the Main Injector. Protons for MiniBooNE skirt the Main Injector and are directed toward the MiniBooNE target hall. Figure 7.1 shows the path the proton beam takes from the Booster to the MiniBooNE target hall and on to the detector. Figure 7.2 shows the MiniBooNE beamline on the Fermilab site.

Inside the target hall, the protons are incident on a 72 cm long BeO target located within a magnetic focusing system called a "horn." Pions and kaons produced in the target are focused by the horn toward the detector. The approximately 1 Tesla focusing field in the horn is created by running high current (170 kA) down the outer conductor, and back along the inner conductor or the reverse of this to focus opposite sign particles. The field produced is approximately that of an infinitely long straight wire, $B = \frac{\mu_0 I}{2\pi r}$. The horn's high current and fast cycle time (15 Hz) make the system a technological feat to construct and operate [86]. Figure 7.3 shows a schematic of the completed horn.

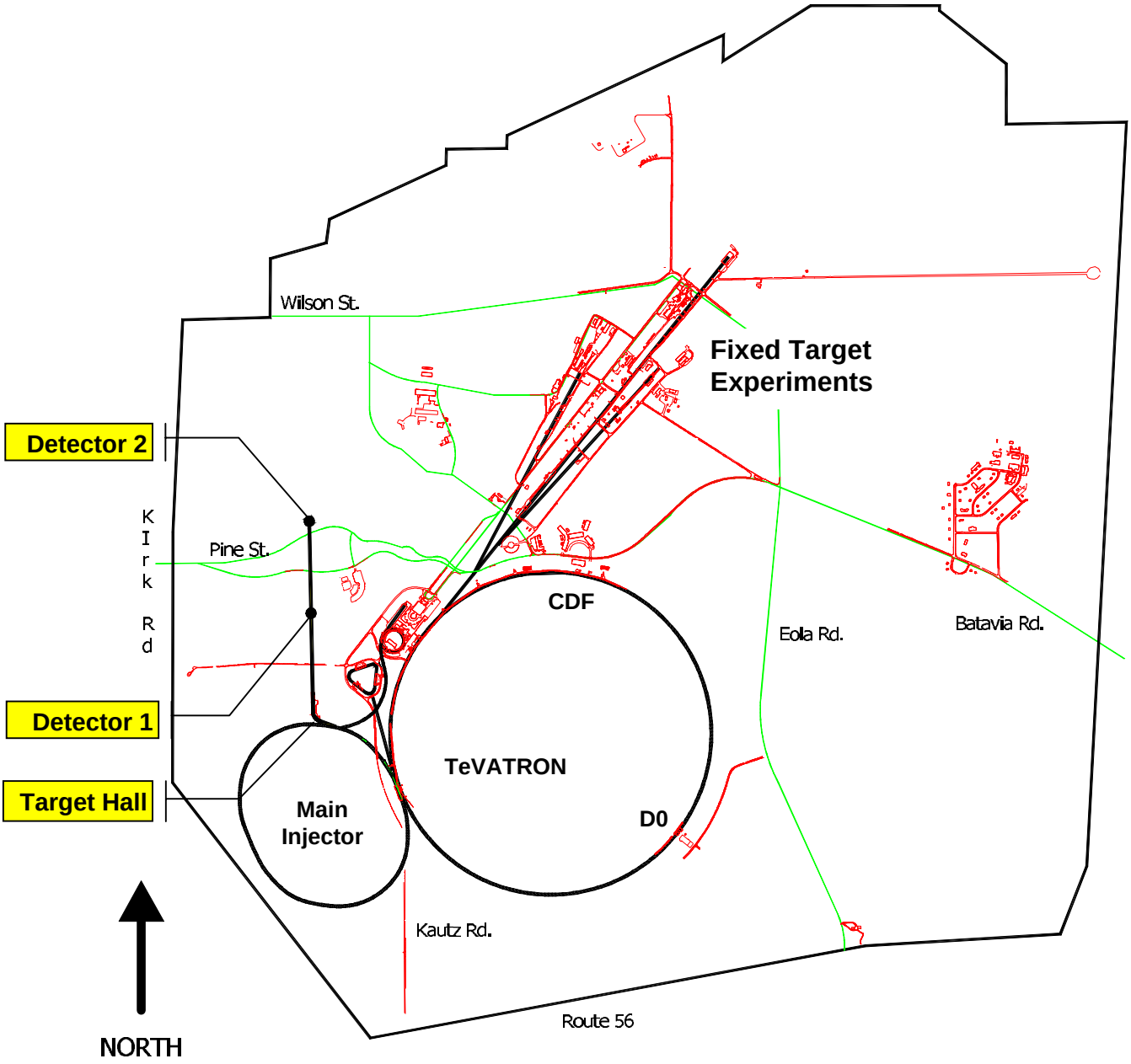

Figure 7.2: Overview of the MiniBooNE beamline on Fermilab site. The Booster is the small red circle at ten-o'clock on the TeVatron. The MiniBooNE detector is indicated by "Detector 1". A possible site for BooNE, a possible upgrade to the MiniBooNE experiment is indicated by "Detector 2".

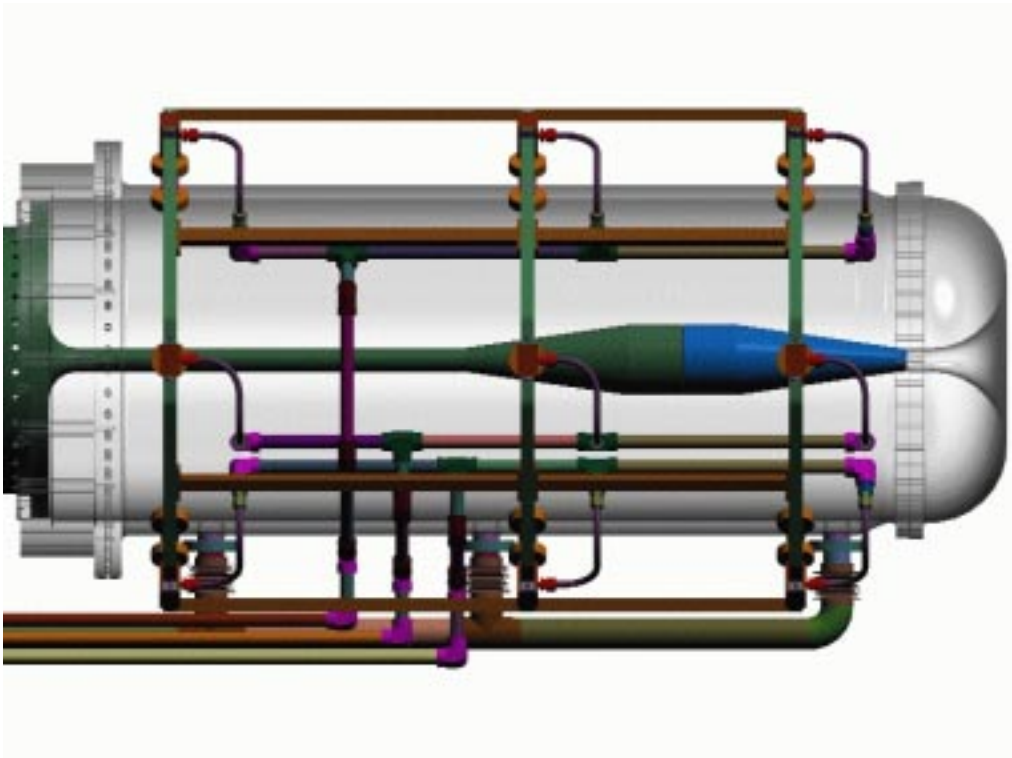

Figure 7.3: Horn focusing system

7.1.1 Neutrino Flux

Pions and kaons produced in the target will decay primarily into muons and muon neutrinos in the decay channel following the target, shown in Figure 7.4. The neutrino spectrum produced in the 50 m decay channel is shown in figure 7.5. The intrinsic electron neutrino background coming from kaon and muon decays, as shown, is several orders of magnitude smaller than the muon neutrino flux. Nevertheless, there are several ways in which the experiment can verify the amount and source of the electron neutrino contamination in the beam. The length of the decay channel is variable (25 or 50 m long) to provide a novel check on the electron neutrinos coming from muon decay. Most muons will not decay before reaching the end of the decay channel. Those that do will produce electron neutrinos that contribute to our background. When the decay channel length is halved from 50 m to 25 m, the number of electron neutrinos should go down by approximately a factor of four if they are all from muon decay, but should go down only by a factor of two if they are due to oscillations. So by comparing the data with different decay channel lengths, we can get a handle on this background. Intrinsic electron neutrinos from kaon decays can be measured using the "Little Muon Counter" (LMC) [87]. The LMC will be a permanent magnet spectrometer or tungsten-scintillator range stack designed to measure $0.75 - 2.0$ GeV muons from $K^+ \rightarrow \mu^+ \nu_\mu$ decays. From this cross section, an estimate on electron neutrinos from K^+ decays can be determined. The LMC is positioned at 7 degrees off axis of the decay channel, in position to see K^+ decays. Events in the detector can also be used to eliminate backgrounds as described in section 8.1. The neutrino beam exits the decay channel through a 3 m deep beam absorber which cleans the beam of all but the neutrinos. The neutrino beam then travels 500 m downstream through earth to the detector.

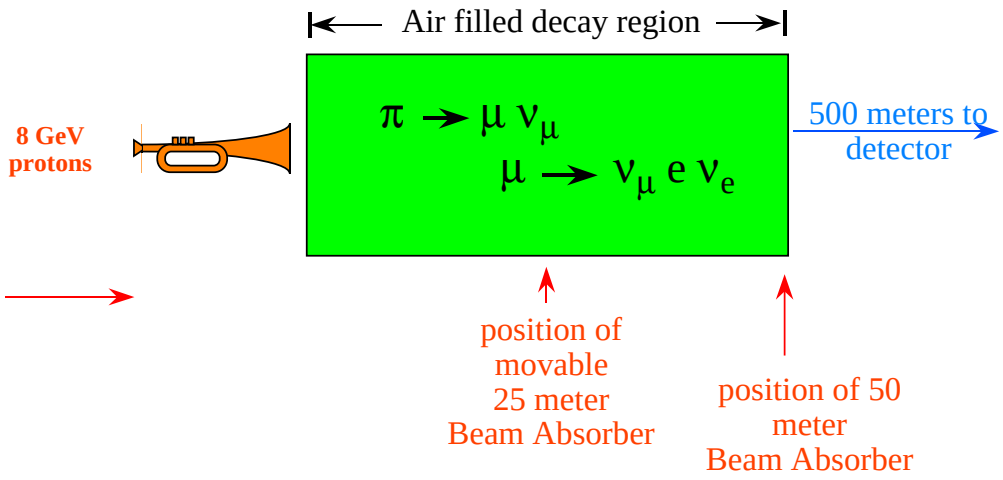

Figure 7.4: Boone target hall

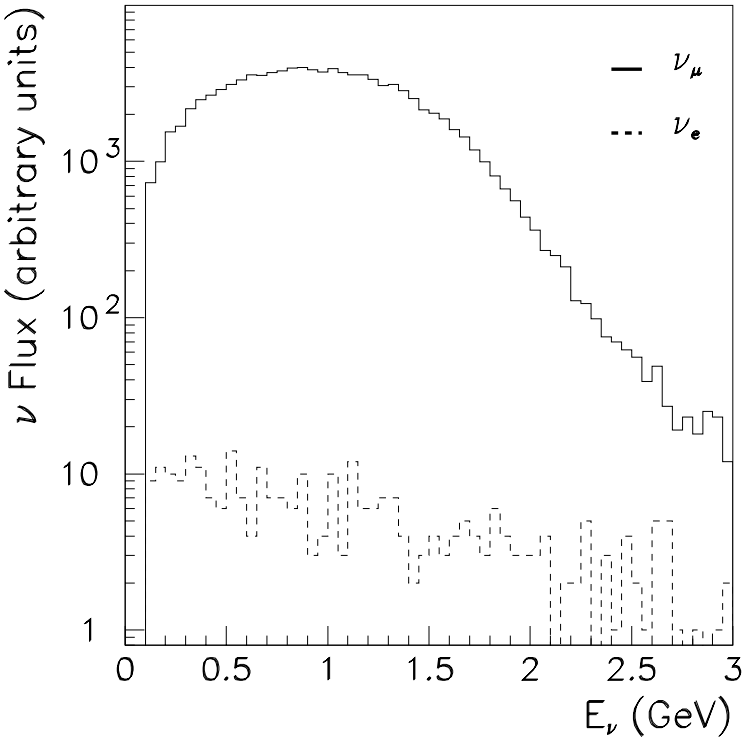

Figure 7.5: Neutrino flux

7.2 The MiniBooNE Detector

The MiniBooNE detector shown in figure 7.6 is a 12 m diameter carbon steel sphere filled with mineral oil and surrounded with light collecting devices called photomultipler tubes (PMTs). The volume where neutrino interactions are observed is a sphere-within-a-sphere. The inner and outer volumes are separated by light tight panels to optically isolate the outer veto region. Surfaces on the inner volume are painted black to minimize scattering of light while surfaces in the veto are white to maximize scattering. Photomultiplier tubes are mounted on both sides of the light tight panels - inward to detect neutrino interactions, outward to "veto" events induced by cosmic rays. High voltage and PMT response rides on PMT cables that run inside the veto, from the PMTs in the main tank and the veto, to the top of the tank where they exit and are connected to high voltage and the electronics. The inner region contains 1280 PMTs providing 10% photocathode coverage. Studies prior to construction of the detector showed that reconstruction efficiency did not improve significantly with photocathode coverage increased up to 40%, making 10% coverage the cost-efficient choice. The outer region contains 240 PMTs, enough to provide a veto with at least 99% efficiency. Appendix D describes the testing, potting, and installation of the PMTs in detail.

The top of the detector is at ground level with a 3 m overburden to provide some reduction from cosmic rays. Because the beam is pulsed, major cosmic ray sheilding is not necessary, unlike non-accelerator neutrino experiments.

7.2.1 Events in the Detector

As discussed previously, we see neutrinos in mineral oil when one hits a proton and interacts weakly by exchange of a W boson. In a charged current interaction such as this, the neutrino turns into its charged lepton partner. An electron neutrino becomes an electron and a muon neutrino becomes a muon. These electrons and muons emit

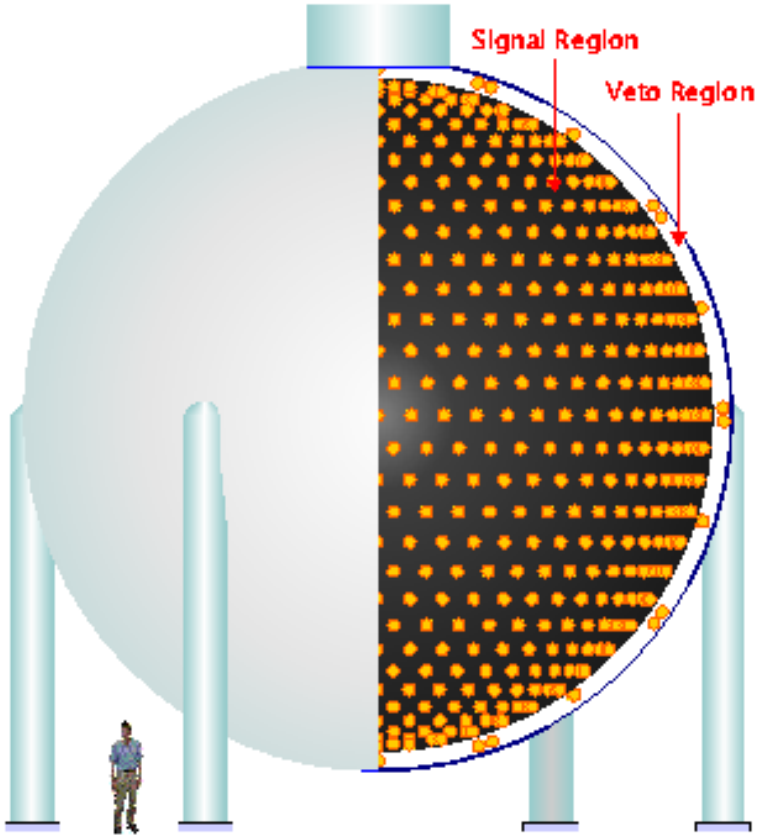

Figure 7.6: The MiniBooNE detector cut-away to show the sphere within a sphere.

distinct light signatures in the tank which we look for. Therefore, "seeing" neutrinos in the detector really means looking for muons and electrons produced from neutrino charged current interactions.

Electrons and muons produce Čerenkov radiation and scintillation light in the visible spectrum in mineral oil. Čerenkov radiation occurs when these particles travel faster than the speed of light in the mineral oil, causing a "sonic boom" of light. Interference effects produce wavefronts of light that travel to the edge of the detector in a cone, casting rings on the inner detector surface. The differences in electron and muon Čerenkov rings allow us to tell the difference between electrons and muons. Figure 7.7 shows Čerenkov rings produced by different particles and a projection of

one ring inside the detector. Electrons produce Čerenkov radiation for only a short period of time and scatter around while they do this. The result is a fuzzy ring. Muons scatter significantly less and slow down as they produce Čerenkov radiation causing the angle of the wavefront to change. A muon ring has a sharp outer edge with a filled in center. π^0's produced in neutral current interactions in the detector decay to two γ's which can pair produce and emit two electron-like rings. If these rings overlap enough or if only one electron produces a ring, the π_0 can be mistaken for an electron. This background must be well understood. Scintillation light, approximately 25% of the light produced in an electron event, will also aid in event reconstruction; because it is isotropic, scintillation light can be used to determine the event vertex.

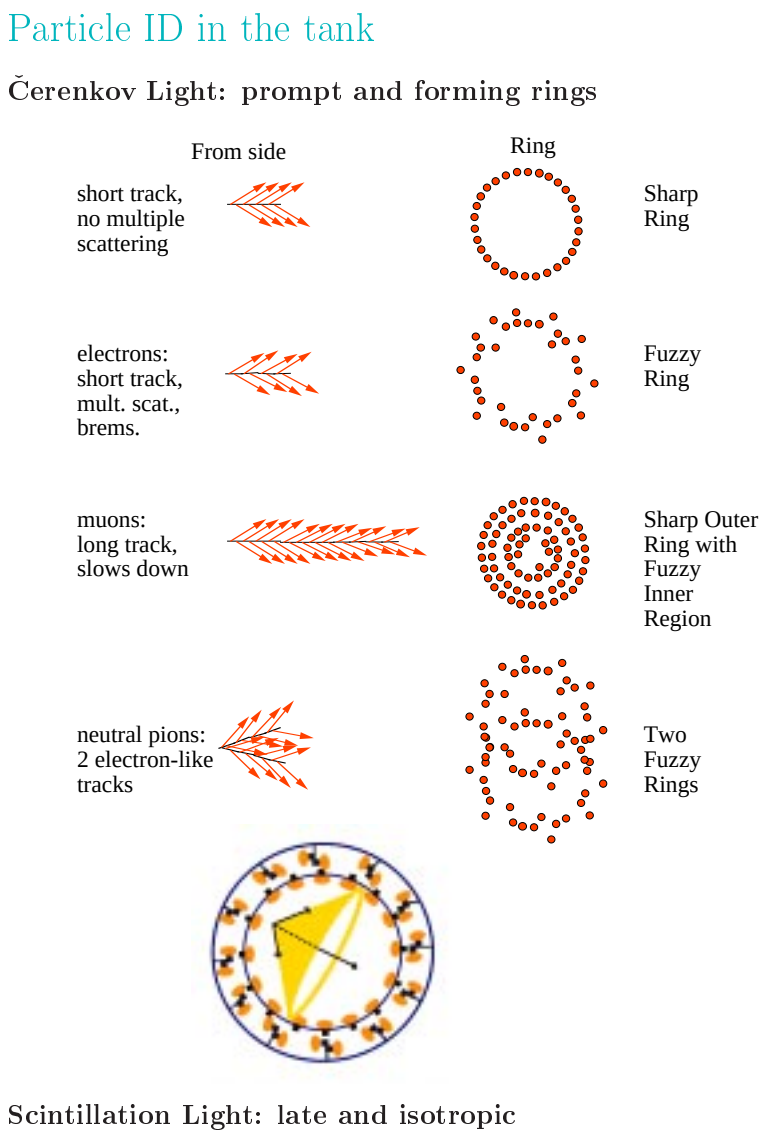

Figure 7.7: Čerenkov rings for electrons, muons and π^0's along with a generic Čerenkov ring projected on the inside of the detector. Čerenkov light is early and produces a ring while scintillation light is late and isotropic. The amount of scintillation light in the detector is limited so that the fraction of Čerenkov light produced is enough to properly identify particles.

7.2.2 Trigger, DAQ, and Event Reconstruction

The light signatures produced by particle interactions in the detector are recorded by the PMTs at the edge of the detector. Time and charge response of each PMT are used to define triggers to record data for analysis off-line. Event reconstruction and particle ID are based on PMT charge and timing response to both Čerenkov and scintillation light.

The electronics used to define the trigger system and record PMT response are inherited from the LSND experiment. Each PMT signal cable is connected to a channel which determines the time of the leading edge with respect to a reference clock and integrates the pulse. PMT signals are sampled every 100 ns by flash analog to digital converters (FADCs) and the digitized data are written to a circular buffer which can hold approximately 200 μs of data in these 100 ns intervals. This time history allows for temporary storage of event information for a time long enough to allow a trigger decision to be made by a mono-board computer. Data are then written to tape with pretrigger information also stored in case, for example, it must be determined if an electron event originated from a muon decay. The trigger system takes into account beam on time, veto activity, and detector activity. When a trigger fires, detector information stored over the appropriate time span is recorded to tape along with trigger information for off-line analysis.

Off-line event reconstruction algorithms [89, 90, 91, 92, 93, 94, 95, 96] use scintillation light and Čerenkov light to reconstruct the vertex position of events, Čerenkov rings produced, and amount of light produced by the charged particle in the detector.

7.2.3 Detector Calibration

Two detector calibration systems will be installed in the detector to measure relevant PMT qualities and aid in determining detector response for event reconstruction.

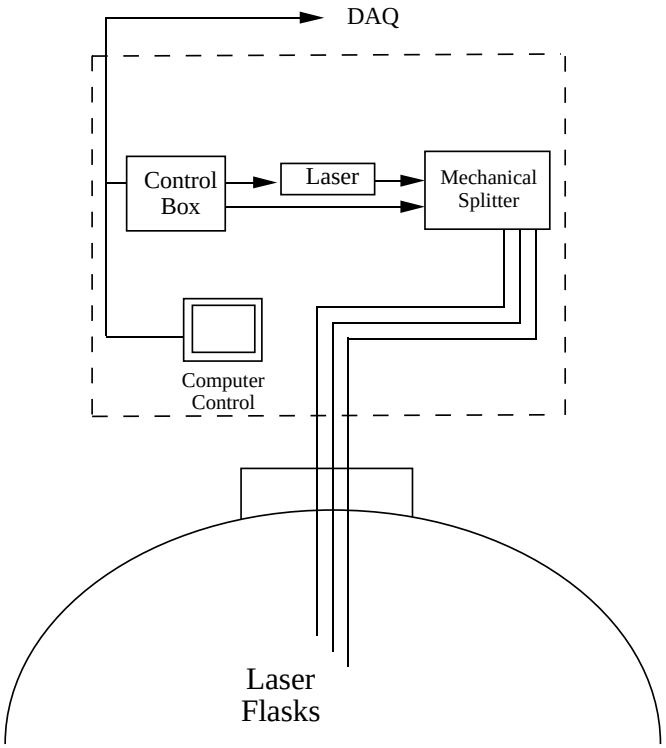

Figure 7.8: Laser calibration system inside the MiniBooNE detector [88]

The laser calibration system, consisting of 4 light dispersion flasks at fixed locations in the detector, will allow measuring and monitoring of properties of each PMT including PMT gain, pulse height, and timing. The system, shown in figure 7.8 [88] pipes light through fiber optic cable to the laser flasks and to reference PMTs or photodiodes to provide a tag signal for the MiniBooNE electronics.

The cosmic ray muon calibration system uses scintillation cubes inside the detector along with the free and constant rain of cosmic rays from overhead to aid in calibration of event reconstruction in the detector. Figure 7.9 shows a muon tracker above the detector along with scintillation cubes inside the detector which comprise this system. Muons that stop and decay as shown in the cubes are excellent calibration tools since their position is known to within 3 cm – the size of the cubes and their energy is known to within 3%. Their decay electrons can be measured in delayed coincidence both in the cubes and in the detector.

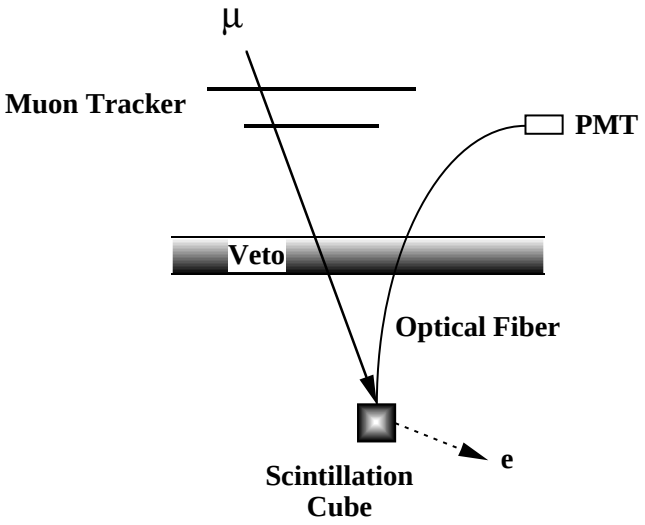

Figure 7.9: Cosmic ray muon calibration system inside the MiniBooNE detector [88]

Understanding the detector elements is crucial to reconstructing electrons and muons and therefore searching for neutrino oscillations. Appendix D describes in detail, the pre-installation testing and placement of the main detector component, the photomultiplier tubes.

Chapter 8

Physics Measurements at MiniBooNE

Whisper in my ear my tiny neutrino friend. Tell me your secrets. The recent discoveries in the neutrino sector in the Standard Model have opened a new frontier in high energy physics. Understanding neutrinos and how they interact is crucial to continuing to verify the Standard Model and look for beyond Standard Model physics. Searches for neutrino mass and electromagnetic properties of neutrinos, such as a non-zero neutrino magnetic moment, can help identify the beyond the Standard Model physics in the neutrino sector and in other sectors, as well as addressing a number of important astrophysical issues.

8.1 Neutrino Oscillation Signal

MiniBooNE is designed to confirm or rule out the LSND signal within 1-2 years of running. To achieve this, high statistics, a good signal-to-background ratio, and a good measurement of the backgrounds are required. MiniBooNE will begin running with the horn polarity set to produce a neutrino beam and, once statistics sufficient

to do a electron neutrino appearance search are achieved, the horn polarity will be reversed in order to produce an anti-neutrino beam. Within $1-2$ years of running, MiniBooNE expects to see $500,000$ muon neutrino charged current events. If the LSND signal is due to oscillations from muon neutrinos to electron neutrinos, MiniBooNE will see approximately $1,000$ electron neutrino events from oscillations as shown in figure 8.1. Background events for the oscillation signal include intrinsic electron neutrino events coming from muon decays, and K_L and K^+ decays. Electron neutrinos coming from muon decay will be constrained by varying the length of the decay channel as described in section 7.1.1. Electron neutrinos from K decays will be constrained using Monte Carlo and the LMC. Muon mis-identification(ID) will be studied using "Michel" electrons, electrons produced from cosmic ray muon decays,. Finally, π_0 mis-ID background will be constrained by looking at the cross section for those events that produce two rings, and extrapolating to energies where only one ring is reconstructed to remove these events.

MiniBooNE will be sensitive to the possible LSND oscillation because it is a high statistics experiment designed to confirm or rule out the LSND signal to $> 5\ \sigma$. It is a decisive test of LSND because it uses higher energy neutrinos resulting in different backgrounds, and a different detector with a different event signature. Sensitivity to the LSND allowed region at 90% confidence level is shown in figure 6.2.

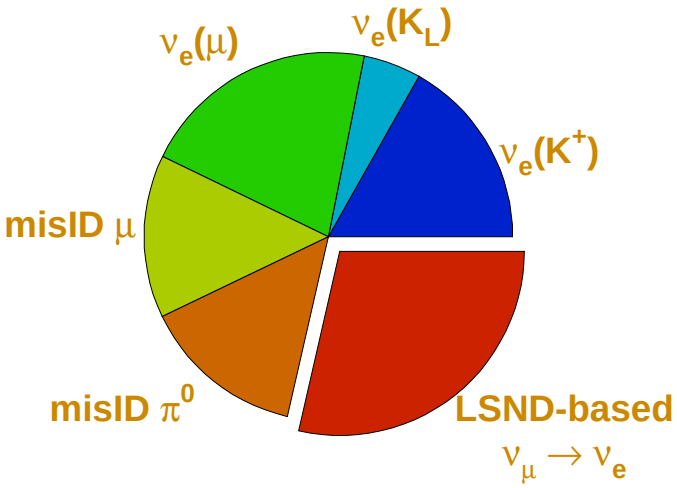

LSND-based $\nu_\mu \to \nu_e$: 1,000

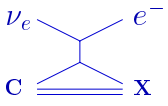

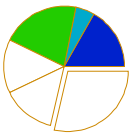

Intrinsic ν_e background: 1,500

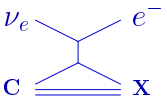

μ mis-ID background: 500

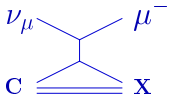

π^0 mis-ID background: 500

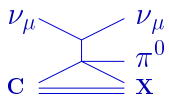

Figure 8.1: Expected number of signal and background events for 1–2 years running at MiniBooNE before energy and timing cuts to isolate the signal [97].

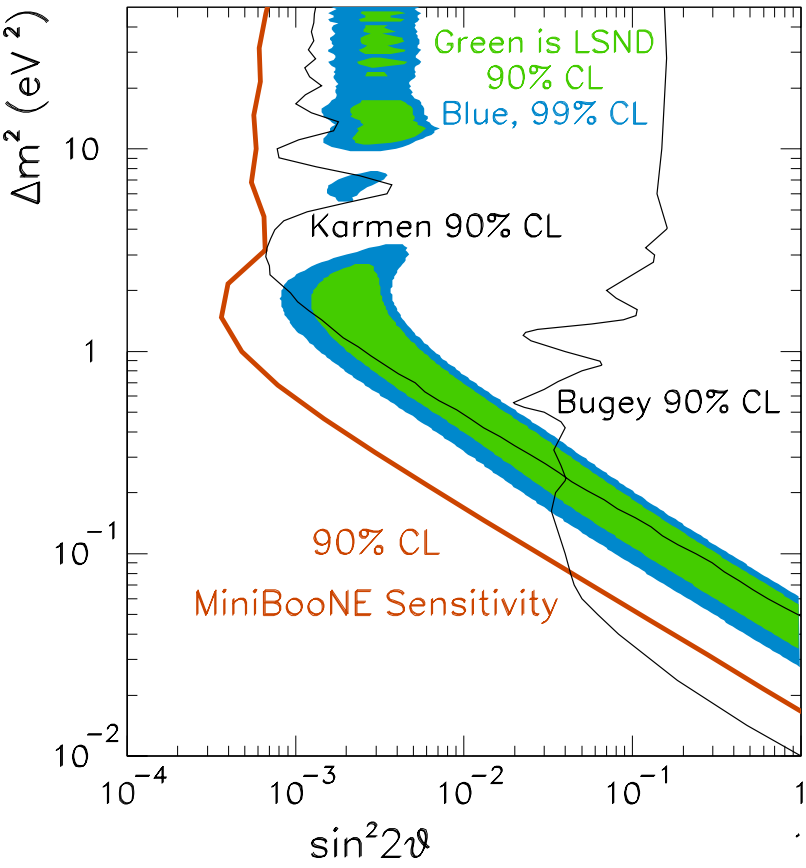

Figure 8.2: MiniBooNE sensitivity to the LSND allowed region.

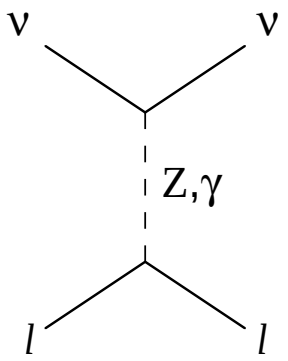

Figure 8.3: Neutrino-lepton elastic scattering shown with weak and electromagnetic contributions.

8.2 Neutrino Magnetic Moment Search

A non-zero neutrino magnetic moment would be an indication of electromagnetic interactions of neutrinos – beyond Standard Model physics. MiniBooNE should be able to extend the search for the muon neutrino magnetic moment and future experiments using MiniBooNE-like beams could extend the search even farther [98].

8.2.1 Muon Neutrino Magnetic Moment Measurement At MiniBooNE

The conventional method to look for a non-zero neutrino magnetic moment is to observe an excess in the neutrino-electron elastic scattering cross section indicating a possible electromagnetic component in addition to the weak component. The extra component is due to γ exchange in addition to the typical Z_0 exchange in muon neutrino-electron scatters as shown in figure 8.3.

Signal and Background

To estimate the MiniBooNE sensitivity to a muon neutrino magnetic moment measurement, I first estimate the expected number of muon neutrino-electron elastic scat-

ters at MiniBooNE and identify sources and sizes of background.

The number of muon neutrino-electron events expected in one year at MiniBooNE, assuming a 1 GeV neutrino beam, can be determined from the muon neutrino-electron cross section, the flux, F, and the number of electrons, or scattering centers, in the target as given by:

$$N(\text{Number of events}) = n_{\text{electrons}} F \sigma^{\nu-e}. \tag{8.1}$$

MiniBooNE expected flux is 3×10^{11} muon neutrinos per cm^2 per year. The fiducial volume of detector contains approximately 1.9×10^{31} CH_2 molecular segments. There are 8 electrons per CH_2 segment, thus $n_{\text{electron}} = 2.6 \times 10^{32}$. The Standard Model neutrino-electron cross section for 1 GeV is 1.8×10^{-42} cm^2. This gives $N_{\text{events}} = 90$ in one year of running distributed from 10 MeV to 1000 MeV. The signature for a muon neutrino-electron elastic scattering is a forward recoil electron. At the lowest electron recoil energy measurable at MiniBooNE, 10 MeV, the angular resolution of an event is ~ 20 degrees. All electrons from muon neutrino-electron scatters will be in this forward cone.

The expected backgrounds are:

- Electrons from charged current and neutral current electron neutrino-electron scattering: This has the same signature as muon neutrino-electron elastic scattering, a forward event with an outgoing electron. We can estimate the number of these background events using the relative flux of electron neutrinos to muon neutrinos and the relative cross sections. Figure 8.4 shows that the relative flux between is approximately 2×10^{-3} at $E_\nu = 1$ GeV. The beam spectrum is peaked in this region at $E_\nu = 1$ GeV and falls of at higher energies as shown in figure 7.5. The cross section for electron neutrino-electron elastic scattering is approximately 6 times greater than the muon neutrino-electron cross section because of the suppression in the charged current interaction. Scaling the num-

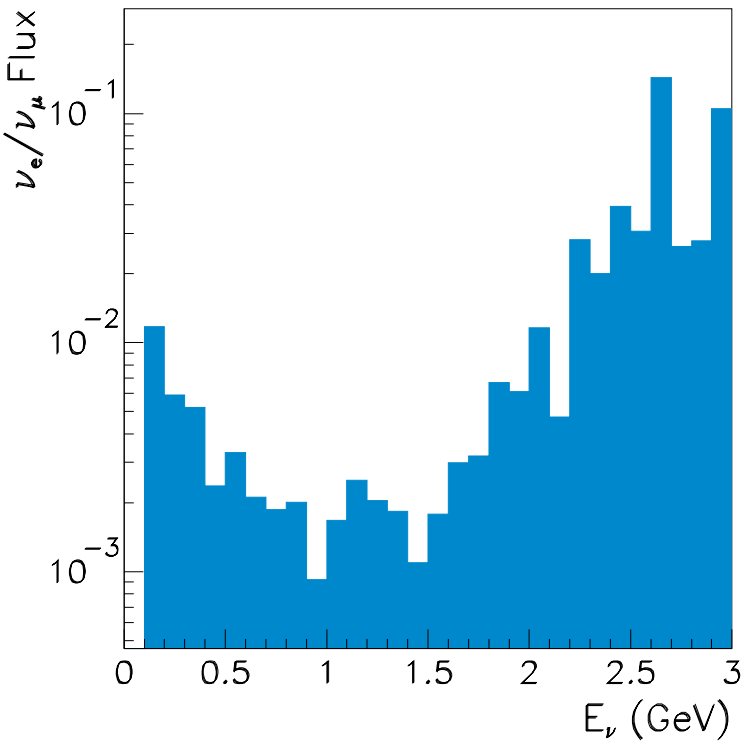

Figure 8.4: Ratio of electron neutrino to muon neutrino fluxes.

ber of expected muon neutrino-electron interactions by $\frac{6}{2\times10^{-3}}$ gives ~ 1 events background from this source.

- Intrinsic electron neutrinos from oscillations: Again the flux of electron neutrinos due to oscillations, if oscillations occur, is on the order of 10^{-3}, yielding a contribution of ~ 1 events or less depending on the oscillation signal.

- Cosmic ray muons passing undetected through the veto, stopping in the detector and being mis-IDed as electrons: Cosmic rays that pass through the detector cannot be mis-IDed because of the large amount of energy they deposit in the detector. The rate of stopped cosmic ray muons in the detector is 1.5 kHz. Given 1×10^{-6} s per beam bucket, there are 1.5×10^{-3} muons per spill. With 10^8 spills per year, the ratio of stopping muons to electrons from muon neutrino-electron scatters is 1500:1. Folding in the veto efficiency (99%), the percentage

of cosmic ray muons mis-ID as electrons (0.1%) and the percentage of cosmic ray muons in the forward cone (0.44%), the background from this source is 6×10^{-5} mis-IDed cosmic rays per electron from the signal. This background estimate is tiny but still an overestimate due to the assumption that the percentage of cosmic rays that can enter the forward cone is calculated assuming a $\cos\theta^2$ distribution with the detector uniformly covered with a 3 m overburden. Since the top of the detector is at ground level, cosmic rays entering from the side will have to pass through a lot more earth as compared to those from above, greatly reducing the number that can get into the forward cone and further reducing this background. Future Monte Carlo studies will be necessary to pinpoint the background level. For our purposes it is sufficient to see that it is negligible.

- Michel electrons: The rate of Michel electrons follows from the rate of stopping cosmic ray muons. Stopping cosmic ray muons decay into Michel electrons 8% of the time. These Michels must be in time with the beam and must be produced from a stopping muon that passed through the veto undetected to be a source of background. The rate of these Michel electrons per electron from muon neutrino-electron scattering is 1.2:1. To be mistaken for the signal, they must also be in the forward cone (3%) and can not be vetoed by looking back along the timeline to see they came from a muon decay (1%). This leaves 0.00036 mis-IDed Michel electron per signal event, a negligible background.

- Electrons produced from ^{12}B beta decay: μ^-'s from stopping cosmic rays can capture to produce ^{12}C. These can then decay to ^{12}B which can beta decay to producing an electron. Only 8% of the 7.5 kHz of stopping μ^-'s capture to produce ^{12}C. Of these ^{12}C's, only 18% decay to ^{12}B. Given this, the ratio of ^{12}B electrons per signal electron is 11:1. These background events are further reduced by folding in the fraction of time they are in time with the beam and the requirement that they be in the forward cone. In addition to this, the ^{12}B

spectrum peaks at 10 MeV and cuts off at 13 MeV so that given MiniBooNE's low energy threshold of 10 MeV, we will only see half of the ^{12}B's produced. Thus, the ratio of mis-IDed electrons from ^{12}B to signal is 0.165:1. This is the largest and most worrisome background particularly because it is in the low T_e signal region however it is a measurable background giving us the ability to use the data to subtract the background. Further Monte Carlo studies are needed to more fully understand this background.

Estimating Neutrino Magnetic Moment Sensitivity Using Total Cross Section

A non-zero magnetic moment, denoted μ, gives rise to an electromagnetic term in the overall neutrino-electron cross section. This contribution to the cross section is of the form:

$$\sigma_{EM} = \frac{\mu^2 \pi G_F^2}{m_e} \left[\frac{T_e}{E_\nu} - ln\left(\frac{T_e}{E_\nu}\right) - 1 \right] \tag{8.2}$$

where m_e is the mass of the electron, G_F is Fermi's coupling constant, T_e is the energy of the recoil electron, and E_ν is the neutrino energy. μ, the neutrino magnetic moment, is measured in units of Bohr magnetons. The precision of the cross section measurement tells us the sensitivity of the neutrino magnetic moment search. Considering only statistical errors on the number of events and flux, cross section precision can be calculated as,

$$\left(\frac{\Delta\sigma}{\sigma}\right)^2 = \left(\frac{\Delta N}{N}\right)^2 + \left(\frac{\Delta F}{F}\right)^2 \tag{8.3}$$

where N equals the number of detected muon neutrino-electron elastic events and F equals the muon neutrino flux. The error on the cross section is the largest the EM contribution could be. Given 100 muon neutrino-electron events in 1 year of running at MiniBooNE with a measured electron recoil energy spectrum of 10-1000 MeV, the sensitivity to neutrino magnetic moment determined by looking for an excess in the total cross section as described would be 6.6×10^{-10} μ_B. The largest error contributing

to this measurement is the flux, determined using the muon neutrino-Carbon event sample at best to 10%. Without the error on the flux, the sensitivity to μ_ν improves to 4.7×10^{-10} $\mu_{\rm B}$. To avoid this 10% flux error, we can take advantage of the relative shapes of the weak and electromagnetic differential cross section in order to perform this measurement.

Estimating Neutrino Magnetic Moment Sensitivity Using Shape of Differential Cross Section

The electromagnetic contribution to muon neutrino-electron scattering due to a non-zero neutrino magnetic moment rises at low electron recoil energy, T_e, with respect to the weak cross section. The error on the flux considered in the last section can be avoided altogether by taking advantage of the shape difference between the different contributions to this differential cross section. By looking for any shape distortion in the measured differential cross section, we can estimate the size of any electromagnetic contribution. The weak contribution to this differential cross section is given by:

$$\frac{d\sigma^{weak}}{dT_e} = \frac{2m_e G_F^2}{\pi}\left[g_L^2 + g_R^2\left(1 - \frac{T_e}{E_\nu}\right)^2 - g_R g_L \frac{m_e}{E_\nu}\frac{T_e}{E_\nu}\right] \tag{8.4}$$

and the electromagnetic contribution is given by:

$$\frac{d\sigma^{EM}}{dT_e} = \frac{\pi\alpha^2\mu_\nu^2}{m_e^2}\left(\frac{1}{T_e} - \frac{1}{E_\nu}\right) \tag{8.5}$$

where, again, T_e=electron recoil energy, E_ν= neutrino energy and μ is the neutrino magnetic moment. Figure 8.5 shows theoretical curves corresponding to the weak contribution only, and weak plus electromagnetic for several different values of μ. Notice the largest differences in the contributions arise at low T_e making the measurement more powerful at lower values of T_e.

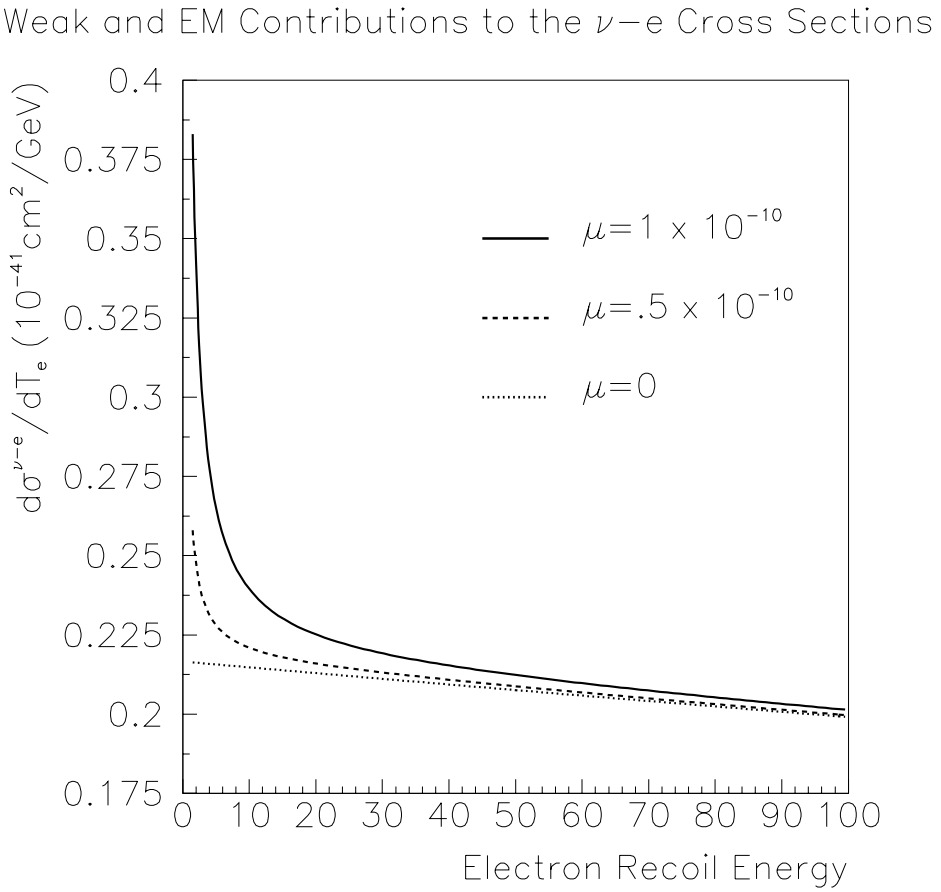

Figure 8.5: Weak and electromagnetic contributions to the differential cross section shown at low T_e to magnify differences between the contributions. Zero is suppressed along the y axis.

In order to estimate the sensitivity of MiniBooNE to a neutrino magnetic moment measurement via this method, 1000 fake data experiments are conducted. Data are thrown against a neutrino-electron cross section with a weak component only. The fake data are then fit to the weak plus electromagnetic distribution with μ^2 and the overall normalization, N allowed to vary. The distribution of reconstructed μ^2's for these 1000 experiments should be centered on zero and have a width corresponding to the sensitivity of each experiment to μ^2.

The number of events to throw is determined from the signal-background outlined

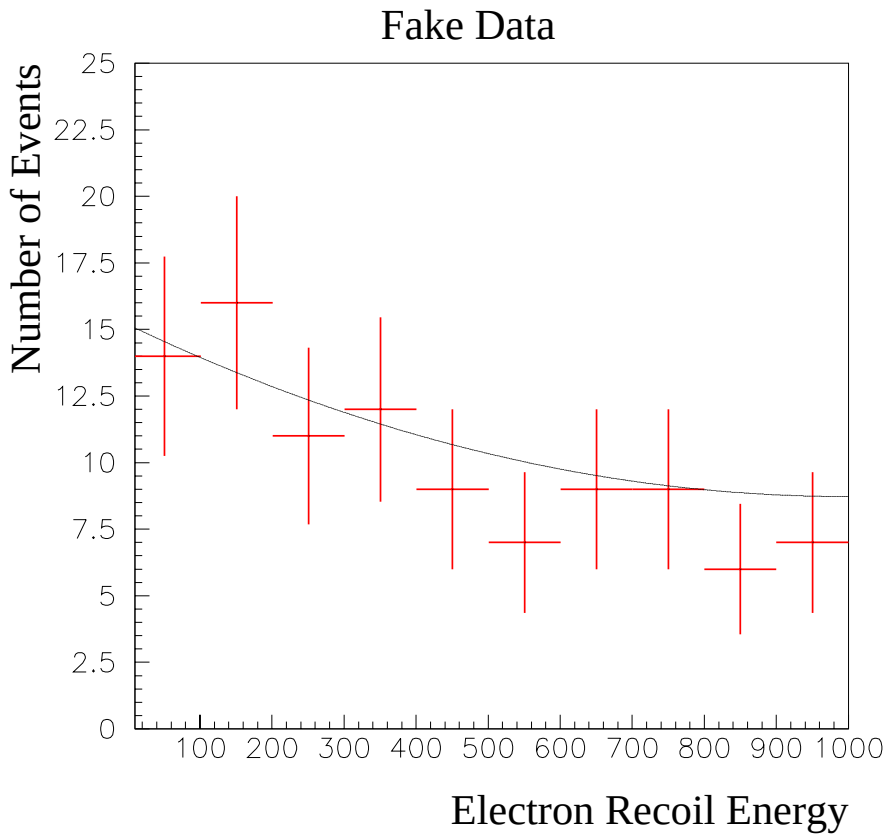

Figure 8.6: Example of 100 fake data events thrown against the weak cross section.

about for approximately 1 year of running. For simplicity, this number is rounded to 100 events and these are thrown against the weak cross section distribution. MiniBooNE will be able to reconstruct electron recoil energies as low as 10 MeV and up to the largest possible energies, $T_e = E_\nu$ where $E_\nu = 1$ GeV. Figure 8.6 shows the fake data as a function of T_e where 10 MeV $< T_e <$ 1000 MeV. The weak cross section, normalized to the data is overlaid on the data in order to see that the shape of the events thrown follows the cross section.

Figure 8.7 shows the distribution of μ^2's from these 1000 fake data experiments with a Gaussian fit overlaid. The mean and σ of the Gaussian are listed on the plot. The square root of the sigma gives the sensitivity MiniBooNE will have to a non-zero

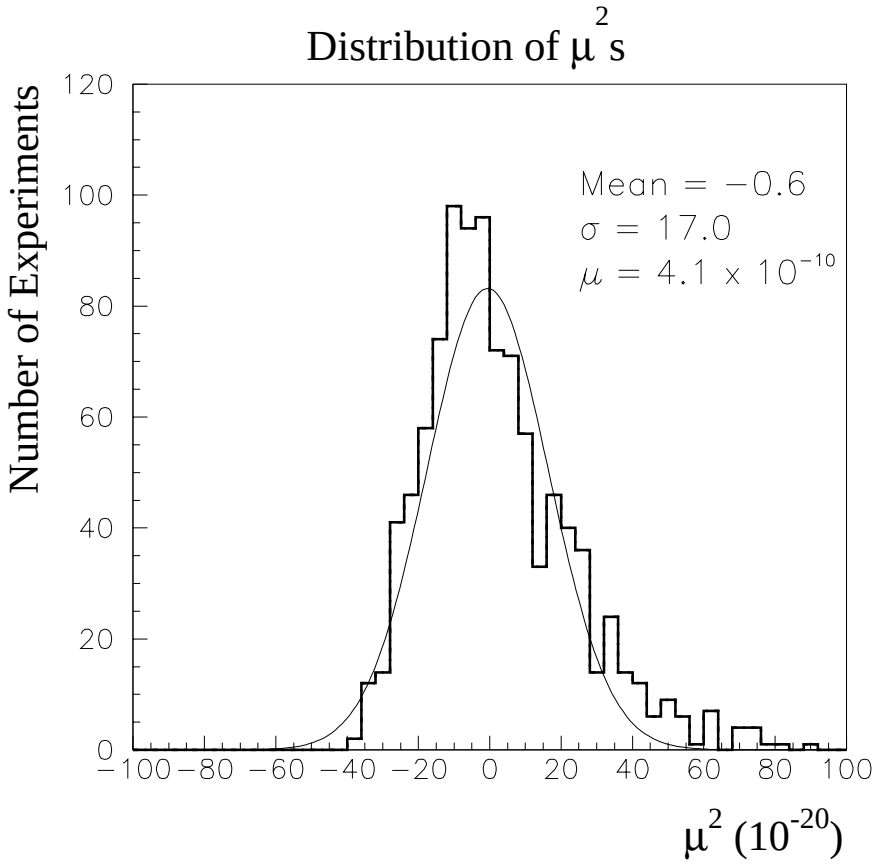

Figure 8.7: Distribution of μ's for 1000 experiments with 100 data events per experiment

muon neutrino magnetic moment, $\mu_\nu = 4.1 \times 10^{-10}\mu_{\rm B}$. This is an improvement over the limit set by LSND which was 6.8×10^{-10}.

The error on the resolution of the electron recoil energy will not affect this measurement since the data bin-widths are 100 MeV wide, much larger than the resolution. This study assumes a fixed neutrino energy of $E_\nu = 1$ GeV. The actual energy spread in the beam indicated by figure 7.5 will not significantly effect these measurements as can be seen in equations. 8.4 and 8.5. The last term in this equation is small with respect to the others because of the factor m_e, the T_e^2/E_ν^2 term has an effect only at high T_e where the EM contribution is small. The other terms which are

constant or factors of T_e/E_ν control the shape of the distribution. Thus, there is not a significant effect on the shape for a reasonably narrow neutrino spectrum.

8.2.2 Muon Neutrino Magnetic Moment Measurement At an Upgrade to MiniBooNE

The sensitivity to neutrino magnetic moment greatly improves as the reconstructed electron recoil energy decreases and moderately improves as the number of events increases. An upgrade to the MiniBooNE experiment to decrease the electron recoil energy measurement threshold and added running time to increase the number of events seen can improve upon this limit. Fig. 8.8 shows the distribution of μ's for an experiment designed to see 300 events distributed from $1 - 1000$ MeV. The improved sensitivity for such an experiment is $\mu = 2.8 \times 10^{-10}$, a factor of 1.5 improvement over MiniBooNE as presently designed.

A new near detector designed to lower the electron recoil energy threshold and to receive a significantly higher beam flux would greatly improve the sensitivity to a non-zero neutrino magnetic moment, perhaps as much as an order of magnitude better than the present limit. Beam flux can be increased first by positioning a near detector closer to the neutrino source than MiniBooNE is positioned. The neutrino beam intensity falls off like inverse distance squared ($1/r^2$). Therefore, the flux would increase by a factor of 25 by placing a detector 5 times closer, at 100 m. In this case, for a detector with a minimum electron recoil sensitivity of 1 MeV that sees 2500 events in one year of running, the fit to the shape of the differential cross section for 1000 fake data experiments produces a distribution of μ^2's as shown in figure 8.9. The reach in sensitivity here is to $\mu = 9.2 \times 10^{-11}$, a factor of 5 improvement over MiniBooNE as presently designed.

The flux can also be increased by an improved proton source sometimes called a super-beam. Proposals for intense proton sources which could be used to create

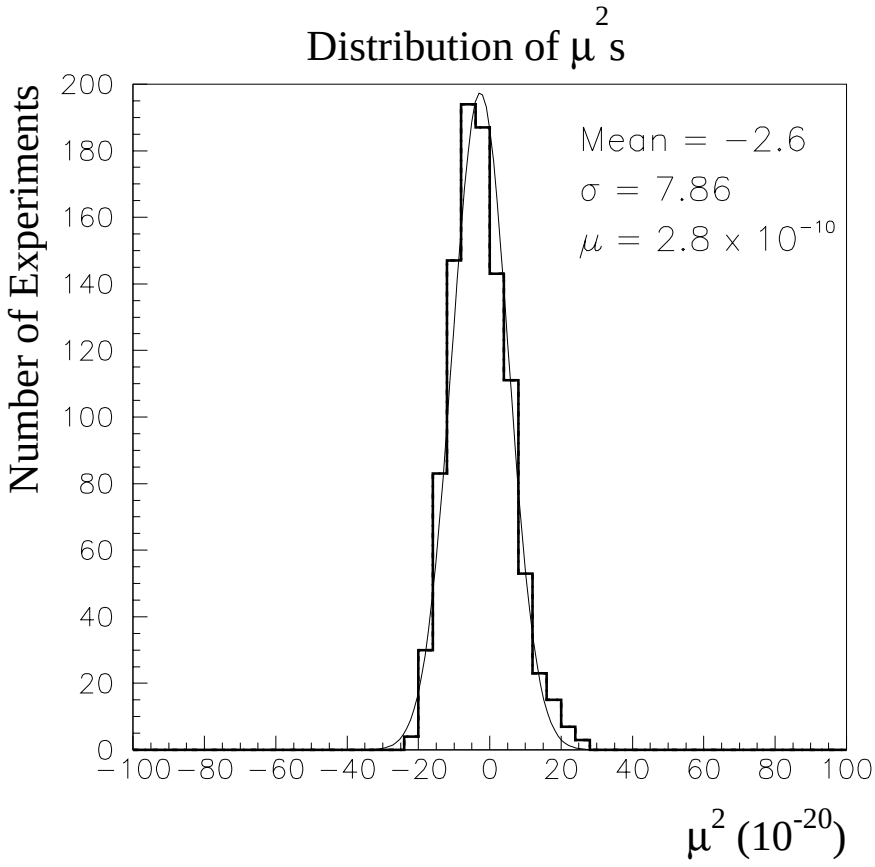

Figure 8.8: Distribution of μ's for 1000 experiments with 300 data events per experiment and an electron recoil energy threshold of 1 MeV.

intense neutrino beams are being considered at a number of HEP laboratories around the world. The proposal for such a facility at Fermilab, called the Fermilab Proton Driver [99] provides beam intensities which could further increase neutrino flux by as much as a factor of 6. To estimate the reach of a neutrino magnetic moment measurement at a super-beam facility, we assume, as before, a near detector located 100 m from the neutrino source which sees 15,000 events per year. Determining the sensitivity by again fitting to the shape of the differential cross section with a minimum electron recoil sensitivity of 1 MeV produces a distribution of μ's as shown in figure 8.10. The reach in sensitivity in this case is to $\mu = 5.2 \times 10^{-11}$. This is at

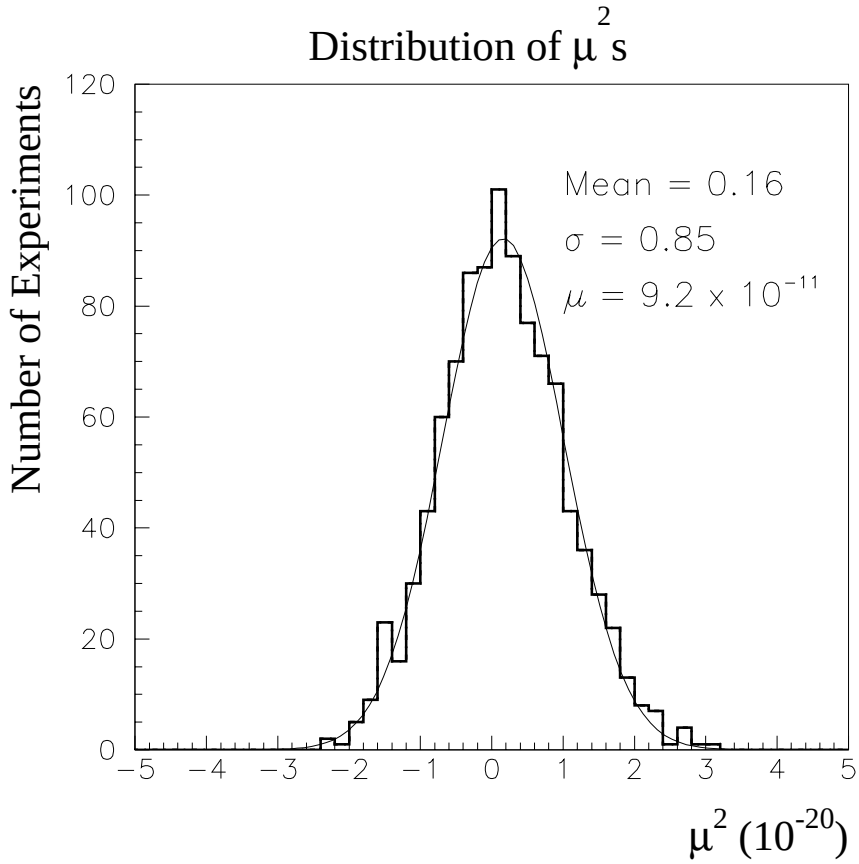

Figure 8.9: Distribution of μ^2's for 1000 experiments with 2500 data events per experiment and an electron recoil energy threshold of 1 MeV.

the level predicted by some beyond the Standard Model theories [77].

Neutrino magnetic moment measurements at a $20 - 50$ GeV neutrino factory [100] via conventional methods are difficult because of the higher neutrino energy. While the weak cross section rises logarithmically with E_ν, the electromagnetic cross section rises linearly making it advantageous to perform measurements at lower energies. Non-conventional methods for measuring neutrino magnetic moments at higher energies have been explored [100] but none of these techniques have yet been demonstrated.

MiniBooNE will be able to improve upon the muon neutrino magnetic moment

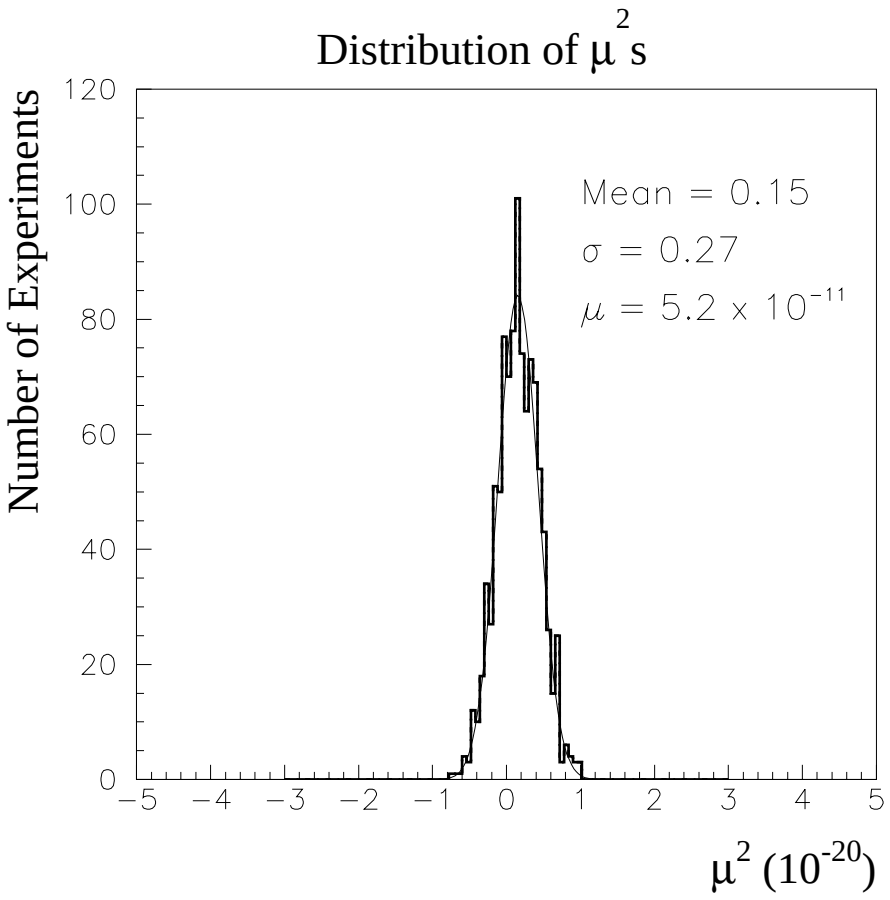

Figure 8.10: Distribution of μ's for 1000 experiments with 15,000 data events per experiment and an electron recoil energy threshold of 1 MeV.

sensitivity as described here. In addition to this there is clear promise that an upgrade to MiniBooNE or a future experiment using a high intensity neutrino source can further improve upon this, pushing these studies into the region where some beyond the Standard Model theories and astrophysical limits predict a sizable magnetic moment. Whether we see something or not, these measurements help fill in one more piece of the neutrino puzzle.

Bibliography

[1] W. Pauli, in a letter to a meeting of physicists in Tubingen, dated 4 December 1930. The letter is reprinted in L. Brown, *Phys. Today* **32**, 1978.

[2] D. E. Groom *et al.* [Particle Data Group Collaboration], "Review of particle physics," Eur. Phys. J. C **15**, 1 (2000).

[3] C. Arroyo *et al.* [CCFR Collaboration], "A precise measurement of the weak mixing angle in neutrino nucleon scattering," Phys. Rev. Lett. **72**, 3452 (1994) [hep-ex/9405008].

[4] G. P. Zeller *et al.* [NuTeV Collaboration], "A precise determination of electroweak parameters in neutrino-nucleon scattering," to be submitted to Phys. Rev. Lett.

[5] O. W. Greenberg, "Quarks: Resource letter Q-1," Am. J. Phys. **50**, 1074 (1982).

[6] D. B. Lichtenberg and S. P. Rosen, "Developments in the Quark Theory of Hadrons. Vol. 1. 1964–1978," *Nonantum, USA: Hadronic Pr. (1980) 508 p.*

[7] W. G. Seligman, "A next-to-leading order QCD analysis of neutrino-iron structure functions at the Tevatron," Ph. D. thesis, Columbia University, New York, 1997, NEVIS-292, UMI-97-23849.

[8] W. G. Seligman *et al.* [CCFR Collaboration], "Improved determination of α_s from neutrino nucleon scattering," Phys. Rev. Lett. **79**, 1213 (1997).

[9] M. Arneodo *et al.* [New Muon Collaboration], "Measurement of the proton and deuteron structure functions, F_2^p and F_2^d, and of the ratio σ_L/σ_T," Nucl. Phys. B **483**, 3 (1997) [hep-ph/9610231].

[10] M. R. Adams *et al.* [E665 Collaboration], "Proton and deuteron structure functions in muon scattering at 470 GeV," Phys. Rev. D **54**, 3006 (1996).

[11] S. L. Adler, "Tests of the conserved vector current and partially conserved axial-vector current hypotheses in high-energy neutrino reactions," Phys. Rev. **135**, B963 (1964).

[12] W. K. Sakumoto *et al.* [CCFR Collaboration], "Calibration of the CCFR target calorimeter," Nucl. Instrum. Meth. A **294**, 179 (1990).

[13] B. J. King *et al.* [CCFR Collaboration], "Measuring muon momenta with the CCFR neutrino detector," Nucl. Instrum. Meth. A **302**, 254 (1991).

[14] `http://www-e815.fnal.gov/~bfleming/`

[15] Application Software and Databases, Information Technology Division, CERN, "GEANT — Detector Description and Simulation Tool," `http://wwwinfo.cern.ch/asd/geant/index.html`.

[16] A. Romosan, "High statistics search for $\nu_\mu(\overline{\nu}_\mu) \to \nu_e(\overline{\nu}_e)$ oscillations in the small mixing angle regime," Ph. D. thesis, Columbia University, New York, 1996, NEVIS-296, UMI-97-28290.

[17] J. H. Kim, "A measurement of α_s from the Gross–Llewellyn-Smith sum rule," Ph. D. thesis, Columbia University, New York, 1999, UMI-99-16890.

[18] Application Software and Databases, Information Technology Division, CERN, "CERN Program Library," `http://wwwinfo.cern.ch/asd/index.html`.

[19] A. J. Buras and K. J. F. Gaemers, "Simple parametrizations of parton distributions with Q^2 dependence given by asymptotic freedom," Nucl. Phys. B **132**, 249 (1978).

[20] M. Glück, E. Reya and A. Vogt, "Dynamical parton distributions of the proton and small x physics," Z. Phys. C **67**, 433 (1995).

[21] A. O. Bazarko, "Determination of the strange quark distribution from a next-to-leading order QCD analysis of neutrino and anti-neutrino production of charm," Ph. D. thesis, Columbia University, New York, 1994, NEVIS-285.

[22] U. K. Yang *et al.* [CCFR/NuTeV Collaboration], "Measurements of F_2 and $xF_3^{\nu} - xF_3^{\overline{\nu}}$ from CCFR ν_μ-Fe and $\overline{\nu}_\mu$-Fe data in a physics model independent way," Phys. Rev. Lett. **86**, 2742 (2001) [hep-ex/0009041].

[23] D. Y. Bardin and V. A. Dokuchaeva, "On the radiative corrections to the neutrino deep inelastic scattering," JINR-E2-86-260.

[24] U. K. Yang, "A Measurement of Differential Cross Sections in Charged-Current Neutrino Interactions on Iron and a Global Structure Functions Analysis," Ph. D. thesis, University of Rochester, New York, 2000.

[25] R. Blair *et al.* [E616 Collaboration], "Measurement of the rate of increase of neutrino cross-sections with energy," Phys. Rev. Lett. **51**, 343 (1983).

[26] R. Belusevic and D. Rein, "Neutrino reactions in the low-y region," Phys. Rev. D **38**, 2753 (1988).

[27] P. S. Auchincloss *et al.* [E701 Collaboration], "Measurement of the inclusive charged current cross-section for neutrino and anti-neutrino scattering on isoscalar nucleons," Z. Phys. C **48**, 411 (1990).

[28] J. P. Berge *et al.* [WA1 Collaboration], "A measurement of differential cross-sections and nucleon structure functions in charged current neutrino interactions on iron," Z. Phys. C **49**, 187 (1991).

[29] L. W. Whitlow, S. Rock, A. Bodek, E. M. Riordan and S. Dasu, "A precise extraction of $R = \sigma_L/\sigma_T$ from a global analysis of the SLAC deep inelastic e-p and e-d scattering cross-sections," Phys. Lett. B **250**, 193 (1990).

[30] U. K. Yang *et al.* [CCFR/NuTeV Collaboration], "Extraction of $R = \sigma_L/\sigma_T$ from CCFR ν_μ-Fe and $\overline{\nu}_\mu$-Fe differential cross sections," hep-ex/0104040.

[31] A. D. Martin, R. G. Roberts, W. J. Stirling and R. S. Thorne, "Estimating the effect of NNLO contributions on global parton analyses," Eur. Phys. J. C **18**, 117 (2000) [hep-ph/0007099].

[32] R. S. Thorne, private communication regarding small x resummed calculation which solves problems with NNLO fit in [31] at low x and low Q^2 to be submitted for publication shortly.

[33] B. T. Fleming *et al.* [CCFR Collaboration], "A first measurement of low x low Q**2 structure functions in neutrino scattering," Phys. Rev. Lett. **86**, 5430 (2001) [arXiv:hep-ex/0011094].

[34] S. A. Rabinowitz *et al.* [CCFR Collaboration], "Measurement of the strange sea distribution using neutrino charm production," Phys. Rev. Lett. **70**, 134 (1993).

[35] C. Boros, F. M. Steffens, J. T. Londergan and A. W. Thomas, "A new analysis of charge symmetry violation in parton distributions," Phys. Lett. B **468**, 161 (1999) [hep-ph/9908280].

[36] A. Bodek, Q. Fan, M. Lancaster, K. S. McFarland and U. K. Yang, "Implication of W boson charge asymmetry measurements in $p\overline{p}$ collisions to models for charge

symmetry violations in parton distributions," Phys. Rev. Lett. **83**, 2892 (1999) [hep-ex/9904022].

[37] R. S. Thorne and R. G. Roberts, "A practical procedure for evolving heavy flavour structure functions," Phys. Lett. B **421**, 303 (1998) [hep-ph/9711223].

[38] A. D. Martin, R. G. Roberts, W. J. Stirling and R. S. Thorne, "Parton distributions: A new global analysis," Eur. Phys. J. C **4**, 463 (1998) [hep-ph/9803445].

[39] M. A. Aivazis, F. I. Olness and W. Tung, "QCD formulation of charm production in deep inelastic scattering and the sea quark – gluon dichotomy," Phys. Rev. Lett. **65**, 2339 (1990).

[40] M. A. Aivazis, J. C. Collins, F. I. Olness and W. Tung, "Leptoproduction of heavy quarks. 2. A Unified QCD formulation of charged and neutral current processes from fixed target to collider energies," Phys. Rev. D **50**, 3102 (1994) [hep-ph/9312319].

[41] E. Laenen, S. Riemersma, J. Smith and W. L. van Neerven, "Complete $O(\alpha_s)$ corrections to heavy flavor structure functions in electroproduction," Nucl. Phys. B **392**, 162 (1993).

[42] L. W. Whitlow, E. M. Riordan, S. Dasu, S. Rock and A. Bodek, "Precise measurements of the proton and deuteron structure functions from a global analysis of the SLAC deep inelastic electron scattering cross-sections," Phys. Lett. B **282**, 475 (1992).

[43] A. Donnachie and P. V. Landshoff, "Charmed quarks: Structure function and nonperturbative interactions," Phys. Lett. B **207**, 319 (1988).

[44] A. Donnachie and P. V. Landshoff, "Proton structure function at small Q^2," Z. Phys. C **61**, 139 (1994) [hep-ph/9305319].

[45] C. S. Wu, E. Ambler, R. W. Hayward, D. D. Hoppes and R. P. Hudson, "Experimental test of parity conservation in beta decay," Phys. Rev. **105**, 1413 (1957).

[46] E. Majorana, "Theory of the symmetry of electrons and positrons," Nuovo Cim. **14**, 171 (1937).

[47] B. Kayser, F. Gibrat-Debu and F. Perrier, "The Physics of Massive Neutrinos," *Singapore, Singapore: World Scientific (1989) 117 p. (World Scientific Lecture Notes in Physics, 25).*

[48] E. Ma, G. Rajasekaran and U. Sarkar, "Light sterile neutrinos from large extra dimensions," Phys. Lett. B **495**, 363 (2000) [hep-ph/0006340].

[49] J. M. Conrad, "Recent results on neutrino oscillations," hep-ex/9811009.

[50] R. J. Davis, D. S. Harmer and K. C. Hoffman, "Search For Neutrinos From The Sun," Phys. Rev. Lett. **20**, 1205 (1968).

[51] W. Hampel *et al.* [GALLEX Collaboration], "GALLEX solar neutrino observations: Results for GALLEX IV," Phys. Lett. B **447**, 127 (1999).

[52] J. N. Abdurashitov *et al.* [SAGE Collaboration], "Measurement of the solar neutrino capture rate with gallium metal," Phys. Rev. C **60**, 055801 (1999) [astro-ph/9907113].

[53] S. Fukuda *et al.* [Super-Kamiokande Collaboration], "Constraints on neutrino oscillations using 1258 days of Super-Kamiokande solar neutrino data," Phys. Rev. Lett. **86**, 5656 (2001) [hep-ex/0103033].

[54] J. N. Bahcall, M. H. Pinsonneault and S. Basu, "Solar models: Current epoch and time dependences, neutrinos, and helioseismological properties," Astrophys. J. **555**, 990 (2001) [astro-ph/0010346].

[55] B. Pontecorvo, "Mesonium and antimesonium," Sov. Phys. JETP **6**, 429 (1957) [Zh. Eksp. Teor. Fiz. **33**, 549 (1957)].

[56] B. Pontecorvo, Sov. Phys. JETP **7**, 172 (1958)

[57] Z. Maki, M. Nakagawa and S. Sakata, "Remarks on the unified model of elementary particles," Prog. Theor. Phys. **28**, 870 (1962).

[58] B. Pontecorvo, "Neutrino experiments and the question of leptonic-charge conservation," Sov. Phys. JETP **26**, 984 (1968) [Zh. Eksp. Teor. Fiz. **53**, 1717 (1968)].

[59] S. M. Bilenkii and B. Pontecorvo, "Lepton mixing and neutrino oscillations," Phys. Rept. **41**, 225 (1978).

[60] J. N. Bahcall, "Neutrino Astrophysics," *Cambridge, UK: Univ. Pr. (1989) 567p.*

[61] L. Wolfenstein, "Neutrino oscillations in matter," Phys. Rev. D **17**, 2369 (1978).

[62] S. P. Mikheev and A. Y. Smirnov, "Resonance enhancement of oscillations in matter and solar neutrino spectroscopy," Sov. J. Nucl. Phys. **42**, 913 (1985) [Yad. Fiz. **42**, 1441 (1985)].

[63] S. P. Mikheev and A. Y. Smirnov, "Resonant amplification of neutrino oscillations in matter and solar neutrino spectroscopy," Nuovo Cim. C **9**, 17 (1986).

[64] J. N. Bahcall, M. C. Gonzalez-Garcia and C. Pena-Garay, "Global analysis of solar neutrino oscillations including SNO CC measurement," JHEP **0108**, 014 (2001) [hep-ph/0106258].

[65] Y. Fukuda *et al.* [Super-Kamiokande Collaboration], "Evidence for oscillation of atmospheric neutrinos," Phys. Rev. Lett. **81**, 1562 (1998) [hep-ex/9807003].

[66] W. W. Allison *et al.* [Soudan-2 Collaboration], Phys. Lett. B **449**, 137 (1999) [hep-ex/9901024].

[67] A. Aguilar *et al.* [LSND Collaboration], "Evidence for neutrino oscillations from the observation of $\overline{\nu}_e$ appearance in a $\overline{\nu}_\mu$ beam," [hep-ex/0104049].

[68] V. Barger, B. Kayser, J. Learned, T. Weiler and K. Whisnant, "Fate of the sterile neutrino," Phys. Lett. B **489**, 345 (2000) [hep-ph/0008019].

[69] C. Giunti and M. Laveder, "Large $\nu_\mu \to \nu_\tau$ and $\nu_e \to \nu_\tau$ transitions in short baseline experiments?," JHEP **0102**, 001 (2001) [hep-ph/0010009].

[70] O. L. Peres and A. Y. Smirnov, "(3+1) spectrum of neutrino masses: A chance for LSND?," Nucl. Phys. B **599**, 3 (2001) [hep-ph/0011054].

[71] N. Okada and O. Yasuda, "A sterile neutrino scenario constrained by experiments and cosmology," Int. J. Mod. Phys. A **12**, 3669 (1997) [hep-ph/9606411].

[72] S. M. Bilenkii, C. Giunti and W. Grimus, "Neutrino mass spectrum from the results of neutrino oscillation experiments," Eur. Phys. J. C **1**, 247 (1998) [hep-ph/9607372].

[73] S. M. Bilenkii, C. Giunti and W. Grimus, "Neutrino oscillation experiments and the neutrino mass spectrum," hep-ph/9609343.

[74] V. Barger, S. Pakvasa, T. J. Weiler and K. Whisnant, "Variations on four-neutrino oscillations," Phys. Rev. D **58**, 093016 (1998) [hep-ph/9806328].

[75] S. M. Bilenkii, C. Giunti, W. Grimus and T. Schwetz, "Four-neutrino mass spectra and the Super-Kamiokande atmospheric up-down asymmetry," Phys. Rev. D **60**, 073007 (1999) [hep-ph/9903454].

[76] M. Frank, "Neutrino magnetic moments in the left-right supersymmetric model," Phys. Rev. D **60**, 093005 (1999).

[77] G. C. McLaughlin and J. N. Ng, "Astrophysical implications of the induced neutrino magnetic moment from large extra dimensions," Phys. Lett. B **470**, 157 (1999) [hep-ph/9909558].

[78] M. Fukugita and S. Yazaki, "Reexamination of astrophysical and cosmological constraints on the magnetic moment of neutrinos," Phys. Rev. D **36**, 3817 (1987).

[79] J. M. Lattimer and J. Cooperstein, "Limits on the neutrino magnetic moment from supernova 1987A," Phys. Rev. Lett. **61**, 23 (1988).

[80] R. Barbieri and R. N. Mohapatra, "Limit on the magnetic moment of the neutrino from supernova 1987A observations," Phys. Rev. Lett. **61**, 27 (1988).

[81] L. B. Auerbach *et al.* [LSND Collaboration], "Measurement of electron-neutrino electron elastic scattering," Phys. Rev. D **63**, 112001 (2001) [hep-ex/0101039].

[82] J. F. Beacom and P. Vogel, "Neutrino magnetic moments, flavor mixing, and the superKamiokande solar data," Phys. Rev. Lett. **83**, 5222 (1999) [hep-ph/9907383].

[83] A. I. Derbin, A. V. Chernyi, L. A. Popeko, V. N. Muratova, G. A. Shishkina and S. I. Bakhlanov, "Experiment on anti-neutrino scattering by electrons at a reactor of the Rovno nuclear power plant," JETP Lett. **57**, 768 (1993) [Pisma Zh. Eksp. Teor. Fiz. **57**, 755 (1993)].

[84] A. V. Derbin, "Restriction on the magnetic dipole moment of reactor neutrinos," Phys. Atom. Nucl. **57**, 222 (1994) [Yad. Fiz. **57**, 236 (1994)].

[85] R. Schwienhorst *et al.* [DONUT Collaboration], "A new upper limit for the tau-neutrino magnetic moment," Phys. Lett. B **513**, 23 (2001) [hep-ex/0102026].

[86] Bartoszek Engineering, "The MiniBooNE Horn System Design," `http://www.bartoszekeng.com/mboone/mboone.htm`.

[87] I. Stancu *et al.* [BooNE Collaboration], "The MiniBooNE Detector Technical Design Report," `http://www-boone.fnal.gov/`, May, 2001.

[88] R. Imlay, *et al.*, "MiniBooNE calibration systems," `http://hep.phys.lsu.edu/boone/calibration/`, 2001.

[89] I. Stancu, "Studies of the charge likelihood for a perfect BooNE detector," BooNE Technical Note 5, 1998.

[90] I. Stancu, "Maximum likelihood event reconstruction for BooNE: Point-like particles in a perfect detector," BooNE Technical Note 6, 1998.

[91] B. P. Roe, "Initial calculations for preliminary BooNE beam experiment," BooNE Technical Note 7, 1998.

[92] I. Stancu, "The high energy electron reconstruction in BooNE," BooNE Technical Note 18, 1999.

[93] I. Stancu, "The muon reconstruction in BooNE and particle identification via artificial neural networks," BooNE Technical Note 19, 1999.

[94] I. Stancu, "The neutral pion reconstruction in BooNE and particle identification via artificial neural networks," BooNE Technical Note 21, 2000.

[95] B. P. Roe, "Combining W. Louis, I. Stancu, N. Wadia, and B. Roe variables," BooNE Technical Note 23, 2000.

[96] P. Kasper, "Cone fit studies," `http://home.fnal.gov/~kasper/boone/cone_fit.html`, 2001.

[97] M. Sorel, "MiniBooNE: A search for neutrino oscillations," New Perspectives 2001, Fermi National Accelerator Laboratory, 12–13 June 2001.

[98] J. Beacom and B. T. Fleming, in preparation.

[99] C. Ankenbrandt *et al.*, "Physics study group report on physics potential at FNAL with stronger proton sources," in preparation, `http://projects.fnal.gov/protondriver/`.

[100] C. Albright *et al.*, "Physics at a neutrino factory," hep-ex/0008064.

[101] R. Page *et al.*, "MiniBooNE PMT testing,"
`http://www-boone.fnal.gov/pmt/pmtwebpage.html`.

Appendix A

F_2 Central Values and Errors

Table A.1: F_2 **Statistical Errors**

F_2 Statistical Errors			
x	Q^2	F_2	Stat. Err
0.0015	0.4	0.5031	0.1956×10^{-1}
0.0015	0.4	0.6239	0.2417×10^{-1}
0.0015	0.6	0.7900	0.3712×10^{-1}
0.0015	0.7	0.8705	0.4505×10^{-1}
0.0015	0.9	1.010	0.7202×10^{-1}
0.0045	0.4	0.6682	0.1728×10^{-1}
0.0045	0.4	0.7835	0.2133×10^{-1}
0.0045	0.6	0.8825	0.2386×10^{-1}
0.0045	0.7	1.058	0.2960×10^{-1}
0.0045	0.9	1.269	0.3679×10^{-1}
0.0045	1.1	1.220	0.4038×10^{-1}
0.0045	1.4	1.389	0.4729×10^{-1}
0.0045	1.8	1.393	0.6578×10^{-1}
0.0045	2.3	1.681	0.1247
0.0080	0.4	0.7362	0.1805×10^{-1}
0.0080	0.4	0.8080	0.1914×10^{-1}
0.0080	0.6	0.9369	0.2061×10^{-1}
0.0080	0.7	1.000	0.2203×10^{-1}
0.0080	0.9	1.147	0.2478×10^{-1}
0.0080	1.1	1.279	0.2805×10^{-1}
0.0080	1.4	1.249	0.2973×10^{-1}
0.0080	1.8	1.238	0.3190×10^{-1}
0.0080	2.3	1.466	0.3869×10^{-1}
0.0080	3.2	1.541	0.4115×10^{-1}
0.0125	0.4	0.6831	0.1783×10^{-1}
0.0125	0.4	0.8121	0.1884×10^{-1}
0.0125	0.6	0.9350	0.1920×10^{-1}
0.0125	0.7	1.067	0.2003×10^{-1}
0.0125	0.9	1.103	0.2121×10^{-1}
0.0125	1.1	1.206	0.2249×10^{-1}
0.0125	1.4	1.282	0.2333×10^{-1}
0.0125	1.8	1.274	0.2476×10^{-1}
0.0125	2.3	1.353	0.2813×10^{-1}
0.0125	3.2	1.470	0.2444×10^{-1}
0.0125	5.1	1.656	0.4056×10^{-1}
0.0175	0.4	0.7790	0.2493×10^{-1}
0.0175	0.4	0.8046	0.2111×10^{-1}
0.0175	0.6	0.8966	0.2103×10^{-1}

F_2 Statistical Errors			
x	Q^2	F_2	Stat. Err
0.0175	0.7	0.9649	0.2074×10^{-1}
0.0175	0.9	1.135	0.2225×10^{-1}
0.0175	1.1	1.179	0.2149×10^{-1}
0.0175	1.4	1.281	0.2286×10^{-1}
0.0175	1.8	1.307	0.2348×10^{-1}
0.0175	2.3	1.403	0.2557×10^{-1}
0.0175	3.2	1.504	0.2104×10^{-1}
0.0175	5.1	1.533	0.2704×10^{-1}
0.0175	8.2	1.541	0.4907×10^{-1}
0.0250	0.6	0.9396	0.1815×10^{-1}
0.0250	0.7	1.022	0.1701×10^{-1}
0.0250	0.9	1.048	0.1602×10^{-1}
0.0250	1.1	1.152	0.1622×10^{-1}
0.0250	1.4	1.207	0.1600×10^{-1}
0.0250	1.8	1.290	0.1626×10^{-1}
0.0250	2.3	1.286	0.1623×10^{-1}
0.0250	3.2	1.418	0.1277×10^{-1}
0.0250	5.1	1.530	0.1545×10^{-1}
0.0250	8.2	1.585	0.2070×10^{-1}
0.0250	12.9	1.814	0.5016×10^{-1}
0.0350	0.7	1.054	0.2255×10^{-1}
0.0350	0.9	1.060	0.1807×10^{-1}
0.0350	1.1	1.097	0.1706×10^{-1}
0.0350	1.4	1.175	0.1673×10^{-1}
0.0350	1.8	1.255	0.1638×10^{-1}
0.0350	2.3	1.304	0.1654×10^{-1}
0.0350	3.2	1.362	0.1184×10^{-1}
0.0350	5.1	1.496	0.1346×10^{-1}
0.0350	8.2	1.557	0.1658×10^{-1}
0.0350	12.9	1.680	0.2453×10^{-1}
0.0350	20.5	1.812	0.7433×10^{-1}
0.0500	1.1	1.131	0.1470×10^{-1}
0.0500	1.4	1.183	0.1323×10^{-1}
0.0500	1.8	1.233	0.1269×10^{-1}
0.0500	2.3	1.311	0.1244×10^{-1}
0.0500	3.2	1.389	0.8614×10^{-2}
0.0500	5.1	1.473	0.8870×10^{-2}
0.0500	8.2	1.564	0.1018×10^{-1}
0.0500	12.9	1.591	0.1287×10^{-1}
0.0500	20.5	1.653	0.2002×10^{-1}
0.0700	1.4	1.253	0.1791×10^{-1}
0.0700	1.8	1.224	0.1434×10^{-1}

F_2 Statistical Errors			
x	Q^2	F_2	Stat. Err
0.0700	2.3	1.262	0.1346×10^{-1}
0.0700	3.2	1.334	0.8914×10^{-2}
0.0700	5.1	1.437	0.8772×10^{-2}
0.0700	8.2	1.484	0.9142×10^{-2}
0.0700	12.9	1.496	0.1051×10^{-1}
0.0700	20.5	1.557	0.1375×10^{-1}
0.0700	32.5	1.524	0.2395×10^{-1}
0.0900	1.8	1.257	0.1888×10^{-1}
0.0900	2.3	1.238	0.1464×10^{-1}
0.0900	3.2	1.315	0.9694×10^{-2}
0.0900	5.1	1.388	0.8934×10^{-2}
0.0900	8.2	1.423	0.8768×10^{-2}
0.0900	12.9	1.449	0.9498×10^{-2}
0.0900	20.5	1.466	0.1142×10^{-1}
0.0900	32.5	1.476	0.1602×10^{-1}
0.0900	51.5	1.491	0.3940×10^{-1}
0.1100	2.3	1.318	0.1889×10^{-1}
0.1100	3.2	1.280	0.1028×10^{-1}
0.1100	5.1	1.333	0.9250×10^{-2}
0.1100	8.2	1.345	0.8600×10^{-2}
0.1100	12.9	1.380	0.8981×10^{-2}
0.1100	20.5	1.406	0.1030×10^{-1}
0.1100	32.5	1.344	0.1273×10^{-1}
0.1100	51.5	1.470	0.2406×10^{-1}
0.1400	3.2	1.221	0.8319×10^{-2}
0.1400	5.1	1.253	0.6801×10^{-2}
0.1400	8.2	1.271	0.6174×10^{-2}
0.1400	12.9	1.291	0.6046×10^{-2}
0.1400	20.5	1.275	0.6506×10^{-2}
0.1400	32.5	1.232	0.7486×10^{-2}
0.1400	51.5	1.210	0.1015×10^{-1}
0.1400	81.5	1.224	0.2796×10^{-1}
0.1800	5.1	1.147	0.7282×10^{-2}
0.1800	8.2	1.146	0.6294×10^{-2}
0.1800	12.9	1.154	0.5862×10^{-2}
0.1800	20.5	1.141	0.5916×10^{-2}
0.1800	32.5	1.112	0.6518×10^{-2}
0.1800	51.5	1.070	0.7712×10^{-2}
0.1800	81.5	1.066	0.1313×10^{-1}
0.2250	5.1	1.050	0.7429×10^{-2}
0.2250	8.2	1.023	0.5852×10^{-2}

F_2 Statistical Errors			
x	Q^2	F_2	Stat. Err
0.2250	12.9	1.006	0.5154×10^{-2}
0.2250	20.5	0.9918	0.4946×10^{-2}
0.2250	32.5	0.9663	0.5214×10^{-2}
0.2250	51.5	0.9268	0.5941×10^{-2}
0.2250	81.5	0.9056	0.7786×10^{-2}
0.2750	8.2	0.8839	0.5969×10^{-2}
0.2750	12.9	0.8564	0.5105×10^{-2}
0.2750	20.5	0.8340	0.4674×10^{-2}
0.2750	32.5	0.8018	0.4696×10^{-2}
0.2750	51.5	0.7833	0.5192×10^{-2}
0.2750	81.5	0.7409	0.6127×10^{-2}
0.2750	129.2	0.7044	0.1029×10^{-1}
0.3500	8.2	0.6881	0.4425×10^{-2}
0.3500	12.9	0.6476	0.3462×10^{-2}
0.3500	20.5	0.6164	0.3048×10^{-2}
0.3500	32.5	0.5928	0.2930×10^{-2}
0.3500	51.5	0.5637	0.3068×10^{-2}
0.3500	81.5	0.5289	0.3355×10^{-2}
0.3500	129.2	0.5140	0.4521×10^{-2}
0.4500	12.9	0.4038	0.3091×10^{-2}
0.4500	20.5	0.3872	0.2659×10^{-2}
0.4500	32.5	0.3570	0.2398×10^{-2}
0.4500	51.5	0.3251	0.2341×10^{-2}
0.4500	81.5	0.3093	0.2490×10^{-2}
0.4500	129.2	0.2880	0.2874×10^{-2}
0.4500	204.8	0.2626	0.4906×10^{-2}
0.5500	12.9	0.2358	0.2589×10^{-2}
0.5500	20.5	0.2100	0.2074×10^{-2}
0.5500	32.5	0.1878	0.1785×10^{-2}
0.5500	51.5	0.1737	0.1731×10^{-2}
0.5500	81.5	0.1575	0.1765×10^{-2}
0.5500	129.2	0.1472	0.1936×10^{-2}
0.5500	204.8	0.1282	0.2583×10^{-2}
0.6500	12.9	0.1125	0.2136×10^{-2}
0.6500	20.5	0.9555×10^{-1}	0.1321×10^{-2}
0.6500	32.5	0.8205×10^{-1}	0.1143×10^{-2}
0.6500	51.5	0.7665×10^{-1}	0.1088×10^{-2}
0.6500	81.5	0.6604×10^{-1}	0.1057×10^{-2}
0.6500	129.2	0.5993×10^{-1}	0.1124×10^{-2}

Table A.2: F_2 **Calibration Systematic Errors**

F_2 Calibration Systematic Errors								
x	Q^2	F_2	Stat. Err	Had Cal 744	Had Cal 770	Ehad shift	Emu Cal	Emu shift
0.0015	0.4	0.5031	0.1956×10^{-1}	0.3640×10^{-2}	0.3049×10^{-2}	0.1111×10^{-2}	-0.5365×10^{-2}	-0.3773×10^{-2}
0.0015	0.4	0.6239	0.2417×10^{-1}	0.7462×10^{-3}	0.6552×10^{-2}	0.4140×10^{-3}	-0.1454×10^{-1}	0.2956×10^{-2}
0.0015	0.6	0.7900	0.3712×10^{-1}	-0.4094×10^{-2}	0.8630×10^{-2}	0.1057×10^{-1}	-0.2344×10^{-1}	-0.1553×10^{-2}
0.0015	0.7	0.8705	0.4505×10^{-1}	0.3850×10^{-1}	0.5387×10^{-2}	0.3843×10^{-2}	-0.1870×10^{-1}	-0.2840×10^{-1}
0.0015	0.9	1.010	0.7202×10^{-1}	0.5073	0.1937×10^{-1}	-0.5005	$0.0000\times10^{+00}$	-0.4998
0.0045	0.4	0.6682	0.1728×10^{-1}	-0.9573×10^{-3}	0.1527×10^{-2}	0.5992×10^{-2}	-0.9840×10^{-2}	0.8945×10^{-3}
0.0045	0.4	0.7835	0.2133×10^{-1}	0.3912×10^{-2}	0.3550×10^{-2}	0.9406×10^{-3}	-0.5615×10^{-2}	-0.6083×10^{-2}
0.0045	0.6	0.8825	0.2386×10^{-1}	0.4361×10^{-2}	0.1134×10^{-1}	0.4522×10^{-2}	-0.2610×10^{-1}	-0.1300×10^{-2}
0.0045	0.7	1.058	0.2960×10^{-1}	0.2843×10^{-2}	-0.1938×10^{-2}	0.4244×10^{-2}	-0.2156×10^{-1}	0.2288×10^{-2}
0.0045	0.9	1.269	0.3679×10^{-1}	0.1034×10^{-2}	0.1796×10^{-1}	0.7351×10^{-2}	-0.1293×10^{-1}	0.7378×10^{-2}
0.0045	1.1	1.220	0.4038×10^{-1}	0.5802×10^{-2}	-0.2605×10^{-2}	-0.1019×10^{-2}	-0.5500×10^{-1}	-0.1160×10^{-1}
0.0045	1.4	1.389	0.4729×10^{-1}	0.1883×10^{-1}	0.2162×10^{-1}	0.1663×10^{-1}	-0.2854×10^{-1}	0.1336×10^{-1}
0.0045	1.8	1.393	0.6578×10^{-1}	0.7500×10^{-3}	0.6804×10^{-2}	0.5778×10^{-2}	-0.6333×10^{-1}	-0.3921×10^{-2}
0.0045	2.3	1.681	0.1247	0.8524	0.5988×10^{-1}	0.8451	$0.0000\times10^{+00}$	-0.8375
0.0080	0.4	0.7362	0.1805×10^{-1}	-0.3727×10^{-3}	0.3554×10^{-2}	0.5141×10^{-2}	-0.1362×10^{-1}	-0.7070×10^{-2}
0.0080	0.4	0.8080	0.1914×10^{-1}	0.1565×10^{-2}	-0.3290×10^{-2}	-0.3750×10^{-2}	-0.1819×10^{-1}	-0.3192×10^{-2}
0.0080	0.6	0.9369	0.2061×10^{-1}	-0.4557×10^{-3}	0.9168×10^{-2}	0.6895×10^{-2}	0.1809×10^{-3}	0.1037×10^{-2}
0.0080	0.7	1.000	0.2203×10^{-1}	0.3076×10^{-2}	0.4353×10^{-2}	0.5191×10^{-2}	-0.3369×10^{-1}	-0.1268×10^{-1}
0.0080	0.9	1.147	0.2478×10^{-1}	0.6549×10^{-2}	0.4984×10^{-2}	0.4741×10^{-2}	-0.2330×10^{-1}	-0.2985×10^{-2}
0.0080	1.1	1.279	0.2805×10^{-1}	0.3911×10^{-2}	0.1132×10^{-1}	-0.2199×10^{-2}	-0.7983×10^{-2}	-0.3735×10^{-3}
0.0080	1.4	1.249	0.2973×10^{-1}	0.6921×10^{-2}	0.6834×10^{-2}	0.3240×10^{-2}	-0.1744×10^{-1}	-0.4430×10^{-2}
0.0080	1.8	1.238	0.3190×10^{-1}	0.1006×10^{-1}	0.7088×10^{-2}	0.5892×10^{-2}	-0.1721×10^{-1}	-0.1160×10^{-2}
0.0080	2.3	1.466	0.3869×10^{-1}	0.1045×10^{-1}	0.2188×10^{-1}	0.7053×10^{-2}	-0.4238×10^{-1}	-0.6717×10^{-2}
0.0080	3.2	1.541	0.4115×10^{-1}	0.6139×10^{-2}	0.8202×10^{-2}	0.4615×10^{-2}	-0.4032×10^{-1}	-0.6670×10^{-3}

F_2 Calibration Systematic Errors								
x	Q^2	F_2	Stat. Err	Had Cal 744	Had Cal 770	Ehad shift	Emu Cal	Emu shift
0.0125	0.4	0.6831	0.1783×10^{-1}	-0.5077×10^{-3}	0.2467×10^{-2}	0.1741×10^{-2}	-0.1991×10^{-2}	0.2289×10^{-2}
0.0125	0.4	0.8121	0.1884×10^{-1}	0.2094×10^{-2}	0.1318×10^{-3}	0.1551×10^{-3}	-0.1542×10^{-1}	-0.8535×10^{-2}
0.0125	0.6	0.9350	0.1920×10^{-1}	0.4801×10^{-2}	0.2725×10^{-2}	0.1129×10^{-1}	-0.1131×10^{-1}	-0.4507×10^{-2}
0.0125	0.7	1.067	0.2003×10^{-1}	-0.1745×10^{-2}	-0.2530×10^{-3}	-0.7650×10^{-3}	-0.1520×10^{-1}	-0.3725×10^{-3}
0.0125	0.9	1.103	0.2121×10^{-1}	0.9400×10^{-2}	0.9567×10^{-2}	0.9348×10^{-2}	-0.1511×10^{-1}	-0.5346×10^{-2}
0.0125	1.1	1.206	0.2249×10^{-1}	0.2322×10^{-2}	-0.1925×10^{-3}	0.3405×10^{-2}	-0.3101×10^{-1}	-0.5502×10^{-2}
0.0125	1.4	1.282	0.2333×10^{-1}	0.3067×10^{-2}	0.4457×10^{-2}	0.5302×10^{-2}	-0.1663×10^{-1}	-0.4654×10^{-2}
0.0125	1.8	1.274	0.2476×10^{-1}	0.7581×10^{-2}	0.9613×10^{-2}	0.3269×10^{-2}	-0.4215×10^{-1}	-0.3520×10^{-2}
0.0125	2.3	1.353	0.2813×10^{-1}	0.6147×10^{-2}	0.1055×10^{-1}	0.7319×10^{-2}	-0.1548×10^{-1}	0.1270×10^{-1}
0.0125	3.2	1.470	0.2444×10^{-1}	0.1104×10^{-1}	0.2047×10^{-1}	0.4232×10^{-2}	-0.3437×10^{-1}	-0.5138×10^{-2}
0.0125	5.1	1.656	0.4056×10^{-1}	0.1139×10^{-1}	0.2560×10^{-1}	0.1095×10^{-1}	-0.6426×10^{-1}	-0.8794×10^{-2}
0.0175	0.4	0.7790	0.2493×10^{-1}	0.4558×10^{-2}	-0.5627×10^{-3}	0.9725×10^{-2}	0.2117×10^{-1}	0.7439×10^{-2}
0.0175	0.4	0.8046	0.2111×10^{-1}	0.8250×10^{-3}	0.2554×10^{-2}	0.8997×10^{-2}	-0.3351×10^{-1}	-0.1041×10^{-1}
0.0175	0.6	0.8966	0.2103×10^{-1}	0.4190×10^{-2}	0.2422×10^{-2}	0.7280×10^{-2}	-0.1554×10^{-1}	-0.1131×10^{-1}
0.0175	0.7	0.9649	0.2074×10^{-1}	0.8938×10^{-2}	0.4201×10^{-2}	0.7458×10^{-2}	-0.2574×10^{-1}	-0.2138×10^{-2}
0.0175	0.9	1.135	0.2225×10^{-1}	0.2845×10^{-2}	0.1260×10^{-2}	0.4065×10^{-3}	-0.9403×10^{-2}	-0.1044×10^{-2}
0.0175	1.1	1.179	0.2149×10^{-1}	0.5891×10^{-2}	0.3929×10^{-2}	0.6653×10^{-2}	-0.2611×10^{-1}	-0.3261×10^{-2}
0.0175	1.4	1.281	0.2286×10^{-1}	0.6498×10^{-2}	0.3866×10^{-2}	0.6040×10^{-3}	-0.1948×10^{-1}	-0.5562×10^{-2}
0.0175	1.8	1.307	0.2348×10^{-1}	0.4476×10^{-2}	0.2218×10^{-2}	0.1886×10^{-2}	-0.1852×10^{-1}	-0.5584×10^{-2}
0.0175	2.3	1.403	0.2557×10^{-1}	0.7279×10^{-2}	0.9767×10^{-2}	-0.3803×10^{-4}	-0.2492×10^{-1}	-0.7969×10^{-2}
0.0175	3.2	1.504	0.2104×10^{-1}	0.1116×10^{-1}	0.8220×10^{-2}	0.5726×10^{-2}	-0.2945×10^{-1}	-0.5745×10^{-2}
0.0175	5.1	1.533	0.2704×10^{-1}	0.1357×10^{-1}	0.9633×10^{-2}	0.6471×10^{-2}	-0.2929×10^{-1}	0.9019×10^{-2}
0.0175	8.2	1.541	0.4907×10^{-1}	0.8750×10^{-2}	0.5109×10^{-1}	0.7421×10^{-2}	-0.1428×10^{-1}	0.1069×10^{-1}
0.0250	0.6	0.9396	0.1815×10^{-1}	-0.6337×10^{-2}	-0.5437×10^{-2}	-0.1996×10^{-2}	-0.1364×10^{-1}	-0.2629×10^{-3}

F_2 Calibration Systematic Errors								
x	Q^2	F_2	Stat. Err	Had Cal 744	Had Cal 770	Ehad shift	Emu Cal	Emu shift
0.0250	0.7	1.022	0.1701×10^{-1}	0.5805×10^{-2}	0.6045×10^{-2}	0.1352×10^{-1}	0.4517×10^{-2}	0.1605×10^{-2}
0.0250	0.9	1.048	0.1602×10^{-1}	-0.1224×10^{-2}	0.1319×10^{-2}	0.6506×10^{-2}	-0.2734×10^{-1}	-0.7982×10^{-2}
0.0250	1.1	1.152	0.1622×10^{-1}	0.2020×10^{-2}	0.2548×10^{-2}	0.5471×10^{-2}	-0.3697×10^{-2}	0.9025×10^{-3}
0.0250	1.4	1.207	0.1600×10^{-1}	-0.9847×10^{-4}	0.1629×10^{-2}	0.3065×10^{-2}	-0.2576×10^{-1}	-0.9195×10^{-2}
0.0250	1.8	1.290	0.1626×10^{-1}	0.8461×10^{-2}	0.6885×10^{-2}	0.8156×10^{-2}	-0.1637×10^{-1}	-0.8755×10^{-3}
0.0250	2.3	1.286	0.1623×10^{-1}	0.1970×10^{-3}	0.5120×10^{-2}	0.1794×10^{-2}	-0.1790×10^{-1}	-0.8670×10^{-3}
0.0250	3.2	1.418	0.1277×10^{-1}	0.4775×10^{-2}	0.9035×10^{-2}	0.4366×10^{-2}	-0.2913×10^{-1}	-0.1400×10^{-2}
0.0250	5.1	1.530	0.1545×10^{-1}	0.8917×10^{-2}	0.1265×10^{-1}	0.5351×10^{-2}	-0.2480×10^{-1}	-0.1724×10^{-2}
0.0250	8.2	1.585	0.2070×10^{-1}	0.1385×10^{-1}	0.1674×10^{-1}	0.8327×10^{-2}	-0.4480×10^{-1}	-0.2452×10^{-2}
0.0250	12.9	1.814	0.5016×10^{-1}	0.1865×10^{-1}	0.3231×10^{-1}	0.1217×10^{-1}	-0.7778×10^{-1}	-0.3982×10^{-2}
0.0350	0.7	1.054	0.2255×10^{-1}	0.9743×10^{-2}	0.4396×10^{-2}	0.2338×10^{-1}	-0.4340×10^{-2}	-0.3348×10^{-2}
0.0350	0.9	1.060	0.1807×10^{-1}	0.4883×10^{-2}	0.2940×10^{-3}	0.8054×10^{-2}	-0.2529×10^{-1}	-0.7549×10^{-2}
0.0350	1.1	1.097	0.1706×10^{-1}	0.7370×10^{-3}	0.9347×10^{-2}	0.8332×10^{-2}	-0.1700×10^{-1}	-0.1020×10^{-1}
0.0350	1.4	1.175	0.1673×10^{-1}	0.2011×10^{-2}	-0.3455×10^{-3}	0.4705×10^{-2}	-0.1532×10^{-1}	-0.2818×10^{-2}
0.0350	1.8	1.255	0.1638×10^{-1}	0.4083×10^{-2}	0.4394×10^{-2}	0.8434×10^{-2}	-0.2359×10^{-1}	-0.4620×10^{-2}
0.0350	2.3	1.304	0.1654×10^{-1}	0.4799×10^{-2}	0.1290×10^{-1}	0.7990×10^{-2}	-0.2207×10^{-1}	-0.8951×10^{-2}
0.0350	3.2	1.362	0.1184×10^{-1}	0.6860×10^{-2}	0.5626×10^{-2}	0.5923×10^{-2}	-0.1558×10^{-1}	-0.4883×10^{-2}
0.0350	5.1	1.496	0.1346×10^{-1}	0.9628×10^{-2}	0.1288×10^{-1}	0.5899×10^{-2}	-0.3248×10^{-1}	-0.5043×10^{-2}
0.0350	8.2	1.557	0.1658×10^{-1}	0.8423×10^{-2}	0.9570×10^{-2}	0.5197×10^{-2}	-0.3790×10^{-1}	-0.3266×10^{-2}
0.0350	12.9	1.680	0.2453×10^{-1}	0.6025×10^{-2}	0.2823×10^{-1}	0.7125×10^{-2}	-0.3905×10^{-1}	0.1045×10^{-2}
0.0350	20.5	1.812	0.7433×10^{-1}	0.6133×10^{-1}	0.1620×10^{-1}	0.2007×10^{-1}	-0.4928×10^{-1}	-0.8894×10^{-2}
0.0500	1.1	1.131	0.1470×10^{-1}	0.6289×10^{-2}	-0.3045×10^{-3}	0.1108×10^{-1}	-0.6432×10^{-2}	-0.3564×10^{-2}
0.0500	1.4	1.183	0.1323×10^{-1}	0.2797×10^{-2}	0.5714×10^{-2}	0.1215×10^{-1}	-0.2058×10^{-1}	-0.4588×10^{-2}
0.0500	1.8	1.233	0.1269×10^{-1}	0.5132×10^{-2}	0.2475×10^{-3}	0.6703×10^{-2}	-0.1357×10^{-1}	-0.4529×10^{-2}

F_2 Calibration Systematic Errors								
x	Q^2	F_2	Stat. Err	Had Cal 744	Had Cal 770	Ehad shift	Emu Cal	Emu shift
0.0500	2.3	1.311	0.1244×10^{-1}	0.4215×10^{-3}	0.2085×10^{-2}	0.4623×10^{-2}	-0.1144×10^{-1}	-0.6016×10^{-2}
0.0500	3.2	1.389	0.8614×10^{-2}	0.4221×10^{-2}	0.2249×10^{-2}	0.3989×10^{-2}	-0.1913×10^{-1}	-0.3115×10^{-2}
0.0500	5.1	1.473	0.8870×10^{-2}	0.5076×10^{-2}	0.7441×10^{-2}	0.6309×10^{-2}	-0.2189×10^{-1}	-0.3382×10^{-2}
0.0500	8.2	1.564	0.1018×10^{-1}	0.7625×10^{-2}	0.9665×10^{-2}	0.6092×10^{-2}	-0.2382×10^{-1}	-0.4780×10^{-2}
0.0500	12.9	1.591	0.1287×10^{-1}	0.1139×10^{-1}	0.1317×10^{-1}	0.6081×10^{-2}	-0.2907×10^{-1}	-0.1060×10^{-3}
0.0500	20.5	1.653	0.2002×10^{-1}	0.2008×10^{-1}	0.3151×10^{-1}	0.8048×10^{-2}	-0.4917×10^{-1}	-0.7618×10^{-2}
0.0700	1.4	1.253	0.1791×10^{-1}	0.4344×10^{-2}	0.2663×10^{-2}	0.1177×10^{-1}	-0.1240×10^{-1}	-0.5186×10^{-2}
0.0700	1.8	1.224	0.1434×10^{-1}	0.8038×10^{-2}	-0.3010×10^{-3}	0.1100×10^{-1}	-0.1554×10^{-1}	-0.4199×10^{-2}
0.0700	2.3	1.262	0.1346×10^{-1}	0.4555×10^{-3}	0.2118×10^{-2}	0.7657×10^{-2}	-0.1842×10^{-1}	-0.2096×10^{-2}
0.0700	3.2	1.334	0.8914×10^{-2}	0.4500×10^{-2}	0.4182×10^{-2}	0.7362×10^{-2}	-0.1563×10^{-1}	-0.5112×10^{-2}
0.0700	5.1	1.437	0.8772×10^{-2}	0.3206×10^{-2}	0.6246×10^{-2}	0.2479×10^{-2}	-0.1601×10^{-1}	-0.2654×10^{-2}
0.0700	8.2	1.484	0.9142×10^{-2}	0.5421×10^{-2}	0.7009×10^{-2}	0.3528×10^{-2}	-0.2237×10^{-1}	0.4390×10^{-3}
0.0700	12.9	1.496	0.1051×10^{-1}	0.1076×10^{-1}	0.1015×10^{-1}	0.6409×10^{-2}	-0.2335×10^{-1}	-0.1756×10^{-2}
0.0700	20.5	1.557	0.1375×10^{-1}	0.1044×10^{-1}	0.1164×10^{-1}	0.5105×10^{-2}	-0.2428×10^{-1}	0.3343×10^{-2}
0.0700	32.5	1.524	0.2395×10^{-1}	0.1721×10^{-1}	0.1882×10^{-1}	0.1050×10^{-1}	-0.5849×10^{-1}	0.2879×10^{-2}
0.0900	1.8	1.257	0.1888×10^{-1}	0.9165×10^{-3}	0.5464×10^{-2}	0.1777×10^{-1}	-0.7268×10^{-2}	-0.8227×10^{-2}
0.0900	2.3	1.238	0.1464×10^{-1}	0.2036×10^{-2}	0.3196×10^{-2}	0.7668×10^{-2}	-0.1405×10^{-1}	0.3250×10^{-2}
0.0900	3.2	1.315	0.9694×10^{-2}	0.2285×10^{-2}	0.3092×10^{-2}	0.7489×10^{-2}	-0.1365×10^{-1}	-0.4834×10^{-2}
0.0900	5.1	1.388	0.8934×10^{-2}	0.4525×10^{-2}	0.1740×10^{-2}	0.5593×10^{-2}	-0.1649×10^{-1}	-0.3491×10^{-2}
0.0900	8.2	1.423	0.8768×10^{-2}	0.5077×10^{-2}	0.5137×10^{-2}	0.3550×10^{-2}	-0.1566×10^{-1}	-0.2717×10^{-2}
0.0900	12.9	1.449	0.9498×10^{-2}	0.5162×10^{-2}	0.9354×10^{-2}	0.4438×10^{-2}	-0.1964×10^{-1}	-0.1197×10^{-2}
0.0900	20.5	1.466	0.1142×10^{-1}	0.1038×10^{-1}	0.1372×10^{-1}	0.7876×10^{-2}	-0.2478×10^{-1}	0.1205×10^{-2}
0.0900	32.5	1.476	0.1602×10^{-1}	0.1208×10^{-1}	0.1638×10^{-1}	0.7533×10^{-2}	-0.3411×10^{-1}	0.1351×10^{-2}
0.0900	51.5	1.491	0.3940×10^{-1}	0.1420×10^{-1}	0.2574×10^{-1}	0.8164×10^{-2}	-0.5158×10^{-1}	-0.1255×10^{-1}

F_2 Calibration Systematic Errors								
x	Q^2	F_2	Stat. Err	Had Cal 744	Had Cal 770	Ehad shift	Emu Cal	Emu shift
0.1100	2.3	1.318	0.1889×10^{-1}	0.6364×10^{-2}	0.9280×10^{-2}	0.2432×10^{-1}	-0.2113×10^{-1}	-0.1477×10^{-2}
0.1100	3.2	1.280	0.1028×10^{-1}	0.1254×10^{-2}	-0.1714×10^{-2}	0.4276×10^{-2}	-0.7387×10^{-2}	-0.2747×10^{-2}
0.1100	5.1	1.333	0.9250×10^{-2}	0.3602×10^{-2}	0.5022×10^{-2}	0.7632×10^{-2}	-0.1052×10^{-1}	-0.5874×10^{-2}
0.1100	8.2	1.345	0.8600×10^{-2}	0.6895×10^{-2}	0.7099×10^{-2}	0.7558×10^{-2}	-0.1872×10^{-1}	-0.5156×10^{-2}
0.1100	12.9	1.380	0.8981×10^{-2}	0.6609×10^{-2}	0.7362×10^{-2}	0.5526×10^{-2}	-0.2220×10^{-1}	-0.2698×10^{-2}
0.1100	20.5	1.406	0.1030×10^{-1}	0.7046×10^{-2}	0.8453×10^{-2}	0.4743×10^{-2}	-0.1560×10^{-1}	-0.9645×10^{-3}
0.1100	32.5	1.344	0.1273×10^{-1}	0.8416×10^{-2}	0.1290×10^{-1}	0.6149×10^{-2}	-0.2912×10^{-1}	0.1078×10^{-2}
0.1100	51.5	1.470	0.2406×10^{-1}	0.1374×10^{-1}	0.2645×10^{-1}	0.7675×10^{-2}	-0.4200×10^{-1}	0.4469×10^{-2}
0.1400	3.2	1.221	0.8319×10^{-2}	0.1833×10^{-2}	0.4205×10^{-3}	0.8656×10^{-2}	-0.4941×10^{-2}	-0.1228×10^{-2}
0.1400	5.1	1.253	0.6801×10^{-2}	0.2526×10^{-2}	0.7815×10^{-3}	0.6761×10^{-2}	-0.8106×10^{-2}	-0.3130×10^{-2}
0.1400	8.2	1.271	0.6174×10^{-2}	0.1844×10^{-2}	0.7465×10^{-3}	0.3462×10^{-2}	-0.5313×10^{-2}	-0.3990×10^{-3}
0.1400	12.9	1.291	0.6046×10^{-2}	0.4577×10^{-2}	0.4193×10^{-2}	0.3293×10^{-2}	-0.1474×10^{-1}	-0.2047×10^{-2}
0.1400	20.5	1.275	0.6506×10^{-2}	0.5306×10^{-2}	0.7195×10^{-2}	0.4242×10^{-2}	-0.1236×10^{-1}	0.1729×10^{-2}
0.1400	32.5	1.232	0.7486×10^{-2}	0.7626×10^{-2}	0.8138×10^{-2}	0.4922×10^{-2}	-0.9130×10^{-2}	0.1345×10^{-3}
0.1400	51.5	1.210	0.1015×10^{-1}	0.9352×10^{-2}	0.1207×10^{-1}	0.5849×10^{-2}	-0.2324×10^{-1}	0.3093×10^{-2}
0.1400	81.5	1.224	0.2796×10^{-1}	0.1597×10^{-1}	0.1752×10^{-1}	0.6369×10^{-2}	-0.5589×10^{-1}	-0.8025×10^{-2}
0.1800	5.1	1.147	0.7282×10^{-2}	-0.3101×10^{-2}	0.9415×10^{-3}	0.3498×10^{-2}	0.2223×10^{-2}	0.1225×10^{-3}
0.1800	8.2	1.146	0.6294×10^{-2}	0.2548×10^{-2}	0.6475×10^{-3}	0.5009×10^{-2}	-0.1345×10^{-2}	0.1197×10^{-2}
0.1800	12.9	1.154	0.5862×10^{-2}	0.4880×10^{-3}	0.2775×10^{-2}	0.3389×10^{-2}	-0.7656×10^{-2}	-0.2183×10^{-2}
0.1800	20.5	1.141	0.5916×10^{-2}	0.6323×10^{-2}	0.3815×10^{-2}	0.4039×10^{-2}	-0.1261×10^{-1}	-0.2522×10^{-2}
0.1800	32.5	1.112	0.6518×10^{-2}	0.5585×10^{-2}	0.7917×10^{-2}	0.4080×10^{-2}	-0.9831×10^{-2}	0.3468×10^{-2}
0.1800	51.5	1.070	0.7712×10^{-2}	0.8910×10^{-2}	0.8057×10^{-2}	0.5303×10^{-2}	-0.1343×10^{-1}	0.1199×10^{-2}
0.1800	81.5	1.066	0.1313×10^{-1}	0.1278×10^{-1}	0.1512×10^{-1}	0.4202×10^{-2}	-0.2028×10^{-1}	0.2925×10^{-2}
0.2250	5.1	1.050	0.7429×10^{-2}	0.2905×10^{-2}	-0.3824×10^{-2}	0.4950×10^{-2}	0.2756×10^{-2}	0.1801×10^{-2}
0.2250	8.2	1.023	0.5852×10^{-2}	-0.2105×10^{-2}	0.1061×10^{-2}	0.2567×10^{-2}	-0.3332×10^{-2}	-0.2185×10^{-2}

F_2 Calibration Systematic Errors								
x	Q^2	F_2	Stat. Err	Had Cal 744	Had Cal 770	Ehad shift	Emu Cal	Emu shift
0.2250	12.9	1.006	0.5154×10^{-2}	0.9250×10^{-3}	-0.1429×10^{-2}	0.1356×10^{-2}	0.3923×10^{-2}	0.2137×10^{-2}
0.2250	20.5	0.9918	0.4946×10^{-2}	0.1673×10^{-2}	0.1409×10^{-2}	0.2969×10^{-2}	-0.1816×10^{-3}	0.1227×10^{-2}
0.2250	32.5	0.9663	0.5214×10^{-2}	0.3091×10^{-2}	0.5184×10^{-2}	0.3081×10^{-2}	-0.3366×10^{-2}	0.4369×10^{-3}
0.2250	51.5	0.9268	0.5941×10^{-2}	0.6018×10^{-2}	0.3978×10^{-2}	0.4029×10^{-2}	-0.6737×10^{-2}	0.1797×10^{-2}
0.2250	81.5	0.9056	0.7786×10^{-2}	0.7056×10^{-2}	0.9752×10^{-2}	0.3664×10^{-2}	-0.1406×10^{-1}	0.5376×10^{-3}
0.2750	8.2	0.8839	0.5969×10^{-2}	0.5847×10^{-3}	-0.3092×10^{-2}	0.8428×10^{-3}	0.8613×10^{-2}	0.1948×10^{-2}
0.2750	12.9	0.8564	0.5105×10^{-2}	-0.7282×10^{-3}	-0.1865×10^{-2}	0.1558×10^{-2}	0.8948×10^{-3}	-0.3273×10^{-3}
0.2750	20.5	0.8340	0.4674×10^{-2}	-0.2619×10^{-3}	0.1054×10^{-2}	0.1727×10^{-2}	0.2776×10^{-2}	0.9382×10^{-3}
0.2750	32.5	0.8018	0.4696×10^{-2}	0.1340×10^{-2}	0.3138×10^{-2}	0.2129×10^{-2}	-0.4968×10^{-3}	0.1150×10^{-2}
0.2750	51.5	0.7833	0.5192×10^{-2}	0.2873×10^{-2}	0.2133×10^{-2}	0.2807×10^{-2}	-0.5898×10^{-3}	0.1566×10^{-2}
0.2750	81.5	0.7409	0.6127×10^{-2}	0.2753×10^{-2}	0.4362×10^{-2}	0.3281×10^{-2}	-0.4664×10^{-2}	0.1793×10^{-2}
0.2750	129.2	0.7044	0.1029×10^{-1}	0.1003×10^{-1}	0.1141×10^{-1}	0.3086×10^{-2}	-0.3375×10^{-2}	0.1625×10^{-2}
0.3500	8.2	0.6881	0.4425×10^{-2}	-0.1206×10^{-2}	-0.3505×10^{-2}	0.1614×10^{-3}	0.8138×10^{-2}	0.1201×10^{-2}
0.3500	12.9	0.6476	0.3462×10^{-2}	-0.1344×10^{-2}	-0.3094×10^{-2}	-0.7531×10^{-4}	0.9472×10^{-2}	0.1627×10^{-2}
0.3500	20.5	0.6164	0.3048×10^{-2}	-0.1230×10^{-2}	-0.1954×10^{-2}	-0.7451×10^{-5}	0.8988×10^{-2}	0.1272×10^{-2}
0.3500	32.5	0.5928	0.2930×10^{-2}	0.4122×10^{-3}	-0.9242×10^{-3}	0.1191×10^{-2}	0.6150×10^{-2}	0.1614×10^{-2}
0.3500	51.5	0.5637	0.3068×10^{-2}	0.4860×10^{-3}	0.7043×10^{-3}	0.1165×10^{-2}	0.6268×10^{-2}	0.2025×10^{-2}
0.3500	81.5	0.5289	0.3355×10^{-2}	0.1874×10^{-2}	0.2032×10^{-2}	0.2094×10^{-2}	0.2457×10^{-2}	0.2032×10^{-2}
0.3500	129.2	0.5140	0.4521×10^{-2}	0.4363×10^{-2}	0.4191×10^{-2}	0.2191×10^{-2}	-0.3576×10^{-3}	0.1586×10^{-2}
0.4500	12.9	0.4038	0.3091×10^{-2}	-0.2256×10^{-2}	-0.2854×10^{-2}	-0.1051×10^{-2}	0.1383×10^{-1}	0.2381×10^{-2}
0.4500	20.5	0.3872	0.2659×10^{-2}	-0.1780×10^{-2}	-0.2065×10^{-2}	-0.5228×10^{-3}	0.1052×10^{-1}	0.2288×10^{-2}

F_2 Calibration Systematic Errors								
x	Q^2	F_2	Stat. Err	Had Cal 744	Had Cal 770	Ehad shift	Emu Cal	Emu shift
0.4500	32.5	0.3570	0.2398×10^{-2}	-0.1668×10^{-2}	-0.2862×10^{-2}	-0.4888×10^{-3}	0.1091×10^{-1}	0.2146×10^{-2}
0.4500	51.5	0.3251	0.2341×10^{-2}	-0.6200×10^{-3}	-0.8975×10^{-3}	0.5679×10^{-3}	0.7980×10^{-2}	0.7693×10^{-3}
0.4500	81.5	0.3093	0.2490×10^{-2}	-0.4059×10^{-3}	-0.1134×10^{-2}	0.5222×10^{-3}	0.8928×10^{-2}	0.1436×10^{-2}
0.4500	129.2	0.2880	0.2874×10^{-2}	0.7353×10^{-3}	-0.7434×10^{-4}	0.1239×10^{-2}	0.2913×10^{-2}	0.1304×10^{-2}
0.4500	204.8	0.2626	0.4906×10^{-2}	0.2213×10^{-2}	0.3764×10^{-2}	0.1270×10^{-2}	0.2290×10^{-2}	0.2250×10^{-2}
0.5500	12.9	0.2358	0.2589×10^{-2}	-0.1534×10^{-2}	-0.2368×10^{-2}	-0.1949×10^{-2}	0.7515×10^{-2}	0.1442×10^{-2}
0.5500	20.5	0.2100	0.2074×10^{-2}	-0.1459×10^{-2}	-0.2222×10^{-2}	-0.9050×10^{-3}	0.7859×10^{-2}	0.1505×10^{-2}
0.5500	32.5	0.1878	0.1785×10^{-2}	-0.1118×10^{-2}	-0.1851×10^{-2}	-0.6735×10^{-3}	0.7443×10^{-2}	0.1270×10^{-2}
0.5500	51.5	0.1737	0.1731×10^{-2}	-0.1001×10^{-2}	-0.1551×10^{-2}	-0.2051×10^{-3}	0.7724×10^{-2}	0.1389×10^{-2}
0.5500	81.5	0.1575	0.1765×10^{-2}	0.3060×10^{-4}	-0.7659×10^{-3}	0.3716×10^{-3}	0.4065×10^{-2}	0.9184×10^{-3}
0.5500	129.2	0.1472	0.1936×10^{-2}	-0.2578×10^{-3}	0.1424×10^{-3}	0.3209×10^{-3}	0.5827×10^{-2}	0.9653×10^{-3}
0.5500	204.8	0.1282	0.2583×10^{-2}	0.4302×10^{-3}	-0.1256×10^{-3}	0.8440×10^{-3}	0.1948×10^{-2}	0.1257×10^{-2}
0.6500	12.9	0.1125	0.2136×10^{-2}	-0.1118×10^{-2}	-0.1714×10^{-2}	-0.1753×10^{-2}	0.5689×10^{-2}	0.1199×10^{-2}
0.6500	20.5	0.9555×10^{-1}	0.1321×10^{-2}	-0.1266×10^{-2}	-0.1765×10^{-2}	-0.1490×10^{-2}	0.5511×10^{-2}	0.1024×10^{-2}
0.6500	32.5	0.8205×10^{-1}	0.1143×10^{-2}	-0.9163×10^{-3}	-0.1125×10^{-2}	-0.4640×10^{-3}	0.5407×10^{-2}	0.5250×10^{-3}
0.6500	51.5	0.7665×10^{-1}	0.1088×10^{-2}	-0.5701×10^{-3}	-0.7636×10^{-3}	-0.2173×10^{-3}	0.4161×10^{-2}	0.3691×10^{-3}
0.6500	81.5	0.6604×10^{-1}	0.1057×10^{-2}	-0.7133×10^{-3}	-0.6198×10^{-3}	0.1973×10^{-3}	0.4257×10^{-2}	0.5018×10^{-3}
0.6500	129.2	0.5993×10^{-1}	0.1124×10^{-2}	0.1323×10^{-3}	-0.2740×10^{-3}	0.2066×10^{-3}	0.3492×10^{-2}	0.4406×10^{-3}

Table A.3: F_2 **Flux Systematic Errors**

F_2 Flux Systematic Errors							
x	Q^2	F_2	Stat. Err	$\frac{B^\nu}{A_7}44$	$\frac{B^\nu}{A_7}70$	$\frac{B^{\overline{\nu}}}{A_7}44$	$\frac{B^{\overline{\nu}}}{A_7}70$
0.0015	0.4	0.5031	0.1956×10^{-1}	-0.8277×10^{-3}	-0.8277×10^{-3}	-0.1864×10^{-3}	-0.9370×10^{-4}
0.0015	0.4	0.6239	0.2417×10^{-1}	-0.1234×10^{-2}	-0.1234×10^{-2}	-0.2856×10^{-3}	-0.3858×10^{-3}
0.0015	0.6	0.7900	0.3712×10^{-1}	-0.1343×10^{-2}	-0.1343×10^{-2}	-0.7324×10^{-3}	-0.6513×10^{-3}
0.0015	0.7	0.8705	0.4505×10^{-1}	-0.2208×10^{-2}	-0.2208×10^{-2}	-0.1224×10^{-2}	-0.6525×10^{-3}
0.0015	0.9	1.010	0.7202×10^{-1}	-0.1519×10^{-2}	-0.1519×10^{-2}	-0.9800×10^{-3}	-0.1430×10^{-2}
0.0045	0.4	0.6682	0.1728×10^{-1}	-0.6025×10^{-3}	-0.6025×10^{-3}	0.1673×10^{-3}	0.4183×10^{-3}
0.0045	0.4	0.7835	0.2133×10^{-1}	-0.7654×10^{-3}	-0.7654×10^{-3}	0.9635×10^{-4}	0.3143×10^{-3}
0.0045	0.6	0.8825	0.2386×10^{-1}	-0.1065×10^{-2}	-0.1065×10^{-2}	-0.2855×10^{-4}	0.1295×10^{-3}
0.0045	0.7	1.058	0.2960×10^{-1}	-0.1663×10^{-2}	-0.1663×10^{-2}	-0.2465×10^{-3}	-0.2035×10^{-3}
0.0045	0.9	1.269	0.3679×10^{-1}	-0.2114×10^{-2}	-0.2114×10^{-2}	-0.5460×10^{-3}	-0.5995×10^{-3}
0.0045	1.1	1.220	0.4038×10^{-1}	-0.2281×10^{-2}	-0.2281×10^{-2}	-0.6430×10^{-3}	-0.9555×10^{-3}
0.0045	1.4	1.389	0.4729×10^{-1}	-0.2942×10^{-2}	-0.2942×10^{-2}	-0.1700×10^{-2}	-0.1321×10^{-2}
0.0045	1.8	1.393	0.6578×10^{-1}	-0.3404×10^{-2}	-0.3404×10^{-2}	-0.2723×10^{-2}	-0.1222×10^{-2}
0.0045	2.3	1.681	0.1247	-0.4445×10^{-2}	-0.4445×10^{-2}	-0.2466×10^{-2}	-0.3790×10^{-2}
0.0080	0.4	0.7362	0.1805×10^{-1}	-0.3995×10^{-3}	-0.3995×10^{-3}	0.2771×10^{-3}	0.8028×10^{-3}
0.0080	0.4	0.8080	0.1914×10^{-1}	-0.8263×10^{-3}	-0.8263×10^{-3}	0.4849×10^{-3}	0.4138×10^{-3}
0.0080	0.6	0.9369	0.2061×10^{-1}	-0.9630×10^{-3}	-0.9630×10^{-3}	0.3899×10^{-3}	0.5150×10^{-3}
0.0080	0.7	1.000	0.2203×10^{-1}	-0.1067×10^{-2}	-0.1067×10^{-2}	0.1875×10^{-3}	0.3990×10^{-3}
0.0080	0.9	1.147	0.2478×10^{-1}	-0.1622×10^{-2}	-0.1622×10^{-2}	0.5847×10^{-4}	0.2300×10^{-3}
0.0080	1.1	1.279	0.2805×10^{-1}	-0.2241×10^{-2}	-0.2241×10^{-2}	-0.4735×10^{-3}	0.1013×10^{-5}
0.0080	1.4	1.249	0.2973×10^{-1}	-0.1765×10^{-2}	-0.1765×10^{-2}	-0.3990×10^{-3}	-0.3605×10^{-3}
0.0080	1.8	1.238	0.3190×10^{-1}	-0.2712×10^{-2}	-0.2712×10^{-2}	-0.9100×10^{-3}	-0.5195×10^{-3}
0.0080	2.3	1.466	0.3869×10^{-1}	-0.2987×10^{-2}	-0.2987×10^{-2}	-0.1527×10^{-2}	-0.1445×10^{-2}
0.0080	3.2	1.541	0.4115×10^{-1}	-0.3468×10^{-2}	-0.3468×10^{-2}	-0.1563×10^{-2}	-0.2444×10^{-2}
0.0125	0.4	0.6831	0.1783×10^{-1}	-0.3491×10^{-3}	-0.3491×10^{-3}	0.3764×10^{-3}	0.6410×10^{-3}
0.0125	0.4	0.8121	0.1884×10^{-1}	-0.5384×10^{-3}	-0.5384×10^{-3}	0.4670×10^{-3}	0.7073×10^{-3}

F_2 Flux Systematic Errors							
x	Q^2	F_2	Stat. Err	$\frac{B^\nu}{A_7}44$	$\frac{B^\nu}{A_7}70$	$\frac{B^{\overline{\nu}}}{A_7}44$	$\frac{B^{\overline{\nu}}}{A_7}70$
0.0125	0.6	0.9350	0.1920×10^{-1}	-0.7342×10^{-3}	-0.7342×10^{-3}	0.5382×10^{-3}	0.6507×10^{-3}
0.0125	0.7	1.067	0.2003×10^{-1}	-0.1002×10^{-2}	-0.1002×10^{-2}	0.6350×10^{-3}	0.6680×10^{-3}
0.0125	0.9	1.103	0.2121×10^{-1}	-0.9240×10^{-3}	-0.9240×10^{-3}	0.3390×10^{-3}	0.7580×10^{-3}
0.0125	1.1	1.206	0.2249×10^{-1}	-0.1229×10^{-2}	-0.1229×10^{-2}	0.1325×10^{-3}	0.5185×10^{-3}
0.0125	1.4	1.282	0.2333×10^{-1}	-0.1646×10^{-2}	-0.1646×10^{-2}	0.8202×10^{-4}	0.2210×10^{-3}
0.0125	1.8	1.274	0.2476×10^{-1}	-0.1952×10^{-2}	-0.1952×10^{-2}	-0.2595×10^{-3}	0.9000×10^{-5}
0.0125	2.3	1.353	0.2813×10^{-1}	-0.2714×10^{-2}	-0.2714×10^{-2}	-0.8660×10^{-3}	-0.2455×10^{-3}
0.0125	3.2	1.470	0.2444×10^{-1}	-0.3286×10^{-2}	-0.3286×10^{-2}	-0.1212×10^{-2}	-0.1024×10^{-2}
0.0125	5.1	1.656	0.4056×10^{-1}	-0.4422×10^{-2}	-0.4422×10^{-2}	-0.2403×10^{-2}	-0.2088×10^{-2}
0.0175	0.4	0.7790	0.2493×10^{-1}	-0.2210×10^{-3}	-0.2210×10^{-3}	0.2649×10^{-3}	0.1099×10^{-2}
0.0175	0.4	0.8046	0.2111×10^{-1}	-0.6416×10^{-3}	-0.6416×10^{-3}	0.7349×10^{-3}	0.6042×10^{-3}
0.0175	0.6	0.8966	0.2103×10^{-1}	-0.4624×10^{-3}	-0.4624×10^{-3}	0.3915×10^{-3}	0.8905×10^{-3}
0.0175	0.7	0.9649	0.2074×10^{-1}	-0.6756×10^{-3}	-0.6756×10^{-3}	0.5668×10^{-3}	0.6993×10^{-3}
0.0175	0.9	1.135	0.2225×10^{-1}	-0.9665×10^{-3}	-0.9665×10^{-3}	0.6670×10^{-3}	0.7215×10^{-3}
0.0175	1.1	1.179	0.2149×10^{-1}	-0.7375×10^{-3}	-0.7375×10^{-3}	0.2650×10^{-3}	0.8820×10^{-3}
0.0175	1.4	1.281	0.2286×10^{-1}	-0.1337×10^{-2}	-0.1337×10^{-2}	0.4725×10^{-3}	0.5705×10^{-3}
0.0175	1.8	1.307	0.2348×10^{-1}	-0.1670×10^{-2}	-0.1670×10^{-2}	0.1470×10^{-3}	0.3325×10^{-3}
0.0175	2.3	1.403	0.2557×10^{-1}	-0.1751×10^{-2}	-0.1751×10^{-2}	-0.7403×10^{-4}	0.1855×10^{-3}
0.0175	3.2	1.504	0.2104×10^{-1}	-0.2631×10^{-2}	-0.2631×10^{-2}	-0.7620×10^{-3}	-0.4200×10^{-3}
0.0175	5.1	1.533	0.2704×10^{-1}	-0.3428×10^{-2}	-0.3428×10^{-2}	-0.1464×10^{-2}	-0.1287×10^{-2}
0.0175	8.2	1.541	0.4907×10^{-1}	-0.4960×10^{-2}	-0.4960×10^{-2}	-0.1905×10^{-2}	-0.2553×10^{-2}
0.0250	0.6	0.9396	0.1815×10^{-1}	-0.6410×10^{-3}	-0.6410×10^{-3}	0.7145×10^{-3}	0.8614×10^{-3}
0.0250	0.7	1.022	0.1701×10^{-1}	-0.7820×10^{-3}	-0.7820×10^{-3}	0.8845×10^{-3}	0.8260×10^{-3}
0.0250	0.9	1.048	0.1602×10^{-1}	-0.6800×10^{-3}	-0.6800×10^{-3}	0.5775×10^{-3}	0.8340×10^{-3}
0.0250	1.1	1.152	0.1622×10^{-1}	-0.7725×10^{-3}	-0.7725×10^{-3}	0.5600×10^{-3}	0.8520×10^{-3}
0.0250	1.4	1.207	0.1600×10^{-1}	-0.1083×10^{-2}	-0.1083×10^{-2}	0.5605×10^{-3}	0.8140×10^{-3}

F_2 Flux Systematic Errors							
x	Q^2	F_2	Stat. Err	$\frac{B^\nu}{A_7}44$	$\frac{B^\nu}{A_7}70$	$\frac{B^{\overline{\nu}}}{A_7}44$	$\frac{B^{\overline{\nu}}}{A_7}70$
0.0250	1.8	1.290	0.1626×10^{-1}	-0.1227×10^{-2}	-0.1227×10^{-2}	0.4965×10^{-3}	0.6190×10^{-3}
0.0250	2.3	1.286	0.1623×10^{-1}	-0.1275×10^{-2}	-0.1275×10^{-2}	0.1840×10^{-3}	0.5316×10^{-3}
0.0250	3.2	1.418	0.1277×10^{-1}	-0.2007×10^{-2}	-0.2007×10^{-2}	-0.1065×10^{-3}	0.1370×10^{-3}
0.0250	5.1	1.530	0.1545×10^{-1}	-0.2752×10^{-2}	-0.2752×10^{-2}	-0.8110×10^{-3}	-0.5635×10^{-3}
0.0250	8.2	1.585	0.2070×10^{-1}	-0.3931×10^{-2}	-0.3931×10^{-2}	-0.1612×10^{-2}	-0.1410×10^{-2}
0.0250	12.9	1.814	0.5016×10^{-1}	-0.5476×10^{-2}	-0.5476×10^{-2}	-0.3434×10^{-2}	-0.2824×10^{-2}
0.0350	0.7	1.054	0.2255×10^{-1}	-0.7445×10^{-3}	-0.7445×10^{-3}	0.9225×10^{-3}	0.9360×10^{-3}
0.0350	0.9	1.060	0.1807×10^{-1}	-0.5295×10^{-3}	-0.5295×10^{-3}	0.6035×10^{-3}	0.1114×10^{-2}
0.0350	1.1	1.097	0.1706×10^{-1}	-0.6880×10^{-3}	-0.6880×10^{-3}	0.6710×10^{-3}	0.8690×10^{-3}
0.0350	1.4	1.175	0.1673×10^{-1}	-0.8140×10^{-3}	-0.8140×10^{-3}	0.6490×10^{-3}	0.9010×10^{-3}
0.0350	1.8	1.255	0.1638×10^{-1}	-0.8890×10^{-3}	-0.8890×10^{-3}	0.5265×10^{-3}	0.7970×10^{-3}
0.0350	2.3	1.304	0.1654×10^{-1}	-0.1117×10^{-2}	-0.1117×10^{-2}	0.4635×10^{-3}	0.6960×10^{-3}
0.0350	3.2	1.362	0.1184×10^{-1}	-0.1535×10^{-2}	-0.1535×10^{-2}	0.2275×10^{-3}	0.4355×10^{-3}
0.0350	5.1	1.496	0.1346×10^{-1}	-0.2223×10^{-2}	-0.2223×10^{-2}	-0.2560×10^{-3}	-0.5400×10^{-4}
0.0350	8.2	1.557	0.1658×10^{-1}	-0.3367×10^{-2}	-0.3367×10^{-2}	-0.1033×10^{-2}	-0.8015×10^{-3}
0.0350	12.9	1.680	0.2453×10^{-1}	-0.4238×10^{-2}	-0.4238×10^{-2}	-0.1526×10^{-2}	-0.1902×10^{-2}
0.0350	20.5	1.812	0.7433×10^{-1}	-0.5831×10^{-2}	-0.5831×10^{-2}	-0.3492×10^{-2}	-0.2919×10^{-2}
0.0500	1.1	1.131	0.1470×10^{-1}	-0.6905×10^{-3}	-0.6905×10^{-3}	0.7970×10^{-3}	0.1134×10^{-2}
0.0500	1.4	1.183	0.1323×10^{-1}	-0.7180×10^{-3}	-0.7180×10^{-3}	0.7270×10^{-3}	0.1109×10^{-2}
0.0500	1.8	1.233	0.1269×10^{-1}	-0.7645×10^{-3}	-0.7645×10^{-3}	0.6615×10^{-3}	0.1069×10^{-2}
0.0500	2.3	1.311	0.1244×10^{-1}	-0.9775×10^{-3}	-0.9775×10^{-3}	0.6624×10^{-3}	0.8290×10^{-3}
0.0500	3.2	1.389	0.8614×10^{-2}	-0.1170×10^{-2}	-0.1170×10^{-2}	0.4680×10^{-3}	0.6915×10^{-3}
0.0500	5.1	1.473	0.8870×10^{-2}	-0.1619×10^{-2}	-0.1619×10^{-2}	0.8148×10^{-4}	0.3530×10^{-3}
0.0500	8.2	1.564	0.1018×10^{-1}	-0.2485×10^{-2}	-0.2485×10^{-2}	-0.4120×10^{-3}	-0.2230×10^{-3}
0.0500	12.9	1.591	0.1287×10^{-1}	-0.3570×10^{-2}	-0.3570×10^{-2}	-0.1166×10^{-2}	-0.9561×10^{-3}
0.0500	20.5	1.653	0.2002×10^{-1}	-0.5020×10^{-2}	-0.5020×10^{-2}	-0.1640×10^{-2}	-0.1816×10^{-2}

F_2 Flux Systematic Errors							
x	Q^2	F_2	Stat. Err	$\frac{B^\nu}{A_7}44$	$\frac{B^\nu}{A_7}70$	$\frac{B^{\overline{\nu}}}{A_7}44$	$\frac{B^{\overline{\nu}}}{A_7}70$
0.0700	1.4	1.253	0.1791×10^{-1}	-0.7340×10^{-3}	-0.7340×10^{-3}	0.8535×10^{-3}	0.1229×10^{-2}
0.0700	1.8	1.224	0.1434×10^{-1}	-0.7850×10^{-3}	-0.7850×10^{-3}	0.8670×10^{-3}	0.1177×10^{-2}
0.0700	2.3	1.262	0.1346×10^{-1}	-0.7365×10^{-3}	-0.7365×10^{-3}	0.7065×10^{-3}	0.1074×10^{-2}
0.0700	3.2	1.334	0.8914×10^{-2}	-0.8505×10^{-3}	-0.8505×10^{-3}	0.5195×10^{-3}	0.9090×10^{-3}
0.0700	5.1	1.437	0.8772×10^{-2}	-0.1253×10^{-2}	-0.1253×10^{-2}	0.3310×10^{-3}	0.6055×10^{-3}
0.0700	8.2	1.484	0.9142×10^{-2}	-0.1927×10^{-2}	-0.1927×10^{-2}	-0.6449×10^{-4}	0.1390×10^{-3}
0.0700	12.9	1.496	0.1051×10^{-1}	-0.2805×10^{-2}	-0.2805×10^{-2}	-0.6515×10^{-3}	-0.3695×10^{-3}
0.0700	20.5	1.557	0.1375×10^{-1}	-0.3805×10^{-2}	-0.3805×10^{-2}	-0.1122×10^{-2}	-0.1086×10^{-2}
0.0700	32.5	1.524	0.2395×10^{-1}	-0.5199×10^{-2}	-0.5199×10^{-2}	-0.1610×10^{-2}	-0.1845×10^{-2}
0.0900	1.8	1.257	0.1888×10^{-1}	-0.6315×10^{-3}	-0.6315×10^{-3}	0.7215×10^{-3}	0.1212×10^{-2}
0.0900	2.3	1.238	0.1464×10^{-1}	-0.6690×10^{-3}	-0.6690×10^{-3}	0.7770×10^{-3}	0.1056×10^{-2}
0.0900	3.2	1.315	0.9694×10^{-2}	-0.8820×10^{-3}	-0.8820×10^{-3}	0.7335×10^{-3}	0.9805×10^{-3}
0.0900	5.1	1.388	0.8934×10^{-2}	-0.9965×10^{-3}	-0.9965×10^{-3}	0.4115×10^{-3}	0.7175×10^{-3}
0.0900	8.2	1.423	0.8768×10^{-2}	-0.1404×10^{-2}	-0.1404×10^{-2}	0.1345×10^{-3}	0.3425×10^{-3}
0.0900	12.9	1.449	0.9498×10^{-2}	-0.2151×10^{-2}	-0.2151×10^{-2}	-0.2880×10^{-3}	-0.9447×10^{-4}
0.0900	20.5	1.466	0.1142×10^{-1}	-0.3133×10^{-2}	-0.3133×10^{-2}	-0.7800×10^{-3}	-0.6640×10^{-3}
0.0900	32.5	1.476	0.1602×10^{-1}	-0.4276×10^{-2}	-0.4276×10^{-2}	-0.1414×10^{-2}	-0.1022×10^{-2}
0.0900	51.5	1.491	0.3940×10^{-1}	-0.6064×10^{-2}	-0.6064×10^{-2}	-0.2181×10^{-2}	-0.1343×10^{-2}
0.1100	2.3	1.318	0.1889×10^{-1}	-0.7510×10^{-3}	-0.7510×10^{-3}	0.8455×10^{-3}	0.1452×10^{-2}
0.1100	3.2	1.280	0.1028×10^{-1}	-0.7515×10^{-3}	-0.7515×10^{-3}	0.7240×10^{-3}	0.1069×10^{-2}
0.1100	5.1	1.333	0.9250×10^{-2}	-0.8960×10^{-3}	-0.8960×10^{-3}	0.5600×10^{-3}	0.7960×10^{-3}
0.1100	8.2	1.345	0.8600×10^{-2}	-0.1164×10^{-2}	-0.1164×10^{-2}	0.2550×10^{-3}	0.4295×10^{-3}
0.1100	12.9	1.380	0.8981×10^{-2}	-0.1794×10^{-2}	-0.1794×10^{-2}	-0.9197×10^{-4}	0.6598×10^{-4}
0.1100	20.5	1.406	0.1030×10^{-1}	-0.2678×10^{-2}	-0.2678×10^{-2}	-0.5115×10^{-3}	-0.4060×10^{-3}
0.1100	32.5	1.344	0.1273×10^{-1}	-0.3677×10^{-2}	-0.3677×10^{-2}	-0.9295×10^{-3}	-0.7845×10^{-3}
0.1100	51.5	1.470	0.2406×10^{-1}	-0.5167×10^{-2}	-0.5167×10^{-2}	-0.1884×10^{-2}	-0.1128×10^{-2}

F_2 Flux Systematic Errors							
x	Q^2	F_2	Stat. Err	$\frac{B^\nu}{A_7}44$	$\frac{B^\nu}{A_7}70$	$\frac{B^{\overline{\nu}}}{A_7}44$	$\frac{B^{\overline{\nu}}}{A_7}70$
0.1400	3.2	1.221	0.8319×10^{-2}	-0.7035×10^{-3}	-0.7035×10^{-3}	0.7340×10^{-3}	0.1049×10^{-2}
0.1400	5.1	1.253	0.6801×10^{-2}	-0.6810×10^{-3}	-0.6810×10^{-3}	0.4975×10^{-3}	0.8980×10^{-3}
0.1400	8.2	1.271	0.6174×10^{-2}	-0.9265×10^{-3}	-0.9265×10^{-3}	0.3210×10^{-3}	0.5235×10^{-3}
0.1400	12.9	1.291	0.6046×10^{-2}	-0.1364×10^{-2}	-0.1364×10^{-2}	0.5049×10^{-4}	0.1910×10^{-3}
0.1400	20.5	1.275	0.6506×10^{-2}	-0.2020×10^{-2}	-0.2020×10^{-2}	-0.2805×10^{-3}	-0.1445×10^{-3}
0.1400	32.5	1.232	0.7486×10^{-2}	-0.2824×10^{-2}	-0.2824×10^{-2}	-0.6505×10^{-3}	-0.4470×10^{-3}
0.1400	51.5	1.210	0.1015×10^{-1}	-0.3878×10^{-2}	-0.3878×10^{-2}	-0.7815×10^{-3}	-0.7030×10^{-3}
0.1400	81.5	1.224	0.2796×10^{-1}	-0.5481×10^{-2}	-0.5481×10^{-2}	-0.1493×10^{-2}	-0.7620×10^{-3}
0.1800	5.1	1.147	0.7282×10^{-2}	-0.6635×10^{-3}	-0.6635×10^{-3}	0.6245×10^{-3}	0.8130×10^{-3}
0.1800	8.2	1.146	0.6294×10^{-2}	-0.7065×10^{-3}	-0.7065×10^{-3}	0.3775×10^{-3}	0.5785×10^{-3}
0.1800	12.9	1.154	0.5862×10^{-2}	-0.9565×10^{-3}	-0.9565×10^{-3}	0.1365×10^{-3}	0.3095×10^{-3}
0.1800	20.5	1.141	0.5916×10^{-2}	-0.1451×10^{-2}	-0.1451×10^{-2}	-0.1055×10^{-3}	0.1198×10^{-4}
0.1800	32.5	1.112	0.6518×10^{-2}	-0.2219×10^{-2}	-0.2219×10^{-2}	-0.3500×10^{-3}	-0.2875×10^{-3}
0.1800	51.5	1.070	0.7712×10^{-2}	-0.2804×10^{-2}	-0.2804×10^{-2}	-0.4305×10^{-3}	-0.5029×10^{-3}
0.1800	81.5	1.066	0.1313×10^{-1}	-0.3963×10^{-2}	-0.3963×10^{-2}	-0.7440×10^{-3}	-0.5360×10^{-3}
0.2250	5.1	1.050	0.7429×10^{-2}	-0.5935×10^{-3}	-0.5935×10^{-3}	0.6090×10^{-3}	0.8550×10^{-3}
0.2250	8.2	1.023	0.5852×10^{-2}	-0.6420×10^{-3}	-0.6420×10^{-3}	0.4435×10^{-3}	0.5835×10^{-3}
0.2250	12.9	1.006	0.5154×10^{-2}	-0.6900×10^{-3}	-0.6900×10^{-3}	0.1755×10^{-3}	0.3460×10^{-3}
0.2250	20.5	0.9918	0.4946×10^{-2}	-0.1034×10^{-2}	-0.1034×10^{-2}	-0.1150×10^{-4}	0.8893×10^{-4}
0.2250	32.5	0.9663	0.5214×10^{-2}	-0.1624×10^{-2}	-0.1624×10^{-2}	-0.2103×10^{-3}	-0.1174×10^{-3}
0.2250	51.5	0.9268	0.5941×10^{-2}	-0.2214×10^{-2}	-0.2214×10^{-2}	-0.3753×10^{-3}	-0.3138×10^{-3}
0.2250	81.5	0.9056	0.7786×10^{-2}	-0.3041×10^{-2}	-0.3041×10^{-2}	-0.4631×10^{-3}	-0.3248×10^{-3}
0.2750	8.2	0.8839	0.5969×10^{-2}	-0.5158×10^{-3}	-0.5158×10^{-3}	0.4143×10^{-3}	0.5543×10^{-3}
0.2750	12.9	0.8564	0.5105×10^{-2}	-0.5664×10^{-3}	-0.5664×10^{-3}	0.2151×10^{-3}	0.3408×10^{-3}
0.2750	20.5	0.8340	0.4674×10^{-2}	-0.7342×10^{-3}	-0.7342×10^{-3}	0.3836×10^{-4}	0.1380×10^{-3}
0.2750	32.5	0.8018	0.4696×10^{-2}	-0.1121×10^{-2}	-0.1121×10^{-2}	-0.9575×10^{-4}	-0.4721×10^{-4}

F_2 Flux Systematic Errors							
x	Q^2	F_2	Stat. Err	$\frac{B^{\nu}}{A_7}44$	$\frac{B^{\nu}}{A_7}70$	$\frac{B^{\overline{\nu}}}{A_7}44$	$\frac{B^{\overline{\nu}}}{A_7}70$
0.2750	51.5	0.7833	0.5192×10^{-2}	-0.1705×10^{-2}	-0.1705×10^{-2}	-0.2215×10^{-3}	-0.1979×10^{-3}
0.2750	81.5	0.7409	0.6127×10^{-2}	-0.2249×10^{-2}	-0.2249×10^{-2}	-0.3062×10^{-3}	-0.2559×10^{-3}
0.2750	129.2	0.7044	0.1029×10^{-1}	-0.2884×10^{-2}	-0.2884×10^{-2}	-0.8163×10^{-4}	-0.3109×10^{-3}
0.3500	8.2	0.6881	0.4425×10^{-2}	-0.3779×10^{-3}	-0.3779×10^{-3}	0.3465×10^{-3}	0.5087×10^{-3}
0.3500	12.9	0.6476	0.3462×10^{-2}	-0.4072×10^{-3}	-0.4072×10^{-3}	0.2216×10^{-3}	0.3061×10^{-3}
0.3500	20.5	0.6164	0.3048×10^{-2}	-0.4845×10^{-3}	-0.4845×10^{-3}	0.7933×10^{-4}	0.1497×10^{-3}
0.3500	32.5	0.5928	0.2930×10^{-2}	-0.7004×10^{-3}	-0.7004×10^{-3}	-0.3120×10^{-4}	0.1058×10^{-4}
0.3500	51.5	0.5637	0.3068×10^{-2}	-0.1077×10^{-2}	-0.1077×10^{-2}	-0.1255×10^{-3}	-0.8360×10^{-4}
0.3500	81.5	0.5289	0.3355×10^{-2}	-0.1369×10^{-2}	-0.1369×10^{-2}	-0.1648×10^{-3}	-0.1533×10^{-3}
0.3500	129.2	0.5140	0.4521×10^{-2}	-0.1782×10^{-2}	-0.1782×10^{-2}	-0.1730×10^{-3}	-0.1179×10^{-3}
0.4500	12.9	0.4038	0.3091×10^{-2}	-0.2207×10^{-3}	-0.2207×10^{-3}	0.1626×10^{-3}	0.2453×10^{-3}
0.4500	20.5	0.3872	0.2659×10^{-2}	-0.2753×10^{-3}	-0.2753×10^{-3}	0.7589×10^{-4}	0.1310×10^{-3}
0.4500	32.5	0.3570	0.2398×10^{-2}	-0.3622×10^{-3}	-0.3622×10^{-3}	0.4098×10^{-5}	0.3031×10^{-4}
0.4500	51.5	0.3251	0.2341×10^{-2}	-0.5134×10^{-3}	-0.5134×10^{-3}	-0.4689×10^{-4}	-0.3000×10^{-4}
0.4500	81.5	0.3093	0.2490×10^{-2}	-0.7124×10^{-3}	-0.7124×10^{-3}	-0.7540×10^{-4}	-0.6889×10^{-4}
0.4500	129.2	0.2880	0.2874×10^{-2}	-0.9219×10^{-3}	-0.9219×10^{-3}	-0.1068×10^{-3}	-0.5496×10^{-4}
0.4500	204.8	0.2626	0.4906×10^{-2}	-0.9886×10^{-3}	-0.9886×10^{-3}	-0.2725×10^{-4}	-0.6355×10^{-4}
0.5500	12.9	0.2358	0.2589×10^{-2}	-0.1341×10^{-3}	-0.1341×10^{-3}	0.9755×10^{-4}	0.1504×10^{-3}
0.5500	20.5	0.2100	0.2074×10^{-2}	-0.1567×10^{-3}	-0.1567×10^{-3}	0.6644×10^{-4}	0.8250×10^{-4}
0.5500	32.5	0.1878	0.1785×10^{-2}	-0.1618×10^{-3}	-0.1618×10^{-3}	0.9552×10^{-5}	0.3375×10^{-4}
0.5500	51.5	0.1737	0.1731×10^{-2}	-0.2459×10^{-3}	-0.2459×10^{-3}	-0.1710×10^{-4}	-0.7100×10^{-5}
0.5500	81.5	0.1575	0.1765×10^{-2}	-0.3245×10^{-3}	-0.3245×10^{-3}	-0.3025×10^{-4}	-0.2830×10^{-4}
0.5500	129.2	0.1472	0.1936×10^{-2}	-0.3896×10^{-3}	-0.3896×10^{-3}	-0.4080×10^{-4}	-0.4055×10^{-4}
0.5500	204.8	0.1282	0.2583×10^{-2}	-0.4807×10^{-3}	-0.4807×10^{-3}	-0.1125×10^{-4}	-0.3190×10^{-4}

F_2 Flux Systematic Errors							
x	Q^2	F_2	Stat. Err	$\frac{B^{\nu}}{A7}44$	$\frac{B^{\nu}}{A7}70$	$\frac{B^{\overline{\nu}}}{A7}44$	$\frac{B^{\overline{\nu}}}{A7}70$
0.6500	12.9	0.1125	0.2136×10^{-2}	-0.7030×10^{-4}	-0.7030×10^{-4}	0.5305×10^{-4}	0.8590×10^{-4}
0.6500	20.5	0.9555×10^{-1}	0.1321×10^{-2}	-0.5537×10^{-4}	-0.5537×10^{-4}	0.2284×10^{-4}	0.4273×10^{-4}
0.6500	32.5	0.8205×10^{-1}	0.1143×10^{-2}	-0.7240×10^{-4}	-0.7240×10^{-4}	0.7182×10^{-5}	0.1422×10^{-4}
0.6500	51.5	0.7665×10^{-1}	0.1088×10^{-2}	-0.9740×10^{-4}	-0.9740×10^{-4}	-0.7950×10^{-5}	-0.1378×10^{-5}
0.6500	81.5	0.6604×10^{-1}	0.1057×10^{-2}	-0.1213×10^{-3}	-0.1213×10^{-3}	-0.1070×10^{-4}	-0.9380×10^{-5}
0.6500	129.2	0.5993×10^{-1}	0.1124×10^{-2}	-0.1626×10^{-3}	-0.1626×10^{-3}	-0.1807×10^{-4}	-0.1340×10^{-4}

Table A.4: F_2 **Model Systematic Errors**

F_2 Model Systematic Errors								
x	Q^2	F_2	Stat. Err	Charm Mass	Kappa	Alpha	Charm Br	Model	dxf3
0.0015	0.4	0.5031	0.1956×10^{-1}	0.2158×10^{-2}	0.1234×10^{-2}	0.1275×10^{-2}	0.1338×10^{-2}	-0.1456×10^{-1}	-0.8452×10^{-2}
0.0015	0.4	0.6239	0.2417×10^{-1}	0.4267×10^{-2}	0.2166×10^{-2}	0.2101×10^{-2}	0.1872×10^{-2}	-0.3101×10^{-1}	-0.3063×10^{-1}
0.0015	0.6	0.7900	0.3712×10^{-1}	0.6870×10^{-2}	0.1843×10^{-2}	0.1692×10^{-2}	0.1163×10^{-2}	-0.2299×10^{-1}	-0.6009×10^{-1}
0.0015	0.7	0.8705	0.4505×10^{-1}	0.1438×10^{-1}	0.5810×10^{-2}	0.5539×10^{-2}	0.4791×10^{-2}	0.8689×10^{-1}	-0.7034×10^{-1}
0.0015	0.9	1.010	0.7202×10^{-1}	0.2318×10^{-1}	0.8337×10^{-2}	0.8046×10^{-2}	0.7229×10^{-2}	0.7713×10^{-2}	-0.1135
0.0045	0.4	0.6682	0.1728×10^{-1}	-0.1697×10^{-2}	-0.3238×10^{-2}	-0.2769×10^{-2}	-0.2812×10^{-2}	0.2682×10^{-1}	-0.4723×10^{-2}
0.0045	0.4	0.7835	0.2133×10^{-1}	0.7874×10^{-4}	-0.3018×10^{-2}	-0.2521×10^{-2}	-0.2852×10^{-2}	-0.1800×10^{-1}	-0.1986×10^{-1}
0.0045	0.6	0.8825	0.2386×10^{-1}	0.4405×10^{-2}	-0.7906×10^{-3}	-0.3867×10^{-3}	-0.1032×10^{-2}	0.6299×10^{-2}	-0.3118×10^{-1}
0.0045	0.7	1.058	0.2960×10^{-1}	0.1182×10^{-1}	0.2666×10^{-2}	0.3027×10^{-2}	0.2202×10^{-2}	-0.4940×10^{-3}	-0.5158×10^{-1}
0.0045	0.9	1.269	0.3679×10^{-1}	0.1864×10^{-1}	0.4228×10^{-2}	0.4579×10^{-2}	0.3848×10^{-2}	-0.8961×10^{-1}	-0.6578×10^{-1}
0.0045	1.1	1.220	0.4038×10^{-1}	0.1859×10^{-1}	-0.7999×10^{-4}	0.2570×10^{-3}	0.7999×10^{-4}	-0.3014×10^{-1}	-0.6596×10^{-1}
0.0045	1.4	1.389	0.4729×10^{-1}	0.3027×10^{-1}	0.2557×10^{-2}	0.3093×10^{-2}	0.3701×10^{-2}	-0.1558	-0.1169
0.0045	1.8	1.393	0.6578×10^{-1}	0.3801×10^{-1}	0.4720×10^{-2}	0.5650×10^{-2}	0.7520×10^{-2}	-0.9891×10^{-3}	-0.6719×10^{-1}
0.0045	2.3	1.681	0.1247	0.5637×10^{-1}	0.9463×10^{-2}	0.1112×10^{-1}	0.1490×10^{-1}	-0.1441	-0.1232
0.0080	0.4	0.7362	0.1805×10^{-1}	0.3481×10^{-3}	-0.2185×10^{-2}	-0.1195×10^{-2}	-0.1548×10^{-2}	-0.1958×10^{-1}	-0.3999×10^{-2}
0.0080	0.4	0.8080	0.1914×10^{-1}	0.1261×10^{-2}	-0.2535×10^{-2}	-0.1418×10^{-2}	-0.2201×10^{-2}	-0.8029×10^{-2}	-0.1234×10^{-1}
0.0080	0.6	0.9369	0.2061×10^{-1}	0.3179×10^{-2}	-0.2782×10^{-2}	-0.1635×10^{-2}	-0.2892×10^{-2}	-0.5846×10^{-2}	-0.2195×10^{-1}
0.0080	0.7	1.000	0.2203×10^{-1}	0.5791×10^{-2}	-0.2717×10^{-2}	-0.1723×10^{-2}	-0.3214×10^{-2}	-0.1595×10^{-1}	-0.3215×10^{-1}
0.0080	0.9	1.147	0.2478×10^{-1}	0.1099×10^{-1}	-0.2029×10^{-2}	-0.1101×10^{-2}	-0.2699×10^{-2}	-0.3892×10^{-1}	-0.4756×10^{-1}
0.0080	1.1	1.279	0.2805×10^{-1}	0.1968×10^{-1}	0.1317×10^{-2}	0.2253×10^{-2}	0.9950×10^{-3}	-0.7773×10^{-1}	-0.4783×10^{-1}
0.0080	1.4	1.249	0.2973×10^{-1}	0.2339×10^{-1}	0.1949×10^{-2}	0.2900×10^{-2}	0.2488×10^{-2}	-0.7522×10^{-1}	-0.6902×10^{-1}
0.0080	1.8	1.238	0.3190×10^{-1}	0.2595×10^{-1}	0.1941×10^{-2}	0.3081×10^{-2}	0.3945×10^{-2}	-0.1063×10^{-1}	-0.7229×10^{-1}
0.0080	2.3	1.466	0.3869×10^{-1}	0.3241×10^{-1}	-0.1085×10^{-2}	0.6731×10^{-3}	0.3252×10^{-2}	-0.2598×10^{-1}	-0.8164×10^{-1}
0.0080	3.2	1.541	0.4115×10^{-1}	0.4040×10^{-1}	0.9930×10^{-3}	0.3465×10^{-2}	0.8001×10^{-2}	0.1762×10^{-1}	-0.4858×10^{-1}
0.0125	0.4	0.6831	0.1783×10^{-1}	0.4480×10^{-2}	0.1098×10^{-2}	0.2393×10^{-2}	0.1623×10^{-2}	-0.2975×10^{-1}	-0.2353×10^{-2}
0.0125	0.4	0.8121	0.1884×10^{-1}	0.4600×10^{-2}	-0.3531×10^{-3}	0.1260×10^{-2}	-0.1647×10^{-3}	-0.3136×10^{-1}	-0.7842×10^{-2}

F_2 Model Systematic Errors									
x	Q^2	F_2	Stat. Err	Charm Mass	Kappa	Alpha	Charm Br	Model	dxf3
0.0125	0.6	0.9350	0.1920×10^{-1}	0.5097×10^{-2}	-0.1711×10^{-2}	0.5180×10^{-4}	-0.2002×10^{-2}	0.3502×10^{-1}	-0.1397×10^{-1}
0.0125	0.7	1.067	0.2003×10^{-1}	0.7135×10^{-2}	-0.2636×10^{-2}	-0.8790×10^{-3}	-0.3397×10^{-2}	-0.4272×10^{-1}	-0.2628×10^{-1}
0.0125	0.9	1.103	0.2121×10^{-1}	0.9288×10^{-2}	-0.3127×10^{-2}	-0.1592×10^{-2}	-0.4109×10^{-2}	-0.3425×10^{-1}	-0.3342×10^{-1}
0.0125	1.1	1.206	0.2249×10^{-1}	0.1344×10^{-1}	-0.3456×10^{-2}	-0.1944×10^{-2}	-0.4266×10^{-2}	-0.5479×10^{-1}	-0.4534×10^{-1}
0.0125	1.4	1.282	0.2333×10^{-1}	0.1890×10^{-1}	-0.2822×10^{-2}	-0.1310×10^{-2}	-0.2994×10^{-2}	-0.4811×10^{-1}	-0.5673×10^{-1}
0.0125	1.8	1.274	0.2476×10^{-1}	0.2366×10^{-1}	0.1420×10^{-3}	0.1710×10^{-2}	0.1321×10^{-2}	-0.2818×10^{-2}	-0.6139×10^{-1}
0.0125	2.3	1.353	0.2813×10^{-1}	0.2840×10^{-1}	0.1792×10^{-2}	0.3636×10^{-2}	0.4578×10^{-2}	0.3415×10^{-2}	-0.6328×10^{-1}
0.0125	3.2	1.470	0.2444×10^{-1}	0.2958×10^{-1}	-0.2074×10^{-2}	0.4330×10^{-3}	0.3572×10^{-2}	0.2096×10^{-1}	-0.4729×10^{-1}
0.0125	5.1	1.656	0.4056×10^{-1}	0.4141×10^{-1}	0.4150×10^{-3}	0.4552×10^{-2}	0.1091×10^{-1}	-0.6240×10^{-1}	-0.4538×10^{-1}
0.0175	0.4	0.7790	0.2493×10^{-1}	0.7832×10^{-2}	0.2194×10^{-2}	0.3727×10^{-2}	0.2450×10^{-2}	-0.6967×10^{-1}	-0.1791×10^{-2}
0.0175	0.4	0.8046	0.2111×10^{-1}	0.8528×10^{-2}	0.1984×10^{-2}	0.3843×10^{-2}	0.1762×10^{-2}	-0.2044×10^{-1}	-0.4991×10^{-2}
0.0175	0.6	0.8966	0.2103×10^{-1}	0.8907×10^{-2}	0.1171×10^{-2}	0.3211×10^{-2}	0.4391×10^{-3}	-0.3466×10^{-1}	-0.9746×10^{-2}
0.0175	0.7	0.9649	0.2074×10^{-1}	0.9234×10^{-2}	-0.2611×10^{-4}	0.2001×10^{-2}	-0.1186×10^{-2}	-0.3927×10^{-1}	-0.1598×10^{-1}
0.0175	0.9	1.135	0.2225×10^{-1}	0.1224×10^{-1}	-0.9520×10^{-3}	0.1171×10^{-2}	-0.2508×10^{-2}	-0.2519×10^{-1}	-0.2578×10^{-1}
0.0175	1.1	1.179	0.2149×10^{-1}	0.1394×10^{-1}	-0.2003×10^{-2}	-0.7403×10^{-4}	-0.3420×10^{-2}	-0.2335×10^{-1}	-0.3659×10^{-1}
0.0175	1.4	1.281	0.2286×10^{-1}	0.1727×10^{-1}	-0.3753×10^{-2}	-0.1765×10^{-2}	-0.4661×10^{-2}	-0.2669×10^{-1}	-0.4801×10^{-1}
0.0175	1.8	1.307	0.2348×10^{-1}	0.1833×10^{-1}	-0.4706×10^{-2}	-0.2699×10^{-2}	-0.4241×10^{-2}	0.1034×10^{-2}	-0.5671×10^{-1}
0.0175	2.3	1.403	0.2557×10^{-1}	0.2364×10^{-1}	-0.2720×10^{-2}	-0.5051×10^{-3}	-0.7350×10^{-3}	-0.6681×10^{-2}	-0.5862×10^{-1}
0.0175	3.2	1.504	0.2104×10^{-1}	0.2950×10^{-1}	-0.2090×10^{-3}	0.2469×10^{-2}	0.4268×10^{-2}	-0.2230×10^{-1}	-0.4761×10^{-1}
0.0175	5.1	1.533	0.2704×10^{-1}	0.2666×10^{-1}	-0.5851×10^{-2}	-0.2137×10^{-2}	0.2382×10^{-2}	-0.2715×10^{-1}	-0.4541×10^{-1}
0.0175	8.2	1.541	0.4907×10^{-1}	0.4202×10^{-1}	0.6979×10^{-2}	0.1198×10^{-1}	0.1858×10^{-1}	0.1178×10^{-1}	-0.4689×10^{-1}
0.0250	0.6	0.9396	0.1815×10^{-1}	0.1373×10^{-1}	0.3835×10^{-2}	0.6005×10^{-2}	0.2165×10^{-2}	-0.1775×10^{-1}	-0.6274×10^{-2}
0.0250	0.7	1.022	0.1701×10^{-1}	0.1502×10^{-1}	0.3542×10^{-2}	0.5850×10^{-2}	0.1331×10^{-2}	-0.3826×10^{-1}	-0.1070×10^{-1}
0.0250	0.9	1.048	0.1602×10^{-1}	0.1444×10^{-1}	0.1781×10^{-2}	0.3984×10^{-2}	-0.5881×10^{-3}	-0.7731×10^{-3}	-0.1648×10^{-1}
0.0250	1.1	1.152	0.1622×10^{-1}	0.1570×10^{-1}	-0.8905×10^{-4}	0.2139×10^{-2}	-0.2487×10^{-2}	-0.3159×10^{-1}	-0.2339×10^{-1}
0.0250	1.4	1.207	0.1600×10^{-1}	0.1737×10^{-1}	-0.1756×10^{-2}	0.4381×10^{-3}	-0.3669×10^{-2}	-0.3992×10^{-1}	-0.3243×10^{-1}

F_2 Model Systematic Errors									
x	Q^2	F_2	Stat. Err	Charm Mass	Kappa	Alpha	Charm Br	Model	dxf3
0.0250	1.8	1.290	0.1626×10^{-1}	0.1708×10^{-1}	-0.4193×10^{-2}	-0.1901×10^{-2}	-0.4817×10^{-2}	-0.3095×10^{-1}	-0.4127×10^{-1}
0.0250	2.3	1.286	0.1623×10^{-1}	0.1662×10^{-1}	-0.5738×10^{-2}	-0.3452×10^{-2}	-0.4994×10^{-2}	0.8596×10^{-2}	-0.4440×10^{-1}
0.0250	3.2	1.418	0.1277×10^{-1}	0.2205×10^{-1}	-0.4214×10^{-2}	-0.1457×10^{-2}	-0.1212×10^{-2}	-0.3359×10^{-2}	-0.4352×10^{-1}
0.0250	5.1	1.530	0.1545×10^{-1}	0.2622×10^{-1}	-0.2197×10^{-2}	0.1369×10^{-2}	0.4042×10^{-2}	0.9278×10^{-2}	-0.4681×10^{-1}
0.0250	8.2	1.585	0.2070×10^{-1}	0.2397×10^{-1}	-0.6702×10^{-2}	-0.1728×10^{-2}	0.3258×10^{-2}	0.1873×10^{-1}	-0.4559×10^{-1}
0.0250	12.9	1.814	0.5016×10^{-1}	0.5446×10^{-1}	0.1732×10^{-1}	0.2497×10^{-1}	0.3255×10^{-1}	-0.1056	-0.4848×10^{-1}
0.0350	0.7	1.054	0.2255×10^{-1}	0.1931×10^{-1}	0.6549×10^{-2}	0.8558×10^{-2}	0.3042×10^{-2}	-0.9923×10^{-2}	-0.6881×10^{-2}
0.0350	0.9	1.060	0.1807×10^{-1}	0.1946×10^{-1}	0.5839×10^{-2}	0.7873×10^{-2}	0.2230×10^{-2}	0.1881×10^{-1}	-0.1084×10^{-1}
0.0350	1.1	1.097	0.1706×10^{-1}	0.1894×10^{-1}	0.3814×10^{-2}	0.5861×10^{-2}	0.2691×10^{-3}	-0.2421×10^{-1}	-0.1586×10^{-1}
0.0350	1.4	1.175	0.1673×10^{-1}	0.1845×10^{-1}	0.9429×10^{-3}	0.3067×10^{-2}	-0.2203×10^{-2}	-0.9595×10^{-2}	-0.2259×10^{-1}
0.0350	1.8	1.255	0.1638×10^{-1}	0.1770×10^{-1}	-0.1469×10^{-2}	0.8141×10^{-3}	-0.3337×10^{-2}	0.1512×10^{-1}	-0.2881×10^{-1}
0.0350	2.3	1.304	0.1654×10^{-1}	0.1734×10^{-1}	-0.3721×10^{-2}	-0.1306×10^{-2}	-0.4240×10^{-2}	-0.2458×10^{-1}	-0.3617×10^{-1}
0.0350	3.2	1.362	0.1184×10^{-1}	0.1729×10^{-1}	-0.5874×10^{-2}	-0.3143×10^{-2}	-0.4247×10^{-2}	0.8698×10^{-2}	-0.3717×10^{-1}
0.0350	5.1	1.496	0.1346×10^{-1}	0.2246×10^{-1}	-0.3666×10^{-2}	-0.1299×10^{-3}	0.9850×10^{-3}	0.3440×10^{-2}	-0.4180×10^{-1}
0.0350	8.2	1.557	0.1658×10^{-1}	0.2236×10^{-1}	-0.3917×10^{-2}	0.6111×10^{-3}	0.3708×10^{-2}	0.2544×10^{-1}	-0.4332×10^{-1}
0.0350	12.9	1.680	0.2453×10^{-1}	0.2587×10^{-1}	-0.3045×10^{-2}	0.3393×10^{-2}	0.8458×10^{-2}	-0.1374×10^{-2}	-0.4449×10^{-1}
0.0350	20.5	1.812	0.7433×10^{-1}	0.6336×10^{-1}	0.3144×10^{-1}	0.4022×10^{-1}	0.4689×10^{-1}	-0.9722×10^{-1}	-0.3840×10^{-1}
0.0500	1.1	1.131	0.1470×10^{-1}	0.2357×10^{-1}	0.8217×10^{-2}	0.9427×10^{-2}	0.3099×10^{-2}	0.9437×10^{-2}	-0.9684×10^{-2}
0.0500	1.4	1.183	0.1323×10^{-1}	0.2286×10^{-1}	0.6057×10^{-2}	0.7485×10^{-2}	0.1384×10^{-2}	-0.3738×10^{-1}	-0.1392×10^{-1}
0.0500	1.8	1.233	0.1269×10^{-1}	0.1958×10^{-1}	0.2059×10^{-2}	0.3798×10^{-2}	-0.1255×10^{-2}	-0.5857×10^{-2}	-0.1921×10^{-1}
0.0500	2.3	1.311	0.1244×10^{-1}	0.1784×10^{-1}	-0.1050×10^{-2}	0.9661×10^{-3}	-0.3083×10^{-2}	0.1252×10^{-1}	-0.2329×10^{-1}
0.0500	3.2	1.389	0.8614×10^{-2}	0.1650×10^{-1}	-0.4789×10^{-2}	-0.2269×10^{-2}	-0.4682×10^{-2}	0.5913×10^{-2}	-0.3047×10^{-1}
0.0500	5.1	1.473	0.8870×10^{-2}	0.1639×10^{-1}	-0.6977×10^{-2}	-0.3625×10^{-2}	-0.4024×10^{-2}	0.4431×10^{-2}	-0.3760×10^{-1}
0.0500	8.2	1.564	0.1018×10^{-1}	0.2107×10^{-1}	-0.2916×10^{-2}	0.1432×10^{-2}	0.2701×10^{-2}	-0.9174×10^{-2}	-0.3793×10^{-1}
0.0500	12.9	1.591	0.1287×10^{-1}	0.1834×10^{-1}	-0.5044×10^{-2}	0.5120×10^{-3}	0.3214×10^{-2}	-0.9089×10^{-2}	-0.3832×10^{-1}
0.0500	20.5	1.653	0.2002×10^{-1}	0.2765×10^{-1}	0.3438×10^{-2}	0.1081×10^{-1}	0.1453×10^{-1}	-0.2875×10^{-1}	-0.3847×10^{-1}

F_2 Model Systematic Errors									
x	Q^2	F_2	Stat. Err	Charm Mass	Kappa	Alpha	Charm Br	Model	dxf3
0.0700	1.4	1.253	0.1791×10^{-1}	0.2506×10^{-1}	0.9245×10^{-2}	0.9125×10^{-2}	0.3009×10^{-2}	-0.2424×10^{-1}	-0.8309×10^{-2}
0.0700	1.8	1.224	0.1434×10^{-1}	0.2327×10^{-1}	0.7379×10^{-2}	0.7951×10^{-2}	0.2816×10^{-2}	0.1174×10^{-1}	-0.1125×10^{-1}
0.0700	2.3	1.262	0.1346×10^{-1}	0.1963×10^{-1}	0.3503×10^{-2}	0.4516×10^{-2}	0.2100×10^{-3}	-0.3136×10^{-2}	-0.1488×10^{-1}
0.0700	3.2	1.334	0.8914×10^{-2}	0.1587×10^{-1}	-0.1774×10^{-2}	-0.9394×10^{-4}	-0.3151×10^{-2}	0.1544×10^{-1}	-0.1907×10^{-1}
0.0700	5.1	1.437	0.8772×10^{-2}	0.1372×10^{-1}	-0.6548×10^{-2}	-0.3768×10^{-2}	-0.5298×10^{-2}	0.4663×10^{-2}	-0.2721×10^{-1}
0.0700	8.2	1.484	0.9142×10^{-2}	0.1473×10^{-1}	-0.6038×10^{-2}	-0.2182×10^{-2}	-0.2336×10^{-2}	0.4632×10^{-2}	-0.3223×10^{-1}
0.0700	12.9	1.496	0.1051×10^{-1}	0.1719×10^{-1}	-0.2201×10^{-2}	0.2518×10^{-2}	0.3403×10^{-2}	-0.2170×10^{-2}	-0.3081×10^{-1}
0.0700	20.5	1.557	0.1375×10^{-1}	0.1427×10^{-1}	-0.5003×10^{-2}	0.1187×10^{-2}	0.2936×10^{-2}	-0.9466×10^{-2}	-0.3197×10^{-1}
0.0700	32.5	1.524	0.2395×10^{-1}	0.3188×10^{-1}	0.1265×10^{-1}	0.2034×10^{-1}	0.2248×10^{-1}	0.2729×10^{-1}	-0.2976×10^{-1}
0.0900	1.8	1.257	0.1888×10^{-1}	0.2219×10^{-1}	0.8047×10^{-2}	0.7189×10^{-2}	0.2813×10^{-2}	-0.1328×10^{-1}	-0.7078×10^{-2}
0.0900	2.3	1.238	0.1464×10^{-1}	0.2008×10^{-1}	0.5884×10^{-2}	0.5751×10^{-2}	0.1978×10^{-2}	0.2455×10^{-1}	-0.9427×10^{-2}
0.0900	3.2	1.315	0.9694×10^{-2}	0.1628×10^{-1}	0.7360×10^{-3}	0.1464×10^{-2}	-0.1556×10^{-2}	0.7341×10^{-2}	-0.1408×10^{-1}
0.0900	5.1	1.388	0.8934×10^{-2}	0.1283×10^{-1}	-0.4409×10^{-2}	-0.2441×10^{-2}	-0.4344×10^{-2}	0.1033×10^{-1}	-0.2013×10^{-1}
0.0900	8.2	1.423	0.8768×10^{-2}	0.1077×10^{-1}	-0.6965×10^{-2}	-0.3813×10^{-2}	-0.4704×10^{-2}	-0.4222×10^{-2}	-0.2459×10^{-1}
0.0900	12.9	1.449	0.9498×10^{-2}	0.1418×10^{-1}	-0.3029×10^{-2}	0.1192×10^{-2}	0.1083×10^{-2}	0.1253×10^{-2}	-0.2602×10^{-1}
0.0900	20.5	1.466	0.1142×10^{-1}	0.1293×10^{-1}	-0.3003×10^{-2}	0.2174×10^{-2}	0.2640×10^{-2}	0.4673×10^{-2}	-0.2634×10^{-1}
0.0900	32.5	1.476	0.1602×10^{-1}	0.1657×10^{-1}	0.7429×10^{-3}	0.7410×10^{-2}	0.8216×10^{-2}	-0.2740×10^{-1}	-0.2712×10^{-1}
0.0900	51.5	1.491	0.3940×10^{-1}	0.5132×10^{-1}	0.3552×10^{-1}	0.4342×10^{-1}	0.4429×10^{-1}	0.3141×10^{-1}	-0.2292×10^{-1}
0.1100	2.3	1.318	0.1889×10^{-1}	0.2104×10^{-1}	0.7322×10^{-2}	0.5972×10^{-2}	0.2865×10^{-2}	-0.4599×10^{-1}	-0.6894×10^{-2}
0.1100	3.2	1.280	0.1028×10^{-1}	0.1651×10^{-1}	0.2971×10^{-2}	0.2758×10^{-2}	0.2680×10^{-3}	0.1813×10^{-1}	-0.9702×10^{-2}
0.1100	5.1	1.333	0.9250×10^{-2}	0.1199×10^{-1}	-0.2648×10^{-2}	-0.1548×10^{-2}	-0.3358×10^{-2}	0.4934×10^{-2}	-0.1430×10^{-1}
0.1100	8.2	1.345	0.8600×10^{-2}	0.8939×10^{-2}	-0.6213×10^{-2}	-0.3800×10^{-2}	-0.4959×10^{-2}	0.7423×10^{-2}	-0.1913×10^{-1}
0.1100	12.9	1.380	0.8981×10^{-2}	0.1042×10^{-1}	-0.4610×10^{-2}	-0.9890×10^{-3}	-0.1652×10^{-2}	-0.1092×10^{-2}	-0.2276×10^{-1}
0.1100	20.5	1.406	0.1030×10^{-1}	0.1286×10^{-1}	-0.1112×10^{-2}	0.3410×10^{-2}	0.3138×10^{-2}	0.2146×10^{-1}	-0.2260×10^{-1}
0.1100	32.5	1.344	0.1273×10^{-1}	0.9876×10^{-2}	-0.2709×10^{-2}	0.2694×10^{-2}	0.2633×10^{-2}	-0.1875×10^{-1}	-0.2197×10^{-1}
0.1100	51.5	1.470	0.2406×10^{-1}	0.3334×10^{-1}	0.1919×10^{-1}	0.2670×10^{-1}	0.2658×10^{-1}	-0.7628×10^{-2}	-0.2304×10^{-1}

F_2 Model Systematic Errors									
x	Q^2	F_2	Stat. Err	Charm Mass	Kappa	Alpha	Charm Br	Model	dxf3
0.1400	3.2	1.221	0.8319×10^{-2}	0.1529×10^{-1}	0.4184×10^{-2}	0.2796×10^{-2}	0.1409×10^{-2}	0.7067×10^{-2}	-0.5714×10^{-2}
0.1400	5.1	1.253	0.6801×10^{-2}	0.1102×10^{-1}	-0.6430×10^{-3}	-0.6500×10^{-3}	-0.1878×10^{-2}	0.5348×10^{-2}	-0.9612×10^{-2}
0.1400	8.2	1.271	0.6174×10^{-2}	0.7728×10^{-2}	-0.4540×10^{-2}	-0.3154×10^{-2}	-0.4201×10^{-2}	0.3367×10^{-2}	-0.1341×10^{-1}
0.1400	12.9	1.291	0.6046×10^{-2}	0.6804×10^{-2}	-0.5358×10^{-2}	-0.2739×10^{-2}	-0.3639×10^{-2}	-0.4520×10^{-3}	-0.1647×10^{-1}
0.1400	20.5	1.275	0.6506×10^{-2}	0.9610×10^{-2}	-0.1517×10^{-2}	0.1975×10^{-2}	0.1203×10^{-2}	0.4138×10^{-2}	-0.1744×10^{-1}
0.1400	32.5	1.232	0.7486×10^{-2}	0.8264×10^{-2}	-0.1319×10^{-2}	0.2683×10^{-2}	0.2032×10^{-2}	0.1804×10^{-2}	-0.1742×10^{-1}
0.1400	51.5	1.210	0.1015×10^{-1}	0.1396×10^{-1}	0.4899×10^{-2}	0.9787×10^{-2}	0.9014×10^{-2}	0.4276×10^{-2}	-0.1748×10^{-1}
0.1400	81.5	1.224	0.2796×10^{-1}	0.4227×10^{-1}	0.3311×10^{-1}	0.3900×10^{-1}	0.3793×10^{-1}	-0.1103×10^{-1}	-0.1667×10^{-1}
0.1800	5.1	1.147	0.7282×10^{-2}	0.1013×10^{-1}	0.1184×10^{-2}	0.2010×10^{-3}	-0.1750×10^{-3}	0.8960×10^{-3}	-0.5314×10^{-2}
0.1800	8.2	1.146	0.6294×10^{-2}	0.6290×10^{-2}	-0.2719×10^{-2}	-0.2440×10^{-2}	-0.2995×10^{-2}	0.2814×10^{-2}	-0.7718×10^{-2}
0.1800	12.9	1.154	0.5862×10^{-2}	0.4422×10^{-2}	-0.4586×10^{-2}	-0.3125×10^{-2}	-0.3861×10^{-2}	0.7113×10^{-2}	-0.1068×10^{-1}
0.1800	20.5	1.141	0.5916×10^{-2}	0.5713×10^{-2}	-0.2613×10^{-2}	-0.2739×10^{-3}	-0.1121×10^{-2}	-0.3434×10^{-2}	-0.1273×10^{-1}
0.1800	32.5	1.112	0.6518×10^{-2}	0.7130×10^{-2}	-0.6199×10^{-4}	0.2726×10^{-2}	0.1864×10^{-2}	0.8501×10^{-2}	-0.1362×10^{-1}
0.1800	51.5	1.070	0.7712×10^{-2}	0.6030×10^{-2}	-0.2230×10^{-3}	0.2999×10^{-2}	0.2068×10^{-2}	-0.9594×10^{-2}	-0.1401×10^{-1}
0.1800	81.5	1.066	0.1313×10^{-1}	0.2355×10^{-1}	0.1724×10^{-1}	0.2129×10^{-1}	0.2006×10^{-1}	0.8091×10^{-2}	-0.1464×10^{-1}
0.2250	5.1	1.050	0.7429×10^{-2}	0.8874×10^{-2}	0.1806×10^{-2}	0.3171×10^{-3}	0.6690×10^{-3}	-0.1712×10^{-1}	-0.2877×10^{-2}
0.2250	8.2	1.023	0.5852×10^{-2}	0.5267×10^{-2}	-0.1485×10^{-2}	-0.1915×10^{-2}	-0.1932×10^{-2}	-0.3638×10^{-2}	-0.4708×10^{-2}
0.2250	12.9	1.006	0.5154×10^{-2}	0.2985×10^{-2}	-0.3498×10^{-2}	-0.2936×10^{-2}	-0.3283×10^{-2}	-0.5403×10^{-2}	-0.6602×10^{-2}
0.2250	20.5	0.9918	0.4946×10^{-2}	0.2823×10^{-2}	-0.3130×10^{-2}	-0.1830×10^{-2}	-0.2413×10^{-2}	-0.5943×10^{-2}	-0.8250×10^{-2}
0.2250	32.5	0.9663	0.5214×10^{-2}	0.5209×10^{-2}	0.1848×10^{-5}	0.1732×10^{-2}	0.1026×10^{-2}	-0.6224×10^{-2}	-0.9139×10^{-2}
0.2250	51.5	0.9268	0.5941×10^{-2}	0.4607×10^{-2}	0.1393×10^{-3}	0.2159×10^{-2}	0.1367×10^{-2}	-0.1133×10^{-2}	-0.1010×10^{-1}
0.2250	81.5	0.9056	0.7786×10^{-2}	0.1042×10^{-1}	0.6358×10^{-2}	0.8717×10^{-2}	0.7776×10^{-2}	-0.7112×10^{-2}	-0.1115×10^{-1}
0.2750	8.2	0.8839	0.5969×10^{-2}	0.4523×10^{-2}	-0.5513×10^{-3}	-0.1231×10^{-2}	-0.9102×10^{-3}	-0.1055×10^{-1}	-0.2452×10^{-2}
0.2750	12.9	0.8564	0.5105×10^{-2}	0.2101×10^{-2}	-0.2545×10^{-2}	-0.2532×10^{-2}	-0.2537×10^{-2}	-0.1394×10^{-1}	-0.3550×10^{-2}
0.2750	20.5	0.8340	0.4674×10^{-2}	0.1302×10^{-2}	-0.2885×10^{-2}	-0.2321×10^{-2}	-0.2581×10^{-2}	-0.3939×10^{-2}	-0.4964×10^{-2}
0.2750	32.5	0.8018	0.4696×10^{-2}	0.2947×10^{-2}	-0.6869×10^{-3}	0.2260×10^{-3}	-0.1960×10^{-3}	-0.3375×10^{-2}	-0.6152×10^{-2}

F_2 Model Systematic Errors									
x	Q^2	F_2	Stat. Err	Charm Mass	Kappa	Alpha	Charm Br	Model	dxf3
0.2750	51.5	0.7833	0.5192×10^{-2}	0.3719×10^{-2}	0.6312×10^{-3}	0.1690×10^{-2}	0.1207×10^{-2}	-0.8943×10^{-2}	-0.6609×10^{-2}
0.2750	81.5	0.7409	0.6127×10^{-2}	0.4687×10^{-2}	0.2001×10^{-2}	0.3270×10^{-2}	0.2675×10^{-2}	-0.4232×10^{-2}	-0.7517×10^{-2}
0.2750	129.2	0.7044	0.1029×10^{-1}	0.1834×10^{-1}	0.1597×10^{-1}	0.1726×10^{-1}	0.1663×10^{-1}	-0.5598×10^{-2}	-0.7337×10^{-2}
0.3500	8.2	0.6881	0.4425×10^{-2}	0.3621×10^{-2}	-0.1145×10^{-3}	-0.6180×10^{-3}	-0.2496×10^{-3}	-0.1389×10^{-1}	-0.8942×10^{-3}
0.3500	12.9	0.6476	0.3462×10^{-2}	0.1494×10^{-2}	-0.1633×10^{-2}	-0.1790×10^{-2}	-0.1633×10^{-2}	-0.8947×10^{-2}	-0.1456×10^{-2}
0.3500	20.5	0.6164	0.3048×10^{-2}	0.4286×10^{-3}	-0.2219×10^{-2}	-0.2109×10^{-2}	-0.2111×10^{-2}	-0.8050×10^{-2}	-0.2087×10^{-2}
0.3500	32.5	0.5928	0.2930×10^{-2}	0.1102×10^{-2}	-0.1122×10^{-2}	-0.8628×10^{-3}	-0.9558×10^{-3}	-0.7322×10^{-2}	-0.2701×10^{-2}
0.3500	51.5	0.5637	0.3068×10^{-2}	0.2402×10^{-2}	0.5627×10^{-3}	0.8779×10^{-3}	0.7437×10^{-3}	-0.6268×10^{-2}	-0.3101×10^{-2}
0.3500	81.5	0.5289	0.3355×10^{-2}	0.2091×10^{-2}	0.5887×10^{-3}	0.9289×10^{-3}	0.7740×10^{-3}	-0.3498×10^{-2}	-0.3565×10^{-2}
0.3500	129.2	0.5140	0.4521×10^{-2}	0.7488×10^{-2}	0.6144×10^{-2}	0.6515×10^{-2}	0.6330×10^{-2}	-0.1277×10^{-1}	-0.3969×10^{-2}
0.4500	12.9	0.4038	0.3091×10^{-2}	0.1199×10^{-2}	-0.8328×10^{-3}	-0.8696×10^{-3}	-0.7848×10^{-3}	-0.1165×10^{-1}	-0.3206×10^{-3}
0.4500	20.5	0.3872	0.2659×10^{-2}	0.2878×10^{-3}	-0.1367×10^{-2}	-0.1355×10^{-2}	-0.1309×10^{-2}	-0.4759×10^{-2}	-0.4833×10^{-3}
0.4500	32.5	0.3570	0.2398×10^{-2}	0.2503×10^{-3}	-0.1047×10^{-2}	-0.1013×10^{-2}	-0.9881×10^{-3}	-0.3893×10^{-2}	-0.7095×10^{-3}
0.4500	51.5	0.3251	0.2341×10^{-2}	0.1070×10^{-2}	0.7552×10^{-4}	0.9400×10^{-4}	0.1187×10^{-3}	-0.4383×10^{-3}	-0.8661×10^{-3}
0.4500	81.5	0.3093	0.2490×10^{-2}	0.1114×10^{-2}	0.3068×10^{-3}	0.3104×10^{-3}	0.3385×10^{-3}	-0.2385×10^{-3}	-0.1029×10^{-2}
0.4500	129.2	0.2880	0.2874×10^{-2}	0.1915×10^{-2}	0.1258×10^{-2}	0.1254×10^{-2}	0.1281×10^{-2}	-0.1867×10^{-2}	-0.1082×10^{-2}
0.4500	204.8	0.2626	0.4906×10^{-2}	0.7335×10^{-2}	0.6755×10^{-2}	0.6753×10^{-2}	0.6770×10^{-2}	0.2569×10^{-2}	-0.1382×10^{-2}
0.5500	12.9	0.2358	0.2589×10^{-2}	0.8402×10^{-3}	-0.5242×10^{-3}	-0.4817×10^{-3}	-0.4741×10^{-3}	0.1566×10^{-2}	-0.6621×10^{-4}
0.5500	20.5	0.2100	0.2074×10^{-2}	0.3306×10^{-3}	-0.7033×10^{-3}	-0.6724×10^{-3}	-0.6636×10^{-3}	-0.6973×10^{-3}	-0.1065×10^{-3}
0.5500	32.5	0.1878	0.1785×10^{-2}	0.1690×10^{-3}	-0.6077×10^{-3}	-0.5944×10^{-3}	-0.5784×10^{-3}	-0.1723×10^{-2}	-0.1421×10^{-3}
0.5500	51.5	0.1737	0.1731×10^{-2}	0.4434×10^{-3}	-0.1555×10^{-3}	-0.1645×10^{-3}	-0.1377×10^{-3}	-0.1310×10^{-2}	-0.1816×10^{-3}
0.5500	81.5	0.1575	0.1765×10^{-2}	0.6625×10^{-3}	0.2026×10^{-3}	0.1776×10^{-3}	0.2135×10^{-3}	0.8335×10^{-3}	-0.2112×10^{-3}
0.5500	129.2	0.1472	0.1936×10^{-2}	0.5839×10^{-3}	0.2245×10^{-3}	0.1927×10^{-3}	0.2283×10^{-3}	-0.2183×10^{-2}	-0.2593×10^{-3}
0.5500	204.8	0.1282	0.2583×10^{-2}	0.2251×10^{-2}	0.1969×10^{-2}	0.1931×10^{-2}	0.1966×10^{-2}	0.1299×10^{-2}	-0.2552×10^{-3}

F_2 Model Systematic Errors									
x	Q^2	F_2	Stat. Err	Charm Mass	Kappa	Alpha	Charm Br	Model	dxf3
0.6500	12.9	0.1125	0.2136×10^{-2}	0.5193×10^{-3}	-0.1816×10^{-3}	-0.1413×10^{-3}	-0.1527×10^{-3}	0.5894×10^{-2}	-0.7197×10^{-5}
0.6500	20.5	0.9555×10^{-1}	0.1321×10^{-2}	0.2601×10^{-3}	-0.3098×10^{-3}	-0.2840×10^{-3}	-0.2898×10^{-3}	0.3025×10^{-2}	-0.1135×10^{-4}
0.6500	32.5	0.8205×10^{-1}	0.1143×10^{-2}	0.1192×10^{-3}	-0.3041×10^{-3}	-0.2944×10^{-3}	-0.2912×10^{-3}	0.6017×10^{-3}	-0.1591×10^{-4}
0.6500	51.5	0.7665×10^{-1}	0.1088×10^{-2}	0.2071×10^{-3}	-0.1236×10^{-3}	-0.1265×10^{-3}	-0.1157×10^{-3}	-0.3140×10^{-3}	-0.2118×10^{-4}
0.6500	81.5	0.6604×10^{-1}	0.1057×10^{-2}	0.2775×10^{-3}	0.4366×10^{-4}	0.3202×10^{-4}	0.4683×10^{-4}	0.1311×10^{-2}	-0.2221×10^{-4}
0.6500	129.2	0.5993×10^{-1}	0.1124×10^{-2}	0.2401×10^{-3}	0.6514×10^{-4}	0.4901×10^{-4}	0.6555×10^{-4}	0.5995×10^{-4}	-0.2389×10^{-4}

Table A.5: F_2 **Cross Section Systematic Errors**

F_2 Cross Section Systematic Errors						
x	Q^2	F_2	Stat. Err	Sigma	Sig Rat	No Smooth
0.0015	0.4	0.5031	0.1956×10^{-1}	0.1021×10^{-1}	0.3096×10^{-2}	0.9866×10^{-3}
0.0015	0.4	0.6239	0.2417×10^{-1}	0.1257×10^{-1}	0.3543×10^{-2}	0.2603×10^{-2}
0.0015	0.6	0.7900	0.3712×10^{-1}	0.1614×10^{-1}	0.5471×10^{-2}	0.4069×10^{-3}
0.0015	0.7	0.8705	0.4505×10^{-1}	0.1816×10^{-1}	0.5672×10^{-2}	0.5553×10^{-2}
0.0015	0.9	1.010	0.7202×10^{-1}	0.2117×10^{-1}	0.6710×10^{-2}	0.6316×10^{-2}
0.0045	0.4	0.6682	0.1728×10^{-1}	0.1336×10^{-1}	0.4040×10^{-2}	-0.2195$\times10^{-2}$
0.0045	0.4	0.7835	0.2133×10^{-1}	0.1574×10^{-1}	0.4722×10^{-2}	-0.1571$\times10^{-2}$
0.0045	0.6	0.8825	0.2386×10^{-1}	0.1792×10^{-1}	0.4921×10^{-2}	0.9900×10^{-3}
0.0045	0.7	1.058	0.2960×10^{-1}	0.2182×10^{-1}	0.6501×10^{-2}	0.1284×10^{-2}
0.0045	0.9	1.269	0.3679×10^{-1}	0.2585×10^{-1}	0.7816×10^{-2}	0.5485×10^{-2}
0.0045	1.1	1.220	0.4038×10^{-1}	0.2499×10^{-1}	0.7535×10^{-2}	-0.4389$\times10^{-3}$
0.0045	1.4	1.389	0.4729×10^{-1}	0.2829×10^{-1}	0.8941×10^{-2}	0.4356×10^{-2}
0.0045	1.8	1.393	0.6578×10^{-1}	0.2855×10^{-1}	0.8733×10^{-2}	0.4340×10^{-2}
0.0045	2.3	1.681	0.1247	0.3450×10^{-1}	0.1190×10^{-1}	0.2164×10^{-1}
0.0080	0.4	0.7362	0.1805×10^{-1}	0.1465×10^{-1}	0.4621×10^{-2}	0.6089×10^{-3}
0.0080	0.4	0.8080	0.1914×10^{-1}	0.1662×10^{-1}	0.4896×10^{-2}	-0.1144$\times10^{-2}$
0.0080	0.6	0.9369	0.2061×10^{-1}	0.1936×10^{-1}	0.5493×10^{-2}	-0.2382$\times10^{-2}$
0.0080	0.7	1.000	0.2203×10^{-1}	0.2077×10^{-1}	0.5616×10^{-2}	-0.2058$\times10^{-2}$
0.0080	0.9	1.147	0.2478×10^{-1}	0.2397×10^{-1}	0.6616×10^{-2}	-0.2012$\times10^{-2}$
0.0080	1.1	1.279	0.2805×10^{-1}	0.2627×10^{-1}	0.7517×10^{-2}	0.1727×10^{-2}
0.0080	1.4	1.249	0.2973×10^{-1}	0.2575×10^{-1}	0.7143×10^{-2}	0.2362×10^{-2}
0.0080	1.8	1.238	0.3190×10^{-1}	0.2607×10^{-1}	0.6700×10^{-2}	0.3907×10^{-2}
0.0080	2.3	1.466	0.3869×10^{-1}	0.3088×10^{-1}	0.1011×10^{-1}	0.3777×10^{-2}
0.0080	3.2	1.541	0.4115×10^{-1}	0.3155×10^{-1}	0.9420×10^{-2}	0.6740×10^{-2}
0.0125	0.4	0.6831	0.1783×10^{-1}	0.1403×10^{-1}	0.3909×10^{-2}	0.2508×10^{-2}
0.0125	0.4	0.8121	0.1884×10^{-1}	0.1673×10^{-1}	0.4924×10^{-2}	0.1853×10^{-2}

F_2 Cross Section Systematic Errors						
x	Q^2	F_2	Stat. Err	Sigma	Sig Rat	No Smooth
0.0125	0.6	0.9350	0.1920×10^{-1}	0.1949×10^{-1}	0.5446×10^{-2}	-0.5943×10^{-3}
0.0125	0.7	1.067	0.2003×10^{-1}	0.2217×10^{-1}	0.6606×10^{-2}	-0.2454×10^{-2}
0.0125	0.9	1.103	0.2121×10^{-1}	0.2294×10^{-1}	0.6643×10^{-2}	-0.2154×10^{-2}
0.0125	1.1	1.206	0.2249×10^{-1}	0.2526×10^{-1}	0.6944×10^{-2}	-0.3105×10^{-2}
0.0125	1.4	1.282	0.2333×10^{-1}	0.2697×10^{-1}	0.7359×10^{-2}	-0.1944×10^{-2}
0.0125	1.8	1.274	0.2476×10^{-1}	0.2675×10^{-1}	0.7214×10^{-2}	0.1286×10^{-2}
0.0125	2.3	1.353	0.2813×10^{-1}	0.2833×10^{-1}	0.7927×10^{-2}	0.3875×10^{-2}
0.0125	3.2	1.470	0.2444×10^{-1}	0.3087×10^{-1}	0.8768×10^{-2}	0.3624×10^{-2}
0.0125	5.1	1.656	0.4056×10^{-1}	0.3458×10^{-1}	0.9819×10^{-2}	0.1384×10^{-1}
0.0175	0.4	0.7790	0.2493×10^{-1}	0.1533×10^{-1}	0.4988×10^{-2}	0.4118×10^{-2}
0.0175	0.4	0.8046	0.2111×10^{-1}	0.1681×10^{-1}	0.5106×10^{-2}	0.3977×10^{-2}
0.0175	0.6	0.8966	0.2103×10^{-1}	0.1864×10^{-1}	0.5396×10^{-2}	0.1558×10^{-2}
0.0175	0.7	0.9649	0.2074×10^{-1}	0.2027×10^{-1}	0.5492×10^{-2}	0.7229×10^{-3}
0.0175	0.9	1.135	0.2225×10^{-1}	0.2400×10^{-1}	0.6869×10^{-2}	-0.1400×10^{-3}
0.0175	1.1	1.179	0.2149×10^{-1}	0.2447×10^{-1}	0.6631×10^{-2}	-0.2414×10^{-2}
0.0175	1.4	1.281	0.2286×10^{-1}	0.2710×10^{-1}	0.7855×10^{-2}	-0.2831×10^{-2}
0.0175	1.8	1.307	0.2348×10^{-1}	0.2758×10^{-1}	0.7424×10^{-2}	-0.2717×10^{-2}
0.0175	2.3	1.403	0.2557×10^{-1}	0.2929×10^{-1}	0.8135×10^{-2}	-0.2610×10^{-2}
0.0175	3.2	1.504	0.2104×10^{-1}	0.3153×10^{-1}	0.8454×10^{-2}	0.4787×10^{-2}
0.0175	5.1	1.533	0.2704×10^{-1}	0.3198×10^{-1}	0.8711×10^{-2}	0.2918×10^{-2}
0.0175	8.2	1.541	0.4907×10^{-1}	0.3188×10^{-1}	0.8423×10^{-2}	0.1451×10^{-1}
0.0250	0.6	0.9396	0.1815×10^{-1}	0.1992×10^{-1}	0.6059×10^{-2}	0.4375×10^{-2}
0.0250	0.7	1.022	0.1701×10^{-1}	0.2174×10^{-1}	0.6505×10^{-2}	0.3629×10^{-2}
0.0250	0.9	1.048	0.1602×10^{-1}	0.2236×10^{-1}	0.6204×10^{-2}	0.9899×10^{-3}
0.0250	1.1	1.152	0.1622×10^{-1}	0.2454×10^{-1}	0.6770×10^{-2}	-0.5690×10^{-3}
0.0250	1.4	1.207	0.1600×10^{-1}	0.2574×10^{-1}	0.7437×10^{-2}	-0.1372×10^{-2}

F_2 Cross Section Systematic Errors						
x	Q^2	F_2	Stat. Err	Sigma	Sig Rat	No Smooth
0.0250	1.8	1.290	0.1626×10^{-1}	0.2736×10^{-1}	0.7284×10^{-2}	-0.2756×10^{-2}
0.0250	2.3	1.286	0.1623×10^{-1}	0.2702×10^{-1}	0.7095×10^{-2}	-0.3475×10^{-2}
0.0250	3.2	1.418	0.1277×10^{-1}	0.2984×10^{-1}	0.7630×10^{-2}	-0.5389×10^{-3}
0.0250	5.1	1.530	0.1545×10^{-1}	0.3189×10^{-1}	0.8076×10^{-2}	0.3228×10^{-2}
0.0250	8.2	1.585	0.2070×10^{-1}	0.3309×10^{-1}	0.8216×10^{-2}	0.4795×10^{-2}
0.0250	12.9	1.814	0.5016×10^{-1}	0.3787×10^{-1}	0.1057×10^{-1}	0.3133×10^{-1}
0.0350	0.7	1.054	0.2255×10^{-1}	0.2269×10^{-1}	0.6757×10^{-2}	0.4575×10^{-2}
0.0350	0.9	1.060	0.1807×10^{-1}	0.2272×10^{-1}	0.6620×10^{-2}	0.4157×10^{-2}
0.0350	1.1	1.097	0.1706×10^{-1}	0.2363×10^{-1}	0.6487×10^{-2}	0.2414×10^{-2}
0.0350	1.4	1.175	0.1673×10^{-1}	0.2520×10^{-1}	0.7008×10^{-2}	-0.2760×10^{-3}
0.0350	1.8	1.255	0.1638×10^{-1}	0.2674×10^{-1}	0.6957×10^{-2}	-0.1469×10^{-2}
0.0350	2.3	1.304	0.1654×10^{-1}	0.2767×10^{-1}	0.7243×10^{-2}	-0.2819×10^{-2}
0.0350	3.2	1.362	0.1184×10^{-1}	0.2879×10^{-1}	0.7136×10^{-2}	-0.3427×10^{-2}
0.0350	5.1	1.496	0.1346×10^{-1}	0.3132×10^{-1}	0.7647×10^{-2}	0.1345×10^{-2}
0.0350	8.2	1.557	0.1658×10^{-1}	0.3259×10^{-1}	0.7879×10^{-2}	0.3763×10^{-2}
0.0350	12.9	1.680	0.2453×10^{-1}	0.3474×10^{-1}	0.8283×10^{-2}	0.1002×10^{-1}
0.0350	20.5	1.812	0.7433×10^{-1}	0.3756×10^{-1}	0.9230×10^{-2}	0.5210×10^{-1}
0.0500	1.1	1.131	0.1470×10^{-1}	0.2462×10^{-1}	0.7338×10^{-2}	0.5437×10^{-2}
0.0500	1.4	1.183	0.1323×10^{-1}	0.2565×10^{-1}	0.7286×10^{-2}	0.3015×10^{-2}
0.0500	1.8	1.233	0.1269×10^{-1}	0.2646×10^{-1}	0.7435×10^{-2}	0.1265×10^{-2}
0.0500	2.3	1.311	0.1244×10^{-1}	0.2806×10^{-1}	0.7351×10^{-2}	-0.5900×10^{-3}
0.0500	3.2	1.389	0.8614×10^{-2}	0.2940×10^{-1}	0.7450×10^{-2}	-0.2701×10^{-2}
0.0500	5.1	1.473	0.8870×10^{-2}	0.3089×10^{-1}	0.7266×10^{-2}	-0.2671×10^{-2}
0.0500	8.2	1.564	0.1018×10^{-1}	0.3265×10^{-1}	0.7376×10^{-2}	0.2542×10^{-2}
0.0500	12.9	1.591	0.1287×10^{-1}	0.3318×10^{-1}	0.7588×10^{-2}	0.3144×10^{-2}
0.0500	20.5	1.653	0.2002×10^{-1}	0.3434×10^{-1}	0.7287×10^{-2}	0.1592×10^{-1}

F_2 Cross Section Systematic Errors						
x	Q^2	F_2	Stat. Err	Sigma	Sig Rat	No Smooth
0.0700	1.4	1.253	0.1791×10^{-1}	0.2736×10^{-1}	0.7905×10^{-2}	0.5789×10^{-2}
0.0700	1.8	1.224	0.1434×10^{-1}	0.2650×10^{-1}	0.7817×10^{-2}	0.4272×10^{-2}
0.0700	2.3	1.262	0.1346×10^{-1}	0.2707×10^{-1}	0.7358×10^{-2}	0.2177×10^{-2}
0.0700	3.2	1.334	0.8914×10^{-2}	0.2834×10^{-1}	0.7166×10^{-2}	-0.1366×10^{-2}
0.0700	5.1	1.437	0.8772×10^{-2}	0.3030×10^{-1}	0.7102×10^{-2}	-0.3226×10^{-2}
0.0700	8.2	1.484	0.9142×10^{-2}	0.3118×10^{-1}	0.6710×10^{-2}	-0.1932×10^{-2}
0.0700	12.9	1.496	0.1051×10^{-1}	0.3127×10^{-1}	0.6467×10^{-2}	0.3821×10^{-2}
0.0700	20.5	1.557	0.1375×10^{-1}	0.3236×10^{-1}	0.6707×10^{-2}	0.3167×10^{-2}
0.0700	32.5	1.524	0.2395×10^{-1}	0.3167×10^{-1}	0.6324×10^{-2}	0.2163×10^{-1}
0.0900	1.8	1.257	0.1888×10^{-1}	0.2723×10^{-1}	0.7649×10^{-2}	0.5895×10^{-2}
0.0900	2.3	1.238	0.1464×10^{-1}	0.2665×10^{-1}	0.7311×10^{-2}	0.3977×10^{-2}
0.0900	3.2	1.315	0.9694×10^{-2}	0.2811×10^{-1}	0.7542×10^{-2}	0.4640×10^{-3}
0.0900	5.1	1.388	0.8934×10^{-2}	0.2931×10^{-1}	0.6857×10^{-2}	-0.1989×10^{-2}
0.0900	8.2	1.423	0.8768×10^{-2}	0.2982×10^{-1}	0.6186×10^{-2}	-0.3356×10^{-2}
0.0900	12.9	1.449	0.9498×10^{-2}	0.3025×10^{-1}	0.5883×10^{-2}	0.1654×10^{-2}
0.0900	20.5	1.466	0.1142×10^{-1}	0.3050×10^{-1}	0.5758×10^{-2}	0.3388×10^{-2}
0.0900	32.5	1.476	0.1602×10^{-1}	0.3069×10^{-1}	0.5394×10^{-2}	0.8230×10^{-2}
0.0900	51.5	1.491	0.3940×10^{-1}	0.3101×10^{-1}	0.4952×10^{-2}	0.4221×10^{-1}
0.1100	2.3	1.318	0.1889×10^{-1}	0.2839×10^{-1}	0.8601×10^{-2}	0.4866×10^{-2}
0.1100	3.2	1.280	0.1028×10^{-1}	0.2737×10^{-1}	0.7497×10^{-2}	0.2752×10^{-2}
0.1100	5.1	1.333	0.9250×10^{-2}	0.2821×10^{-1}	0.6849×10^{-2}	-0.1059×10^{-2}
0.1100	8.2	1.345	0.8600×10^{-2}	0.2829×10^{-1}	0.5871×10^{-2}	-0.3547×10^{-2}
0.1100	12.9	1.380	0.8981×10^{-2}	0.2886×10^{-1}	0.5449×10^{-2}	-0.1352×10^{-2}
0.1100	20.5	1.406	0.1030×10^{-1}	0.2929×10^{-1}	0.5317×10^{-2}	0.3607×10^{-2}
0.1100	32.5	1.344	0.1273×10^{-1}	0.2800×10^{-1}	0.4693×10^{-2}	0.3478×10^{-2}
0.1100	51.5	1.470	0.2406×10^{-1}	0.3053×10^{-1}	0.5037×10^{-2}	0.2656×10^{-1}

F_2 Cross Section Systematic Errors						
x	Q^2	F_2	Stat. Err	Sigma	Sig Rat	No Smooth
0.1400	3.2	1.221	0.8319×10^{-2}	0.2612×10^{-1}	0.7195×10^{-2}	0.3513×10^{-2}
0.1400	5.1	1.253	0.6801×10^{-2}	0.2647×10^{-1}	0.6518×10^{-2}	0.3890×10^{-3}
0.1400	8.2	1.271	0.6174×10^{-2}	0.2673×10^{-1}	0.5661×10^{-2}	-0.2300×10^{-2}
0.1400	12.9	1.291	0.6046×10^{-2}	0.2706×10^{-1}	0.4901×10^{-2}	-0.2334×10^{-2}
0.1400	20.5	1.275	0.6506×10^{-2}	0.2659×10^{-1}	0.4413×10^{-2}	0.1313×10^{-2}
0.1400	32.5	1.232	0.7486×10^{-2}	0.2563×10^{-1}	0.3836×10^{-2}	0.2418×10^{-2}
0.1400	51.5	1.210	0.1015×10^{-1}	0.2516×10^{-1}	0.3165×10^{-2}	0.9165×10^{-2}
0.1400	81.5	1.224	0.2796×10^{-1}	0.2545×10^{-1}	0.3008×10^{-2}	0.3679×10^{-1}
0.1800	5.1	1.147	0.7282×10^{-2}	0.2433×10^{-1}	0.6213×10^{-2}	0.1974×10^{-2}
0.1800	8.2	1.146	0.6294×10^{-2}	0.2406×10^{-1}	0.5293×10^{-2}	-0.1263×10^{-2}
0.1800	12.9	1.154	0.5862×10^{-2}	0.2416×10^{-1}	0.4394×10^{-2}	-0.2423×10^{-2}
0.1800	20.5	1.141	0.5916×10^{-2}	0.2380×10^{-1}	0.3658×10^{-2}	-0.5629×10^{-3}
0.1800	32.5	1.112	0.6518×10^{-2}	0.2313×10^{-1}	0.3125×10^{-2}	0.2364×10^{-2}
0.1800	51.5	1.070	0.7712×10^{-2}	0.2213×10^{-1}	0.2486×10^{-2}	0.2898×10^{-2}
0.1800	81.5	1.066	0.1313×10^{-1}	0.2213×10^{-1}	0.2214×10^{-2}	0.1949×10^{-1}
0.2250	5.1	1.050	0.7429×10^{-2}	0.2223×10^{-1}	0.6002×10^{-2}	0.3110×10^{-2}
0.2250	8.2	1.023	0.5852×10^{-2}	0.2153×10^{-1}	0.5112×10^{-2}	-0.1190×10^{-3}
0.2250	12.9	1.006	0.5154×10^{-2}	0.2101×10^{-1}	0.3931×10^{-2}	-0.1896×10^{-2}
0.2250	20.5	0.9918	0.4946×10^{-2}	0.2069×10^{-1}	0.3054×10^{-2}	-0.1499×10^{-2}
0.2250	32.5	0.9663	0.5214×10^{-2}	0.2012×10^{-1}	0.2524×10^{-2}	0.1273×10^{-2}
0.2250	51.5	0.9268	0.5941×10^{-2}	0.1922×10^{-1}	0.2228×10^{-2}	0.2033×10^{-2}
0.2250	81.5	0.9056	0.7786×10^{-2}	0.1879×10^{-1}	0.1525×10^{-2}	0.7985×10^{-2}
0.2750	8.2	0.8839	0.5969×10^{-2}	0.1858×10^{-1}	0.4519×10^{-2}	0.6258×10^{-3}
0.2750	12.9	0.8564	0.5105×10^{-2}	0.1794×10^{-1}	0.3551×10^{-2}	-0.1501×10^{-2}
0.2750	20.5	0.8340	0.4674×10^{-2}	0.1738×10^{-1}	0.2649×10^{-2}	-0.1666×10^{-2}
0.2750	32.5	0.8018	0.4696×10^{-2}	0.1665×10^{-1}	0.2056×10^{-2}	0.1509×10^{-3}

F_2 Cross Section Systematic Errors						
x	Q^2	F_2	Stat. Err	Sigma	Sig Rat	No Smooth
0.2750	51.5	0.7833	0.5192×10^{-2}	0.1626×10^{-1}	0.1718×10^{-2}	0.1660×10^{-2}
0.2750	81.5	0.7409	0.6127×10^{-2}	0.1538×10^{-1}	0.1370×10^{-2}	0.3112×10^{-2}
0.2750	129.2	0.7044	0.1029×10^{-1}	0.1446×10^{-1}	0.7184×10^{-3}	0.1652×10^{-1}
0.3500	8.2	0.6881	0.4425×10^{-2}	0.1445×10^{-1}	0.3743×10^{-2}	0.9209×10^{-3}
0.3500	12.9	0.6476	0.3462×10^{-2}	0.1356×10^{-1}	0.2899×10^{-2}	-0.5078×10^{-3}
0.3500	20.5	0.6164	0.3048×10^{-2}	0.1286×10^{-1}	0.2110×10^{-2}	-0.1327×10^{-2}
0.3500	32.5	0.5928	0.2930×10^{-2}	0.1233×10^{-1}	0.1513×10^{-2}	-0.5092×10^{-3}
0.3500	51.5	0.5637	0.3068×10^{-2}	0.1171×10^{-1}	0.1153×10^{-2}	0.9462×10^{-3}
0.3500	81.5	0.5289	0.3355×10^{-2}	0.1095×10^{-1}	0.9192×10^{-3}	0.1159×10^{-2}
0.3500	129.2	0.5140	0.4521×10^{-2}	0.1064×10^{-1}	0.5271×10^{-3}	0.6279×10^{-2}
0.4500	12.9	0.4038	0.3091×10^{-2}	0.8434×10^{-2}	0.1979×10^{-2}	-0.1311×10^{-3}
0.4500	20.5	0.3872	0.2659×10^{-2}	0.8087×10^{-2}	0.1520×10^{-2}	-0.7020×10^{-3}
0.4500	32.5	0.3570	0.2398×10^{-2}	0.7441×10^{-2}	0.1004×10^{-2}	-0.6757×10^{-3}
0.4500	51.5	0.3251	0.2341×10^{-2}	0.6755×10^{-2}	0.6502×10^{-3}	0.1908×10^{-3}
0.4500	81.5	0.3093	0.2490×10^{-2}	0.6412×10^{-2}	0.4908×10^{-3}	0.6437×10^{-3}
0.4500	129.2	0.2880	0.2874×10^{-2}	0.5973×10^{-2}	0.3256×10^{-3}	0.1453×10^{-2}
0.4500	204.8	0.2626	0.4906×10^{-2}	0.5389×10^{-2}	0.1499×10^{-3}	0.6833×10^{-2}
0.5500	12.9	0.2358	0.2589×10^{-2}	0.4947×10^{-2}	0.1210×10^{-2}	-0.1940×10^{-4}
0.5500	20.5	0.2100	0.2074×10^{-2}	0.4395×10^{-2}	0.9385×10^{-3}	-0.3546×10^{-3}
0.5500	32.5	0.1878	0.1785×10^{-2}	0.3910×10^{-2}	0.5900×10^{-3}	-0.3856×10^{-3}
0.5500	51.5	0.1737	0.1731×10^{-2}	0.3619×10^{-2}	0.3842×10^{-3}	-0.3280×10^{-4}
0.5500	81.5	0.1575	0.1765×10^{-2}	0.3262×10^{-2}	0.2703×10^{-3}	0.2405×10^{-3}
0.5500	129.2	0.1472	0.1936×10^{-2}	0.3038×10^{-2}	0.2180×10^{-3}	0.3204×10^{-3}
0.5500	204.8	0.1282	0.2583×10^{-2}	0.2647×10^{-2}	0.7430×10^{-4}	0.2045×10^{-2}

F_2 Cross Section Systematic Errors						
x	Q^2	F_2	Stat. Err	Sigma	Sig Rat	No Smooth
0.6500	12.9	0.1125	0.2136×10^{-2}	0.2364×10^{-2}	0.6496×10^{-3}	0.6431×10^{-4}
0.6500	20.5	0.9555×10^{-1}	0.1321×10^{-2}	0.2004×10^{-2}	0.4138×10^{-3}	-0.9697×10^{-4}
0.6500	32.5	0.8205×10^{-1}	0.1143×10^{-2}	0.1718×10^{-2}	0.2669×10^{-3}	-0.1832×10^{-3}
0.6500	51.5	0.7665×10^{-1}	0.1088×10^{-2}	0.1602×10^{-2}	0.1663×10^{-3}	-0.5674×10^{-4}
0.6500	81.5	0.6604×10^{-1}	0.1057×10^{-2}	0.1370×10^{-2}	0.1101×10^{-3}	0.7880×10^{-4}
0.6500	129.2	0.5993×10^{-1}	0.1124×10^{-2}	0.1246×10^{-2}	0.8938×10^{-4}	0.1333×10^{-3}

F_2 Cross Section Systematic Errors cont.							
x	Q^2	F_2	Stat. Err	R	R_{minus}	R_{plus}	Radcorr
0.0015	0.4	0.5031	0.1956×10^{-1}	0.2895×10^{-2}	0.1676×10^{-2}	0.4114×10^{-2}	-0.4829×10^{-1}
0.0015	0.4	0.6239	0.2417×10^{-1}	0.6447×10^{-2}	0.4853×10^{-2}	0.8041×10^{-2}	-0.5814×10^{-1}
0.0015	0.6	0.7900	0.3712×10^{-1}	0.1428×10^{-1}	0.1630×10^{-1}	0.1226×10^{-1}	-0.7562×10^{-1}
0.0015	0.7	0.8705	0.4505×10^{-1}	0.2810×10^{-1}	0.3524×10^{-1}	0.2096×10^{-1}	-0.8327×10^{-1}
0.0015	0.9	1.010	0.7202×10^{-1}	0.3734×10^{-1}	0.4413×10^{-1}	0.3055×10^{-1}	-0.8748×10^{-1}
0.0045	0.4	0.6682	0.1728×10^{-1}	0.2342×10^{-2}	0.5189×10^{-2}	-0.5045×10^{-3}	-0.2127×10^{-1}
0.0045	0.4	0.7835	0.2133×10^{-1}	0.5459×10^{-2}	0.8516×10^{-2}	0.2402×10^{-2}	-0.2235×10^{-1}
0.0045	0.6	0.8825	0.2386×10^{-1}	0.9373×10^{-2}	0.1086×10^{-1}	0.7883×10^{-2}	-0.1891×10^{-1}
0.0045	0.7	1.058	0.2960×10^{-1}	0.2658×10^{-1}	0.3747×10^{-1}	0.1568×10^{-1}	-0.2105×10^{-1}
0.0045	0.9	1.269	0.3679×10^{-1}	0.3559×10^{-1}	0.4913×10^{-1}	0.2205×10^{-1}	-0.2187×10^{-1}
0.0045	1.1	1.220	0.4038×10^{-1}	0.3963×10^{-1}	0.5939×10^{-1}	0.1987×10^{-1}	-0.7033×10^{-2}
0.0045	1.4	1.389	0.4729×10^{-1}	0.7664×10^{-1}	0.1241	0.2921×10^{-1}	0.5189×10^{-3}
0.0045	1.8	1.393	0.6578×10^{-1}	0.3482×10^{-1}	0.3344×10^{-1}	0.3620×10^{-1}	0.1802×10^{-1}
0.0045	2.3	1.681	0.1247	0.5715×10^{-1}	0.6079×10^{-1}	0.5350×10^{-1}	0.3963×10^{-1}
0.0080	0.4	0.7362	0.1805×10^{-1}	0.1135×10^{-2}	0.2591×10^{-2}	-0.3220×10^{-3}	-0.1531×10^{-1}
0.0080	0.4	0.8080	0.1914×10^{-1}	0.3257×10^{-2}	0.5507×10^{-2}	0.1006×10^{-2}	-0.1265×10^{-1}
0.0080	0.6	0.9369	0.2061×10^{-1}	0.6729×10^{-2}	0.9905×10^{-2}	0.3553×10^{-2}	-0.1202×10^{-1}
0.0080	0.7	1.000	0.2203×10^{-1}	0.1676×10^{-1}	0.2717×10^{-1}	0.6356×10^{-2}	-0.1009×10^{-1}
0.0080	0.9	1.147	0.2478×10^{-1}	0.2831×10^{-1}	0.4564×10^{-1}	0.1098×10^{-1}	-0.7741×10^{-2}
0.0080	1.1	1.279	0.2805×10^{-1}	0.3297×10^{-1}	0.4801×10^{-1}	0.1792×10^{-1}	-0.3454×10^{-2}
0.0080	1.4	1.249	0.2973×10^{-1}	0.3474×10^{-1}	0.4963×10^{-1}	0.1985×10^{-1}	0.4537×10^{-2}
0.0080	1.8	1.238	0.3190×10^{-1}	0.3466×10^{-1}	0.4785×10^{-1}	0.2146×10^{-1}	0.9359×10^{-2}
0.0080	2.3	1.466	0.3869×10^{-1}	0.3838×10^{-1}	0.5061×10^{-1}	0.2615×10^{-1}	0.1544×10^{-1}
0.0080	3.2	1.541	0.4115×10^{-1}	0.3547×10^{-1}	0.3521×10^{-1}	0.3572×10^{-1}	0.2564×10^{-1}
0.0125	0.4	0.6831	0.1783×10^{-1}	0.3736×10^{-3}	-0.1412×10^{-2}	0.2159×10^{-2}	-0.8060×10^{-2}
0.0125	0.4	0.8121	0.1884×10^{-1}	0.1472×10^{-2}	0.1529×10^{-2}	0.1415×10^{-2}	-0.7563×10^{-2}

F_2 Cross Section Systematic Errors cont.							
x	Q^2	F_2	Stat. Err	R	R_{minus}	R_{plus}	Radcorr
0.0125	0.6	0.9350	0.1920×10^{-1}	0.3620×10^{-2}	0.5679×10^{-2}	0.1561×10^{-2}	-0.6408×10^{-2}
0.0125	0.7	1.067	0.2003×10^{-1}	0.1655×10^{-1}	0.2984×10^{-1}	0.3247×10^{-2}	-0.6755×10^{-2}
0.0125	0.9	1.103	0.2121×10^{-1}	0.2065×10^{-1}	0.3598×10^{-1}	0.5327×10^{-2}	-0.6480×10^{-2}
0.0125	1.1	1.206	0.2249×10^{-1}	0.2829×10^{-1}	0.4805×10^{-1}	0.8522×10^{-2}	-0.5748×10^{-2}
0.0125	1.4	1.282	0.2333×10^{-1}	0.3132×10^{-1}	0.4999×10^{-1}	0.1264×10^{-1}	-0.1542×10^{-2}
0.0125	1.8	1.274	0.2476×10^{-1}	0.3172×10^{-1}	0.4602×10^{-1}	0.1742×10^{-1}	0.4035×10^{-2}
0.0125	2.3	1.353	0.2813×10^{-1}	0.3031×10^{-1}	0.3890×10^{-1}	0.2171×10^{-1}	0.9133×10^{-2}
0.0125	3.2	1.470	0.2444×10^{-1}	0.2562×10^{-1}	0.2821×10^{-1}	0.2302×10^{-1}	0.1691×10^{-1}
0.0125	5.1	1.656	0.4056×10^{-1}	0.2907×10^{-1}	0.2023×10^{-1}	0.3790×10^{-1}	0.2806×10^{-1}
0.0175	0.4	0.7790	0.2493×10^{-1}	0.3152×10^{-3}	-0.2367×10^{-2}	0.2998×10^{-2}	-0.1005×10^{-1}
0.0175	0.4	0.8046	0.2111×10^{-1}	0.9378×10^{-3}	-0.1018×10^{-2}	0.2894×10^{-2}	-0.9352×10^{-2}
0.0175	0.6	0.8966	0.2103×10^{-1}	0.2019×10^{-2}	0.1539×10^{-2}	0.2500×10^{-2}	-0.8940×10^{-2}
0.0175	0.7	0.9649	0.2074×10^{-1}	0.6768×10^{-2}	0.1118×10^{-1}	0.2352×10^{-2}	-0.7614×10^{-2}
0.0175	0.9	1.135	0.2225×10^{-1}	0.1552×10^{-1}	0.2689×10^{-1}	0.4145×10^{-2}	-0.8555×10^{-2}
0.0175	1.1	1.179	0.2149×10^{-1}	0.2173×10^{-1}	0.3751×10^{-1}	0.5947×10^{-2}	-0.7737×10^{-2}
0.0175	1.4	1.281	0.2286×10^{-1}	0.2571×10^{-1}	0.4349×10^{-1}	0.7940×10^{-2}	-0.5691×10^{-2}
0.0175	1.8	1.307	0.2348×10^{-1}	0.2781×10^{-1}	0.4574×10^{-1}	0.9887×10^{-2}	-0.1427×10^{-2}
0.0175	2.3	1.403	0.2557×10^{-1}	0.2800×10^{-1}	0.4042×10^{-1}	0.1557×10^{-1}	0.3392×10^{-2}
0.0175	3.2	1.504	0.2104×10^{-1}	0.2318×10^{-1}	0.2461×10^{-1}	0.2176×10^{-1}	0.9889×10^{-2}
0.0175	5.1	1.533	0.2704×10^{-1}	0.2086×10^{-1}	0.2023×10^{-1}	0.2149×10^{-1}	0.1646×10^{-1}
0.0175	8.2	1.541	0.4907×10^{-1}	0.2576×10^{-1}	0.9051×10^{-2}	0.4247×10^{-1}	0.2184×10^{-1}
0.0250	0.6	0.9396	0.1815×10^{-1}	0.2595×10^{-2}	0.1284×10^{-2}	0.3907×10^{-2}	-0.1394×10^{-1}
0.0250	0.7	1.022	0.1701×10^{-1}	0.6476×10^{-2}	0.8998×10^{-2}	0.3954×10^{-2}	-0.1263×10^{-1}
0.0250	0.9	1.048	0.1602×10^{-1}	0.9878×10^{-2}	0.1661×10^{-1}	0.3143×10^{-2}	-0.1069×10^{-1}
0.0250	1.1	1.152	0.1622×10^{-1}	0.1568×10^{-1}	0.2792×10^{-1}	0.3452×10^{-2}	-0.9591×10^{-2}
0.0250	1.4	1.207	0.1600×10^{-1}	0.1872×10^{-1}	0.3245×10^{-1}	0.4981×10^{-2}	-0.8814×10^{-2}

F_2 Cross Section Systematic Errors cont.							
x	Q^2	F_2	Stat. Err	R	R_{minus}	R_{plus}	Radcorr
0.0250	1.8	1.290	0.1626×10^{-1}	0.2192×10^{-1}	0.3784×10^{-1}	0.5999×10^{-2}	-0.7091×10^{-2}
0.0250	2.3	1.286	0.1623×10^{-1}	0.2094×10^{-1}	0.3461×10^{-1}	0.7272×10^{-2}	-0.3150×10^{-2}
0.0250	3.2	1.418	0.1277×10^{-1}	0.1899×10^{-1}	0.2421×10^{-1}	0.1376×10^{-1}	0.3934×10^{-2}
0.0250	5.1	1.530	0.1545×10^{-1}	0.1734×10^{-1}	0.1474×10^{-1}	0.1993×10^{-1}	0.1200×10^{-1}
0.0250	8.2	1.585	0.2070×10^{-1}	0.2034×10^{-1}	0.1880×10^{-1}	0.2188×10^{-1}	0.1733×10^{-1}
0.0250	12.9	1.814	0.5016×10^{-1}	0.2796×10^{-1}	-0.2388×10^{-2}	0.5831×10^{-1}	0.2334×10^{-1}
0.0350	0.7	1.054	0.2255×10^{-1}	0.5964×10^{-2}	0.6427×10^{-2}	0.5501×10^{-2}	-0.1193×10^{-1}
0.0350	0.9	1.060	0.1807×10^{-1}	0.8437×10^{-2}	0.1167×10^{-1}	0.5200×10^{-2}	-0.9999×10^{-2}
0.0350	1.1	1.097	0.1706×10^{-1}	0.1067×10^{-1}	0.1723×10^{-1}	0.4101×10^{-2}	-0.7697×10^{-2}
0.0350	1.4	1.175	0.1673×10^{-1}	0.1203×10^{-1}	0.2100×10^{-1}	0.3066×10^{-2}	-0.5230×10^{-2}
0.0350	1.8	1.255	0.1638×10^{-1}	0.1536×10^{-1}	0.2675×10^{-1}	0.3972×10^{-2}	-0.3119×10^{-2}
0.0350	2.3	1.304	0.1654×10^{-1}	0.1625×10^{-1}	0.2722×10^{-1}	0.5268×10^{-2}	-0.1427×10^{-2}
0.0350	3.2	1.362	0.1184×10^{-1}	0.1464×10^{-1}	0.2158×10^{-1}	0.7702×10^{-2}	0.2678×10^{-2}
0.0350	5.1	1.496	0.1346×10^{-1}	0.1549×10^{-1}	0.1563×10^{-1}	0.1535×10^{-1}	0.9286×10^{-2}
0.0350	8.2	1.557	0.1658×10^{-1}	0.1595×10^{-1}	0.1363×10^{-1}	0.1827×10^{-1}	0.1374×10^{-1}
0.0350	12.9	1.680	0.2453×10^{-1}	0.2047×10^{-1}	0.1374×10^{-1}	0.2721×10^{-1}	0.1751×10^{-1}
0.0350	20.5	1.812	0.7433×10^{-1}	0.2637×10^{-1}	-0.1848×10^{-1}	0.7121×10^{-1}	0.2057×10^{-1}
0.0500	1.1	1.131	0.1470×10^{-1}	0.9957×10^{-2}	0.1346×10^{-1}	0.6455×10^{-2}	-0.2688×10^{-2}
0.0500	1.4	1.183	0.1323×10^{-1}	0.9866×10^{-2}	0.1459×10^{-1}	0.5143×10^{-2}	-0.6220×10^{-3}
0.0500	1.8	1.233	0.1269×10^{-1}	0.1041×10^{-1}	0.1758×10^{-1}	0.3231×10^{-2}	0.2169×10^{-2}
0.0500	2.3	1.311	0.1244×10^{-1}	0.1122×10^{-1}	0.1944×10^{-1}	0.2997×10^{-2}	0.4878×10^{-2}
0.0500	3.2	1.389	0.8614×10^{-2}	0.1088×10^{-1}	0.1736×10^{-1}	0.4395×10^{-2}	0.7450×10^{-2}
0.0500	5.1	1.473	0.8870×10^{-2}	0.1259×10^{-1}	0.1739×10^{-1}	0.7791×10^{-2}	0.9858×10^{-2}
0.0500	8.2	1.564	0.1018×10^{-1}	0.1408×10^{-1}	0.1242×10^{-1}	0.1575×10^{-1}	0.1200×10^{-1}
0.0500	12.9	1.591	0.1287×10^{-1}	0.1460×10^{-1}	0.1267×10^{-1}	0.1654×10^{-1}	0.1334×10^{-1}
0.0500	20.5	1.653	0.2002×10^{-1}	0.1852×10^{-1}	0.5483×10^{-2}	0.3156×10^{-1}	0.1438×10^{-1}

F_2 Cross Section Systematic Errors cont.							
x	Q^2	F_2	Stat. Err	R	R_{minus}	R_{plus}	Radcorr
0.0700	1.4	1.253	0.1791×10^{-1}	0.8237×10^{-2}	0.1008×10^{-1}	0.6396×10^{-2}	-0.1228×10^{-2}
0.0700	1.8	1.224	0.1434×10^{-1}	0.7194×10^{-2}	0.8238×10^{-2}	0.6150×10^{-2}	0.8961×10^{-3}
0.0700	2.3	1.262	0.1346×10^{-1}	0.6828×10^{-2}	0.9856×10^{-2}	0.3800×10^{-2}	0.3187×10^{-2}
0.0700	3.2	1.334	0.8914×10^{-2}	0.6783×10^{-2}	0.1119×10^{-1}	0.2378×10^{-2}	0.6123×10^{-2}
0.0700	5.1	1.437	0.8772×10^{-2}	0.9181×10^{-2}	0.1490×10^{-1}	0.3465×10^{-2}	0.8704×10^{-2}
0.0700	8.2	1.484	0.9142×10^{-2}	0.1122×10^{-1}	0.1422×10^{-1}	0.8228×10^{-2}	0.1017×10^{-1}
0.0700	12.9	1.496	0.1051×10^{-1}	0.1138×10^{-1}	0.8823×10^{-2}	0.1394×10^{-1}	0.1080×10^{-1}
0.0700	20.5	1.557	0.1375×10^{-1}	0.1266×10^{-1}	0.1080×10^{-1}	0.1451×10^{-1}	0.1176×10^{-1}
0.0700	32.5	1.524	0.2395×10^{-1}	0.1538×10^{-1}	-0.5893×10^{-2}	0.3665×10^{-1}	0.1140×10^{-1}
0.0900	1.8	1.257	0.1888×10^{-1}	0.5619×10^{-2}	0.5521×10^{-2}	0.5718×10^{-2}	0.1907×10^{-2}
0.0900	2.3	1.238	0.1464×10^{-1}	0.4766×10^{-2}	0.4847×10^{-2}	0.4684×10^{-2}	0.3525×10^{-2}
0.0900	3.2	1.315	0.9694×10^{-2}	0.4799×10^{-2}	0.7545×10^{-2}	0.2054×10^{-2}	0.5886×10^{-2}
0.0900	5.1	1.388	0.8934×10^{-2}	0.6393×10^{-2}	0.1090×10^{-1}	0.1888×10^{-2}	0.7659×10^{-2}
0.0900	8.2	1.423	0.8768×10^{-2}	0.8595×10^{-2}	0.1369×10^{-1}	0.3501×10^{-2}	0.8623×10^{-2}
0.0900	12.9	1.449	0.9498×10^{-2}	0.9578×10^{-2}	0.9062×10^{-2}	0.1009×10^{-1}	0.9208×10^{-2}
0.0900	20.5	1.466	0.1142×10^{-1}	0.9416×10^{-2}	0.7503×10^{-2}	0.1133×10^{-1}	0.9484×10^{-2}
0.0900	32.5	1.476	0.1602×10^{-1}	0.1138×10^{-1}	0.4070×10^{-2}	0.1868×10^{-1}	0.9494×10^{-2}
0.0900	51.5	1.491	0.3940×10^{-1}	0.1391×10^{-1}	-0.2939×10^{-1}	0.5722×10^{-1}	0.9252×10^{-2}
0.1100	2.3	1.318	0.1889×10^{-1}	0.4359×10^{-2}	0.3419×10^{-2}	0.5298×10^{-2}	0.3152×10^{-2}
0.1100	3.2	1.280	0.1028×10^{-1}	0.3708×10^{-2}	0.4534×10^{-2}	0.2881×10^{-2}	0.5004×10^{-2}
0.1100	5.1	1.333	0.9250×10^{-2}	0.4237×10^{-2}	0.7572×10^{-2}	0.9010×10^{-3}	0.6675×10^{-2}
0.1100	8.2	1.345	0.8600×10^{-2}	0.6479×10^{-2}	0.1163×10^{-1}	0.1328×10^{-2}	0.7376×10^{-2}
0.1100	12.9	1.380	0.8981×10^{-2}	0.7753×10^{-2}	0.9761×10^{-2}	0.5746×10^{-2}	0.7888×10^{-2}
0.1100	20.5	1.406	0.1030×10^{-1}	0.7820×10^{-2}	0.5175×10^{-2}	0.1046×10^{-1}	0.8178×10^{-2}
0.1100	32.5	1.344	0.1273×10^{-1}	0.8003×10^{-2}	0.5982×10^{-2}	0.1002×10^{-1}	0.7835×10^{-2}
0.1100	51.5	1.470	0.2406×10^{-1}	0.1088×10^{-1}	-0.1489×10^{-1}	0.3666×10^{-1}	0.8023×10^{-2}

F_2 Cross Section Systematic Errors cont.							
x	Q^2	F_2	Stat. Err	R	R_{minus}	R_{plus}	Radcorr
0.1400	3.2	1.221	0.8319×10^{-2}	0.2815×10^{-2}	0.2420×10^{-2}	0.3211×10^{-2}	0.4172×10^{-2}
0.1400	5.1	1.253	0.6801×10^{-2}	0.2299×10^{-2}	0.4001×10^{-2}	0.5970×10^{-3}	0.5473×10^{-2}
0.1400	8.2	1.271	0.6174×10^{-2}	0.4238×10^{-2}	0.8443×10^{-2}	0.3302×10^{-4}	0.5996×10^{-2}
0.1400	12.9	1.291	0.6046×10^{-2}	0.5538×10^{-2}	0.9327×10^{-2}	0.1748×10^{-2}	0.6123×10^{-2}
0.1400	20.5	1.275	0.6506×10^{-2}	0.5852×10^{-2}	0.4898×10^{-2}	0.6806×10^{-2}	0.5624×10^{-2}
0.1400	32.5	1.232	0.7486×10^{-2}	0.5467×10^{-2}	0.3766×10^{-2}	0.7167×10^{-2}	0.5904×10^{-2}
0.1400	51.5	1.210	0.1015×10^{-1}	0.6463×10^{-2}	-0.2146×10^{-2}	0.1507×10^{-1}	0.5596×10^{-2}
0.1400	81.5	1.224	0.2796×10^{-1}	0.7814×10^{-2}	-0.2967×10^{-1}	0.4530×10^{-1}	0.5108×10^{-2}
0.1800	5.1	1.147	0.7282×10^{-2}	0.1130×10^{-2}	0.1032×10^{-2}	0.1228×10^{-2}	0.3904×10^{-2}
0.1800	8.2	1.146	0.6294×10^{-2}	0.2189×10^{-2}	0.5041×10^{-2}	-0.6640×10^{-3}	0.4434×10^{-2}
0.1800	12.9	1.154	0.5862×10^{-2}	0.3501×10^{-2}	0.7339×10^{-2}	-0.3380×10^{-3}	0.4495×10^{-2}
0.1800	20.5	1.141	0.5916×10^{-2}	0.4013×10^{-2}	0.5196×10^{-2}	0.2829×10^{-2}	0.3440×10^{-2}
0.1800	32.5	1.112	0.6518×10^{-2}	0.3855×10^{-2}	0.2106×10^{-2}	0.5605×10^{-2}	0.3132×10^{-2}
0.1800	51.5	1.070	0.7712×10^{-2}	0.3842×10^{-2}	0.1944×10^{-2}	0.5740×10^{-2}	0.3955×10^{-2}
0.1800	81.5	1.066	0.1313×10^{-1}	0.4766×10^{-2}	-0.1509×10^{-1}	0.2462×10^{-1}	0.3742×10^{-2}
0.2250	5.1	1.050	0.7429×10^{-2}	0.9250×10^{-3}	0.3120×10^{-3}	0.1538×10^{-2}	0.2564×10^{-2}
0.2250	8.2	1.023	0.5852×10^{-2}	0.1046×10^{-2}	0.2759×10^{-2}	-0.6660×10^{-3}	0.2996×10^{-2}
0.2250	12.9	1.006	0.5154×10^{-2}	0.2043×10^{-2}	0.5211×10^{-2}	-0.1124×10^{-2}	0.3019×10^{-2}
0.2250	20.5	0.9918	0.4946×10^{-2}	0.2617×10^{-2}	0.4986×10^{-2}	0.2481×10^{-3}	0.2577×10^{-2}
0.2250	32.5	0.9663	0.5214×10^{-2}	0.2709×10^{-2}	0.1680×10^{-2}	0.3739×10^{-2}	0.1126×10^{-2}
0.2250	51.5	0.9268	0.5941×10^{-2}	0.2451×10^{-2}	0.1112×10^{-2}	0.3789×10^{-2}	0.2494×10^{-2}
0.2250	81.5	0.9056	0.7786×10^{-2}	0.2853×10^{-2}	-0.4869×10^{-2}	0.1058×10^{-1}	0.2500×10^{-2}
0.2750	8.2	0.8839	0.5969×10^{-2}	0.4758×10^{-3}	0.1149×10^{-2}	-0.1975×10^{-3}	0.1850×10^{-2}
0.2750	12.9	0.8564	0.5105×10^{-2}	0.1076×10^{-2}	0.3452×10^{-2}	-0.1300×10^{-2}	0.2001×10^{-2}
0.2750	20.5	0.8340	0.4674×10^{-2}	0.1643×10^{-2}	0.4125×10^{-2}	-0.8387×10^{-3}	0.1821×10^{-2}
0.2750	32.5	0.8018	0.4696×10^{-2}	0.1801×10^{-2}	0.1934×10^{-2}	0.1669×10^{-2}	0.1656×10^{-3}

F_2 Cross Section Systematic Errors cont.							
x	Q^2	F_2	Stat. Err	R	R_{minus}	R_{plus}	Radcorr
0.2750	51.5	0.7833	0.5192×10^{-2}	0.1715×10^{-2}	0.4621×10^{-3}	0.2968×10^{-2}	0.1037×10^{-2}
0.2750	81.5	0.7409	0.6127×10^{-2}	0.1701×10^{-2}	-0.9989×10^{-3}	0.4400×10^{-2}	0.1674×10^{-2}
0.2750	129.2	0.7044	0.1029×10^{-1}	0.2033×10^{-2}	-0.1463×10^{-1}	0.1869×10^{-1}	0.1535×10^{-2}
0.3500	8.2	0.6881	0.4425×10^{-2}	0.1639×10^{-3}	0.1992×10^{-3}	0.1285×10^{-3}	0.7978×10^{-3}
0.3500	12.9	0.6476	0.3462×10^{-2}	0.4101×10^{-3}	0.1881×10^{-2}	-0.1061×10^{-2}	0.1024×10^{-2}
0.3500	20.5	0.6164	0.3048×10^{-2}	0.8112×10^{-3}	0.2808×10^{-2}	-0.1186×10^{-2}	0.1013×10^{-2}
0.3500	32.5	0.5928	0.2930×10^{-2}	0.1005×10^{-2}	0.1877×10^{-2}	0.1328×10^{-3}	0.2600×10^{-3}
0.3500	51.5	0.5637	0.3068×10^{-2}	0.1012×10^{-2}	0.1980×10^{-3}	0.1826×10^{-2}	-0.5405×10^{-3}
0.3500	81.5	0.5289	0.3355×10^{-2}	0.9072×10^{-3}	0.7427×10^{-4}	0.1740×10^{-2}	0.7255×10^{-3}
0.3500	129.2	0.5140	0.4521×10^{-2}	0.1062×10^{-2}	-0.5324×10^{-2}	0.7447×10^{-2}	0.9236×10^{-3}
0.4500	12.9	0.4038	0.3091×10^{-2}	0.1063×10^{-3}	0.7688×10^{-3}	-0.5561×10^{-3}	0.3628×10^{-3}
0.4500	20.5	0.3872	0.2659×10^{-2}	0.2849×10^{-3}	0.1498×10^{-2}	-0.9282×10^{-3}	0.5034×10^{-3}
0.4500	32.5	0.3570	0.2398×10^{-2}	0.4371×10^{-3}	0.1356×10^{-2}	-0.4823×10^{-3}	0.3786×10^{-3}
0.4500	51.5	0.3251	0.2341×10^{-2}	0.4647×10^{-3}	0.2928×10^{-3}	0.6367×10^{-3}	-0.7185×10^{-3}
0.4500	81.5	0.3093	0.2490×10^{-2}	0.4434×10^{-3}	0.5710×10^{-4}	0.8297×10^{-3}	-0.1212×10^{-3}
0.4500	129.2	0.2880	0.2874×10^{-2}	0.4291×10^{-3}	-0.8931×10^{-3}	0.1751×10^{-2}	0.4546×10^{-3}
0.4500	204.8	0.2626	0.4906×10^{-2}	0.5219×10^{-3}	-0.6290×10^{-2}	0.7334×10^{-2}	0.4966×10^{-3}
0.5500	12.9	0.2358	0.2589×10^{-2}	0.2895×10^{-4}	0.4253×10^{-3}	-0.3674×10^{-3}	0.1043×10^{-3}
0.5500	20.5	0.2100	0.2074×10^{-2}	0.8580×10^{-4}	0.6883×10^{-3}	-0.5167×10^{-3}	0.2041×10^{-3}
0.5500	32.5	0.1878	0.1785×10^{-2}	0.1653×10^{-3}	0.7007×10^{-3}	-0.3701×10^{-3}	0.2199×10^{-3}
0.5500	51.5	0.1737	0.1731×10^{-2}	0.1979×10^{-3}	0.3030×10^{-3}	0.9289×10^{-4}	-0.9300×10^{-4}
0.5500	81.5	0.1575	0.1765×10^{-2}	0.1929×10^{-3}	-0.4651×10^{-4}	0.4323×10^{-3}	-0.4830×10^{-3}
0.5500	129.2	0.1472	0.1936×10^{-2}	0.1772×10^{-3}	-0.7540×10^{-4}	0.4298×10^{-3}	0.1834×10^{-3}
0.5500	204.8	0.1282	0.2583×10^{-2}	0.1951×10^{-3}	-0.1791×10^{-2}	0.2181×10^{-2}	0.2502×10^{-3}

F_2 Cross Section Systematic Errors cont.							
x	Q^2	F_2	Stat. Err	R	R_{minus}	R_{plus}	Radcorr
0.6500	12.9	0.1125	0.2136×10^{-2}	0.2725×10^{-4}	0.1601×10^{-3}	-0.1056×10^{-3}	-0.5201×10^{-5}
0.6500	20.5	0.9555×10^{-1}	0.1321×10^{-2}	0.2381×10^{-4}	0.2839×10^{-3}	-0.2362×10^{-3}	0.6657×10^{-4}
0.6500	32.5	0.8205×10^{-1}	0.1143×10^{-2}	0.5266×10^{-4}	0.3227×10^{-3}	-0.2174×10^{-3}	0.9429×10^{-4}
0.6500	51.5	0.7665×10^{-1}	0.1088×10^{-2}	0.7375×10^{-4}	0.1736×10^{-3}	-0.2610×10^{-4}	0.3973×10^{-4}
0.6500	81.5	0.6604×10^{-1}	0.1057×10^{-2}	0.7259×10^{-4}	0.1360×10^{-4}	0.1316×10^{-3}	-0.3119×10^{-3}
0.6500	129.2	0.5993×10^{-1}	0.1124×10^{-2}	0.6616×10^{-4}	-0.1028×10^{-4}	0.1426×10^{-3}	0.8650×10^{-5}

Appendix B

Published Article: First Measurement of the Low-x, Low-Q^2 Structure Function F_2 in Neutrino Scattering

VOLUME 86, NUMBER 24 PHYSICAL REVIEW LETTERS 11 JUNE 2001

First Measurement of the Low-x, Low-Q^2 Structure Function F_2 in Neutrino Scattering

B. T. Fleming,[2] T. Adams,[4] A. Alton,[4] C. G. Arroyo,[2] S. Avvakumov,[7] L. de Barbaro,[5] P. de Barbaro,[7] A. O. Bazarko,[2] R. H. Bernstein,[3] A. Bodek,[7] T. Bolton,[4] J. Brau,[6] D. Buchholz,[5] H. Budd,[7] L. Bugel,[3] J. Conrad,[2] R. B. Drucker,[6] J. A. Formaggio,[2] R. Frey,[6] J. Goldman,[4] M. Goncharov,[4] D. A. Harris,[7] R. A. Johnson,[1] J. H. Kim,[2] B. J. King,[2] T. Kinnel,[8] S. Koutsoliotas,[2] M. J. Lamm,[3] W. Marsh,[3] D. Mason,[6] K. S. McFarland,[7] C. McNulty,[2] S. R. Mishra,[2] D. Naples,[4] P. Nienaber,[3] A. Romosan,[2] W. K. Sakumoto,[7] H. Schellman,[5] F. J. Sciulli,[2] W. G. Seligman,[2] M. H. Shaevitz,[2] W. H. Smith,[8] P. Spentzouris,[2] E. G. Stern,[2] N. Suwonjandee,[1] A. Vaitaitis,[2] M. Vakili,[1] U. K. Yang,[7] J. Yu,[3] G. P. Zeller,[5] and E. D. Zimmerman[2]

(CCFR/NuTeV Collaboration)

[1]*University of Cincinnati, Cincinnati, Ohio 45221*
[2]*Columbia University, New York, New York 10027*
[3]*Fermi National Accelerator Laboratory, Batavia, Illinois 60510*
[4]*Kansas State University, Manhattan, Kansas 66506*
[5]*Northwestern University, Evanston, Illinois 60208*
[6]*University of Oregon, Eugene, Oregon 97403*
[7]*University of Rochester, Rochester, New York 14627*
[8]*University of Wisconsin, Madison, Wisconsin 53706*

(Received 28 November 2000)

A new structure function analysis of CCFR deep inelastic ν-N and $\overline{\nu}$-N scattering data is presented for previously unexplored kinematic regions down to Bjorken $x = 0.0045$ and $Q^2 = 0.3$ GeV^2. Comparisons to charged lepton scattering data from NMC and E665 experiments are made and the behavior of the structure function F_2^ν is studied in the limit $Q^2 \to 0$.

DOI: 10.1103/PhysRevLett.86.5430 PACS numbers: 12.38.Qk, 13.15.+g

Neutrino structure function measurements in the low Bjorken x, low-Q^2 region can be used to study the axial-vector component of the weak interaction as well as to test the limits of parton distribution universality. In this paper, we present a first measurement of the structure function F_2 in neutrino scattering, from the CCFR data, for $Q^2 < 1$ GeV^2, where Q^2 is the square of the four momentum transfer in the interaction, and $0.0045 < x < 0.035$. A combination of new theoretical interest and new techniques using improved pdf models have allowed extension of the previous CCFR structure function analysis to $Q^2 < 1$ GeV^2. In this region where perturbative and nonperturbative QCD meet, we present a parametrization of the data which allows us to test the predicted partially conserved axial current (PCAC) limit of F_2 in neutrino scattering.

The universality of parton distributions can be tested by comparing neutrino scattering data to charged lepton scattering data. Past measurements for $0.0075 < x < 0.1$ and $Q^2 > 1.0$ GeV^2 have indicated that F_2^ν differs from F_2^μ by 10%–15% [1]. This discrepancy has been partially resolved by recent analyses of F_2^ν at $Q^2 > 1.0$ GeV^2 [2,3]. While we expect and have now observed that parton distribution universality holds in this region, this need not be the case at lower values of Q^2. Deviations from this universality at lower Q^2 are expected due to differences in vector and axial components of electromagnetic and weak interactions. In particular, the electromagnetic interaction has only a vector component while the weak interaction has both vector and axial-vector components. Vector currents are conserved but axial-vector currents are only partially conserved (PCAC). Adler [4] proposed a test of the PCAC hypothesis using high energy neutrino interactions, a consequence of which is the prediction that F_2^ν approaches a nonzero constant as $Q^2 \to 0$ due to U(1) gauge invariance. A determination of this constant is performed here by fitting the low-Q^2 data to a phenomenological curve developed by Donnachie and Landshoff [5].

The differential cross sections for the νN charged-current process $\nu_\mu(\overline{\nu}_\mu) + N \to \mu^-(\mu^+) + X$ in the limit of negligible quark masses and neglecting lepton masses, in terms of the Lorentz-invariant structure functions F_2, $2xF_1$, and xF_3, are

$$\frac{d\sigma^{\nu,\overline{\nu}}}{dx\,dy} = \frac{G_F^2 M E_\nu}{\pi}\left[\left(1 - y - \frac{Mxy}{2E_\nu}\right)F_2(x,Q^2) + \frac{y^2}{2}\,2xF_1(x,Q^2) \pm y\left(1 - \frac{y}{2}\right)xF_3(x,Q^2)\right], \tag{1}$$

where G_F is the weak Fermi coupling constant, M is the nucleon mass, E_ν is the incident ν energy, Q^2 is the square of the four-momentum transfer to the nucleon, the scaling variable $y = E_{\mathrm{HAD}}/E_\nu$ is the fractional energy transferred to the hadronic vertex with E_{HAD} equal to the measured

 0031-9007/01/86(24)/5430(4)$15.00

hadronic energy, and $x = Q^2/2ME_\nu y$, the Bjorken scaling variable, is the fractional momentum carried by the struck quark. The structure function $2xF_1$ is expressed in terms of F_2 by $2xF_1(x, Q^2) = F_2(x, Q^2) \times \frac{1+4M^2x^2/Q^2}{1+R(x,Q^2)}$, where $R = \frac{\sigma_L}{\sigma_T}$ is the ratio of the cross sections of longitudinally to transversely polarized W bosons. In the leading order (LO) quark-parton model, F_2 is the sum of the momentum densities of all interacting quark constituents, and xF_3 is the difference of these, the valence quark momentum density; these relations are modified by higher-order QCD corrections.

The ν deep inelastic scattering (DIS) data were collected in two high-energy high-statistics runs, FNAL E744 and E770, in the Fermilab Tevatron fixed-target quadrupole triplet beam line by the CCFR Collaboration. The detector [6,7] consists of a target calorimeter instrumented with both scintillators and drift chambers for measuring the energy of the hadron shower, $E_{\rm HAD}$, and the muon angle, θ_μ, followed by a toroid spectrometer for measuring the muon momentum p_μ. There are 1 030 000 ν_μ events and 179 000 $\overline{\nu}_\mu$ events in the data sample after fiducial volume and geometric cuts, and kinematic cuts of $p_\mu > 15$ GeV, $\theta_\mu < 150$ mr, $E_{\rm HAD} > 10$ GeV, and $30 < E_\nu < 360$ GeV. These cuts were applied to select regions of high efficiency and small systematic errors in reconstruction.

The structure function F_2^ν in Eq. (1) can be calculated from the observed number of ν_μ and $\overline{\nu}_\mu$ events combined with the ν_μ and $\overline{\nu}_\mu$ fluxes. The ratio of fluxes between different energies in the ν mode and that between the $\overline{\nu}$ and ν modes was determined using the events with $E_{\rm HAD} < 20$ GeV [8–10]. The overall normalization of the flux was constrained such that the measured total neutrino-nucleon cross section for νs equaled the world average cross section for isoscalar-corrected iron target experiments, $\sigma^{\nu\rm Fe}/E = (0.677 \pm 0.014) \times 10^{-38}$ cm^2/GeV [9,11] and for $\overline{\nu}$s equaled the world average cross section including this experiment for isoscalar-corrected iron target experiments, $\sigma^{\overline{\nu}\rm Fe}/E = (0.340 \pm 0.007) \times 10^{-38}$ cm^2/GeV. Negligible corrections for nonisoscalarity of the iron target and the mass of the W boson propagator are applied.

Sources of systematic error on F_2^ν arise from limitations of the models used for corrections and from the level of our knowledge of the detector calibration. Muon and hadron energy calibrations relevant for the low-x, low-Q^2 data were determined from test beam data collected during the course of the experiment [6,7]. For acceptance, smearing, and radiative corrections we chose an appropriate model for the low-x, low-Q^2 region, the Glück-Reya-Vogt (GRV) [12] model of the parton distribution functions. The GRV model is used up to $Q^2 = 1.35$ GeV^2, where it is normalized to a LO parametrization like that first suggested by Buras and Gaemers [13] used above this. Inclusion of the GRV model in the radiative correction calculation caused a systematic decrease in F_2^ν by as much as 10% in the lowest x bin, decreasing to 1%–2% at $x = 0.015$ as compared to the effects of the LO model used in the previous analysis [8]. Because of the systematic uncertainty in the model at low x, the radiative correction error is 3% in the lowest x bin. A correction is applied for the difference between xF_3^ν and $xF_3^{\overline{\nu}}$, determined using a LO calculation of $\Delta xF_3 = xF_3^\nu - xF_3^{\overline{\nu}}$. The recent CCFR ΔxF_3 measurement [2] is higher than this LO model [13] and all other current LO and next to leading order (NLO) theoretical predictions in this kinematic region. An appropriate systematic error is applied to account for the differences between the theory and this measurement. Finally, a systematic error is applied to account for the uncertainty in the value of R which comes from a global fit to the world's measurements [14].

In previous analyses a slow rescaling correction was applied to account for massive charm effects. This is not applied here since the corrections are model dependent and uncertain in this kinematic range. As a result, neutrino and charged lepton DIS data must be compared within the framework of charm production models, accomplished by plotting the ratio of data to theoretical model. The theoretical calculation corresponding to the CCFR data employs NLO QCD including heavy flavor effects as implemented in the TR-VFS(MRST99) scheme [15,16]. The theoretical calculation corresponding to NMC [17] and E665 [18] data is determined using TR-VFS(MRST99) for charged lepton scattering. Other theoretical predictions such as ACOT-VFS(CTEQ4HQ) [19,20] and FFS(GRV94) [21] do not significantly change the comparison.

The combination of the inclusion of the GRV model at low x and low Q^2, its effect on the radiative corrections, and removal of the slow rescaling correction help to resolve the long-standing discrepancy between the neutrino and charged lepton DIS data above $x = 0.015$. F_2^ν is plotted in Fig. 1. Errors are statistical and systematic added in quadrature. A line is drawn at $Q^2 = 1$ GeV^2 to highlight the kinematic region this analysis accesses. Figure 2 compares F_2 (data/theoretical model) for CCFR, NMC, and E665. There is agreement to within 5% down to $x = 0.0125$. Below this, as x decreases, CCFR F_2^ν (data/theory) becomes systematically higher than NMC F_2^μ (data/theory). Differences between scattering via the weak interaction and via the electromagnetic interaction as $Q^2 \to 0$ may account for the disagreement in this region.

In charged lepton DIS, the structure function F_2^μ is constrained by gauge invariance to vanish with Q^2 as $Q^2 \to 0$. Donnachie and Landshoff predict that in the low-Q^2 region, F_2^μ will follow the form [5]

$$C\left(\frac{Q^2}{Q^2 + A^2}\right). \tag{2}$$

However, in the case of neutrino DIS, the axial component of the weak interaction may contribute a nonzero component to F_2^ν as Q^2 approaches zero. Donnachie and

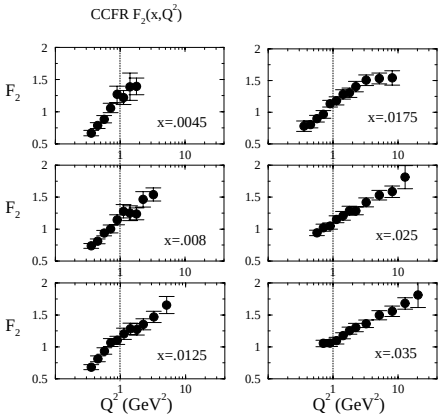

FIG. 1. CCFR F_2 at low x, low Q^2. Data to the left of the vertical line at $Q^2 = 1.0$ represent the new kinematic regime for this analysis.

Landshoff predict that F_2^{ν} should follow a form with a nonzero contribution at $Q^2 = 0$:

$$\frac{C}{2}\left(\frac{Q^2}{Q^2 + A^2} + \frac{Q^2 + D}{Q^2 + B^2}\right). \tag{3}$$

Using NMC and E665 data, corrected in this case to be equivalent to scattering from an iron target using a parametrization of SLAC Fe/D data [8], we do a combined fit to the form predicted for μ DIS and extract the parameter $A = 0.81 \pm 0.02$ with $\chi^2/\text{d.o.f.} = 27/17$. Results of fits in each x bin for each experiment are shown in Table I for comparison to parameters in the CCFR fit. The error

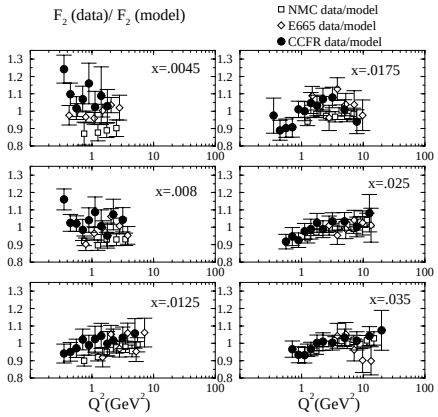

FIG. 2. F_2 data/theory from CCFR ν-Fe DIS compared to F_2 from NMC and E665 DIS. Errors bars are statistical and systematic added in quadrature. Theoretical predictions are those of TR-VFS(MRST99).

TABLE I. Results for NMC and E665 data fit to Eq. (2).

x	A	χ^2/N	N
0.0045(NMC)	0.87 ± 0.16	0.02	2
0.0045(E665)[a]	0.90 ± 0.10	0.43	4
0.0045(E665)[b]	0.94 ± 0.09	0.31	5
0.0080(NMC)	0.75 ± 0.07	0.38	3
0.0080(E665)[c]	0.87 ± 0.10	0.24	4
0.0080(E665)[d]	0.85 ± 0.11	1.19	4
0.0125(NMC)	0.81 ± 0.05	0.55	5
0.0125(E665)	0.97 ± 0.14	1.12	4
0.0175(NMC)	0.78 ± 0.06	0.38	5
0.0175(E665)	0.76 ± 0.13	0.88	5

[a]Bin center corrected from $x = 0.004$.
[b]Bin center corrected from $x = 0.005$.
[c]Bin center corrected from $x = 0.007$.
[d]Bin center corrected from $x = 0.009$.

on A is incorporated in the systematic error on the final fit. Inserting this value for A into the form predicted for νN DIS, we fit CCFR data to extract parameters B, C, and D, and determine the value of F_2^{ν} at $Q^2 = 0$. Only data below $Q^2 = 1.4$ GeV^2 are used in the fits. The CCFR x bins that contain enough data to produce a good fit in this Q^2 region are $x = 0.0045$, $x = 0.0080$, $x = 0.0125$, and $x = 0.0175$. Figure 3 and Table II show the results of the fits. Error bars consist of statistical and systematic terms added in quadrature but exclude an overall correlated normalization uncertainty of 1%–2%. The values of F_2^{ν} at $Q^2 = 0$ GeV^2 in the three highest x bins are statistically significant and are within 1σ of each other. The lowest x bin has large error bars but is within 1.5σ of the others. Taking a weighted average of the parameters B, C, D, and F_2^{ν} yields $B = 1.53 \pm 0.02$, $C = 2.31 \pm 0.03$, $D = 0.48 \pm 0.03$, and $F_2^{\nu}(Q^2 = 0) = 0.21 \pm 0.02$. Figure 4 shows $F_2^{\nu}(Q^2 = 0)$ for the different x bins. Inclusion of an x dependence of the form x^{β} in a combined fit to all

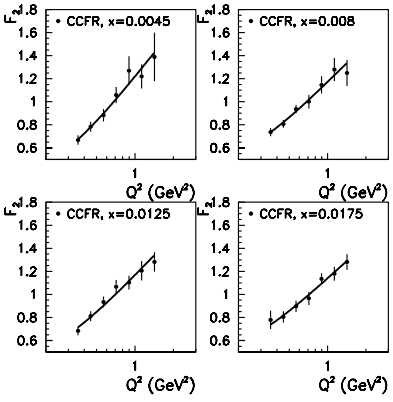

FIG. 3. Results from fit to CCFR data to extrapolate to $F_2(Q^2 = 0)$.

TABLE II. Fit results for CCFR data. CCFR data are fit to Eq. 4 with $A = 0.81 \pm 0.02$ as determined by fits to NMC and E665 data. B, C, D, and F_2 at $Q^2 = 0$ results shown below. $N = 4$ for all fits.

x	B	C	D	$F_2^{\nu}(Q^2 = 0)$	χ^2/N
0.0045	1.49 ± 0.02	2.62 ± 0.26	0.06 ± 0.17	0.04 ± 0.10	0.5
0.0080	1.63 ± 0.05	2.32 ± 0.05	0.50 ± 0.05	0.22 ± 0.03	0.5
0.0125	1.63 ± 0.05	2.39 ± 0.05	0.40 ± 0.05	0.18 ± 0.03	1.0
0.0175	1.67 ± 0.05	2.20 ± 0.05	0.65 ± 0.07	0.26 ± 0.03	0.5

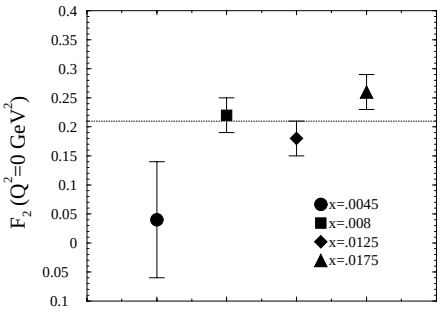

FIG. 4. $F_2(Q^2 = 0\ \mathrm{GeV}^2)$ from different x bins. A line is drawn at the weighted average of all four measurements.

four x bins does not significantly improve the overall fits or χ^2.

In summary, a comparison of F_2 from neutrino DIS to that from charged lepton DIS shows good agreement above $x = 0.0125$ but shows differences at smaller x. This low-x discrepancy can be explained by the different behavior of F_2 from ν DIS to that from e/μ DIS as $Q^2 \to 0$. CCFR F_2^{ν} data favors a nonzero value for F_2^{ν} as $Q^2 \to 0$.

We thank the management and staff of Fermilab and acknowledge the help of many individuals at our home institutions. We also thank Fred Olness for many useful discussions [22]. This research was supported by the National Science Foundation and the Department of Energy of the United States, which should be credited for their continued support of basic research.

[1] W. G. Seligman *et al.,* Phys. Rev. Lett. **79**, 1213 (1997).
[2] U. K. Yang *et al.,* Phys. Rev. Lett. **86**, 2742 (2001).
[3] C. Boros, F. M. Steffens, J. T. Londergan, and A. W. Thomas, Phys. Lett. B **468**, 161 (1999).
[4] S. L. Adler, Phys. Rev. **135**, B963 (1964).
[5] A. Donnachie and P. V. Landshoff, Z. Phys. C **61**, 139 (1994).
[6] W. K. Sakumoto *et al.,* Nucl. Instrum. Methods Phys. Res., Sect. A **294**, 179 (1990).
[7] B. J. King *et al.,* Nucl. Instrum. Methods Phys. Res., Sect. A **302**, 254 (1991).
[8] W. G. Seligman, Ph.D. thesis, Columbia University, Nevis Report No. 292 (1997).
[9] P. S. Auchincloss *et al.,* Z. Phys. C **48**, 411 (1990).
[10] R. Belusevic and D. Rein, Phys. Rev. D **38**, 2753 (1988).
[11] R. Blair *et al.,* Phys. Rev. Lett. **51**, 343 (1983); P. Berge *et al.,* Z. Phys. C **49**, 187 (1991).
[12] M. Glück, E. Reya, and A. Vogt, Z. Phys. C **67**, 433 (1995).
[13] A. J. Buras and K. J. F. Gaemers, Nucl. Phys. **B132**, 249 (1978).
[14] L. W. Whitlow *et al.,* Phys. Lett. B **250**, 193 (1990).
[15] R. S. Thorne and R. G. Roberts, Phys. Lett. B **421**, 303 (1998).
[16] A. D. Martin *et al.,* Eur. Phys. J. C **4**, 463 (1998) (we have used the post DIS-2000 MRST corrected code).
[17] M. Arneodo *et al.,* Nucl. Phys. **B483**, 3 (1997).
[18] M. R. Adams *et al.,* Phys. Rev. D **54**, 3006 (1996).
[19] M. Aivazis, J. Collins, F. Olness, and W. K. Tung, Phys. Rev. D **50**, 3102 (1994).
[20] M. Aivazis, F. Olness, and W. K. Tung, Phys. Rev. Lett. **65**, 2339 (1990).
[21] E. Laenen, S. Riemersma, J. Smith, and W. L. Van Neerven, Nucl. Phys. **B392**, 162 (1993).
[22] F. Olness (private communication).

Appendix C

Article Submitted for Publication: Photomultiplier Tube Testing for the MiniBooNE Experiment

Photomultiplier Tube Testing for the MiniBooNE Experiment

B. T. Fleming, L. Bugel, E. Hawker, S. Koutsoliotas, S. McKenney, V. Sandberg, and D. Smith for the MiniBooNE Collaboration

Abstract— **The recent discoveries in the neutrino sector in the Standard Model have opened a new frontier in high energy physics. Understanding neutrinos and how they interact is crucial to continuing to verify the Standard Model and look for beyond Standard Model physics. The MiniBooNE experiment is a $\nu_\mu \rightarrow \nu_e$ oscillation search designed to confirm or rule out the neutrino oscillation signal seen by the LSND [1] experiment at the Los Alamos National Laboratory. The MiniBooNE detector, a sphere filled with mineral oil and lined with 8" Hamamatsu photomultiplier tubes (PMTs), uses Čerenkov imaging to identify ν_μ and ν_e interactions. The PMTs are the main detector component and must be well understood. They underwent a series of tests to determine their functionality and figures of merit in order to be placed in the detector, as described here.**

Keywords— **Neutrinos, Photomultipliers, Cerenkov detectors, Scintillation detectors.**

I. Introduction

Recent experimental data indicate that neutrinos oscillate among their different flavors and therefore have mass. Data from experiments looking for the solar neutrino deficit, those looking for the atmospheric neutrino deficit, and the LSND experiment cannot all be explained by the three Standard Model neutrinos. Further checks on these signals are necessary.

The BooNE experiment, now under construction at the Fermi National Accelerator Laboratory, is specifically designed to confirm or rule out the LSND signal. MiniBooNE, the first stage of the BooNE experiment, looks for ν_e appearance in a ν_μ beam created from 8 GeV protons from the Fermilab Booster. ν_μ's, ν_e's, and background events such as π^0's are identified in a detector 500 m downstream from the target hall where the ν_μ beam is created. The detector is a 12 m diameter sphere filled with mineral oil. It is a sphere within a sphere with an inner light tight signal region and an outer veto region. Neutrinos will be identified in the detector when they interact with a nucleon via a charged or neutral current interaction. The outgoing charged particle produces Čerenkov and scintillation light in the mineral oil. These light signatures are recorded by photomultiplier tubes lining the inside of the detector, and events are later reconstructed from this information.

There are 1280 8" photomultiplier tubes lining the inner signal region of the detector. 241 PMTs in the veto region look for light indicating a charge particle has entered the detector. Of these 1521 PMTs, 1197 are inherited from the LSND experiment. They are Hamamatsu R1408 9 stage, 8" PMTs. 324 new Hamamatsu R5912 10 stage 8" PMTs fill the rest of the detector. Before installing the PMTs in the MiniBooNE detector, they were tested to ensure they are operational, to determine their operating voltages, and to measure their figures of merit. The following sections discuss the results of these tests and the PMT's placement in the detector.

B. T. Fleming formerly with Columbia University, New York, New York is now with the Fermi National Accelerator Laboratory. L. Bugel is with the Fermi National Accelerator Laboratory. E. Hawker is with the University of Cinncinnati, Cinncinnati, OH. S. Koutsoliotas is with Bucknell University, Lewisburg PA. S. McKenney and D. Smith are with Embry Riddle Aeronautical University, Prescott, AZ. V. Sandberg is with the Los Alamos National Laboratory, Los Alamos, NM. For the full MiniBooNE collaboration list, see http://www-boone.fnal.gov

II. Testing Setup and Tests Performed

Testing was conducted at Fermilab in a darkroom in air where up to 46 PMTs could be tested in one day. A "wine-rack" assembly was constructed against one wall of the dark room. Each PMT was secured on its side facing an optical fiber carrying light from an LED flasher. The rack accomadated 30 LSND PMTs and 16 new PMTs held in place using Styrofoam molds.

The PMTs were conditioned in the darkroom for 12-24 hours at approximately 1000 V. After conditioning, PMTs were tested using an automated VXI readout system with a built-in oscilloscope having a maximum capture rate of 10,000 waveforms/90 seconds. The VXI readout system set PMTs at a recommended testing voltage using a serial I/O interface, determined darkrate, and recorded PMT pulse response to an LED flasher. The system allowed for automatic testing of 22 tubes in a single run. The number of tubes that could be tested simultaneously was limited by our use of one multiplexer. A schematic diagram of the system is shown in Fig. 1. Once the testing was complete, the data files were stored for data analysis.

A. Testing Procedure

There is a trade off between amount of test data that can be taken and the amount of time it takes to perform the tests. For this reason, tests performed are optimized to set operating voltages and determine PMT quality while keeping the testing procedure short.

The testing data were acquired in two modes. In the first mode, the dark currents were collected by recording the noise rates measured at different voltages with no light source. Pulses passing a 3 mV threshold were counted as dark noise and used to determine the dark noise rate. The dark noise was measured at various voltages starting at approximately 1000 V and at increments of 100 V above this to approximately 100 V above the PMTs suggested operating voltage. Suggested operating voltages for the new

PMTs were supplied by Hamamatsu; suggested operating voltages for the LSND PMTs were assumed to be their operating voltage during the LSND experimental run.

After the dark noise rates were recorded, the PMTs were strobed with an LED light source at 450 nm for a duration of 1 ns at 1 kHz to look at light induced waveforms. PMT response to 600-1000 LED flashes piped in through an optical fiber were recorded and used to determine the operating voltage at a chosen gain, to study the charge and time resolutions, and to search for pre- and post-pulsing anomalies.

Responses were triggered off the LED pulse and delayed so that they appear about 40% of the way in time into the scope. This timing allows for adequate determination of the pre-pulse baseline and ample time after the pulse to look for post-pulsing. Light levels were set low enough to allow adequate determination of PMT response to one photoelectron (PE), and high enough to ensure sufficient data events.

LED tests were performed at two different voltages for the LSND PMTs, at LSND operating voltage ±50 volts. New PMTs underwent testing at four different voltages, at -100, 0, +100, and +150 V from the Hamamatsu suggested operating voltage. Multiple tests are necessary for determination of the gain and should be conducted near the nominal operating voltage. The number of tests is as great as needed to determine unknowns about the PMTs while being as few as possible due to time constraints. Using the VXI system, pulse responses were read from the internal oscilloscope, recorded to data files and analyzed off-line.

Testing setups were calibrated and measurement errors determined by taking calibration data. A *rover* PMT which was tested in each possible testing position and a *permanent* PMT which was tested in the same spot in the same way almost every test cycle provided this calibration data.

For each PMT, the 2-4 test data files corresponding to LED response tests taken were analyzed off-line to determine figures of merit for that data file. These figures of merit include PMT functionality and operating voltage, PMT gain, charge resolution, timing resolution, double-pulsing rate and darkrate.

III. PMT Characteristics: Results of Tests

PMTs were tested to determine their operating voltages and figures of merit. Results are outlined below.

A. Gain

PMT gain corresponds to the mean number of electrons produced by the phototube in response to one PE. Ideally, one could just read off the gain as the mean of the one PE peak in a plot of the integrated charge of the responses to the 600-1000 LED flashes. The width of this one PE peak then corresponds to the charge resolution. However, the one PE peak for these tests contains responses to 2 and 3 PEs and possibly more. Gain is instead determined by weighting the average response of the PMT – all but null responses to the LED – with the ideal response of a PMT to one PE, determined from Poisson statistics.

$$gain = \left(\frac{1-e^{-\mu}}{\mu}\right)\left(\frac{Q_{tot}}{N}\right) \quad (1)$$

The first term in Eq. 1 is the average number of PEs seen by a PMT for a given light level, μ, excluding zero responses, predicted from Poisson statistics. The second term is what the PMT actually sees: the total charge for all PMTs with response past threshold divided by the number of responses past threshold. Total charge is computed by summing up charge in main PMT pulse for all responses with in-time pulses that pass threshold. Double-pulses are not counted in total charge.

PMTs in the MiniBooNE detector need to have a gain of 16×10^6 electrons per incoming PE as dictated by MiniBooNE electronics. Operating voltage for each PMT is chosen to pick out this gain. The distribution of operating voltages at which the PMTs will run in the detector is shown in Fig. 2.

B. Darkrate

Darkrate is the number of pulses larger than 3 mV in one second for a PMT that has conditioned in a light tight environment for $12-48$ or more hours. PMTs should operate at a darkrate below 8 kHz in the main tank and below 4 kHz in the veto. These levels ensure that the electronics can keep up and that this noise does not interfere with signal. Darkrates are measured from several hundred volts below suggested operating voltage up to operating voltage and above. PMTs with darkrates above 8 kHz are re-tested and either improve with more conditioning or are not used in the detector. Darkrate versus voltage plots, or plateau plots, are another indicator of PMT quality. PMTs should operate where they are stable – on the plateau on these plots where darkrate does not change significantly as the voltage increases. For the new PMTs, this is at about 1550 V and above. The LSND PMTs tend to have a less well defined plateaus. They are considered functional if operating voltage is on a steady, not a steep rise.

C. Charge Resolution

Charge resolution, σ_q, is determined by extracting the width of the one photo-electron peak also derived from possion statistics. The distribution of charge resolutions for all PMTs is shown in Fig. 3.

D. Timing Resolution

PMT response to LED pulses is recorded from an oscilloscope triggered by the LED pulses. The amount of jitter in this response corresponds to the timing resolution. To measure this, the time the PMT pulse crosses half max for each of the 1000 LED responses is histogramed. The width of this distribution corresponds to the timing resolution of the PMT. Pre- and post-pulses are not included in this histogram. Timing resolutions do not change significantly when response time is recorded at 10% of the PMT pulse. The distribution of timing resolutions for all PMTs is shown in Fig. 4.

E. Double-pulsing Rate

Pre- and post-pulsing are expected phenomena with these Hamamatsu PMTs. When it occurs, the main PMT response is either preceded or followed by another pulse or more. Pre-pulsing is thought to occur when the ejected electron from the photocathode skips the first dynode. Pre-pulses occur at nearly the same time relative to the main pulse because the time it takes for an electron to travel from one dynode to the next is fixed. Pre-pulsing occurs very infrequently (observed on four of the 1240 LSND PMTs) and can come and go. PMTs exhibiting pre-pulsing behavior were not placed in the signal region in the detector.

Post-pulsing is categorized by Hamamatsu as either early post-pulsing occurring between 8-60 ns after the main pulse or after pulsing occurring 100 ns-16 μs after the main pulse. We are only worried about early post-pulsing because data in the detector is recorded in 100 *ns* intervals making afterpulsing an unlikely issue for event contamination. Early post-pulsing can occur when an electron accelerated to the first dynode starts a typical cascade and causes another electron to be ejected from the first dynode. This second particle can move around the inside of the PMT dome before settling back to the first dynode and initiating a second cascade. This post-pulse can occur almost on top of the main pulse to many ns afterwards. Post-pulsing can also occur without any main pulse. Unlike pre-pulses, post-pulses are spread out in time since there is no typical time for a particle to bounce off the first dynode before initiating a second cascade.

Hamamatsu reports that R5912 PMTs are expected to early post-pulse 3% of the time. Many new PMTs had higher double-pulsing rates than this after conditioning for 12-24 hours. After further conditioning, PMT double pulsing rate was reduced. Based on this, we set a double-pulsing rate limit of 6% for the new PMTs and 3% for the LSND PMTs. The distribution of PMT double-pulsing rates for all PMTs is shown in Fig. 5.

F. Categorizing PMTs

PMTs with darkrates below 8 kHz, low double-pulsing rates and reasonable charge and timing response are placed in the detector according to their charge and timing resolutions. Placement according to this figure of merit is designed to ensure that PMTs of higher quality are equally distributed around the detector. PMTs chosen for the veto are those with the worst charge and timing resolution but the lowest darkrate. These PMTs are needed only to see light from a passing charged particle and not for particle identification. PMTs with low noise rates are ideal for this.

G. Calibration Data

Calibration data taken during the course of testing help to quantify errors on these measurements. Table I shows the spread in measurements taken by calibration PMTs which correspond to the errors on those measurements for each PMT.

Darkrates decrease as a function of conditioning time.

TABLE I
Errors on PMT figures of merit as determined from calibration data

gain	0.19
charge resolution	0.34
timing resolution	0.13
double-pulsing percentage	0.60

This was seen by a steady decrease in darkrate on the calibration PMT as it moved, day by day, to different positions in the testing room, conditioning more each day. Light level seen by this PMT varied from 0.5 to 1.5 PEs from winerack location to location. Calibration information helped us to understand the error on our measurements as well as to track any changes in the winerack as a function of time.

IV. Conclusions

The MiniBooNE detector uses Čerenkov and scintillation light signatures from charged particles produced in charged current neutrino interactions to tag the flavor of the incident neutrino. Appearance of electron neutrinos in the muon neutrino beam would indicate neutrino oscillations like those reported by the LSND experiment. The 1280 PMTs in the signal region as well as the 241 PMTs in the veto are the only detector component to resolve these light signatures. The detailed tests performed have allowed us to properly place these PMTs in the detector as well as study properties of the PMTs which will affect our measurement.

References

[1] A. Aguilar *et al.* [LSND Collaboration], "Evidence for neutrino oscillations from the observation of $\overline{\nu}_e$ appearance in a $\overline{\nu}_\mu$ beam," [hep-ex/0104049].

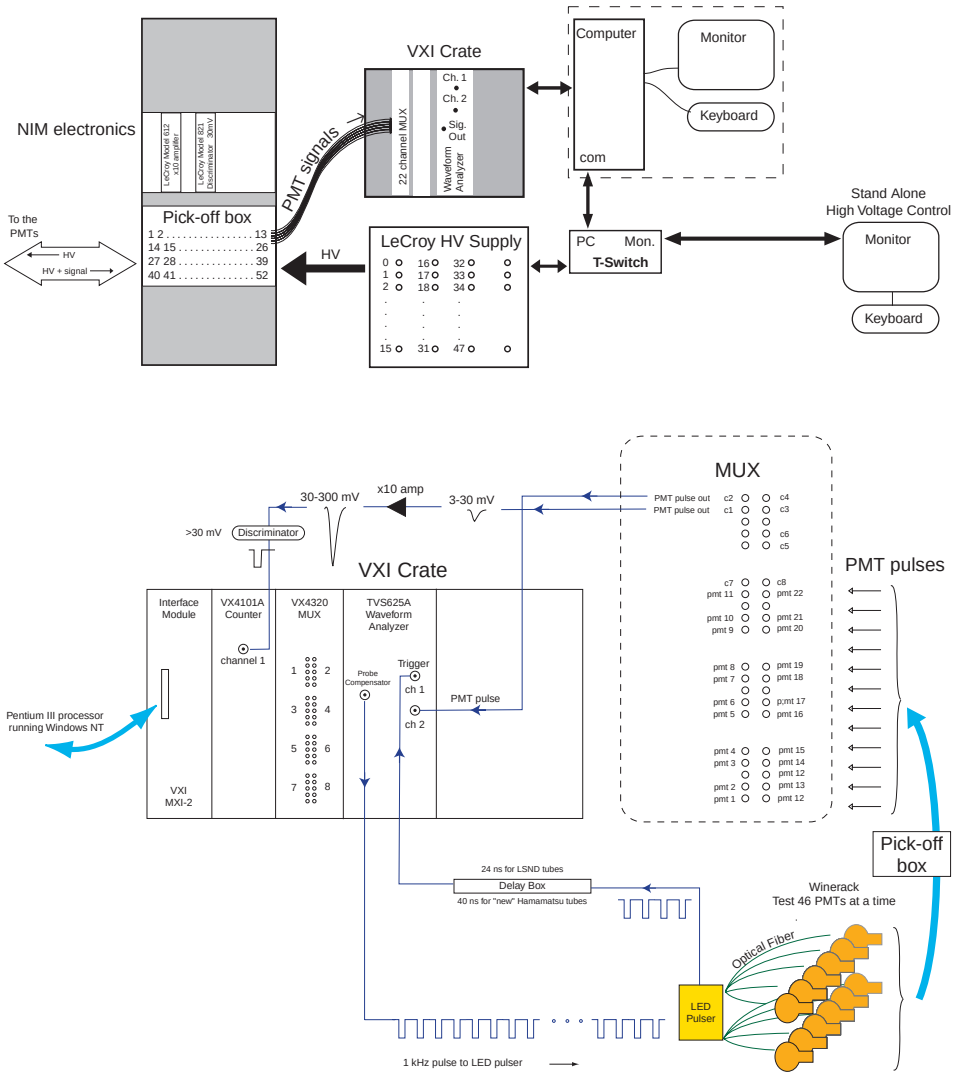

Fig. 1. PMT testing facility with the VXI crate.

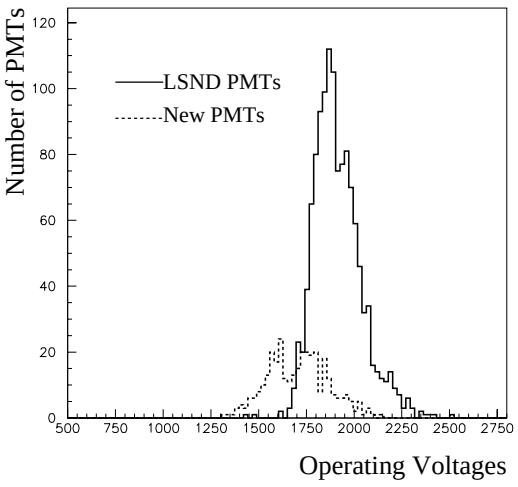

Fig. 2. Distribution of operating voltages for PMTs in the detector

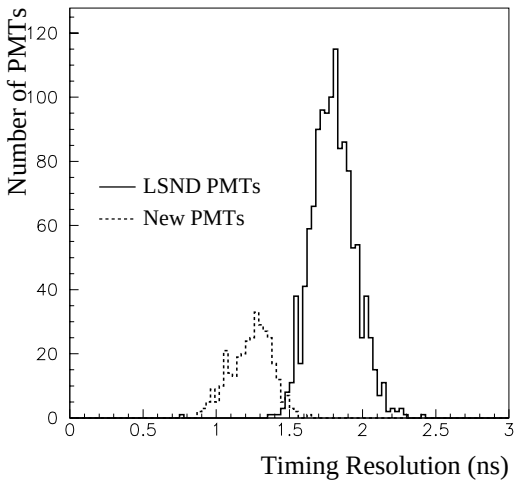

Fig. 4. Distribution of PMT time resolutions.

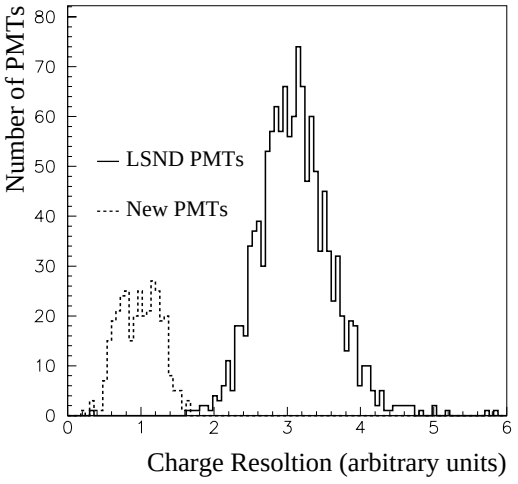

Fig. 3. Distribution of PMT charge resolutions.

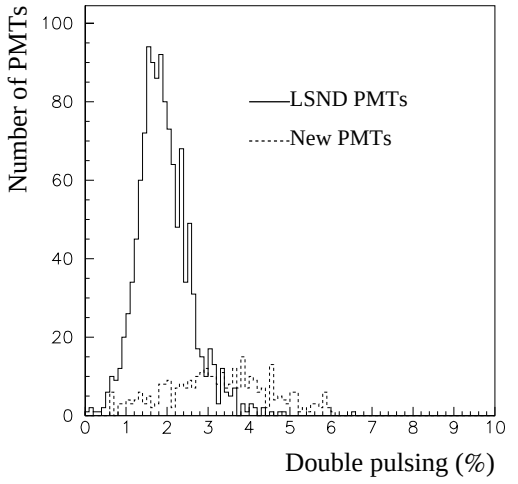

Fig. 5. Distribution of PMT double-pulsing rates.

Appendix D

MiniBooNE Photomultipier Tubes

PhotoMultiplier Tubes (PMTs) work like light bulbs in reverse: light comes in, electric pulse comes out. Specifically, light falls on the photocathode, the emitted electrons are amplified in a dynode chain so that a current corresponding to the number of photons that hit the photocathode is produced. PMTs must be set at a specific voltage to pick out the proper gain, or output current per each input photon. Then, the charge and timing information recorded from each PMT can be used to reconstruct the events off-line. Ideally, one knows exactly when and how many photons from the muons or electrons hit each PMT. In the real world, we must test the PMTs to determine these resolutions. To this end, each PMT is tested to determine if the PMTs are functional, what their operating voltage should be set to, and how good their timing and charge resolutions are. The PMTs are the only detector elements in the MiniBooNE experiment. Thus, it is important to measure their operating characteristics so the sensitivity of the MiniBooNE detector can be optimized.

D.1 Pre-installation Testing of the Photomultiplier Tubes

There are 1280 8 inch PMTs that will line the inner volume of the detector. Another 240 PMTs are in the veto region to detect light produced by charged particles entering from outside the detector–most likely from cosmic rays. Of the total 1520 PMTs in the MiniBooNE detector, 1197 are inherited from the LSND experiment and the rest are recently purchased from Hamamatsu. The LSND PMTs are 8 inch in diameter, 9 stage, Hamamatsu model R1408 PMTs while, the newly purchased PMTs are 8 inch, 10 stage, Hamamatsu model R5912 PMTs. The R5912 is an upgraded version of the R1408. Detailed description of how PMTs work and specifications for the R1408 and R5912 can be found in Appendix E. There are many spare LSND PMTs and a few spare new PMTs that have not been installed in the detector and can be used for specialty tests to determine PMT characteristics [101].

Before installing the PMTs in the MiniBooNE detector, they were all tested to measure their operating characteristics. Although two varieties of tubes were tested, it was important that they give a similar response to a single photon striking the photocathode. In particular, the PMT operating voltage for the chosen gain for MiniBooNE, that is, an output of 16×10^6 electrons for each photoelecton (PE) was determined for each PMT. Other characteristics of the PMTs were also recorded during the tests such as dark current, time jitter, charge resolution, double-pulsing, and pulse shape. Using these other characteristics, the PMTs were grouped into five categories. Tubes assigned to categories 1 through 4, with 1 being the best and four the worst, were put in the inner sphere while tubes in the 5^{th} category were placed into the veto region. Tubes in the first four categories were randomly distributed throughout the detector to insure an even distribution of the best and worst PMTs around the detector. PMTs in the veto do not have to have the best charge and timing resolution as they are not relied upon for reconstruction, but should have the

lowest possible darkrate, or noise levels. Therefore, category 5 PMTs in the veto are of the same quality as category 4s, the worst, but are chosen to have the lowest darkrates to ensure the lowest possible noise levels in the veto.

D.1.1 Testing Setup

The PMT testing began in the northeast Lab E portakamps starting March 31, 2000. The tubes were placed in light tight 55-gallon drums with high voltage and optical fiber feedthroughs for light for PMT tests from an LED flasher at the top. Up to 12 PMTs at a time were conditioned under high voltage at 1000-1500 volts in darkness for 12-24 hours before testing. Once conditioned, the PMTs were tested in air and their dark currents and waveforms, acquired on an oscilloscope and transferred via GPIB, were recorded on disk files to be studied off-line.

The Lab E testing setup proved time consuming so the setup was streamlined by moving it to a darkroom in the New Muon Lab where up to 46 PMTs could be tested in one day. A "wine-rack" assembly was constructed against one wall of the dark room. The PMTs were propped on their sides facing an optical fiber carrying light from the LED flasher. A side view of a PMT in the wine-rack is shown in Fig. D.2. The rack accomadates 30 LSND PMTs affixed by their stands and 16 new PMTs resting in Styrofoam molds. Stands were affixed to the new PMTs after the testing stage was completed as described in section D.4.

The PMTs were conditioned in the darkroom for 12-24 hours at approximately 1000 volts. Testing procedure to determine dark rates and waveform response to an LED proceeded as in Lab E. PMTs were tested individually; darkrates recorded and waveforms acquired from an oscilloscope, to data files. In September 2000, the testing procedure was automated by introducing a VXI readout system with a built-in oscilloscope having a maximum capture rate of 10,000 waveforms/90 seconds. The high voltage settings were automated by using a serial I/O interface. Figure D.3

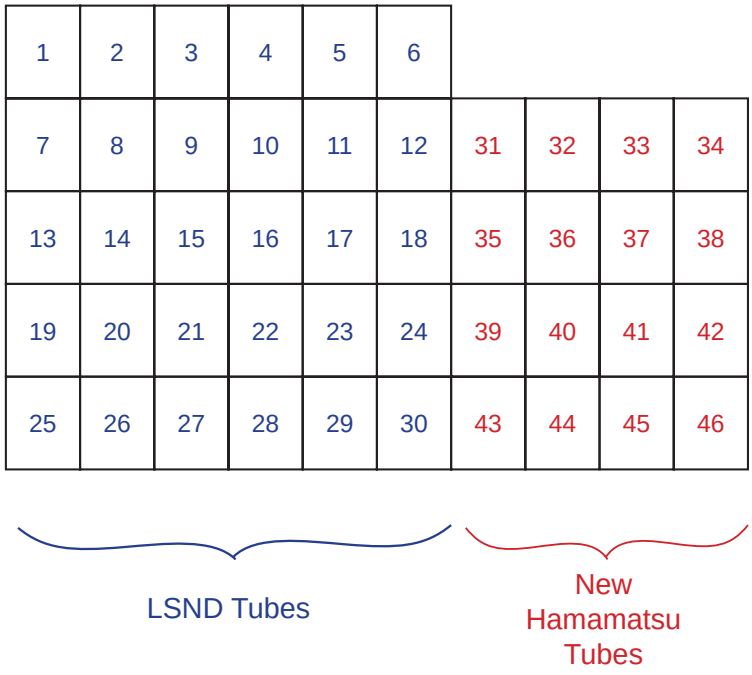

Figure D.1: Wine-rack structure inside the New Muon Lab darkroom

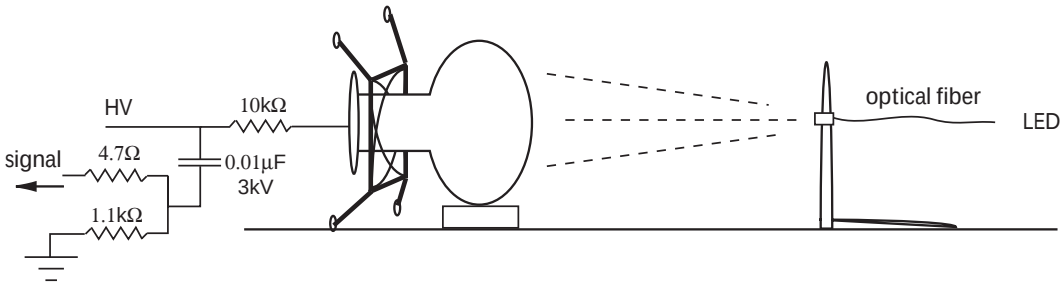

Figure D.2: LSND PMT in the wine-rack

shows the rate at which the PMTs were tested over the course of a year. Testing rate improved greatly after the move from Lab E to the New Muon Lab, and again after the arrival of the VXI readout system.

The VXI Readout System

The VXI readout system allowed for automatic testing of 22 tubes in a single run. The number of tubes that could be tested simultaneously was limited by our use of one multiplexer. A schematic diagram of the system is shown in Fig. D.4. Tests were

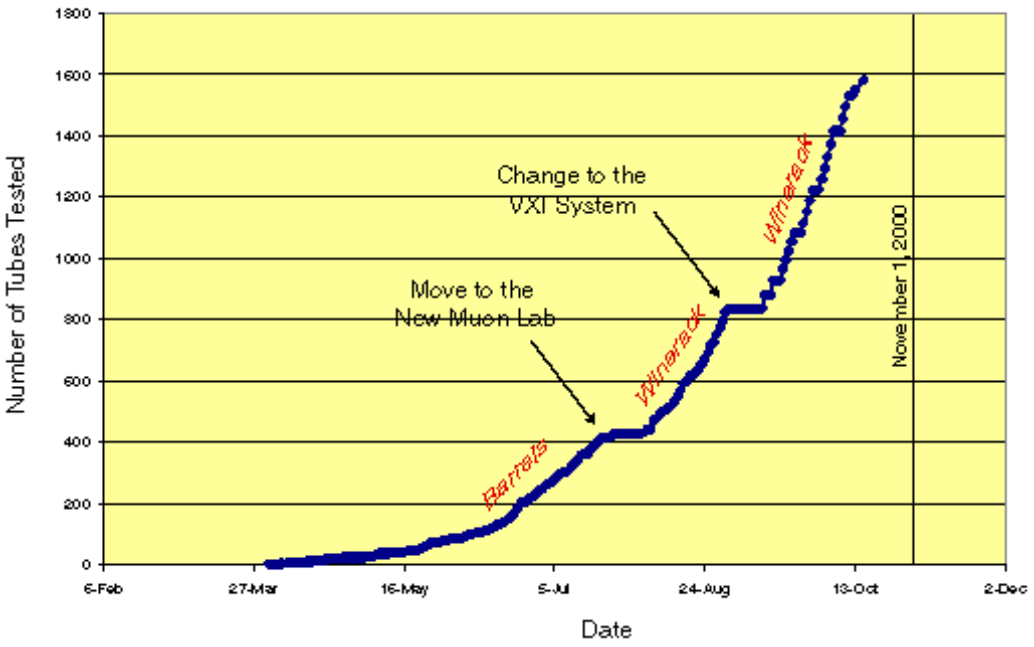

Figure D.3: PMT testing rate.

performed to make sure that the VXI readout did not introduce systematic changes when compared to the previous GPIB interface used to test tubes one at a time. Once the testing was complete, the data files were stored for data analysis.

PMT Testing Facility with the VXI Crate

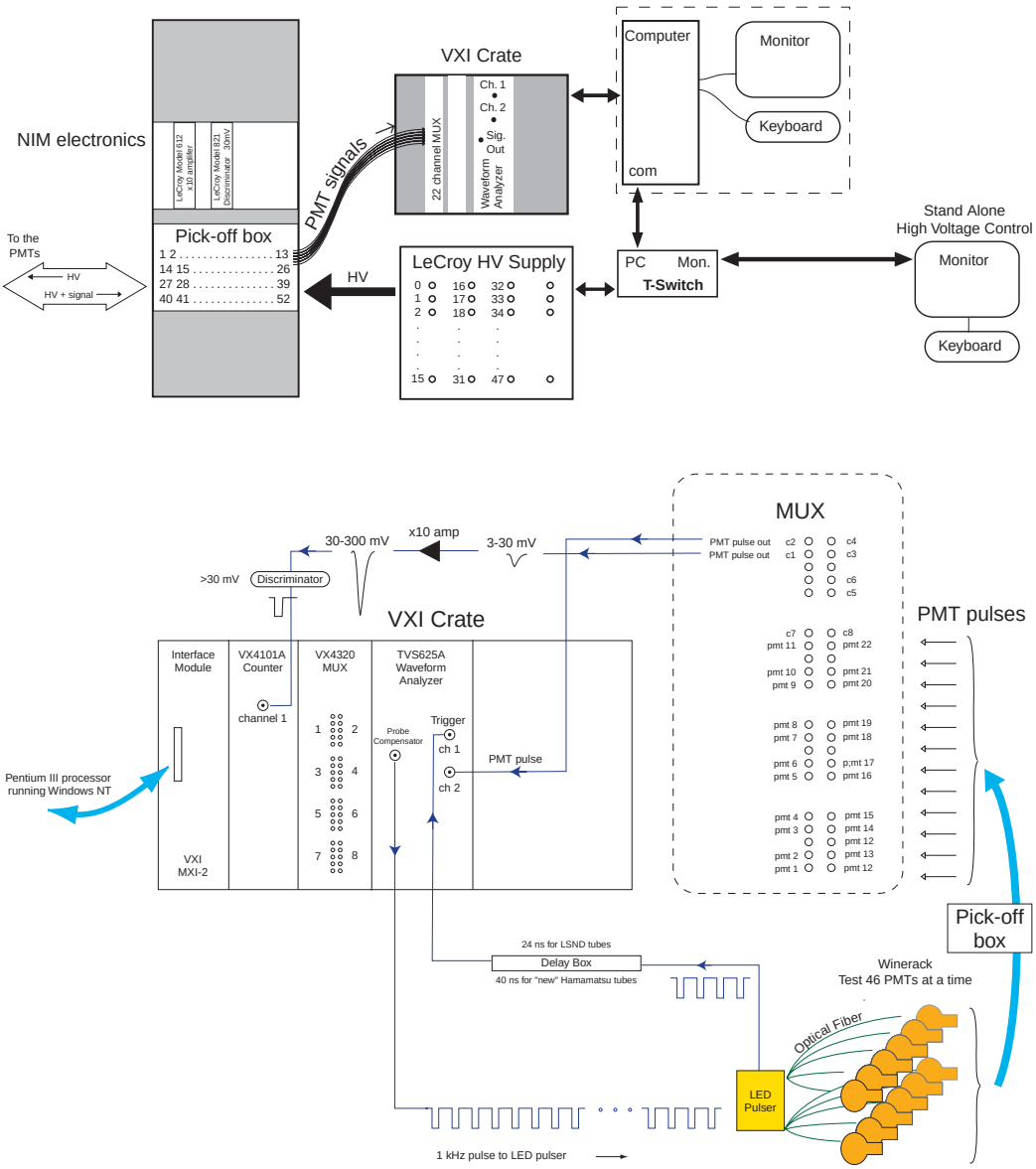

Figure D.4: PMT testing facility with the VXI crate.

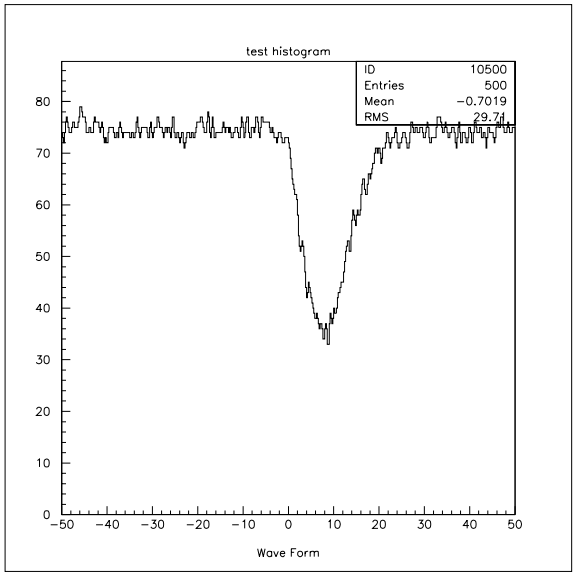

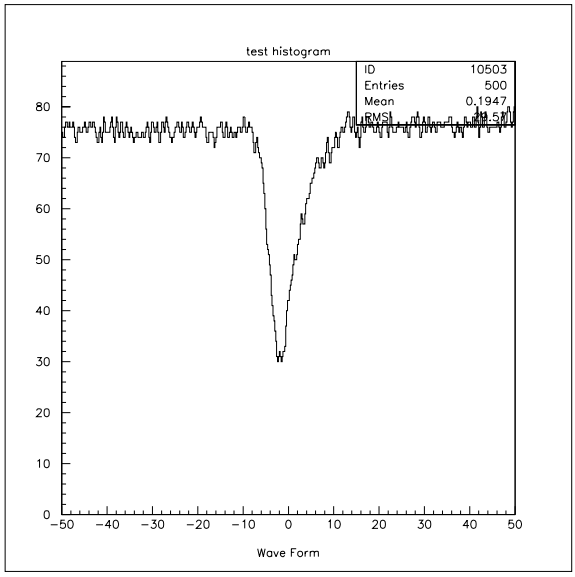

Figure D.5: LSND PMT response to LED Figure D.6: New PMT response to LED

D.1.2 Testing Procedure

There is a trade off between amount of test data that can be taken and the amount of time it takes to perform the tests. For this reason, tests performed are enough to set operating voltages and determine PMT quality while keeping the testing procedure short.

For all test setups described above, PMTs were tested in dark room conditions in air under high voltage. Their signal response returning from the PMT (Fig. D.2) rides on top of the input high voltage cable where it passes through an AC capacitive pick-off to reset its baseline voltage to zero. A typical response from an LSND and new PMT is shown in figures D.5 and D.6.

The testing data acquisition occurred in two modes. In the first mode, the dark currents were collected by recording the noise rates measured at different voltages with no light source. Pulses passing a 3 mV threshold were counted as dark noise and used to determine the dark noise rate. The dark noise was measured at various voltages starting at approximately 1000 V and at increments of 100 V above this to

approximately 100 V above the PMTs suggested operating voltage. Suggested operating voltages for the new PMTs were supplied by Hamamatsu; suggested operating voltages for the LSND PMTs was assumed to be their operating voltage during the LSND experimental run.

After the dark noise rates were recorded, the tube was strobed with an LED light source at 450 nm for a duration of 1 ns at 1 kHz to look at light induced waveforms. PMT response to 600-1000 LED flashes piped in through fiber optic, were recorded and used to determine the operating voltage at a chosen gain, to study the charge and time resolutions and to search for pre- and post-pulsing anomalies. Responses were triggered off the LED pulse and delayed so that they appear about $\frac{2}{5}$ths of the way in time into the scope. This timing allows for adequate determination of the pre-pulse baseline and ample time after the pulse to look for post-pulsing. Because the new Hamamatsu tubes (R5912) have one more dynode element in the dynode chain compared to the LSND tubes (i.e., 10 instead of 9) an additional 16-18 ns was required in the trigger delay when testing new tubes. Measurements with various trigger delays are shown in figure D.7.

LED tests were performed at two different voltages for the LSND PMTs:

- LSND operating voltage - 50 volts.
- LSND operating voltage + 50 volts.

and 4 different voltages for the new PMTs:

- Hamamatsu suggested operating voltage - 100 volts.
- Hamamatsu suggested operating voltage
- Hamamatsu suggested operating voltage + 100 volts.
- Hamamatsu suggested operating voltage + 150 volts.

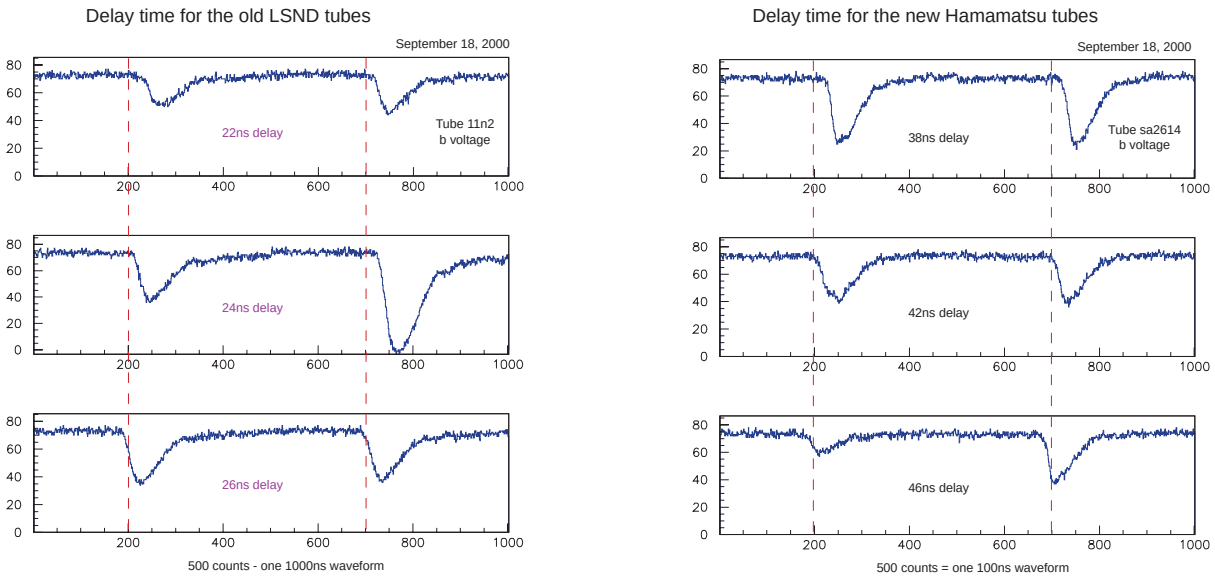

Figure D.7: Pulses should have 200 counts (40 ns) to determine their baseline pedestal. Likewise pulses should start soon after the 200^{th} count. An appropriate trigger delay for the two types of tubes is determined from the above waveforms.

Multiple tests are necessary for determination of the gain and should be conducted near the nominal operating voltage (see section D.1.2). The number of tests is as great as needed to determine unknowns about the PMTs while being as few as possible due to time constraints.

Initially, pulses were fed into an oscilloscope triggered off the LED flash and read from the scope via a GPIB interface to a PC running Windows NT. The PC converted the data to charge and timing distributions for visual check and saved the data files to permanent directory for later analysis. With the VXI system, pulses were read of the internal oscilloscope, recorded to data files and analyzed off-line.

Testing setups were calibrated and measurement errors determined by taking calibration data. In the Lab E setup and at the New Muon Lab, we took data on a *rover* PMT which was tested in each possible testing position. In the New Muon Lab we had a *permanent* PMT in addition to the *rover* which was tested in the same spot in the same way almost every test cycle. See section D.3 for details. PMTs whose

testing data was corrupted or who showed questionable behavior were re-tested.

Figures of merit for each PMT

For each PMT, there are 2-4 test data files corresponding to LED response tests taken at different test voltages. Each of these data files is analyzed off-line to determine figures of merit for that data file. Listed below are these figures of merit followed by a more complete description of each.

- PMT testing parameters to be determined are:
  - average number of photo-electrons PMT sees during LED flash
- PMT data file figures of merit determined are:
  - gain
  - charge resolution
  - timing resolution
  - double-pulsing rate
  - darkrate

Light levels: The number of photoelectrons produced in a phototube follows a Poisson distribution. PMT response for each of the 1000 LED flashes for typical old and new PMTs are shown in figures D.8 and D.9. There is a spike corresponding to the null responses, when there was no response from the PMT to the LED flash, followed by a valley and then a rise to the one photo-electron peak. Equation D.1 describes the probability for seeing N photo-electrons given a light level, μ as predicted by Poisson statistics.

$$P(n) = \frac{\mu^n}{n!} e^{-\mu} \tag{D.1}$$

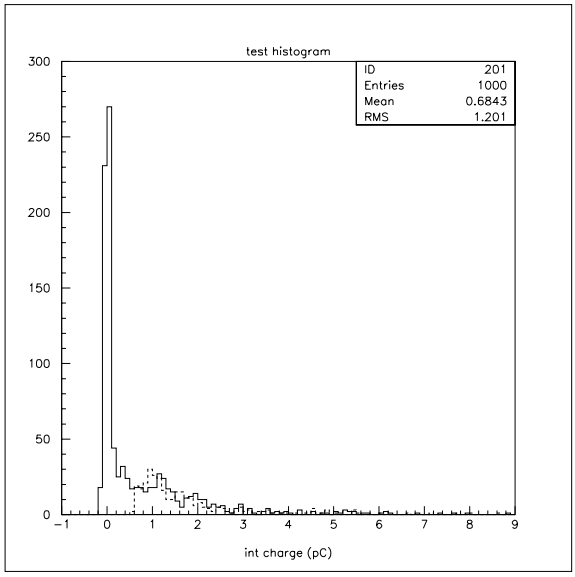

Figure D.8: LSND PMT charge response

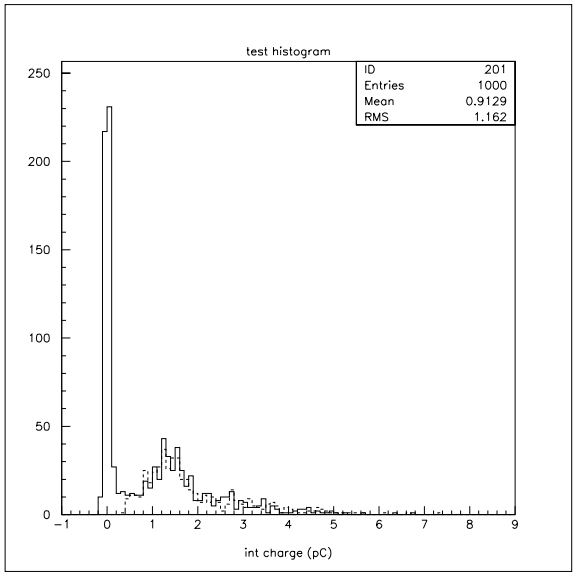

Figure D.9: New PMT charge response

The percentage of null responses, $P(0)$, can be used to determine the average light level, μ, seen by the PMT using the above equation for the case $N = 0$.

In order for the PMT to see a clear one PE response peak to the LED, light levels should be very low ($<$ .1 PE) and statistics very high. This was not possible for our test setup, so light levels were kept between $<$ .5 PEs$>$ and $<$ 1.5 PEs$>$ for the old PMTs and $<$ .5 PEs$>$ and $<$ 2.0 PEs$>$ for the new PMTs. The lower limit was set to be as low as possible with acceptable statistics. The upper limits were determined by how well we could calculate figures of merit at higher light levels. Specifically, when do gain and charge distribution measurements change as light levels increase. This was tested using new and old PMTs tested at different light levels. The measurements do not change up to 2 PEs for the new PMTs and up to 1.5 PEs for the old ones. The new PMTs have a more distinct valley between the null responses and the one PE peak. This distinct valley could cause less smearing between the null responses and the one PE peak as the light level changes than for the old PMTs. Since the gain and charge resolution calculations depend on the amount of light the PMT saw (see below), determined from the null responses, the new PMT's gain calculation is

more robust at higher light levels than the old PMT's. PMTs tested with light levels outside of these cuts are studied and possibly re-tested.

Gain: PMT gain corresponds to the mean number of electrons produced by the phototube in response to one photo-electron. Ideally, one could just read off the gain as the mean of the one PE peak in fig. D.9. The width of this one PE peak then corresponds to the to charge resolution. However, the one PE peak for these tests contains response to 2 and 3 PEs and maybe more. Gain is then determined by weighting the average response of the PMT – all but null responses to the LED – with the ideal response of a PMT to one photo-electron determined from Poisson statistics. Equation D.2 shows how this is calculated.

$$gain = \left(\frac{1 - e^{-\mu}}{\mu}\right)\left(\frac{Q_{tot}}{N}\right) \tag{D.2}$$

The first term in Eq D.2 is the average number of photo-electrons seen by a PMT for a given light level, excluding zero responses, predicted from Poisson statistics. The second term is what the PMT actually sees: the total charge for all PMTs with response past threshold divided by the number of responses past threshold. Total charge is computed by summing up charge in main PMT pulse for all responses with in-time pulses that pass threshold. Double-pulses are not counted in total charge. Error on the gain can be determined from calibration data discussed in section D.3.

Charge Resolution: Charge resolution, σ_q, is determined by extracting the width of the one photo-electron peak also derived from possion statistics. Equation D.3 is the width of the one PE peak in terms of μ and the total charge, as determined for the gain calculation. See section D.5 for a derivation of equation D.3.

$$\sigma^2_{1pe} = \left(\left(\frac{Q^2_{tot}}{N}\right) - \left(\frac{Q_{tot}}{N}\right)^2\right)\left(\frac{1 - e^{-\mu}}{\mu}\right) + \left(\frac{1 - e^{-\mu}}{\mu}\frac{Q_{tot}}{N}\right)^2\left(\frac{\mu e^{-\mu}}{1 - e^{-\mu}} - 1\right) \tag{D.3}$$

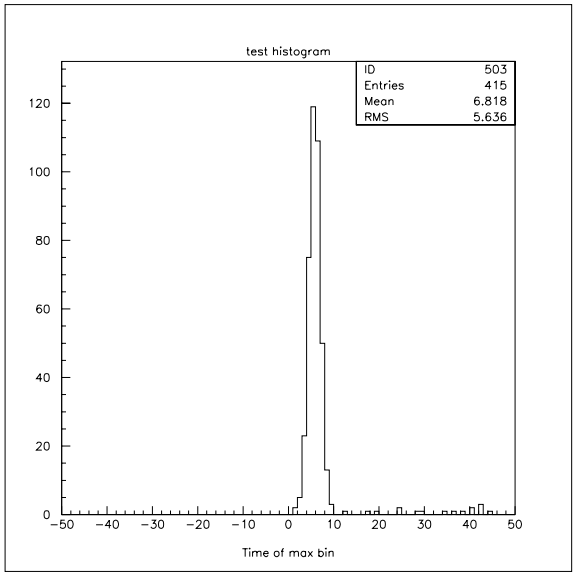

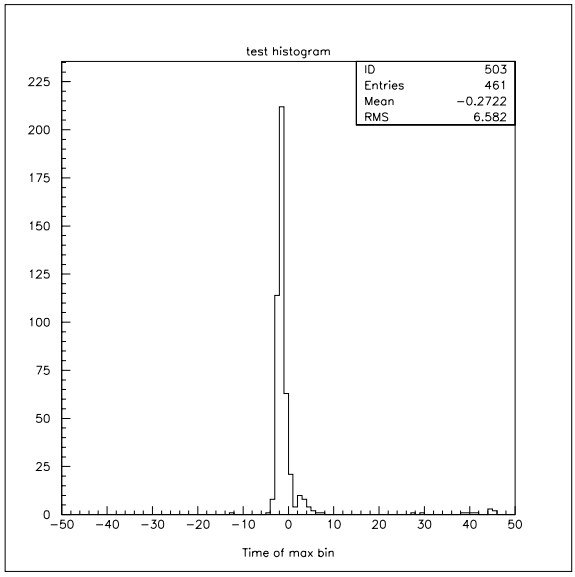

Figure D.10: LSND PMT timing response Figure D.11: New PMT timing response

Timing Resolution: PMT response to LED pulses is recorded from an oscilloscope triggered off the LED pulses. The amount of jitter in this response corresponds to the timing resolution. To measure this, the time the PMT pulse crosses half max for each of the 1000 LED responses is histogram ed. Width of this distribution corresponds to the timing resolution of the PMT. Pre- and post-pulses are not included in this histogram. Typical timing response histograms for new and LSND pmts are shown in figures D.10 and D.11. Error on the timing resolution measurements can be determined from calibration data (see section D.3).

Double-pulsing Rate: Pre- and post-pulsing is a well-documented phenomena with these Hamamatsu PMT's. When it occurs, the main PMT response is either preceded or followed by another pulse or more. Pre-pulsing is though to occur when the ejected electron from the photocathode skips the first dynode. Pre-pulses occur at nearly the same time relative to the main pulse because the time it takes for an electron to travel from one dynode to the next is fixed. Pre-pulsing occurs very infrequently (we've seen it on four of the 1240 LSND PMTs) and can come and go. Figures D.12 and D.13 shows a typical pre-pulse for a troubled PMT and the timing

distribution for the same PMT. Notice the distinct first peak corresponding to pre-pulses. PMT's exhibiting pre-pulsing will not be placed in the signal region in the detector.

Post-pulsing is categorized by Hamamatsu as either early post-pulsing occurring between 8-60 ns after the main pulse or after pulsing occurring 100 ns-16 μs after the main pulse. We are only worried about early post-pulsing because data in the detector is recorded in 100 ns intervals making after-pulsing an unlikely issue for event contamination. Early post-pulsing can occur when an electron accelerated to the first dynode starts a typical cascade and makes another electron jump off the first dynode. This second particle takes a trip around the inside of the PMT dome before settling back to the first dynode and initiating a second cascade. This post-pulse can occur almost on top of the main pulse to many ns afterwards. Post-pulsing can also occur without any main pulse. Figures D.14 and D.15 show a few typical post-pulses and figure D.16 the timing distribution for a post-pulser. The charge comparison plot shows total charge versus charge in the main pulse only. Data points below the line correspond to waveforms exhibiting double-pulsing. Unlike pre-pulsers, post-pulses are spread out in time since there is no typical time for a particle to bounce off the first dynode before initiating a second cascade.

Operating Voltage: Figures of merit for each PMT data file for all PMTs are determined and written to files. A chosen gain is then set to be 16×10^6 electrons per incoming PE as dictated by MiniBooNE electronics. All data files from one PMT are read in to the PMT testing analysis package and voltage at this chosen gain is determined. Operating voltage is related to the gain by equation D.4

$$logG(V) = nlog\frac{k}{n} + nlogV \tag{D.4}$$

A typical plot of gain versus test voltage for each data file is shown in fig. D.17 Points should form a line on this log-log plot. New PMTs will have 3-4 data points

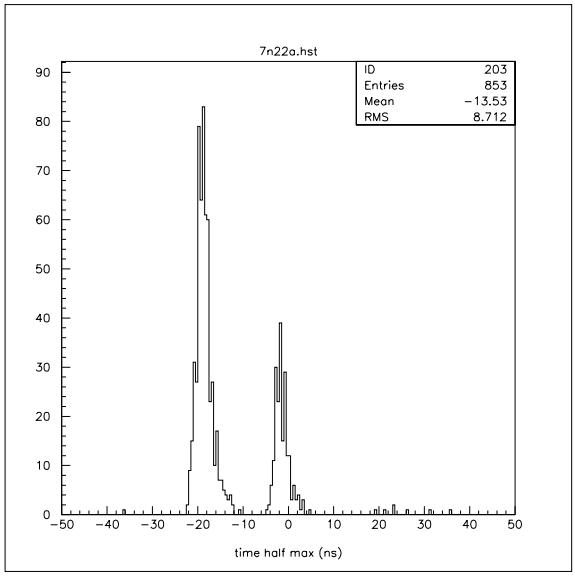

Figure D.12: Timing distribution for pre-pulsing PMT

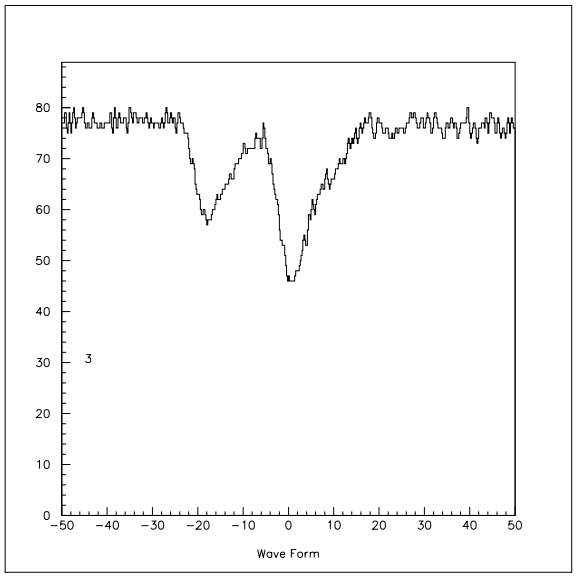

Figure D.13: Pre-pulsing behavior for the same PMT

and LSND PMTs should have 2 corresponding to the number of LED tests taken for each PMT. Fewer tests were performed for the LSND PMTs because these are already somewhat understood. Operating voltage corresponding to the chosen gain is then read off this plot. The distribution of operating voltages at which the PMTs will run in the detector is shown in figure D.18

Darkrate: Once the operating voltage has been determined, the darkrate can be studied. As previously stated, darkrate is the number of pulses larger than 3 mV in one second for a PMT that has conditioned in a light tight environment for $12-48+$ hours. PMT's should operate at a darkrate below 8 kHz in the main tank and below 4 kHz in the veto. These levels ensure that the electronics can keep up and that this noise does not interfere with signal. Darkrates are measured from several hundred volts below suggested operating voltage up to operating voltage and sometimes above. PMTs with darkrates above 8 kHz are re-tested and either improve with more conditioning or are deemed bad. Darkrate versus voltage plots are another indicator of PMT quality. These plots, called plateau plots, are shown in figures D.19

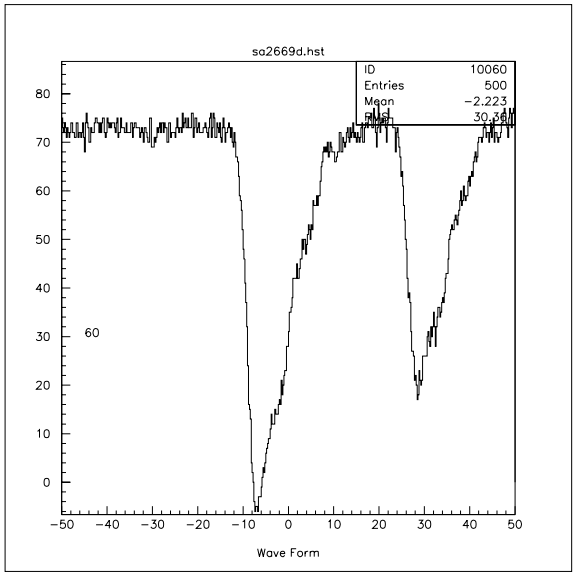

Figure D.14: Timing distribution for post-pulsing behavior

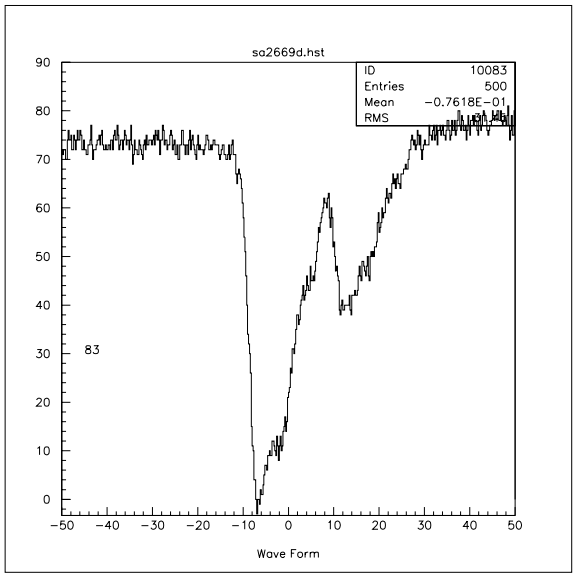

Figure D.15: Post-pulsing behavior for the same PMT

and D.20 for a new and LSND PMT.

PMTs should operate where they are stable – on the plateau on these plots. For the new PMT shown, this is very clearly at about 1550 V and above. The LSND PMTs, like the one shown, tend to have a really wimpy plateau. They are considered OK if operating voltage is on a steady, not a steep rise. PMTs that have a large slope on their plateau plot are re-tested or deemed bad.

D.1.3 Categorizing Photomultiplier Tubes

Threshold cuts:

Once all PMT data files are analyzed and a specific file corresponding to a set gain is chosen, the PMT is categorized for placement in the tank. There are four possible categories in the main tank each populated equally, and one category in the veto. PMTs must first pass threshold cuts in order to go in the detector at all, and are then categorized according to their charge and timing resolution. Threshold cuts along

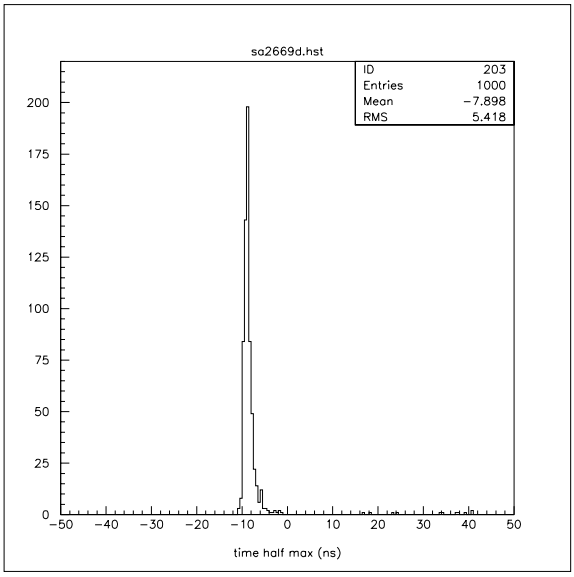

Figure D.16: Timing distribution for a double-pulsing PMT

with PMTs passing each cut, are listed below:

- Average number of PEs seen during test. Fig. D.21 shows light levels each PMT saw.
  - LSND PMT: $.5 << PEs >< 1.5$
  - New PMT : $.5 << PEs >< 2.0$

  PMTs tested with light levels below .5 PEs are individually checked and either accepted or re-tested.

- Darkrate.
  - Main tank : < 8 kHz
  - Veto Region: < 4 kHz

  Darkrates are set to accomadate electronics and to keep noise levels well below signal as shown in figure D.22.

- Darkrate slope (to ensure we are on the plateau): < 50.

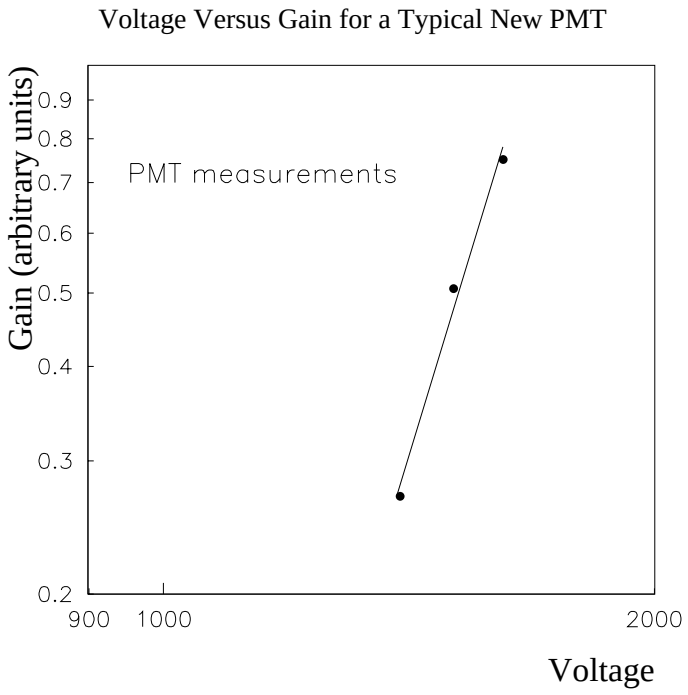

Figure D.17: Operating voltage versus gain on a log-log plot. The line fit points correspond to the best fit to the PMT measurements.

- Double-pulsing rate
  - LSND PMT: $< 3\%$
  - New PMT : $< 6\%$

  Hamamatsu reports that R5912 PMTs are expected to double-pulse 3% of the time. Based on this, we originally set the double-pulsing cut for new and old PMTs to 3%. We found many new PMTs did not pass this cut and would have to be re-tested. Because of the large number of re-tests, we started by studying the double-pulsing rate as a function of conditioning time on a subset of these PMTs with double-pulsing rates as high as 6%. For all new PMTs studied, darkrate decreased continually as PMT continued to condition until darkrate fell below 3%. Based on these results, we set a double-pulsing rate limit of 6%

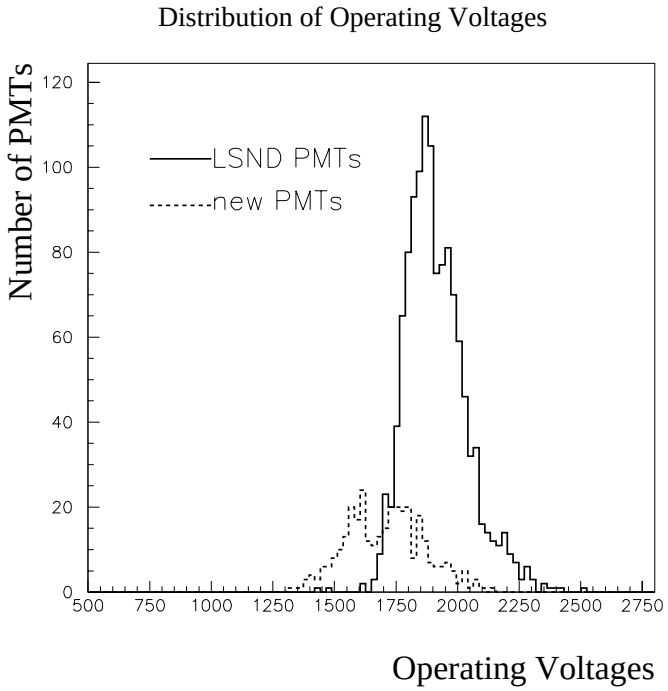

Figure D.18: Distribution of operating voltages for PMTs in the detector

for the new PMTs. These PMTs will have plenty of conditioning time in the tank to decrease their double-pulsing rates. LSND pmts have been conditioning for 6 years in the LSND tank which explains their quieter double-pulsing rates. Any LSND PMTs with double-pulsing rates above 3% are checked individually. PMTs deemed adequate are considered for placement in the main tank. PMTs deemed noisy but otherwise good are considered for placement in the veto.

- Variance in Voltage versus gain fit: $< .001$

  The goodness of the line fit for the new PMTs must be below 0.001 in order for the data files to be accepted otherwise the PMT is inspected individually and placed in the detector or re-tested. The value of 0.001 was determined by looking at the PMTs voltage versus gain plots with the worst fits to see that the error was less than the error in the gain measurement. See calibration data section for discussion of error on gain measurement. Goodness of the fit for

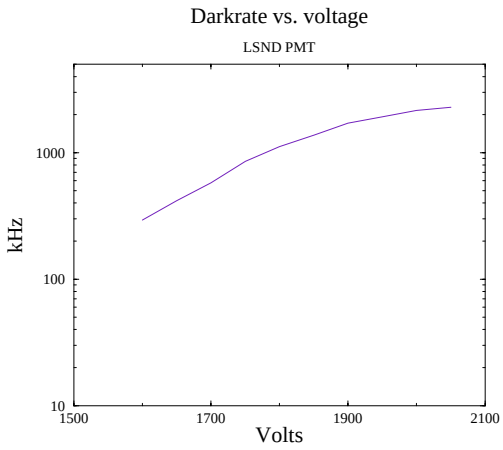

Figure D.19: LSND pmt plateau plot

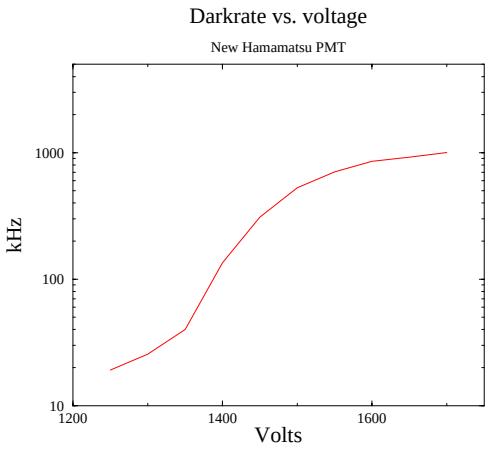

Figure D.20: NEW pmt plateau plot

LSND PMT voltage plots is not considered as there are only two points on these plots.

- Timing Resolution: $.8 < \sigma_t < 2.3$

  Threshold cuts on timing resolution remove data points that are physically unlikely and probably the result of a corrupted data file. PMT data files are fixed or PMTs are re-tested if necessary.

- Charge resolution: $.1 < \sigma_q < 5.8$

  As in the case of the timing resolution threshold cut, charge resolution threshold cut removes only data files with physically unlikely values. PMT data files are fixed or PMT's are re-tested if necessary.

Quality cuts:

Once these threshold cuts are passed, PMTs are categorized according to the value of their charge and timing resolutions added in quadrature ($\sigma_{q,t}$). The cuts on this figure of merit are determined so that there are approximately 320 PMTs in each of

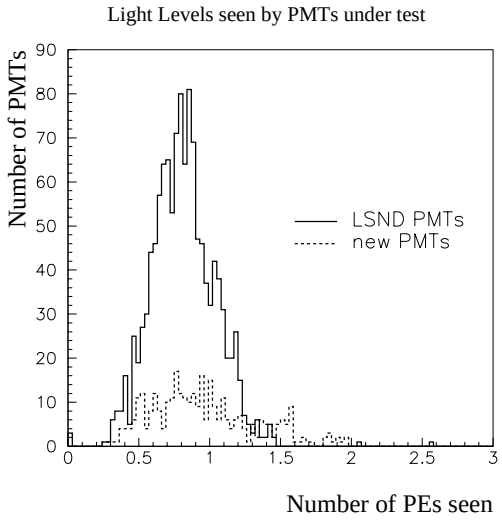

Figure D.21: Distribution of light levels in PEs at which each PMT was tested.

the categories 1-4, and 240 in the veto category. Again, veto PMTs are just category 4 PMTs with darkrates below 4 kHz. Fig. D.27 shows PMTs split by category according to $\sigma_{q,t}$.

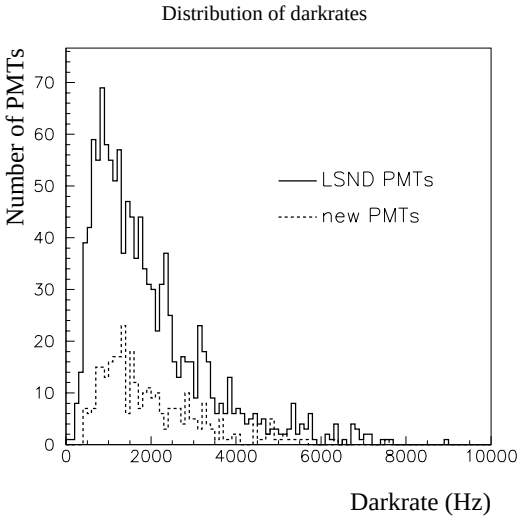

Figure D.22: Distribution of darkrates in the main tank and the veto.

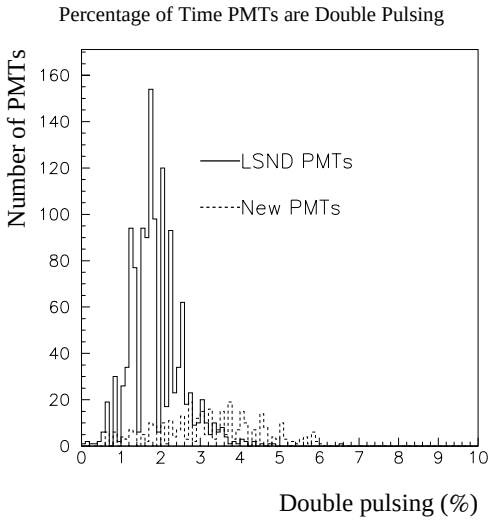

Figure D.23: Dsitributiong of PMT double-pulsing rates.

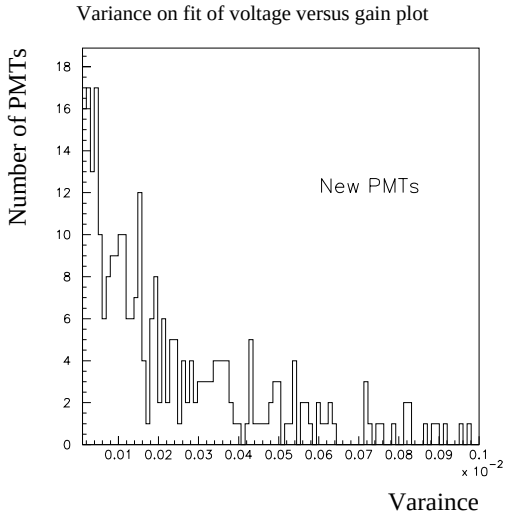

Figure D.24: Variance on line fit to voltage versus gain.

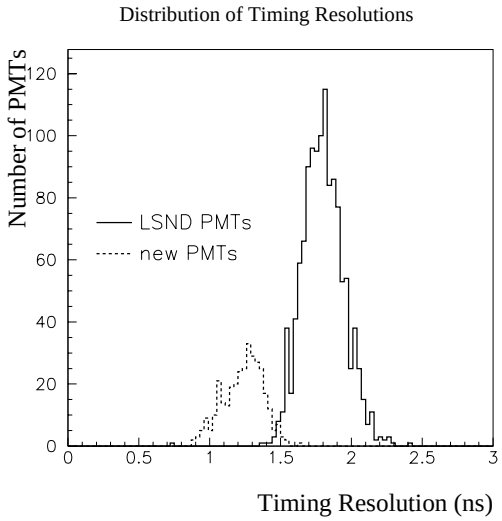

Figure D.25: Distribution of PMT time resolutions.

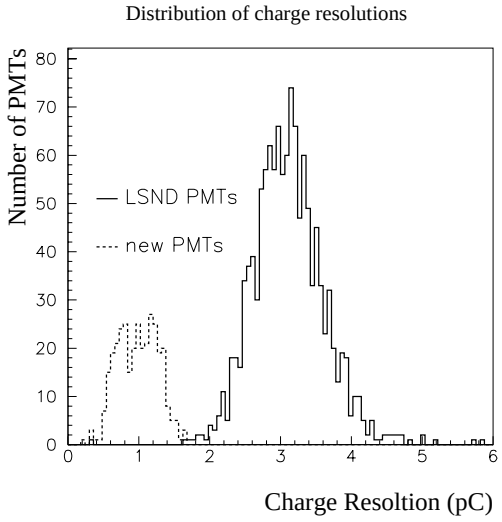

Figure D.26: Distribution of PMT charge resolutions.

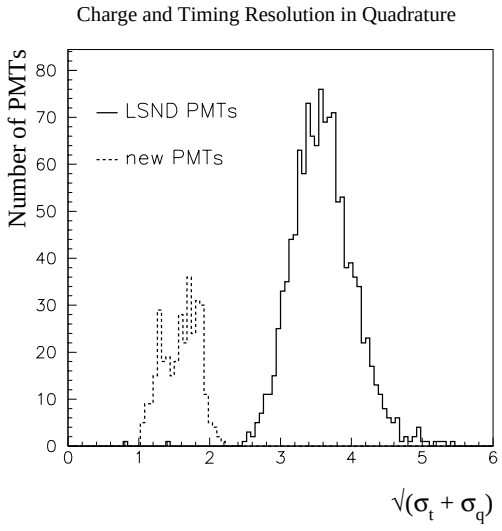

Figure D.27: PMT timing and charge resolution added in quadrature.

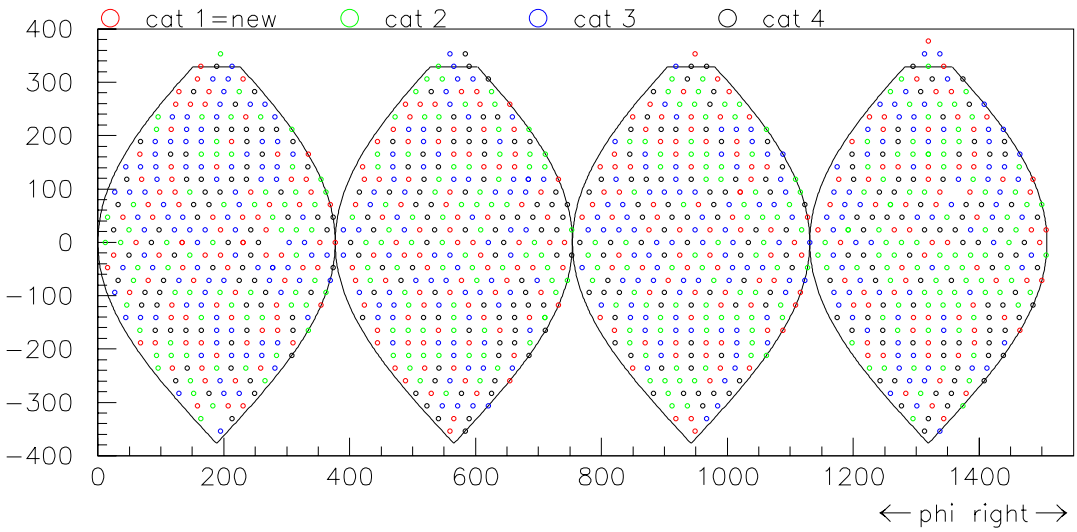

Figure D.28: Distribution by category of each PMT in the detector. Different categories are indicated by different colors. Please see [14] for a version of this picture in color.

D.2 Photomultiplier Tube Distribution in the Detector

Once categorized, PMTs are distributed randomly, category by category, around the main detector. Since there is only one category in the veto, these PMTs are simply assigned a space according to the list. Finally, we check by eye to make sure that there are no unusually high groupings of category one PMTs in any section of the detector. Categories 2-4 are enough a like that bunches of each in any one place are not very worrisome. PMT location and other detector information is then added to each PMT entry in the database. Figure D.28 shows the distribution of PMTs by category in the main tank.

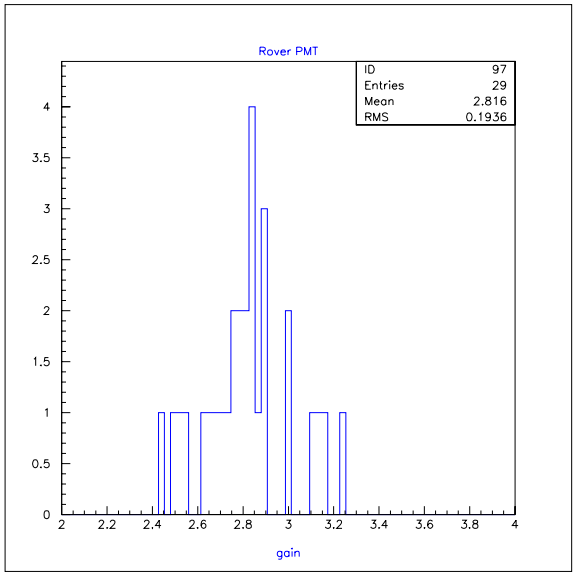

Figure D.29: Gain spread from *rover* PMT measurements.

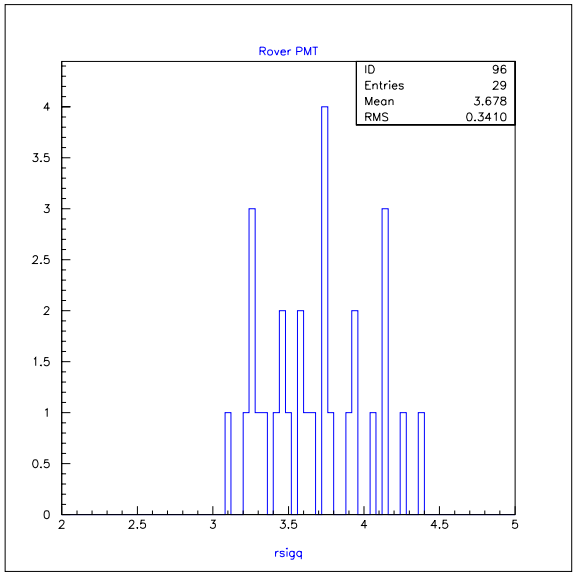

Figure D.30: Charge resolution spread from *rover* PMT measurements.

D.3 Calibration Data

Calibration data taken at the New Muon Lab is used to make sure the system is working properly as well as to determine errors on the measurements. Calibration data taken at Lab E can be used to investigate any oddities in the data for PMTs tested there.

The *rover* PMT data from the New Muon Lab can give us errors on the gain measurement, the charge and timing resolution measurements, and the double-pulsing measurements. The error on each of these corresponds to the width of the distribution of measurements at each location. Figures D.29, D.30, D.31,and D.32 show these distributions and Table D.1 lists the corresponding errors on these measurements.

Both the *rover* and the *permanent* PMT can provide information on the stability of the test setup from position to position as well as from day to day. The range of light levels at different positions in the wine-rack varies from .5 PEs to 1.5 PEs as shown using the *rover* data while the amount of light at the same location has

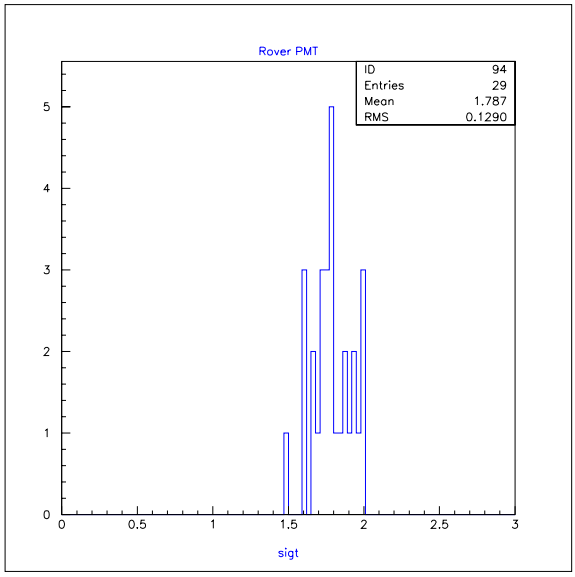

Figure D.31: Timing resolution from *rover* PMT.

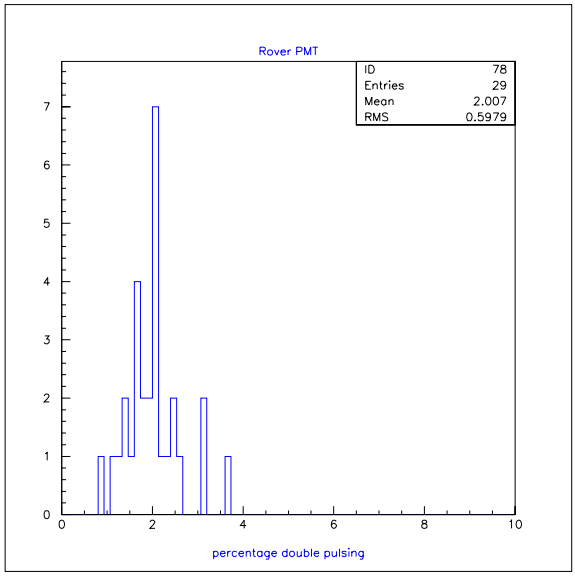

Figure D.32: Double Pulsing % from *rover* PMT.

Table D.1: Errors on PMT figures of merit as determined from calibration data

gain	0.19
charge resolution	0.34
timing resolution	0.13
double-pulsing percentage	0.60

remained constant over time as shown (BTF: insert figure) using the *permanent* PMT.

Darkrates decrease as a function of conditioning time. This is most clearly seen by the steady decrease in darkrate on the *rover* PMT as a function of date, or rather, increasing conditioning time. Figure D.33 shows the steady decrease in darkrate of the rover PMT as it moved from positon to position over time. Also shown are the average light level seen by the PMT, the gain and the charge resolution at different locations in the winerack. All three of these are relatively constant except for the measurment at position 18. This information helped to understand the error on our

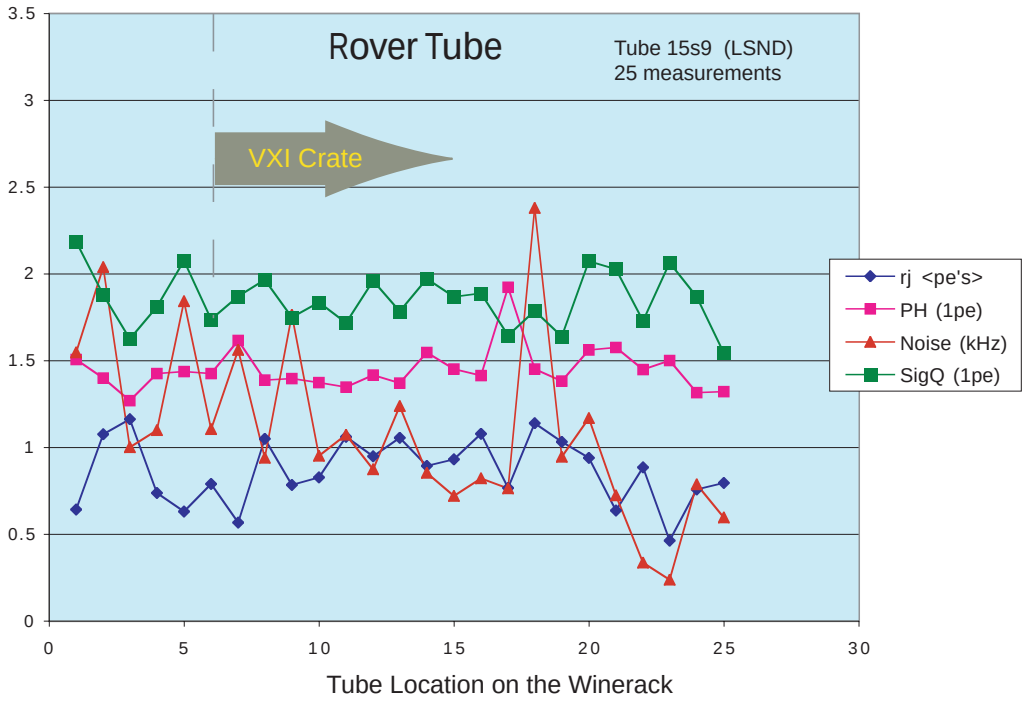

Figure D.33: The rover PMT response as a function of position and time in the winerack. The rover started out in position 1 and moved up one position in the winerack each time a new batch of PMTs was tested. Average light level the PMT saw depictd by the "rj $< pes >$" line. Gain is indicated by the "PH (1pe)" line, darkrate by the "Noise (kHz)" line, and charge resolution by the "SigQ (1pe)" line.

measurements as well as to track any changes in the winerack as a function of time.

D.4 Potting and Installation

Once PMTS were tested and assigned to a location in the tank, they were stored until installation. Approximately two weeks prior to installation, PMTs were removed from storage, prepped in a clean room in Lab E, and transported to the detector for installation. Prepping the PMTs involved:

- Cleaning each PMT with slightly soapy de-ionized water (Dawn dish soap used

as detergent) and rinsing each in clean, de-ionized water bath

- Repairing LSND PMT stands and putting new stands on new PMTs
- Dipping each PMT up to the top of the neck in Masterbond to seal the electronics from the mineral oil and prevent light emission from the next
- Painting Masterbond over metal arms to affix arms to PMT neck
- Storing PMT until Masterbond drys and PMT is ready for installation

PMTs were then transported to the detector and installed along with the inner sphere, row by row.

PMT installation was completed in August of 2001. Figure D.34 shows PMTs after installation from the reflection of all PMTs in one PMT in the detector. A beautiful sight!

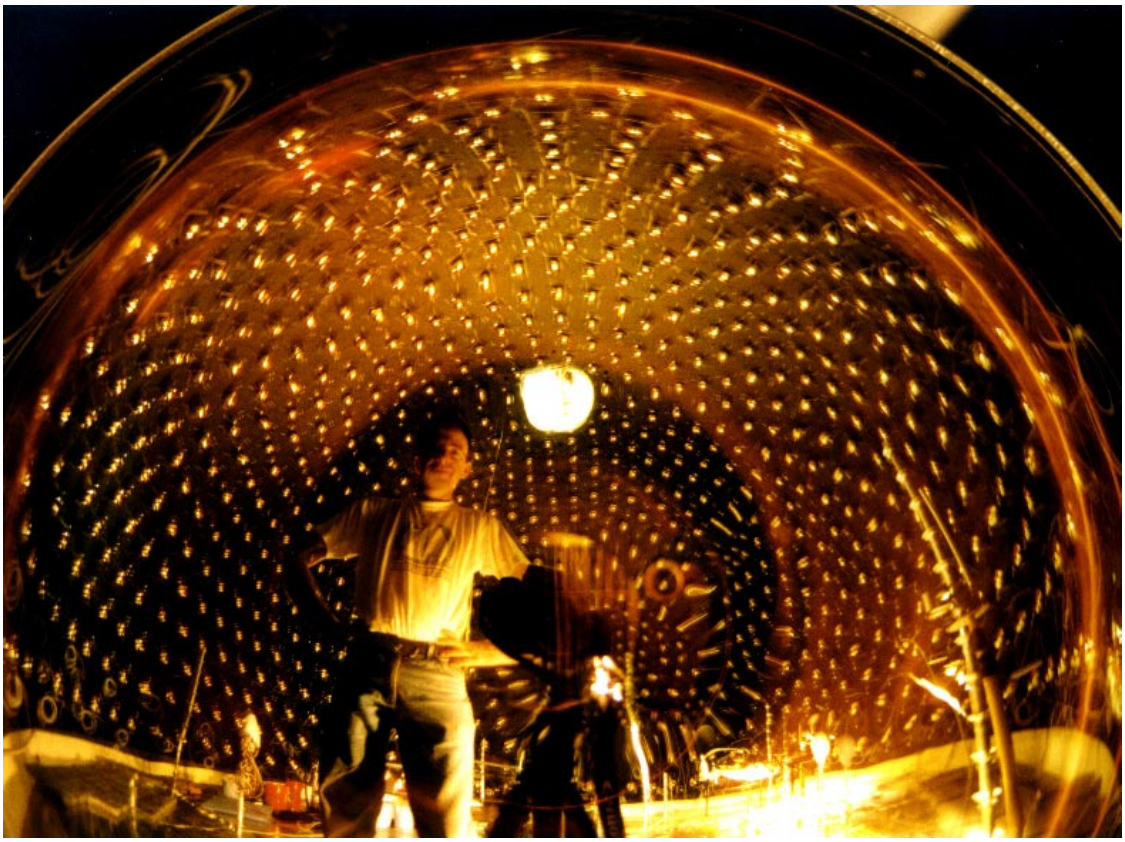

Figure D.34: MiniBooNE collaborator Peter Meyers in the reflection of the inside of the tank as reflected from the face of one PMT.

D.5 Derivation of Charge Resolution Function

Width of 1 PE Peak The number of photoelectrons produced in a phototube follows a Poisson distribution:

$$P(n) = \frac{\mu^n}{n!} e^{-\mu}$$

where μ is the average number of photoelectrons (PEs). This distribution is normalized since:

$$\sum_{n=0}^{\infty} P(n) = \sum_{n=0}^{\infty} \frac{\mu^n}{n!} e^{-\mu} = e^{-\mu} \sum_{n=0}^{\infty} \frac{\mu^n}{n!} = e^{-\mu} e^{\mu} = 1.$$

The average of this distribution is given by:

$$\begin{aligned}
\langle n \rangle_0 &= \frac{\sum_{n=0}^{\infty} nP(n)}{\sum_{n=0}^{\infty} P(n)} \\
&= \frac{\sum_{n=0}^{\infty} \frac{n\mu^n}{n!} e^{-\mu}}{1} \\
&= \mu e^{-\mu} \sum_{\mathbf{n}=1}^{\infty} \frac{\mu^{n-1}}{(n-1)!} \\
&= \mu e^{-\mu} \sum_{\mathbf{n}=0}^{\infty} \frac{\mu^n}{(n)!} \\
&= \mu e^{-\mu} e^{\mu} \\
&= \mu
\end{aligned}$$

and the second moment is given by:

$$\begin{aligned}
\langle n^2 \rangle_0 &= \sum_{n=0}^{\infty} n^2 P(n) \\
&= \sum_{n=0}^{\infty} \frac{n^2 \mu^n}{n!} e^{-\mu} \\
&= \mu e^{-\mu} \sum_{\mathbf{n}=1}^{\infty} \frac{n\mu^{n-1}}{(n-1)!} \\
&= \mu e^{-\mu} \sum_{\mathbf{n}=0}^{\infty} \frac{(n+1)\mu^n}{n!} \\
&= \mu e^{-\mu} \left(\sum_{\mathbf{n}=0}^{\infty} \frac{n\mu^n}{n!} + \sum_{\mathbf{n}=0}^{\infty} \frac{\mu^n}{n!} \right)
\end{aligned}$$

$$= \mu e^{-\mu}(\mu+1)e^{\mu}$$
$$= \mu(\mu+1)$$

Thus the sigma of the distribution is given by:

$$\sigma_0 = \sqrt{\langle n^2\rangle - \langle n\rangle^2}$$
$$= \sqrt{\mu(\mu+1)-\mu^2}$$
$$= \sqrt{\mu}$$

Going through the same derivations for the situation where you ignore the the events with no photoelectrons give:

$$\langle n\rangle_1 = \frac{\mu}{1-e^{-\mu}}$$
$$\langle n^2\rangle_1 = \frac{\mu(\mu+1)}{1-e^{-\mu}}$$
$$\sigma_1 = \sqrt{\frac{\mu}{1-e^{-\mu}} - \frac{\mu^2 e^{-\mu}}{(1-e^{-\mu})^2}}.$$

The limits for small n and large n are:

$$\lim_{\mu\to 0}\langle n\rangle_1 = 1$$
$$\lim_{\mu\to 0}\sigma_1 = 0$$
$$\lim_{\mu\to\infty}\langle n\rangle_1 = \mu$$
$$\lim_{\mu\to\infty}\sigma_1 = \sqrt{\mu}$$

The above assumes that the distribution for the photon electrons average at n and have zero width. If, instead, we assume that the distributions are still centered on n but have a width $\sigma(n) = \sqrt{n}\sigma_{pe}$. With this assumption, the above averages do not

change but the second moments become:

$$\left\langle n^2 \right\rangle_0 = \mu(\mu+1) + \mu\sigma_{pe}^2$$

$$\sigma_0^2 = \mu\left(1+\sigma_{pe}^2\right)$$

$$\sigma_1^2 = \frac{\mu\left(\left(1-e^{-\mu}\right)\left(1+\sigma_{pe}^2\right) - \mu e^{-\mu}\right)}{\left(1-e^{-\mu}\right)^2}$$

Limits for small and large numbers of PEs are:

$$\lim_{\mu\to 0}\sigma_1^2 = \sigma_{pe}^2 + \frac{1+\sigma_{pe}^2}{2}\mu$$

$$\lim_{\mu\to\infty}\sigma_1^2 = \mu\left(1+\sigma_{pe}^2\right)$$

Appendix E

R5912 Specifications from Hamamatsu

HAMAMATSU

PHOTOMULTIPLIER TUBE R5912

APPLICATIONS

● **For High Energy Physics**

GENERAL

Parameter		Description/Value	Unit
Spectral Response		300 to 650	nm
Wavelength of Maximum Response		420	nm
Photocathode	Material	Bialkali	—
	Effective Area	530 (Min. 450)	cm^2 Typ.
Window Material		Borosilicate glass	—
Dynode	Structure	Box and Line	—
	Number of Stages	10	—
Direct Interelectrode Capacitances (Approx.)	Anode to Last Dynode	3	pF
	Anode to All Other Dynode	7	pF
Base		20-pin base JEDEC B20-102	—
Weight		Approx. 720	g
Suitable Socket		E678-20A (supplied)	—

CHARACTERISTICS (at 25°C)

Parameter		Min.	Typ.	Max.	Unit
Cathode Sensitivity	Luminous (2856K)	—	70	—	μA/lm
	Radiant at 420nm	—	72	—	mA/W
	Blue (CS 5-58 filter)	—	9.0	—	μA/lm-b
	Quantum Efficiency at 390nm	—	22	—	%
Anode Sensitivity [1]	Luminous (2856K)	—	700	—	A/lm
	Radiant at 420nm	—	7.2×10^5	—	A/W
Gain [1]		—	1.0×10^7	—	—
Supply Voltage for Gain of 10^7		—	1500	1800	V
Anode Dark Current (after 30min. storage in darkness) [1]		—	50	700	nA
Dark Count (after dark condition for 15 hours) [1]		—	4	8	kcps
Time Response [1]	Anode Pulse Rise Time	—	3.8	—	ns
	Electron Transit Time	—	55	—	ns
	Transit Time Spread (FWHM) [3]	—	2.4	—	ns
Pre Pulse [4]	4ns to 20ns before Main pulse	—	0.5	2	%
Late Pulse [3]	8ns to 60ns after Main pulse	—	1.5	3	%
After Pulse [3]	100ns to 16μns after Main pulse	—	2	10	%
Single Photoelectron	PHD (Peak to Valley Ratio)	—	2.5	—	—
Pulse Linearity [2]	at ±2% Deviation	—	60	—	mA
	at ±5% Deviation	—	80	—	mA
Magnetic characteristics (at 200mG/20μT)	Sensitivity Degradation	—	10	—	%

1) Measured with the condition shown in the Table 1. 2) Measured with the condition shown in the Table 2.
3) Measured with 0.25 photoelectrons detection threshold (at single photoelectron/ event).
4) Measured with 0.25 photoelectrons detection threshold (at 50 photoelectron/ event).

PHOTOMULTIPLIER TUBE R5912

Table 1: VOLTAGE DISTRIBUTION RATIO AND SUPPLY VOLTAGE

Electrodes	K	Dy1	F2	F1	F3	Dy2	Dy3	Dy4	Dy5	Dy6	Dy7	Dy8	Dy9	Dy10	P
Ratio	11.3	0	0.6	0	3.4	5	3.33	1.67	1	1	1	1	1	1	

Supply Voltage: 1500Vdc, K: Cathode, Dy: Dynode, P: Anode, F: Focus

Table 2: TAPERED VOLTAGE DISTRIBUTION RATIO FOR LINEARITY MEASUREMENT

Electrodes	K	Dy1	F2	F1	F3	Dy2	Dy3	Dy4	Dy5	Dy6	Dy7	Dy8	Dy9	Dy10	P
Ratio	11.3	0	0.6	0	3.4	5	3.33	1.67	1	1.2	1.5	2.2	3	2.4	
Capacitors in µF												0.01	0.01	0.01	

Supply Voltage: 1500Vdc, K: Cathode, Dy: Dynode, P: Anode, F: Focus

MAXIMUM RATINGS (Absolute Maximum Values)

Parameter		Value	Unit
Supply Voltage	Between Anode and Cathode	1800	Vdc
	Between Anode and Last Dynode	300	V
Average Anode Current		0.1	mA
Average Cathode Current		100	nA
Ambient Temperature		-60 to +50	°C
Presure		7	atm

Figure 1: Typical Spectral Response

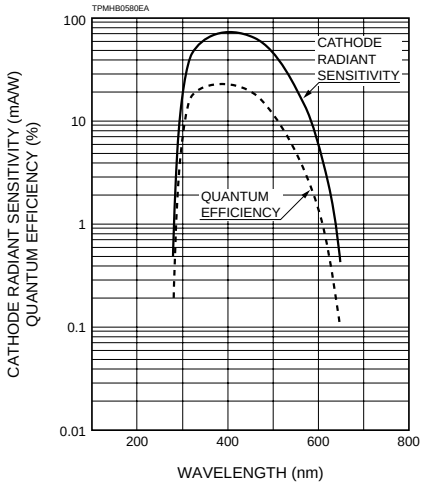

Figure 2: Typical Gain Caracteristic

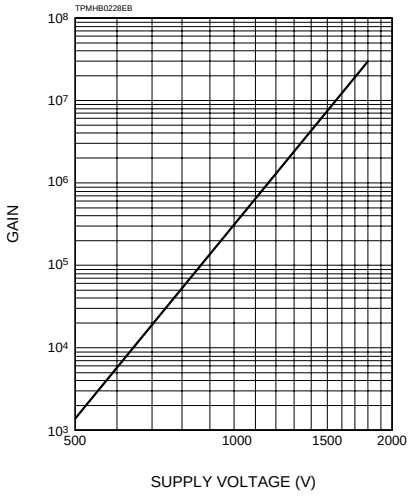

Figure 3: Pulse Height Distribution

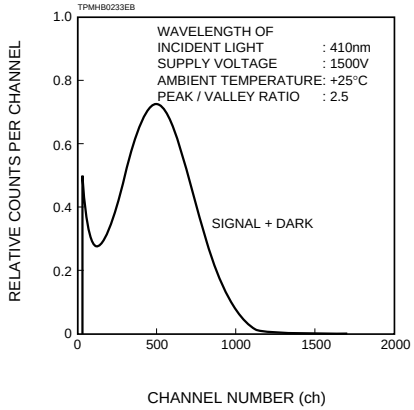

Figure 4: Transit Time Spread

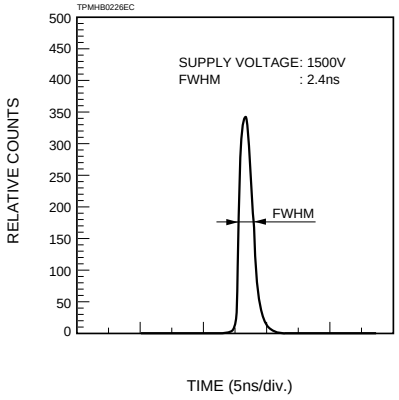

Figure 5: Typical Time Response

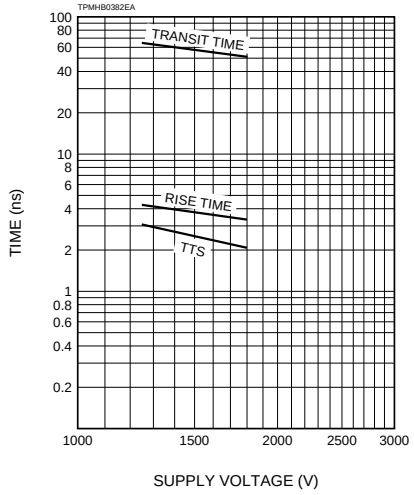

PHOTOMULTIPLIER TUBE R5912

Figure 6: Dimensional Outline and Voltage Divider (Unit: mm)

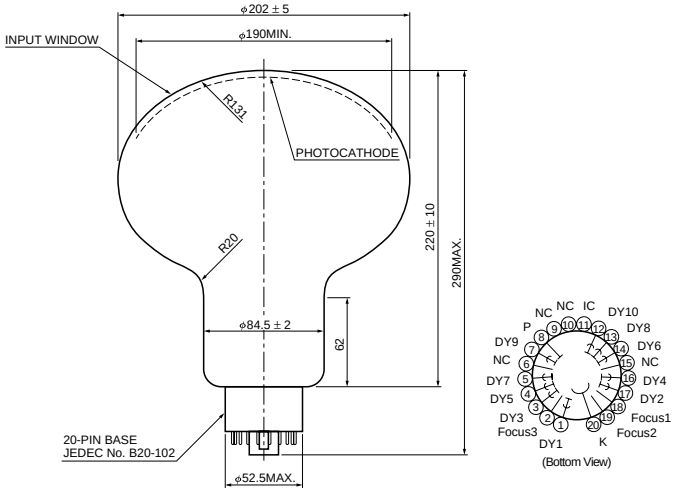

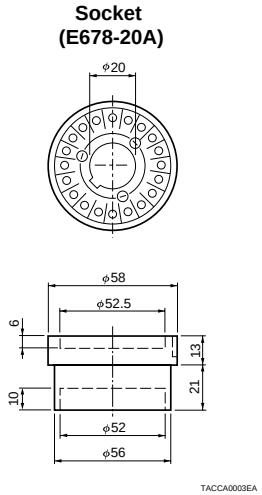

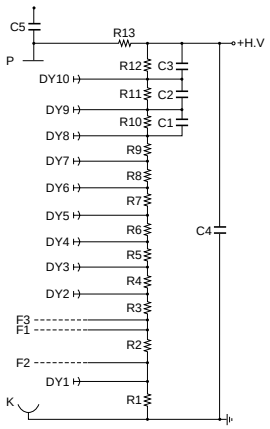

HAMAMATSU

HAMAMATSU PHOTONICS K.K., Electoron Tube Center
314-5, Shimokanzo, Toyooka-village, Iwata-gun, Shizuoka-ken, 438-0193, Japan, Telephone: (81)539/62-5248, Fax: (81)539/62-2205
U.S.A.: Hamamatsu Corporation: 360 Foothill Road, P. O. Box 6910, Bridgewater. N.J. 08807-0910, U.S.A., Telephone: (1)908-231-0960, Fax: (1)908-231-1218
Germany: Hamamatsu Photonics Deutschland GmbH: Arzbergerstr. 10, D-82211 Herrsching am Ammersee, Germany, Telephone: (49)8152-375-0, Fax: (49)8152-2658
France: Hamamatsu Photonics France S.A.R.L.: 8, Rue du Saule Trapu, Parc du Moulin de Massy, 91882 Massy Cedex, France, Telephone: (33)1 69 53 71 00, Fax: (33)1 69 53 71 10
United Kingdom: Hamamatsu Photonics UK Limited: Lough Point, 2 Gladbeck Way, Windmill Hill, Enfield, Middlesex EN2 7JA, United Kingdom, Telephone: (44)181-367-3560, Fax: (44)181-367-6384
North Europe: Hamamatsu Photonics Norden AB: Färögatan 7, S-164-40 Kista Sweden, Telephone: (46)8-703-29-50, Fax: (46)8-750-58-95
Italy: Hamamatsu Photonics Italia: S.R.L.: Strada della Moia, 1/E, 20020 Arese, (Milano), Italy, Telephone: (39)02-935 81 733, Fax: (39)02-935 81 741

TPMH1235E01
SEPT. 1998 IP